TUM School of Computation, Information and Technology

Single-Anchor Multi-Antenna Positioning for Millimeter-Wave Systems

Anastasios Kakkavas

Vollständiger Abdruck der von der TUM School of Computation, Information and Technology der Technischen Universität München zur Erlangung des akademischen Grades eines

Doktors der Ingenieurwissenschaften

genehmigten Dissertation.

Vorsitz: Prof. Dr.-Ing. Thomas Eibert

Prüfer*innen der Dissertation:

1. Prof. Dr. techn. Dr. h. c. Josef A. Nossek
2. Prof. Gonzalo Seco-Granados, Ph.D.
3. Prof. Dr.-Ing. Eckehard Steinbach

Die Dissertation wurde am 08.02.2023 bei der Technischen Universität München eingereicht und durch die TUM School of Computation, Information and Technology am 12.09.2023 angenommen.

Abstract

Single-anchor positioning has been identified as a promising solution for fifth generation (5G) wireless networks, easing the requirement for multi-anchor connectivity and resource allocation, leveraging the large bandwidths available at millimeter-wave (mm-Wave) frequencies and the large number of antennas that can be packed in mm-Wave transceivers. In this work, we investigate single-anchor positioning with multi-antenna transceivers in sparse mm-Wave channels, focusing on the effect of imperfect time synchronization between the transmitter and the receiver. We study how single-bounce non-LOS (NLOS) paths can be used to jointly estimate the target's position and the synchronization error and improve positioning accuracy. The study includes the analysis of the theoretical performance bounds, as well as the development of a novel Cramér-Rao lower bound (CRLB)-achieving single-anchor localization algorithm that exploits the information about the synchronization error offered by NLOS multipath components. Furthermore, we propose reference signal optimization strategies using prior information about the target and the environment and investigate the effect of the synchronization error in the resulting optimized reference signals.

Contents

1. Introduction

Radio-based positioning, that is the estimation of the location of a target by transmission, reception and processing of radio frequency (RF) signals, is a problem that has been studied for decades. The first wireless direction finding system was patented in 1902 by Stone and the first ranging system, i.e., a system that estimates the distance of a target from a reference location, was patented in 1904 by de Forest [1]. Initially and for a long time, positioning techniques were developed for military and safety applications [2]. A big leap forward was the introduction of the Global Positioning System (GPS), which was originally developed for use by the United States (US) military and was the first global navigation satellite system (GNSS). GPS made positioning services available to and easily accessible by the public, as anybody could use it by just employing a GPS receiver, and unlocked a vast spectrum of new use cases.

Safety-related services were also the main driver for adoption of positioning technologies in cellular systems. Although positioning methods were already used in the first generation (1G) of cellular systems, their standardization efforts in the Third Generation Partnership Project (3GPP), the standardization body developing cellular network standards, started some years later in 2G and were intensified after the release of accuracy requirements by the US Federal Communications Commission (FCC) for positioning devices on 911 emergency calls [3]. 2G standardized techniques were based on time difference of arrival (TDOA), cell identity (CID) and GPS (autonomous or assisted) [4]. Since then, a lot of progress has been made regarding the support of positioning services by 3GPP standards. With Release 17 (the third release of 5G) a variety of positioning techniques, based on measurements from the cellular network, other wireless technologies and sensors, as well as combinations thereof [5], have been incorporated.

5G has already been deployed in many countries worldwide, with the vision of providing unprecedentedly high data rates, massive connectivity and reduced latency, among others, which can be enabled by the large bandwidth available at millimeter-wave (mm-Wave) frequencies, massive number of antennas and dense deployment of base stations. Coincidentally or not, these enablers provide fertile ground for a radical improvement of the positioning capabilities of wireless communication networks [6]. The expected improvement of localization[1] accuracy of communication networks can be a key driving force in the realization of scenarios such as assisted living [7], smart factories [8] and automated driving [9], where GNSS and other existing technologies may not be able to guarantee the desired positioning accuracy under all conditions. Moreover, it is anticipated that position information will be used as an input to communication-related tasks, such as proactive resource allocation [10], beamforming [11] and beam-alignment [12].

[1] The terms "localization" and "positioning" are used interchangeably throughout the document

In an effort to unlock the great potential of wireless networks to provide accurate positioning, numerous works on the topic have been published. Theoretical analyses of the achievable positioning accuracy under a multi-anchor setup have been presented in [13]–[17]. The achievable positioning accuracy is evaluated in these works using the Cramér-Rao lower bound (CRLB), which is a bound on the variance of the error of any unbiased estimator and is based on Fisher information (FI), which quantifies the amount of information about a parameter that can be extracted by observation of a random variable, whose probability distribution is parameterized by the said parameter. Despite promising high accuracy, multi-anchor positioning might not always be possible at millimeter-wave (mm-Wave) frequencies due to the lack of significantly strong links to two or more anchors. In mm-Wave frequencies the path loss between isotropic antennas[2] is increased as a consequence of their decreased effective area/aperture and beamforming gains are required to compensate for it.

On the other hand, the fact that, in mm-Wave frequencies, more antennas can be packed in the same physical area allows for transceivers with a large number of antenna elements, both on the netowrk and the user equipment (UE) side, which in turn enable accurate angle of departure (AOD) and angle of arrival (AOA) estimation. Also, the large bandwidth available at mm-Wave frequencies enables accurate time of arrival (TOA) or TDOA measurements. Apart from higher accuracy, the large bandwidth and number of antennas provide superior temporal and spatial resolution. Therefore, multipath components are more likely to be resolved and exploited for the localization task. Hence, reliable position estimation is possible with a single anchor. In this thesis, we focus on single-anchor positioning, by studying its theoretical performance bounds, developing a single-anchor positioning algorithm and optimizing the reference signal for single-anchor positioning.

1.1 Related Works

In recent years, single-anchor localization, which is the focus of this thesis, has received increasing attention. In [18] the CRLB for single-anchor line-of-sight (LOS)-only positioning was presented, deriving a necessary condition on the reference signal for a non-singular Fisher information matrix (FIM). Single-anchor localization performance bounds were derived in [19] for arrays with different beamforming strategies, considering multipath propagation and taking synchronization errors and quantization errors of beamforming weights into account. The authors of [20] provided asymptotic expressions for the position error bounds in sparse mm-Wave channels with large bandwidth and large number of antennas, exploiting the asymptotic orthogonality of multipath components, and conducted a comparison between downlink and uplink positioning. In [21] it was shown that the FIM provided by single-bounce non-LOS (NLOS) paths is rank-1 and analytic expressions for the direction and intensity of position and orientation information were obtained. In [22], the single-anchor localization error bounds with a multicarrier waveform were derived and an algorithm approaching these bounds for sufficiently high signal-to-noise ratio (SNR) was presented. Apart from [19], the aforementioned works assume no synchronization errors, which is difficult to obtain in practical communication systems. Although [19] considered imperfect synchronization and multipath propagation, the potential exploitation of multipath components to estimate the synchronization errors was not considered.

[2]Isotropic antennas are only assumed as a theoretical tool; in practice, antenna elements with potentially similar properties are used.

As far as single-anchor localization algorithms are concerned, relevant works in the literature can be classified into two categories: one-shot schemes without tracking [22]–[29], and approaches with tracking [30]–[36]. While the latter mainly focus on positon estimation and tracking given the channel parameter measurements, the former also deal with the estimation of the channel parameters, as done in this work. A three-stage algorithm for the estimation of the UE state (position and orientation) with a multiple-input multiple-output (MIMO)-orthogonal frequency-division multiplexing (OFDM) system was proposed in [22], where in the first stage a compressed sensing-based algorithm is used to obtain coarse estimates of the multipath parameters (number of paths, TOAs, AODs, AOAs and gains), with the coarse estimates refined in the second stage. In the third stage, the refined estimates are mapped to the receiver (Rx) position and orientation and the positions of the points of incidence (POIs), which correspond to scattering or reflection, using the extended invariance principle (EXIP). A similar approach is followed in [23], with the main difference being the mapping from channel parameters to position parameters, where an iterative Gibbs sampling method is employed. In [24] range-free angle-based approaches are developed assuming prior map information. A downlink (DL) positioning algorithm for a single-antenna Rx, based on TOA and AOD measurements is proposed in [28]. The work is extended in [29], where a two-step process is used, with the coarse parameter estimates obtained in the first step used for adaptation of the transmitter (Tx) beamforming matrix in the second step. Additionally, in [37] an iterative Tx beamforming refinement and position estimation algorithm is developed.

Similar to [29], [37], many works have considered the use of prior knowledge of the Rx position at the Tx to design beamformers that improve the Rx's localization accuracy. In [38] CRLB-optimal precoders for tracking the AOD and AOA of a path were designed, taking the uncertainty about their value into account. In [39], assuming a LOS channel and a multicarrier system, beamformers minimizing the TOA and AOA error bounds were proposed, based on the current estimate of the Rx position. Using a similar setup, but additionally considering multiple users, the authors of [40] designed beamformers maximizing a weighted sum of Fisher information on delay, AOD and AOA. Although in a different context, the algorithms and conclusions of [41] and [42] are relevant to our Tx beamforming problem. In [41] and [42], robust beamformers under angular uncertainty were designed and it was concluded that the Rx steering vector and its derivative contain all the localization information. Again in a different but still relevant setup, the authors of [43] and [44] computed the optimal power allocation among multiple anchors for ranging-based localization by solving a semidefinite program (SDP). The power allocation problem was formulated as the computation of either the optimal sharing of a fixed available total power budget among the network anchors so as to minimize the squared position error bound (SPEB) of a target or the power allocation vector with the minimum sum power that satisfies a set of predefined positioning accuracy constraints.

1.2 Outline and Main Contributions

In Chapter 2, we introduce the signal model for two-dimensional (2D) single-anchor positioning with a MIMO-OFDM system in sparse mm-Wave channels, where only single-bounce NLOS paths are assumed strong enough for reception [45]–[47]. Through asymptotic FI analysis for large bandwidth and number of antennas, we extend prior works showing that the direction of position information offered by single-bounce reflections is parallel to the reflecting surface, independent of the Tx and Rx locations and study the effect of prior environmental knowledge at the Rx, expressed as knowledge about the location of virtual anchors (VAs) corresponding to multipath components,

on the achievable positioning accuracy. Furthermore, we study the impact of synchronization errors on the achievable positioning accuracy and their joint estimation with position and orientation exploiting multipath components. Additionally, considering a mobile Tx or Rx, we study the effect of the Doppler shift on the Fisher information and prove that the FIM corresponding to the information contribution of each single-bounce NLOS path is rank-2. We also compare DL and uplink (UL) positioning under device-specific Tx/Rx constraints and show that the link with the highest Rx SNR offers the highest accuracy.

In Chapter 3, we propose a novel algorithm for single-anchor position, orientation and clock offset estimation in a static setup. The first stage consists of an off-grid channel parameter estimation method, based on [48]. For the required on-grid potential path search step, we consider both a full dimensional (three-dimensional (3D)) search, as well as a lower-complexity 2D search, based on a lower bound on the objective. For the required local refinement step, which enables the off-grid path parameter estimation, we employ a modified Newton step approach. The second stage maps the channel parameter estimates to position parameters. The information about the clock offset offered by NLOS paths in combination with the LOS path is exploited, so as to discard false alarms, i.e. to reject detected NLOS paths from the first stage of the algorithm which are unlinkely to correspond to a single-bounce. Numerical results, including comparison with the state of the art (SotA) are presented to show the importance of off-grid channel parameter estimation and path rejection.

In Chapter 4, we consider the problem of optimized reference signal transmission under perfect or imperfect prior knowledge of the positioning-related parameters at the Tx. For a LOS-only channel and perfect prior knowledge at the Tx, i.e., uncertainty about the Rx location not considered in the design, we compute the optimal beamforming directions and their corresponding energy allocation, as well as the optimal energy allocation over a fixed set of beams, which we refer to as a beam codebook. For a multipath channel, we consider a fixed beam codebook and propose energy allocation strategies under perfect and imperfect prior knowledge. Different optimization approaches with varying complexity are proposed and evaluated in terms of their resulting position error bound (PEB), as well as their root mean square error (RMSE) performance using the algorithm proposed in Chapter 3. The effect of imperfect synchronization and LOS illumination are studied and taken into account in the proposed designs.

1.3 Notation and List of Frequently Used Symbols

We use bold lowercase for column vectors, bold uppercase for matrices, non-bold for scalars and calligraphic letters for sets. Depending on its argument, $|\cdot|$ denotes the absolute value of a scalar, the determinant of a matrix or the cardinality of a set. The operators $(\cdot)^{\mathrm{T}}$ and $(\cdot)^{\mathrm{H}}$ denote the transpose and the conjugate transpose of a vector or matrix, $\|\cdot\|_2$ denotes the Euclidean norm of a vector and $\Re\{\cdot\}$ and $\Im\{\cdot\}$ denote the real and imaginary part of a complex number. The i-th element of a vector $\boldsymbol{x}$ and the (i,j)-th element of a matrix $\boldsymbol{X}$ are denoted by x_i and $X_{i,j}$, respectively. The expectation operator is denoted by $\mathbb{E}[\cdot]$ and the sets of real and complex numbers are denoted by $\mathbb{R}$ and $\mathbb{C}$. A multivariate (circularly symmetric complex) Gaussian distribution with mean $\boldsymbol{\mu}$ and covariance matrix $\boldsymbol{C}$ is denoted by $\mathcal{N}(\boldsymbol{\mu},\boldsymbol{C})$ ($\mathcal{N}_{\mathbb{C}}(\boldsymbol{\mu},\boldsymbol{C})$). A list of frequently used symbols is provided in Table 1.1.

Table 1.1: List of frequently used symbols

$\boldsymbol{a}_{\mathrm{R},p}(\cdot)$	Rx steering vector at the p-th subcarrier
$\boldsymbol{a}_{\mathrm{T},p}(\cdot)$	Tx steering vector at the p-th subcarrier
c	speed of light
$d_{\mathrm{R,s},l}$	distance of the l-th POI (scatterer/reflector) from the Rx
$d_{\mathrm{T,s},l}$	distance of the l-th POI (scatterer/reflector) from the Tx
E_{RE}	average transmit energy per resource element
E_{tot}	total transmit energy
$\boldsymbol{F}$, $\boldsymbol{f}_k$	beam codebook and its k-th beamforming vector
f_{s}	sampling rate
f_{c}	carrier frequency
$\boldsymbol{H}[p]$	channel matrix at the p-th OFDM subcarrier
h_l	complex gain of the l-th path
$\boldsymbol{J}_{\boldsymbol{\nu}}$	FIM of the parameter vector $\boldsymbol{\nu}$
L	number of propagation paths
M_{T}	number of beamforming vectors in the beam codebook
N	number of OFDM subcarriers
N_{B}	number of OFDM symbols
N_{P}	number of used OFDM subcarriers
N_{R}	number of Rx antennas
N_{T}	number of Tx antennas
$\mathcal{P}$	set of used OFDM subcarriers
P_{fa}	probability of false alarm
$\boldsymbol{p}_{\mathrm{s},l}$	position of l-th POI corresponding to scatterer or reflector
$\boldsymbol{p}_{\mathrm{R}}$	Rx position
$\boldsymbol{p}_{\mathrm{T}}$	Tx position
$\boldsymbol{p}_{\mathrm{VA},l}$	position of l-th VA
q_k	fraction of E_{tot} allocated to the k-th beamforming vector in the beam codebook
$\mathcal{R}$	resource grid
$\mathcal{R}_k$	set of resource elements allocated to the k-th beamforming vector of the beam codebook
$S_{\mathrm{R}}(\tilde{\theta})$	Rx squared array aperture function (SAAF)
$S_{\mathrm{T}}(\tilde{\theta})$	Tx SAAF

Continued on next page

Table 1.1: List of frequently used symbols (Continued)

$t_{\mathrm{rms},l}$	root mean square duration of the signal propagated through the l-th path
T_{s}	sampling period
$\boldsymbol{u}(\theta)$, $\boldsymbol{u}_{\perp}(\theta)$	2D unit vectors at angles θ and $\theta - \pi/2$
$\boldsymbol{v}_{\mathrm{R}}$	Rx velocity
$\boldsymbol{v}_{\mathrm{T}}$	Tx velocity
$\boldsymbol{W}_{\mathrm{R}}$	Rx analog beamforming matrix
$\boldsymbol{W}_{\mathrm{T}}$	Tx analog beamforming matrix
$\boldsymbol{x}[p, b]$	reference signal at the p-th subcarrier of the b-th OFDM symbol
$\boldsymbol{y}[p, b]$	received signal at the p-th subcarrier of the b-th OFDM symbol
α_{R}	Rx orientation
α_{T}	Tx orientation
β	effective baseband bandwidth
$\gamma_k[p, b]$	fraction of q_k allocated to the p-th subcarrier of the b-th OFDM symbol
$\delta_{\mathrm{R,T}}$	pseudo SNR
ϵ_{clk}	clock synchronization error
$\tilde{\theta}_{\mathrm{T},l}$, $\theta_{\mathrm{T},l}$,	AOD of the l-th path relative to the array's and the global frame of reference
$\tilde{\theta}_{\mathrm{R},l}$, $\theta_{\mathrm{R},l}$,	AOA of the l-th path relative to the array's and the global frame of reference
ρ_l	transverse velocity component of the l-th path
σ^2_{clk}	clock synchronization error variance
$\sigma^2_{\eta,\mathrm{R}}$	noise variance
τ_l	TOA of the l-th path
ξ_l	intensity effect of Doppler shift on path l
$\bar{\omega}_c$	effective carrier angular frequency
ω_p	angular (baseband) frequency of the p-th OFDM subcarrier

2. Performance Limits of Single-Anchor Millimeter-Wave Positioning

2.1 System Model

In this section we present the signal model when both the transmitter and the receiver are static, and then we extend the model to the dynamic scenario, where either the transmitter or the receiver is moving.

2.1.1 Static Scenario

2.1.1.1 Geometry

The Tx consists of an array with N_{T} antennas, with its reference point located at $\boldsymbol{p}_{\mathrm{T}} = \left[p_{\mathrm{T,x}},\ p_{\mathrm{T,y}}\right]^{\mathrm{T}} \in \mathbb{R}^2$ and orientation α_{T}. The Rx consists of an array with N_{R} antennas, a reference point located at $\boldsymbol{p}_{\mathrm{R}} = \left[p_{\mathrm{R,x}},\ p_{\mathrm{R,y}}\right]^{\mathrm{T}} \in \mathbb{R}^2$ and orientation α_{R}. The position of the j-th element of the Tx array is given by

$$\boldsymbol{p}_{\mathrm{T},j} = \boldsymbol{p}_{\mathrm{T}} + d_{\mathrm{T},j}\boldsymbol{u}(\psi_{\mathrm{T},j} + \alpha_{\mathrm{T}}) \in \mathbb{R}^2, \quad j = 0, \ldots, N_{\mathrm{T}} - 1, \tag{2.1}$$

where $\boldsymbol{u}(\psi) = \left[\cos(\psi),\ \sin(\psi)\right]^{\mathrm{T}}$ and $d_{\mathrm{T},j}$ and $\psi_{\mathrm{T},j}$ are its distance and angle from the Tx array's reference point, as shown in Fig. 2.1. Accordingly, the position of the i-th element of the Rx array is given by

$$\boldsymbol{p}_{\mathrm{R},i} = \boldsymbol{p}_{\mathrm{R}} + d_{\mathrm{R},i}\boldsymbol{u}(\psi_{\mathrm{R},i} + \alpha_{\mathrm{R}}) \in \mathbb{R}^2, \quad i = 0, \ldots, N_{\mathrm{R}} - 1. \tag{2.2}$$

We assume that for all Tx-Rx antenna pairs there are L discrete propagation paths. The first of these L paths ($l = 0$) is either the LOS path or a single-bounce NLOS path and the rest ($l = 1, \ldots, L-1$) are single-bounce NLOS paths. The POI of the l-th single-bounce path, which corresponds either to scattering or reflection, is $\boldsymbol{p}_{\mathrm{s},l} = \left[p_{\mathrm{s},l,\mathrm{x}},\ p_{\mathrm{s},l,\mathrm{y}}\right]^{\mathrm{T}}$.

The arrays' dimensions are assumed to be small compared to the distance between the Tx and Rx, as well as the distance between each of the scatterers/reflectors and the Tx or Rx, i.e.,

$$D_{\max} \ll \min\left(\|\boldsymbol{p}_{\mathrm{R}} - \boldsymbol{p}_{\mathrm{T}}\|_2, \min_l \|\boldsymbol{p}_{\mathrm{s},l} - \boldsymbol{p}_{\mathrm{T}}\|_2, \min_l \|\boldsymbol{p}_{\mathrm{R}} - \boldsymbol{p}_{\mathrm{s},l}\|_2\right), \tag{2.3}$$

where

$$D_{\max} = \max(D_{\max,\mathrm{T}}, D_{\max,\mathrm{R}}) \tag{2.4}$$

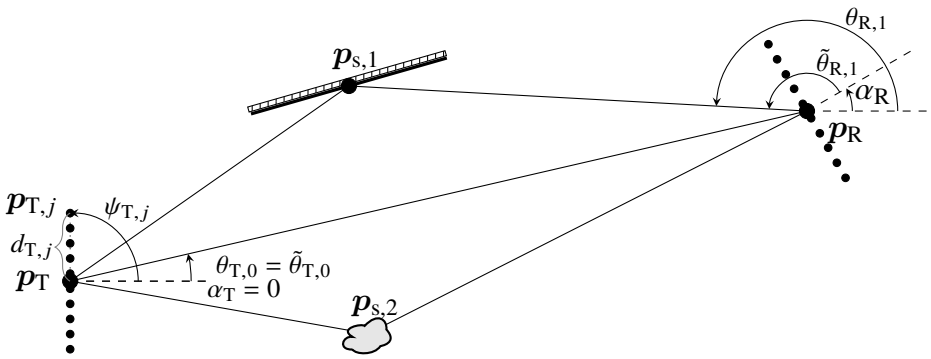

Fig. 2.1. Geometric model, example with uniform linear arrays (ULAs) at the Tx and Rx.

and

$$D_{\max,\mathrm{T}} = \max_{j,j'} \|\boldsymbol{p}_{\mathrm{T},j} - \boldsymbol{p}_{\mathrm{T},j'}\|_2, \tag{2.5}$$

$$D_{\max,\mathrm{R}} = \max_{i,i'} \|\boldsymbol{p}_{\mathrm{R},i} - \boldsymbol{p}_{\mathrm{R},i'}\|_2 \tag{2.6}$$

are the largest dimensions of the Tx and Rx arrays. Using this assumption, the delay of the l-th path from the j-th Tx element to the i-th Rx element can be approximated by

$$\tau_{l,i,j} \approx \tau_l - \tau_{\mathrm{T},j}(\tilde{\theta}_{\mathrm{T},l}) - \tau_{\mathrm{R},i}(\tilde{\theta}_{\mathrm{R},l}), \quad l = 0, \ldots, L-1, \tag{2.7}$$

where

$$\tau_l = \frac{1}{c} \cdot \begin{cases} \|\boldsymbol{p}_{\mathrm{R}} - \boldsymbol{p}_{\mathrm{T}}\|_2, & l\text{-th path is LOS}, \\ \|\boldsymbol{p}_{\mathrm{s},l} - \boldsymbol{p}_{\mathrm{T}}\|_2 + \|\boldsymbol{p}_{\mathrm{R}} - \boldsymbol{p}_{\mathrm{s},l}\|_2, & \text{otherwise}, \end{cases} \tag{2.8}$$

$$\tau_{\mathrm{T},j}(\tilde{\theta}_{\mathrm{T},l}) = \frac{d_{\mathrm{T},j}}{c} \boldsymbol{u}^{\mathrm{T}}(\psi_{\mathrm{T},j}) \boldsymbol{u}(\tilde{\theta}_{\mathrm{T},l}) = \frac{d_{\mathrm{T},j}}{c} \cos(\tilde{\theta}_{\mathrm{T},l} - \psi_{\mathrm{T},j}), \tag{2.9}$$

$$\tau_{\mathrm{R},i}(\tilde{\theta}_{\mathrm{R},l}) = \frac{d_{\mathrm{R},i}}{c} \boldsymbol{u}^{\mathrm{T}}(\psi_{\mathrm{R},i}) \boldsymbol{u}(\tilde{\theta}_{\mathrm{R},l}) = \frac{d_{\mathrm{R},i}}{c} \cos(\tilde{\theta}_{\mathrm{R},l} - \psi_{\mathrm{R},i}), \tag{2.10}$$

and c is the speed of light. τ_l represents the time of flight (TOF) of the signal propagated through the $l-$th path from the Tx reference point to $\boldsymbol{p}_{\mathrm{T}}$ to the Rx reference point to $\boldsymbol{p}_{\mathrm{R}}$. The AOD relative to the orientation of the Tx array and the AOA relative to the orientation of the Rx array for the l-th path are defined as

$$\tilde{\theta}_{\mathrm{T},l} = \begin{cases} \operatorname{atan2}\Big(p_{\mathrm{R,y}} - p_{\mathrm{T,y}}, p_{\mathrm{R,x}} - p_{\mathrm{T,x}}\Big) - \alpha_{\mathrm{T}}, & l\text{-th path is LOS}, \\ \operatorname{atan2}\Big(p_{\mathrm{s},l,\mathrm{y}} - p_{\mathrm{T,y}}, p_{\mathrm{s},l,\mathrm{x}} - p_{\mathrm{T,x}}\Big) - \alpha_{\mathrm{T}}, & \text{otherwise}, \end{cases} \tag{2.11}$$

$$\tilde{\theta}_{\mathrm{R},l} = \begin{cases} \operatorname{atan2}\Big(p_{\mathrm{T,y}} - p_{\mathrm{R,y}}, p_{\mathrm{T,x}} - p_{\mathrm{R,x}}\Big) - \alpha_{\mathrm{R}}, & l\text{-th path is LOS}, \\ \operatorname{atan2}\Big(p_{\mathrm{s},l,\mathrm{y}} - p_{\mathrm{R,y}}, p_{\mathrm{s},l,\mathrm{x}} - p_{\mathrm{R,x}}\Big) - \alpha_{\mathrm{R}}, & \text{otherwise}, \end{cases} \tag{2.12}$$

with $\operatorname{atan2}\big(y, x\big)$ being the four-quadrant inverse tangent function. The absolute AOD $\theta_{\mathrm{T},l}$ and AOA $\theta_{\mathrm{R},l}$ are computed as

$$\theta_{\mathrm{T},l} = \tilde{\theta}_{\mathrm{T},l} + \alpha_{\mathrm{T}}, \ l = 0, \ldots, L-1, \tag{2.13}$$

$$\theta_{\mathrm{R},l} = \tilde{\theta}_{\mathrm{R},l} + \alpha_{\mathrm{R}}, \ l = 0, \ldots, L-1, \tag{2.14}$$

and for $l = 0$ being the LOS we have $\theta_{\mathrm{R},0} = \theta_{\mathrm{T},0} + \pi$.

2.1.1.2 Signal Model

An OFDM waveform with subcarrier spacing Δf, N subcarriers and cyclic prefix (CP) duration $T_{\mathrm{CP}} = N_{\mathrm{CP}} T_{\mathrm{s}}$ is considered, where $T_{\mathrm{s}} = 1/(N\Delta f)$ and $f_{\mathrm{s}} = 1/T_{\mathrm{s}}$ are the sampling period and frequency, respectively. The reference signal is transmitted on N_{B} OFDM symbols and N_{P} subcarriers, whose indices are $\mathcal{P} = \{-N_{\mathrm{P}}/2, \ldots, -1, 1, \ldots, N_{\mathrm{P}}/2\}$, while the rest of the subcarriers are left empty, where, without loss of generality we assume that N_{P} is even and $N_{\mathrm{P}} < N$. The edge subcarriers with indices $-N/2, \ldots, -N_{\mathrm{P}}/2 - 1, N_{\mathrm{P}}/2, \ldots, N$ form the so called guard bands, which are commonly introduced in practical OFDM systems to ease the requirements on the analog filtering after the digital-to-analog conversion (DAC). We note that here we have assumed, without loss of generality, that all occupied subcarriers carry reference signals. The reference signal resource grid $\mathcal{R}$ comprises all resource elements at the time-frequency points $(p, b),\ p \in \mathcal{P},\ b = 0, \ldots, N_{\mathrm{B}} - 1$.

In mm-Wave systems with potentially large number of antennas, in order to keep the power consumption at acceptable levels, the Tx might be equipped with only $N_{\mathrm{RF,T}} \leq N_{\mathrm{T}}$ RF chains. The transmitter uses a digital beam codebook $\boldsymbol{F}' \in \mathbb{C}^{N_{\mathrm{RF,T}} \times M_{\mathrm{T}}}$

$$\boldsymbol{F}' = [\boldsymbol{f}'_1,\ \ldots,\ \boldsymbol{f}'_{M_{\mathrm{T}}}], \tag{2.15}$$

$\{\boldsymbol{f}'_k\}_{k=1}^{M_{\mathrm{T}}}$, where $\boldsymbol{f}'_k \in \mathbb{C}^{N_{\mathrm{RF,T}}}$ is the $k-th$ beamforming vector of the codebook, with $\|\boldsymbol{f}'_k\|_2 = 1, \forall k$, and M_{T} is the number of beamforming vectors in the codebook. The k-th beamforming vector is used on a subset $\mathcal{R}_k$ of resource elements (REs) (p, b), with $\mathcal{R}_k \cap \mathcal{R}_{k'} = \emptyset$ for $k \neq k'$ and $\cup_k \mathcal{R}_k = \mathcal{R}$. The digital Tx signal vector $\boldsymbol{s}[p, b] \in \mathbb{C}^{N_{\mathrm{RF,T}}}$ at the p-th subcarrier, $p \in \mathcal{P}$, of the b-th OFDM symbol, $b = 0, \ldots, N_{\mathrm{B}} - 1$, then is

$$\boldsymbol{s}[p, b] = \lambda_k[p, b]\boldsymbol{f}'_k,\ (p, b) \in \mathcal{R}_k, \tag{2.16}$$

where

$$\lambda_k[p, b] = \sqrt{E_{\mathrm{tot}} q_k \gamma_k[p, b]}\, \mathrm{e}^{\mathrm{j}\beta_k[p,b]} \tag{2.17}$$

is the symbol assigned to $\boldsymbol{f}'_k$ at the p-th subcarrierof the b-th OFDM symbol, E_{tot} is the total Tx energy of the reference signal, q_k is the fraction of E_{tot} allocated to $\boldsymbol{f}'_k$, with $\sum_{k=1}^{M_{\mathrm{T}}} q_k = 1$, $\gamma_k[p, b]$ is the fraction of q_k allocated to the RE (p, b), with $\sum_{(p,b)\in\mathcal{R}_k} \gamma_k[p, b] = 1$, and $\beta_k[p, b]$ is the phase of $\lambda_k[p, b]$.

The digital signal vector is then multiplied with the analog beamforming matrix $\boldsymbol{W}_{\mathrm{T}}$ to get the Tx signal vector $\boldsymbol{x}[p, b]$:

$$\begin{aligned} \boldsymbol{x}[p, b] &= \boldsymbol{W}_{\mathrm{T}}^* \boldsymbol{s}[p, b] \\ &= \lambda_k[p, b]\boldsymbol{f}_k,\ (p, b) \in \mathcal{R}_k, \end{aligned} \tag{2.18}$$

where

$$\boldsymbol{f}_k = \boldsymbol{W}_{\mathrm{T}}^* \boldsymbol{f}'_k, \quad k = 1, \ldots, M_{\mathrm{T}}, \tag{2.19}$$

are the beamforming vectors of the effective beam codebook $\boldsymbol{F} = \boldsymbol{W}_{\mathrm{T}}^* \boldsymbol{F}'$. When no analog precoding is applied, $N_{\mathrm{T}} = N_{\mathrm{RF,T}}$ and $\boldsymbol{W}_{\mathrm{T}} = \boldsymbol{I}_{N_{\mathrm{T}}}$. We note that the average Tx energy per resource element is

$$E_{\mathrm{RE}} = \frac{E_{\mathrm{tot}}}{N_{\mathrm{P}} N_{\mathrm{B}}} \tag{2.20}$$

and the average Tx energy per time-domain sample (disregarding the energy spent on the CP) is

$$E_{\mathrm{T}} = E_{\mathrm{RE}} \frac{N_{\mathrm{P}}}{N}. \tag{2.21}$$

Similar to the Tx, the Rx might be equipped with only $N_{\mathrm{RF,R}} \leq N_{\mathrm{R}}$ RF chains, applying an analog receive combiner $\boldsymbol{W}_{\mathrm{R}}^{\mathrm{H}}$, with $\boldsymbol{W}_{\mathrm{R}} \in \mathbb{C}^{N_{\mathrm{R}} \times N_{\mathrm{RF,R}}}$, to obtain an $N_{\mathrm{RF,R}}$-dimensional signal that is fed to the analog-to-digital conversions (ADCs). When no analog Rx combiner, is applied $N_{\mathrm{R}} = N_{\mathrm{RF,R}}$ and $\boldsymbol{W}_{\mathrm{R}} = \boldsymbol{I}_{N_{\mathrm{R}}}$.

Assuming high resolution ADC and DAC, such that the system is practically linear, the pulse $\tilde{g}(t)$ models all the Tx and Rx processing steps, namely upsampling, digital Tx filtering/pulse shaping, DAC, analog Tx filtering, upconversion and amplification, downconversion, Rx filtering, ADC, digital Rx filtering/pulse shaping and downsampling. The time support of $\tilde{g}(t)$ is included in $[0, \tau_g]$. The pulse $\tilde{g}(t)$ is also assumed to be essentially band-limited, with its Fourier transform being essentially non-zero in $[-f_s/2, f_s/2]$, which is an approximation, as a pulse can only be either time-limited or band-limited.

The Tx and Rx are assumed to be imperfectly time-synchronized, with a clock synchronization error ϵ_{clk}, which is assumed to be a zero-mean Gaussian distributed random variable with variance σ_{clk}^2. We note that $\sigma_{\mathrm{clk}}^2 = 0$ corresponds to perfectly time-synchronization and $\sigma_{\mathrm{clk}}^2 \to \infty$ to asynchronous operation, i.e., to the case when the Rx has no knowledge about the time of transmisssion (TOT).

The received signal at the p-th subcarrier of the b-th OFDM symbol is

$$\boldsymbol{y}[p,b] = \boldsymbol{m}[p,b] + \boldsymbol{W}_{\mathrm{R}}^{\mathrm{H}} \boldsymbol{\eta}[p,b], \tag{2.22}$$

where

$$\boldsymbol{m}[p,b] = \boldsymbol{W}_{\mathrm{R}}^{\mathrm{H}} \boldsymbol{H}[p] \boldsymbol{x}[p,b], \tag{2.23}$$

$$\boldsymbol{H}[p] = \sum_{l=0}^{L-1} h_l \, \mathrm{e}^{-\mathrm{j}\,\omega_p \tau_l'} \, \boldsymbol{a}_{\mathrm{R},p}(\tilde{\theta}_{\mathrm{R},l}) \boldsymbol{a}_{\mathrm{T},p}^{\mathrm{T}}(\tilde{\theta}_{\mathrm{T},l}) \tag{2.24}$$

$$\boldsymbol{a}_{\mathrm{T},p}(\tilde{\theta}_{\mathrm{T},l}) = \left[e^{\mathrm{j}(\omega_{\mathrm{c}}+\omega_p)\tau_{\mathrm{T},1}(\tilde{\theta}_{\mathrm{T},l})}, \; \ldots, \mathrm{e}^{\mathrm{j}(\omega_{\mathrm{c}}+\omega_p)\tau_{\mathrm{T},N_{\mathrm{T}}}(\tilde{\theta}_{\mathrm{T},l})} \right]^{\mathrm{T}} \in \mathbb{C}^{N_{\mathrm{T}}} \tag{2.25}$$

$$\tau_l' = \tau_l + \epsilon_{\mathrm{clk}}. \tag{2.26}$$

We note that the Tx array steering vector $\boldsymbol{a}_{\mathrm{T},p}(\tilde{\theta}_{\mathrm{T},l})$ depends not only on the angle, but also on the subcarrier index. The Rx steering vector $\boldsymbol{a}_{\mathrm{R},p}(\tilde{\theta}_{\mathrm{R},l})$ is defined accordingly. Also, $\omega_p = 2\pi p \Delta f$, $\omega_{\mathrm{c}} = 2\pi f_{\mathrm{c}}$, f_{c} is the carrier frequency, h_l is the gain of the l-th path and $\boldsymbol{\eta}[p,b] \sim \mathcal{N}_{\mathbb{C}}(\boldsymbol{0}, \sigma_{\eta,\mathrm{R}}^2 \boldsymbol{I}_{N_{\mathrm{R}}})$ is the additive white Gaussian noise (AWGN). The derivation of the signal model can be found in Appendix A1.

Through (2.22)-(2.25), we can see that the observations $\boldsymbol{y}[p,b]$ depend on the channel parameter vector $\tilde{\boldsymbol{\nu}}$, defined as

$$\tilde{\boldsymbol{\nu}} = [\tau_0', \tilde{\theta}_{\mathrm{T},0}, \tilde{\theta}_{\mathrm{R},0}, \boldsymbol{h}_0^{\mathrm{T}}, \ldots, \tau_{L-1}', \tilde{\theta}_{\mathrm{T},L-1}, \tilde{\theta}_{\mathrm{R},L-1}, \boldsymbol{h}_{L-1}^{\mathrm{T}}]^{\mathrm{T}} \in \mathbb{R}^{5L}, \tag{2.27}$$

with $\boldsymbol{h}_l = [|h_l|, \arg(h_l)]^{\mathrm{T}}$. For Rx localization, the position parameter vector $\boldsymbol{\nu}$ is defined as

$$\boldsymbol{\nu} = \begin{cases} [\boldsymbol{p}_{\mathrm{R}}^{\mathrm{T}}, \alpha_{\mathrm{R}}, \epsilon_{\mathrm{clk}}, \boldsymbol{h}_0^{\mathrm{T}}, \boldsymbol{p}_{\mathrm{s},1}^{\mathrm{T}}, \boldsymbol{h}_1^{\mathrm{T}}, \ldots, \boldsymbol{p}_{\mathrm{s},L-1}^{\mathrm{T}}, \boldsymbol{h}_{L-1}^{\mathrm{T}}]^{\mathrm{T}} \in \mathbb{R}^{4L+2}, & \text{0-th path is LOS,} \\ [\boldsymbol{p}_{\mathrm{R}}^{\mathrm{T}}, \alpha_{\mathrm{R}}, \epsilon_{\mathrm{clk}}, \boldsymbol{p}_{\mathrm{s},0}^{\mathrm{T}}, \boldsymbol{h}_0^{\mathrm{T}}, \boldsymbol{p}_{\mathrm{s},1}^{\mathrm{T}}, \boldsymbol{h}_1^{\mathrm{T}}, \ldots, \boldsymbol{p}_{\mathrm{s},L-1}^{\mathrm{T}}, \boldsymbol{h}_{L-1}^{\mathrm{T}}]^{\mathrm{T}} \in \mathbb{R}^{4L+4}, & \text{otherwise,} \end{cases} \tag{2.28}$$

and is related to $\tilde{\boldsymbol{\nu}}$ as described by (2.8), (2.11)-(2.12) and (2.26). We can similarly define the position parameter vector for Tx localization by replacing $\boldsymbol{p}_{\mathrm{R}}$ and α_{R} with $\boldsymbol{p}_{\mathrm{T}}$ and α_{T} in (2.28).

2.1.2 Dynamic Scenario

We extend the signal model to the dynamic scenario, with the receiver moving with constant velocity $\boldsymbol{v}_\mathrm{R} = [v_{\mathrm{R,x}}, v_{\mathrm{R,y}}]^\mathrm{T} \in \mathbb{R}^2$. Let $n_0 T_\mathrm{s}$ be the TOA of the first sample of the received signal fed to the discrete Fourier transform (DFT) and $\boldsymbol{p}_\mathrm{R}$ be the receiver's position at that time instant. The position of the receiver at time nT_s is $\boldsymbol{p}_\mathrm{R}(nT_\mathrm{s}) = \boldsymbol{p}_\mathrm{R} + \boldsymbol{v}_\mathrm{R} \cdot (n - n_0)T_\mathrm{s}$. As in the static scenario, we make use of the far field assumption and also assume that the angles and the channel gains are approximately invariant during the observation interval $N_\mathrm{B} M T_\mathrm{s}$, with $M = N + N_\mathrm{CP}$. The received signal at the p-th subcarrier of the b-th OFDM symbol after Rx combining is

$$\boldsymbol{y}[p,b] \approx \sum_{q \in \mathcal{P}} \boldsymbol{W}_\mathrm{R}^\mathrm{H} \boldsymbol{H}[p,q,b] \boldsymbol{x}[q,b] + \boldsymbol{W}_\mathrm{R}^\mathrm{H} \boldsymbol{\eta}[p,b], \tag{2.29}$$

where

$$\boldsymbol{H}[p,q,b] = \sum_{l=0}^{L-1} h_l \, \mathrm{e}^{-\mathrm{j}\left(\omega_q \tau_l' - \frac{\omega_\mathrm{c}+\omega_q}{c} v_l b M T_\mathrm{s}\right)} \boldsymbol{a}_{\mathrm{R},q}(\tilde{\theta}_{\mathrm{R},l}) \boldsymbol{a}_{\mathrm{T},q}^\mathrm{T}(\tilde{\theta}_{\mathrm{T},l}) Q_N\left(\left(\omega_p - \omega_q - \frac{\omega_\mathrm{c}+\omega_q}{c} v_l\right)\frac{T_\mathrm{s}}{2}\right), \tag{2.30}$$

with $v_l = \boldsymbol{v}_\mathrm{R}^\mathrm{T} \boldsymbol{u}\left(\theta_{\mathrm{R},l}\right)$ being the speed of the receiver in the direction of the AOA and

$$Q_N(x) = \mathrm{e}^{-\mathrm{j}(N-1)x} \, \frac{\sin(Nx)}{N \sin(x)}. \tag{2.31}$$

The derivation of the signal model is provided in Appendix A1.2. The Doppler shift $v_l\left(\omega_\mathrm{c} + \omega_q\right)/c$ is subcarrier-dependent and an increasing function of the subcarrier index. Similar to [17], we assume that the observation interval is much smaller than the channel coherence time $T_\mathrm{co} \propto c/\left(f_\mathrm{c} \|\boldsymbol{v}_\mathrm{R}\|_2\right)$ [49]. When the transmitter is moving with velocity $\boldsymbol{v}_\mathrm{T}$ and the receiver is static, the signal model (2.29) is still valid with $v_l = \boldsymbol{v}_\mathrm{T}^\mathrm{T} \boldsymbol{u}\left(\theta_{\mathrm{T},l}\right)$.

The channel parameter vector in the dynamic scenario reads as

$$\tilde{\boldsymbol{\nu}} = [\tau_0', \tilde{\theta}_{\mathrm{T},0}, \tilde{\theta}_{\mathrm{R},0}, v_0, \boldsymbol{h}_0^\mathrm{T}, \ldots, \tau_{L-1}', \tilde{\theta}_{\mathrm{T},L-1}, \tilde{\theta}_{\mathrm{R},L-1}, v_{L-1} \boldsymbol{h}_{L-1}^\mathrm{T}]^\mathrm{T} \in \mathbb{R}^{6L}, \tag{2.32}$$

and the position parameter vector reads as

$$\boldsymbol{\nu} = \begin{cases} [\boldsymbol{p}_\mathrm{R}^\mathrm{T}, \alpha_\mathrm{R}, \boldsymbol{v}_\mathrm{R}, \epsilon_\mathrm{clk}, \boldsymbol{h}_0^\mathrm{T}, \boldsymbol{p}_{\mathrm{s},1}^\mathrm{T}, \boldsymbol{h}_1^\mathrm{T}, \ldots, \boldsymbol{p}_{\mathrm{s},L-1}^\mathrm{T}, \boldsymbol{h}_{L-1}^\mathrm{T}]^\mathrm{T} \in \mathbb{R}^{4L+4}, & \text{0-th path is LOS,} \\ [\boldsymbol{p}_\mathrm{R}^\mathrm{T}, \alpha_\mathrm{R}, \boldsymbol{v}_\mathrm{R}, \epsilon_\mathrm{clk}, \boldsymbol{p}_{\mathrm{s},0}^\mathrm{T}, \boldsymbol{h}_0^\mathrm{T}, \boldsymbol{p}_{\mathrm{s},1}^\mathrm{T}, \boldsymbol{h}_1^\mathrm{T}, \ldots, \boldsymbol{p}_{\mathrm{s},L-1}^\mathrm{T}, \boldsymbol{h}_{L-1}^\mathrm{T}]^\mathrm{T} \in \mathbb{R}^{4L+6}, & \text{otherwise.} \end{cases} \tag{2.33}$$

2.2 Fisher Information and Cramér-Rao Lower Bound (CRLB)

2.2.1 Static Scenario

The achievable positioning accuracy of the Rx can be characterized in terms of the hybrid CRLB [50]. We assume that the parameter vector $\boldsymbol{\nu}$ contains both deterministic and random parameters and denote the latter as $\boldsymbol{\nu}_r$. Let $p(\boldsymbol{\nu}_r)$ be the prior probability density function (pdf) of $\boldsymbol{\nu}_r$ and $p(\boldsymbol{Y}|\boldsymbol{\nu})$ be the likelihood of the observations $\boldsymbol{Y}$ given $\boldsymbol{\nu}$, according to (2.22), with

$$\boldsymbol{Y} = [\boldsymbol{Y}_0^\mathrm{T}, \ldots, \boldsymbol{Y}_{N_\mathrm{B}-1}^\mathrm{T}]^\mathrm{T} \in \mathbb{C}^{N_\mathrm{R} N_\mathrm{B} \times N_\mathrm{P}}, \tag{2.34}$$

$$\boldsymbol{Y}_b = [\boldsymbol{y}[p_1, b], \ldots, \boldsymbol{y}[p_{N_\mathrm{P}}, b]] \in \mathbb{C}^{N_\mathrm{R} \times N_\mathrm{P}}. \tag{2.35}$$

Under the regularity conditions

$$\mathbb{E}_{\boldsymbol{\nu}_r}\left[\frac{\partial \ln p(\boldsymbol{\nu}_r)}{\partial \boldsymbol{\nu}}\right] = 0, \tag{2.36}$$

$$\mathbb{E}_{\boldsymbol{Y},\boldsymbol{\nu}_r}\left[\frac{\partial \ln p(\boldsymbol{Y}|\boldsymbol{\nu})}{\partial \boldsymbol{\nu}}\right] = 0, \tag{2.37}$$

the hybrid CRLB states that, for a parameter vector $\boldsymbol{\nu}$ containing both deterministic and random parameters, the covariance matrix $\boldsymbol{C}$ of any unbiased estimator $\hat{\boldsymbol{\nu}}$ of $\boldsymbol{\nu}$ satisfies [50], [51]

$$\boldsymbol{C} - \boldsymbol{J}_{\boldsymbol{\nu}}^{-1} \succeq \boldsymbol{0}, \tag{2.38}$$

where $\succeq \boldsymbol{0}$ denotes positive semi-definiteness and $\boldsymbol{J}_{\boldsymbol{\nu}}$ is the hybrid FIM of $\boldsymbol{\nu}$. $\boldsymbol{J}_{\boldsymbol{\nu}}$ is defined as

$$\boldsymbol{J}_{\boldsymbol{\nu}} = \boldsymbol{J}_{\boldsymbol{\nu}}^{(\mathrm{p})} + \boldsymbol{J}_{\boldsymbol{\nu}}^{(\mathrm{o})}, \tag{2.39}$$

where

$$\boldsymbol{J}_{\boldsymbol{\nu}}^{(\mathrm{p})} = \mathbb{E}_{\boldsymbol{\nu}_r}\left[\frac{\partial \ln p(\boldsymbol{\nu}_r)}{\partial \boldsymbol{\nu}}\frac{\partial \ln p(\boldsymbol{\nu}_r)}{\partial \boldsymbol{\nu}^{\mathrm{T}}}\right] = -\mathbb{E}_{\boldsymbol{\nu}_r}\left[\frac{\partial^2 \ln p(\boldsymbol{\nu}_r)}{\partial \boldsymbol{\nu}\partial \boldsymbol{\nu}^{\mathrm{T}}}\right] \tag{2.40}$$

accounts for the prior information and

$$\boldsymbol{J}_{\boldsymbol{\nu}}^{(\mathrm{o})} = \mathbb{E}_{\boldsymbol{Y},\boldsymbol{\nu}_r}\left[\frac{\partial \ln p(\boldsymbol{Y}|\boldsymbol{\nu})}{\partial \boldsymbol{\nu}}\frac{\partial \ln p(\boldsymbol{Y}|\boldsymbol{\nu})}{\partial \boldsymbol{\nu}^{\mathrm{T}}}\right] = -\mathbb{E}_{\boldsymbol{Y},\boldsymbol{\nu}_r}\left[\frac{\partial^2 \ln p(\boldsymbol{Y}|\boldsymbol{\nu})}{\partial \boldsymbol{\nu}\partial \boldsymbol{\nu}^{\mathrm{T}}}\right] \tag{2.41}$$

accounts for the observation-related information, with $\boldsymbol{\nu}_r$ representing the random parameters in $\boldsymbol{\nu}$. The last equality in (2.40) and (2.41) follows from the regularity conditions (2.36) and (2.37). When the LOS path exists, $\boldsymbol{J}_{\boldsymbol{\nu}} \in \mathbb{R}^{(4L+2)\times(4L+2)}$, otherwise $\boldsymbol{J}_{\boldsymbol{\nu}} \in \mathbb{R}^{(4L+4)\times(4L+4)}$. Intuitively, Fisher information quantifies the amount of information on $\boldsymbol{\nu}$ carried by the observations and the prior and is equal to the variance of the score function $\frac{\partial \ln p(\boldsymbol{\nu}_r)}{\partial \boldsymbol{\nu}}$. In the following, we derive the Fisher information matrix and the CRLB for single-anchor positioning for a MIMO-OFDM system.

We assume that ϵ_{clk} is the only random parameter in $\boldsymbol{\nu}$, i.e., $\boldsymbol{\nu}_r = \epsilon_{\mathrm{clk}}$, and it is zero-mean Gaussian distributed with variance σ_{clk}^2. It is straightforward to find that the only non-zero entry of $\boldsymbol{J}_{\boldsymbol{\nu}}^{(\mathrm{p})}$ is

$$\left[\boldsymbol{J}_{\boldsymbol{\nu}}^{(\mathrm{p})}\right]_{4,4} = \mathbb{E}\left[-\frac{\partial^2 \ln p(\epsilon_{\mathrm{clk}})}{\partial \epsilon_{\mathrm{clk}}^2}\right] = \frac{1}{\sigma_{\mathrm{clk}}^2}, \tag{2.42}$$

where $p(\epsilon_{\mathrm{clk}})$ is the pdf of ϵ_{clk}.

As already explained above, the observations are only indirectly related to $\boldsymbol{\nu}$ through $\tilde{\boldsymbol{\nu}}$. To facilitate computations, but also to quantify how much position information each TOF, AOD, AOA and Doppler measurement offers, we first compute the (observation-related) FIM $\boldsymbol{J}_{\tilde{\boldsymbol{\nu}}}^{(\mathrm{o})}$ of channel parameters $\tilde{\boldsymbol{\nu}}$ and use the following transformation to obtain the observation-related part of the FIM $\boldsymbol{J}_{\tilde{\boldsymbol{\nu}}}^{(\mathrm{o})}$ of the position parameters $\boldsymbol{\nu}$ [52]:

$$\boldsymbol{J}_{\boldsymbol{\nu}}^{(\mathrm{o})} = \boldsymbol{T}\boldsymbol{J}_{\tilde{\boldsymbol{\nu}}}^{(\mathrm{o})}\boldsymbol{T}^{\mathrm{T}}, \tag{2.43}$$

where

$$[\boldsymbol{T}]_{i,j} = \partial\tilde{\nu}_j/\partial\nu_i. \tag{2.44}$$

Since $\tilde{\boldsymbol{\nu}}$ is observed under Gaussian noise, the (i,j)-th entry of $\boldsymbol{J}_{\boldsymbol{\nu}}^{(\mathrm{o})}$ is [53, Sec. 3.9]

$$\left[\boldsymbol{J}_{\tilde{\boldsymbol{\nu}}}^{(\mathrm{o})}\right]_{i,j} = \frac{2}{\sigma_{\eta,\mathrm{R}}^2}\sum_{b=0}^{N_\mathrm{B}-1}\sum_{p\in\mathcal{P}}\Re\left\{\frac{\partial\boldsymbol{m}^\mathrm{H}[p,b]}{\partial\tilde{\nu}_i}\left(\boldsymbol{W}_\mathrm{R}^\mathrm{H}\boldsymbol{W}_\mathrm{R}\right)^{-1}\frac{\partial\boldsymbol{m}[p,b]}{\partial\tilde{\nu}_j}\right\}. \tag{2.45}$$

The required derivatives of $\boldsymbol{m}[p,b]$ are provided in Appendix A2 and the entries of $\boldsymbol{T}$ are given in Appendix A3.

We use the notion of the equivalent FIM (EFIM) [15] to focus on the available information on the position and orientation parameters. The EFIM can have much lower dimensions (3×3) than $\boldsymbol{J}_{\boldsymbol{\nu}}$, but still fully describes the available information on the parameters of interest. The CRLB of the position and orientation parameters is obtained by the 3×3 upper left block of $\boldsymbol{J}_{\boldsymbol{\nu}}^{-1}$ and the EFIM $\boldsymbol{J}_\mathrm{po}$ for the position and orientation parameters is its inverse

$$\boldsymbol{J}_\mathrm{po} = \left([\boldsymbol{J}_{\boldsymbol{\nu}}^{-1}]_{1:3,1:3}\right)^{-1}. \tag{2.46}$$

Splitting $\boldsymbol{T}$ as $\boldsymbol{T} = \left[\boldsymbol{T}_\mathrm{po}^\mathrm{T},\ \boldsymbol{T}_\mathrm{np}^\mathrm{T}\right]^\mathrm{T}$, with $\boldsymbol{T}_\mathrm{po}$ consisting of the first three rows of $\boldsymbol{T}$, which correspond to the position and orientation parameters, and $\boldsymbol{T}_\mathrm{np}$ containing the rest, and using (2.43) and block matrix inversion, $\boldsymbol{J}_\mathrm{po}$ can be expressed as

$$\boldsymbol{J}_\mathrm{po} = \boldsymbol{T}_\mathrm{po}\boldsymbol{J}_{\tilde{\boldsymbol{\nu}}}\boldsymbol{T}_\mathrm{po}^\mathrm{T} - \boldsymbol{T}_\mathrm{po}\boldsymbol{J}_{\tilde{\boldsymbol{\nu}}}\boldsymbol{T}_\mathrm{np}^\mathrm{T}\left(\boldsymbol{T}_\mathrm{np}\boldsymbol{J}_{\tilde{\boldsymbol{\nu}}}\boldsymbol{T}_\mathrm{np}^\mathrm{T} + \frac{1}{\sigma_\mathrm{clk}^2}\boldsymbol{e}_1\boldsymbol{e}_1^\mathrm{T}\right)^{-1}\boldsymbol{T}_\mathrm{np}\boldsymbol{J}_{\tilde{\boldsymbol{\nu}}}\boldsymbol{T}_\mathrm{po}^\mathrm{T}, \tag{2.47}$$

where $\boldsymbol{e}_i$ is the vector of appropriate size whose i-th entry is equal to 1 and the rest of its entries are 0.

The measures we use for characterizing the achievable position and orientation estimation accuracy are the PEB and the orientation error bound (OEB) defined as [18]

$$\mathrm{PEB} = \sqrt{\left[\boldsymbol{J}_\mathrm{po}^{-1}\right]_{1,1} + \left[\boldsymbol{J}_\mathrm{po}^{-1}\right]_{2,2}}, \tag{2.48}$$

$$\mathrm{OEB} = \sqrt{\left[\boldsymbol{J}_\mathrm{po}^{-1}\right]_{3,3}}. \tag{2.49}$$

2.2.2 Dynamic Scenario

In the dynamic scenario we are also interested in the velocity of the target. We can, therefore, compute the position, orientation and velocity EFIM $\boldsymbol{J}_\mathrm{pov}$ in a similar fashion

$$\boldsymbol{J}_\mathrm{pov} = \boldsymbol{T}_\mathrm{pov}\boldsymbol{J}_{\tilde{\boldsymbol{\nu}}}\boldsymbol{T}_\mathrm{pov}^\mathrm{T} - \boldsymbol{T}_\mathrm{pov}\boldsymbol{J}_{\tilde{\boldsymbol{\nu}}}\boldsymbol{T}_\mathrm{np}^\mathrm{T}\left(\boldsymbol{T}_\mathrm{np}\boldsymbol{J}_{\tilde{\boldsymbol{\nu}}}\boldsymbol{T}_\mathrm{np}^\mathrm{T} + \frac{1}{\sigma_\mathrm{clk}^2}\boldsymbol{e}_1\boldsymbol{e}_1^\mathrm{T}\right)^{-1}\boldsymbol{T}_\mathrm{np}\boldsymbol{J}_{\tilde{\boldsymbol{\nu}}}\boldsymbol{T}_\mathrm{pov}^\mathrm{T}, \tag{2.50}$$

where $\boldsymbol{T}_\mathrm{po}$ consists of the first five rows of $\boldsymbol{T}$, which correspond to the position, orientation and velocity parameters, and $\boldsymbol{T}_\mathrm{np}$ contains the rest. In addition to the PEB and the OEB, we use the velocity error bound (VEB) for the characterization of the achievable estimation accuracy of the velocity:

$$\mathrm{VEB} = \sqrt{\left[\boldsymbol{J}_\mathrm{pov}^{-1}\right]_{4,4} + \left[\boldsymbol{J}_\mathrm{pov}^{-1}\right]_{5,5}}. \tag{2.51}$$

2.3 Downlink Versus Uplink Comparison

In the following, we discuss the positioning and orientation estimation of a UE in a communication system, assuming the position and orientation of the base station (BS) are known. In contrast to [20], we assume that the devices (BS or UE) use the same set of beamforming vectors for transmission and reception, e.g., $\boldsymbol{W}_{\mathrm{R}}$ in the DL is equal to $\boldsymbol{W}_{\mathrm{T}}$ in the UL. We consider this setup because the presence of $\boldsymbol{W}_{\mathrm{T}}$ and $\boldsymbol{W}_{\mathrm{R}}$ usually results from some hardware constraints, which are device-specific and independent of whether the device is in Tx or Rx mode. For example, due to the limited number of RF chains, a UE might only be able to process a signal in Tx and Rx mode with a set of analog beamforming vectors. We consider here the static scenario, but a similar analysis can be conducted in the dynamic scenario. With known BS position and orientation, positioning of a UE in the DL corresponds to receiver localization, whereas positioning of a UE in the UL corresponds to transmitter localization. Thus, by replacing the subscripts 'T' and 'R' with 'BS' and 'UE' in (2.22)-(2.24) for the DL and vice-versa for the UL, we obtain the signal model for the DL and the UL, respectively:

$$\text{(DL)}: \boldsymbol{y}^{(\mathrm{DL})}[p,b] = \boldsymbol{W}_{\mathrm{UE}}^{\mathrm{H}}\boldsymbol{H}^{(\mathrm{DL})}[p]\boldsymbol{W}_{\mathrm{BS}}^{*}\boldsymbol{s}^{(\mathrm{DL})}[p,b] + \boldsymbol{W}_{\mathrm{UE}}^{\mathrm{H}}\boldsymbol{\eta}[p,b] \tag{2.52}$$

$$\text{(UL)}: \boldsymbol{y}^{(\mathrm{UL})}[p,b] = \boldsymbol{W}_{\mathrm{BS}}^{\mathrm{H}}\boldsymbol{H}^{(\mathrm{UL})}[p]\boldsymbol{W}_{\mathrm{UE}}^{*}\boldsymbol{s}^{(\mathrm{UL})}[p,b] + \boldsymbol{W}_{\mathrm{BS}}^{\mathrm{H}}\boldsymbol{\eta}[p,b], \tag{2.53}$$

where we have that

$$\boldsymbol{H}^{(\mathrm{UL})}[p] = \left(\boldsymbol{H}^{(\mathrm{DL})}[p]\right)^{\mathrm{T}} \tag{2.54}$$

and that the BS and UE use the same beamforming vectors for transmission and reception, as mentioned above. We note that (2.54) holds exactly only for arrays with isotropic radiators and the distance between each element pair being a multiple of $\lambda_{\mathrm{c}}/2$, where $\lambda_{\mathrm{c}} = c/f_{\mathrm{c}}$ is the carrier wavelength. If this is not the case, (2.54) does not hold due to mutual coupling among the antenna elements and it is used as an approximation. For further details on the topic the reader is referred to [54]. Both in the DL and UL the position parameter vector is

$$\boldsymbol{\nu} = \begin{cases} [\boldsymbol{p}_{\mathrm{UE}}^{\mathrm{T}}, \alpha_{\mathrm{UE}}, \epsilon_{\mathrm{clk}}, \boldsymbol{h}_0^{\mathrm{T}}, \boldsymbol{p}_{\mathrm{s},1}^{\mathrm{T}}, \boldsymbol{h}_1^{\mathrm{T}}, \ldots, \boldsymbol{p}_{\mathrm{s},L-1}^{\mathrm{T}}, \boldsymbol{h}_{L-1}^{\mathrm{T}}]^{\mathrm{T}} \in \mathbb{R}^{4L+2}, & \text{0-th path is LOS,} \\ [\boldsymbol{p}_{\mathrm{UE}}^{\mathrm{T}}, \alpha_{\mathrm{UE}}, \epsilon_{\mathrm{clk}}, \boldsymbol{p}_{\mathrm{s},0}^{\mathrm{T}}, \boldsymbol{h}_0^{\mathrm{T}}, \boldsymbol{p}_{\mathrm{s},1}^{\mathrm{T}}, \boldsymbol{h}_1^{\mathrm{T}}, \ldots, \boldsymbol{p}_{\mathrm{s},L-1}^{\mathrm{T}}, \boldsymbol{h}_{L-1}^{\mathrm{T}}]^{\mathrm{T}} \in \mathbb{R}^{4L+4}, & \text{otherwise,} \end{cases} \tag{2.55}$$

We now compare the positioning accuracy between the DL and the UL, under the following assumptions:

1) $\boldsymbol{W}_{\mathrm{UE}}$ and $\boldsymbol{W}_{\mathrm{BS}}$ have orthonormal columns.
2) The signals transmitted through different analog beamforming vectors on each subcarrier are uncorrelated and have equal energy, i.e.,

$$\begin{aligned} \sum_{k=1}^{M_{\mathrm{BS}}}\sum_{b=0}^{N_{\mathrm{B}}-1} \boldsymbol{s}^{(\mathrm{DL})}[p,b]\left(\boldsymbol{s}^{(\mathrm{DL})}[p,b]\right)^{\mathrm{H}} &= \sum_{k=1}^{M_{\mathrm{BS}}}\sum_{b=0}^{N_{\mathrm{B}}-1} E_{\mathrm{tot,BS}} q_k \gamma_k[p,b]\boldsymbol{f}_k'\boldsymbol{f}_k'^{\mathrm{H}} \\ &= E_{\mathrm{tot,BS}}\sum_{k=1}^{M_{\mathrm{BS}}} q_k\gamma_k[p]\boldsymbol{f}_k'\boldsymbol{f}_k'^{\mathrm{H}} \\ &= \boldsymbol{I}_{N_{\mathrm{RF,BS}}}\gamma[p]\frac{E_{\mathrm{tot,BS}}}{N_{\mathrm{RF,BS}}}, \end{aligned} \tag{2.56}$$

where

$$\gamma_k[p] = \sum_{b=0}^{N_B-1} \gamma_k[p,b] \tag{2.57}$$

is the fraction of q_k allocated on the p-th subcarrier and

$$\gamma[p] = N_{RF,BS} \sum_{k=1}^{M_{BS}} q_k \gamma_k[p] |f'_{k,j}|^2, \quad \forall j \in \{1,\dots,N_{RF,BS}\} \tag{2.58}$$

is the fraction of the total energy used on the p-th subcarrier and $E_{tot,BS}$ is the total Tx energy of the BS. Similarly

$$\sum_{k=1}^{M_{UE}} \sum_{b=0}^{N_B-1} \boldsymbol{s}^{(UL)}[p,b] \left(\boldsymbol{s}^{(UL)}[p,b]\right)^H = \boldsymbol{I}_{N_{RF,UE}} \gamma[p] \frac{E_{tot,UE}}{N_{RF,UE}}, \tag{2.59}$$

where $E_{tot,UE}$ is the total Tx energy of the UE.
We define $\boldsymbol{Z}$ as the matrix which has the same dimensions as $\boldsymbol{J}_{\boldsymbol{\nu}}$ and its (i,j)-th element is

$$[\boldsymbol{Z}]_{i,j} = \mathrm{tr}\left(\Re\left\{\sum_{b=0}^{N_B-1} \sum_{p\in\mathcal{P}} \frac{\partial \boldsymbol{G}^H[p]}{\partial \nu_i} \frac{\partial \boldsymbol{G}[p]}{\partial \nu_j}\right\}\right), \tag{2.60}$$

where $\boldsymbol{G}[p] = \boldsymbol{W}_{UE}^H \boldsymbol{H}^{(DL)}[p] \boldsymbol{W}_{UE}^*$. From (2.39), (2.42), (2.45), (2.52) and taking the expectation over $\boldsymbol{s}^{(DL)}[p,b]$ we can compute $\boldsymbol{J}_{\boldsymbol{\nu}}^{(DL)}$ as

$$\boldsymbol{J}_{\boldsymbol{\nu}}^{(DL)} = \frac{2E_{tot,BS}}{\sigma_{\eta,UE}^2 N_{RF,BS}} \boldsymbol{Z} + \boldsymbol{e}_4 \boldsymbol{e}_4^T \frac{1}{\sigma_{clk}^2}, \tag{2.61}$$

where $\sigma_{\eta,UE}^2$ is the noise variance at the UE in the DL. Given that $\boldsymbol{H}^{(UL)}[p] = \left(\boldsymbol{H}^{(DL)}[p]\right)^T$, we can show by using simple properties of the trace operator that

$$\boldsymbol{J}_{\boldsymbol{\nu}}^{(UL)} = \frac{2E_{tot,UE}}{\sigma_{\eta,BS}^2 N_{RF,UE}} \boldsymbol{Z} + \boldsymbol{e}_4 \boldsymbol{e}_4^T \frac{1}{\sigma_{clk}^2}, \tag{2.62}$$

where $\sigma_{\eta,BS}^2$ is the noise variance at the BS in the UL. Using the Sherman-Morrison formula we invert $\boldsymbol{J}_{\boldsymbol{\nu}}^{(DL)}$ and $\boldsymbol{J}_{\boldsymbol{\nu}}^{(UL)}$ and after a few steps we find that the ratio of the DL and UL PEB (see (2.48)) is given by

$$\frac{\mathrm{PEB}^{(DL)}}{\mathrm{PEB}^{(UL)}} = \sqrt{\frac{\delta_{UL}}{\delta_{DL}} \frac{\zeta - \frac{1}{\delta_{DL}\sigma_{clk}^2 + [\boldsymbol{Z}^{-1}]_{4,4}}}{\zeta - \frac{1}{\delta_{UL}\sigma_{clk}^2 + [\boldsymbol{Z}^{-1}]_{4,4}}}}, \tag{2.63}$$

where

$$\zeta = \left([\boldsymbol{Z}^{-1}]_{1,1} + [\boldsymbol{Z}^{-1}]_{2,2}\right) / \left(\left([\boldsymbol{Z}^{-1}]_{1,4}\right)^2 + \left([\boldsymbol{Z}^{-1}]_{2,4}\right)^2\right), \tag{2.64}$$

$$\delta_{DL} = 2E_{tot,BS} N_{RF,UE} / \sigma_{\eta,UE}^2, \tag{2.65}$$

$$\delta_{UL} = 2E_{tot,UE} N_{RF,BS} / \sigma_{\eta,BS}^2. \tag{2.66}$$

We refer to δ_{DL} and δ_{UL} as the DL and UL pseudo-SNRs. It follows from (2.63) that the link with the highest pseudo-SNR will provide the best positioning performance. For perfectly synchronized ($\sigma^2_{\mathrm{clk}} = 0$) or asynchronous ($\sigma^2_{\mathrm{clk}} \to \infty$) clocks we have

$$\frac{\mathrm{PEB}^{(\mathrm{DL})}}{\mathrm{PEB}^{(\mathrm{UL})}} = \sqrt{\frac{\delta_{\mathrm{UL}}}{\delta_{\mathrm{DL}}}}. \tag{2.67}$$

From (2.63) and (2.67) we see that DL and UL positioning have different accuracy, owing to different pseudo-SNR. When $\delta_{\mathrm{DL}} = \delta_{\mathrm{UL}}$, again from (2.63), we find that $\mathrm{PEB}^{(\mathrm{DL})} = \mathrm{PEB}^{(\mathrm{UL})}$. We stress that (2.63) and (2.67) hold when each of the devices (BS or UE) employs the same set of orthonormal beamforming vectors for transmission and reception. In the case that the sets of beamforming vectors for transmission and reception are not the same, there is a mismatch between the subspaces spanned for transmission and reception. Although an analytic result has not been derived for this case, in Section 2.6, we compare DL and UL positioning using random beamforming matrices for transmission and reception.

2.4 Asymptotic Analysis

The expressions for the FIMs and their entries provided in Section 2.2, although useful for numerical evaluation of the achievable accuracy, do not provide much intuition about the positioning information that is available in the considered single-anchor MIMO-OFDM setup. Our aim is to obtain a geometric interpretation of the Fisher information, as in [17], [21]. Following [20]–[22], we will consider asymptotic expressions for the position and orientation EFIM for large bandwidth[1] ($f_{\mathrm{s}} \to \infty$) and large number of transmit and receive antennas ($N_{\mathrm{T}}, N_{\mathrm{R}} \to \infty$). The accuracy of the asymptotic expressions will be evaluated in Sec. 2.6 and has also been investigated in [20], where it was shown that they can provide a very accurate approximation of the exact PEB, even for moderate bandwidth and number of transmit and receive antennas.

Since for arrays with a fixed aperture the asymptotic orthogonality/favorable propagation condition [55], [56] may not be satisfied [57], we consider arrays whose aperture grows with increasing number of elements. In addition to the standard favorable propagation condition

$$\lim_{N_{\mathrm{T}}\to\infty} \boldsymbol{a}^{\mathrm{H}}_{\mathrm{T},p}(\tilde{\theta}_{\mathrm{T},l})\boldsymbol{a}_{\mathrm{T},p}(\tilde{\theta}_{\mathrm{T},l'})/N_{\mathrm{T}} = 0, \tag{2.68}$$

we also assume

$$\lim_{N_{\mathrm{T}}\to\infty} \frac{\partial}{\partial\tilde{\theta}_{\mathrm{T},l}} \boldsymbol{a}^{\mathrm{H}}_{\mathrm{T},p}(\tilde{\theta}_{\mathrm{T},l})\boldsymbol{a}_{\mathrm{T},p}(\tilde{\theta}_{\mathrm{T},l'})/N^2_{\mathrm{T}} = 0, \tag{2.69}$$

$$\lim_{N_{\mathrm{T}}\to\infty} \frac{1}{N^3_{\mathrm{T}}} \left\| \partial\boldsymbol{a}_{\mathrm{T},p}(\tilde{\theta}_{\mathrm{T},l})/\partial\tilde{\theta}_{\mathrm{T},l} \right\|^2_2 > 0, \tag{2.70}$$

implying that asymptotic orthogonality holds also for the inner product of the derivative of the array steering vector and the array steering vector at any angle. Similar assumptions are made for the Rx array. We verify that these conditions hold for ULAs and uniform circular arrays (UCAs) in Appendix A5.

In order to focus on the characteristics of the channel and obtain geometrically intuitive expressions for the Fisher information, we also use the following simplifying assumptions:

[1] In an OFDM system with a given number of subcarriers and a fixed set of occupied subcarriers, the occupied bandwidth increases linearly with the sampling rate. Hence, equivalently to writing that the bandwidth goes to infinity, we write $f_{\mathrm{s}} \to \infty$

1) $\boldsymbol{W}_{\mathrm{T}} = \boldsymbol{I}_{N_{\mathrm{T}}}$ and $\boldsymbol{W}_{\mathrm{R}} = \boldsymbol{I}_{N_{\mathrm{R}}}$, i.e., fully digital beamforming is used and the whole transmit and receive spaces can be sensed. This assumption holds for the rest of the thesis.
2) Similar to (2.56)-(2.59), we assume

$$\sum_{b=0}^{N_{\mathrm{B}}-1} \boldsymbol{x}[p,b]\boldsymbol{x}^{\mathrm{H}}[p,b] = \boldsymbol{I}_{N_{\mathrm{T}}}\gamma[p]\frac{E_{\mathrm{tot}}}{N_{\mathrm{T}}}. \tag{2.71}$$

To make the following expressions more compact we set

$$d_{\mathrm{T,s},l} = \begin{cases} \|\boldsymbol{p}_{\mathrm{R}} - \boldsymbol{p}_{\mathrm{T}}\|_2, & l\text{-th path is LOS,} \\ \left\|\boldsymbol{p}_{\mathrm{s},l} - \boldsymbol{p}_{\mathrm{T}}\right\|_2, & \text{otherwise,} \end{cases} \tag{2.72}$$

$$d_{\mathrm{T,s},l} = \begin{cases} \|\boldsymbol{p}_{\mathrm{R}} - \boldsymbol{p}_{\mathrm{T}}\|_2, & l\text{-th path is LOS,} \\ \left\|\boldsymbol{p}_{\mathrm{R}} - \boldsymbol{p}_{\mathrm{s},l}\right\|_2, & \text{otherwise.} \end{cases} \tag{2.73}$$

As before, we distinguish between the static and dynamic scenario.

2.4.1 Static Scenario

Before presenting the main results, we define a few useful quantities.

Definition 1. The *effective baseband bandwidth* β of the signal is defined as

$$\beta = \sqrt{\sum\nolimits_{p\in\mathcal{P}} \gamma[p]\omega_p^2 - \left(\sum\nolimits_{p\in\mathcal{P}} \gamma[p]\omega_p\right)^2}. \tag{2.74}$$

□

Definition 2. The *effective angular carrier frequency* $\bar{\omega}_{\mathrm{c}}$ of the signal is defined as

$$\bar{\omega}_{\mathrm{c}} = \sqrt{\sum\nolimits_{p\in\mathcal{P}} \gamma[p]\left(\omega_{\mathrm{c}} + \omega_p\right)^2}. \tag{2.75}$$

□

The definitions in (2.74) and (2.75) are the multi-carrier counterparts of the effective baseband bandwidth and the effective carrier frequency defined in [17] for single-carrier systems.

Definition 3. The *squared array aperture function (SAAF)* of the Tx array is defined as [17]

$$S_{\mathrm{T}}(\tilde{\theta}_{\mathrm{T},l}) = \frac{1}{N_{\mathrm{T}}}\sum_{j=1}^{N_{\mathrm{T}}}\left(d_{\mathrm{T},j}\boldsymbol{u}_{\perp}^{\mathrm{T}}(\psi_{\mathrm{T},j})\boldsymbol{u}(\tilde{\theta}_{\mathrm{T},l})\right)^2, \tag{2.76}$$

where $\boldsymbol{u}_{\perp}(\psi) = \boldsymbol{u}(\psi - \pi/2)$, with the array's centroid chosen at its reference point. The SAAF of the Rx array is defined accordingly. The Tx (Rx) SAAF fully describes the effect of the Tx (Rx) array structure on the AOD (AOA) information. □

Theorem 2.1. *(Static receiver localization)* The EFIM for the position $\boldsymbol{p}_{\mathrm{R}}$ and orientation α_{R} of an imperfectly synchronized static receiver, when the position $\boldsymbol{p}_{\mathrm{T}}$ and orientation α_{T} of the transmitter are known, can be asymptotically expressed as

$$\boldsymbol{J}_{\mathrm{po}}^{(\mathrm{s})} \to \begin{cases} \boldsymbol{J}_{\mathrm{LOS}}^{(\mathrm{s})} + \sum_{l=1}^{L-1}\boldsymbol{J}_{\mathrm{NLOS},l}^{(\mathrm{s})} - \boldsymbol{J}_{\epsilon_{\mathrm{clk}}}^{(\mathrm{s})}, & \text{if LOS exists,} \\ \sum_{l=0}^{L-1}\boldsymbol{J}_{\mathrm{NLOS},l}^{(\mathrm{s})} - \boldsymbol{J}_{\epsilon_{\mathrm{clk}}}^{(\mathrm{s})}, & \text{otherwise.} \end{cases} \tag{2.77}$$

The information from the LOS path is given by

$$\boldsymbol{J}_{\mathrm{LOS}}^{(\mathrm{s})} = i_{\tau_0}\boldsymbol{z}_{\tau_0}\boldsymbol{z}_{\tau_0}^{\mathrm{T}} + i_{\theta_{\mathrm{T},0}}\boldsymbol{z}_{\theta_{\mathrm{T},0}}\boldsymbol{z}_{\theta_{\mathrm{T},0}}^{\mathrm{T}} + i_{\theta_{\mathrm{R},0}}\boldsymbol{z}_{\theta_{\mathrm{R},0}}\boldsymbol{z}_{\theta_{\mathrm{R},0}}^{\mathrm{T}}, \tag{2.78}$$

where

$$\boldsymbol{z}_{\tau_l} = [-\boldsymbol{u}^{\mathrm{T}}(\theta_{\mathrm{R},l}),\ 0]^{\mathrm{T}}, \tag{2.79}$$
$$\boldsymbol{z}_{\theta_{\mathrm{T},l}} = [\boldsymbol{u}_{\perp}^{\mathrm{T}}(\theta_{\mathrm{R},l}),\ 0]^{\mathrm{T}}, \tag{2.80}$$
$$\boldsymbol{z}_{\theta_{\mathrm{R},l}} = [\boldsymbol{u}_{\perp}^{\mathrm{T}}(\theta_{\mathrm{R},l}),\ -d_{\mathrm{R,s},l}]^{\mathrm{T}}, \tag{2.81}$$

and

$$i_{\tau_l} = \delta_{\mathrm{R,T}}|h_l|^2\frac{\beta^2}{c^2}, \tag{2.82}$$
$$i_{\theta_{\mathrm{T},l}} = \delta_{\mathrm{R,T}}|h_l|^2\frac{\bar{\omega}_{\mathrm{c}}^2 S_{\mathrm{T}}(\tilde{\theta}_{\mathrm{T},l})}{c^2 d_{\mathrm{T,s},l}^2}, \tag{2.83}$$
$$i_{\theta_{\mathrm{R},l}} = \delta_{\mathrm{R,T}}|h_l|^2\frac{\bar{\omega}_{\mathrm{c}}^2 S_{\mathrm{R}}(\tilde{\theta}_{\mathrm{R},l})}{c^2 d_{\mathrm{R,s},l}^2}, \tag{2.84}$$

for $l = 0, \ldots, L-1$, with $\delta_{\mathrm{R,T}} = 2N_{\mathrm{R}}E_{\mathrm{tot}}/\sigma_{\eta,\mathrm{R}}^2$ being the pseudo-SNR. The information from the l-th NLOS path is described by

$$\boldsymbol{J}_{\mathrm{NLOS},l}^{(\mathrm{s})} = i_l\boldsymbol{z}_l\boldsymbol{z}_l^{\mathrm{T}}, \tag{2.85}$$

where

$$i_l^{-1} = \cos^2(\Delta\theta_l/2)\Big(\frac{1}{i_{\theta_{\mathrm{T},l}}} + \frac{1}{i_{\theta_{\mathrm{R},l}}}\Big) + \sin^2(\Delta\theta_l/2)\frac{1}{i_{\tau_l}}, \tag{2.86}$$
$$\boldsymbol{z}_l = [\boldsymbol{u}_{\perp}^{\mathrm{T}}(\theta_{\mathrm{ref},l}),\ -\cos(\Delta\theta_l/2)d_{\mathrm{R,s},l}]^{\mathrm{T}}, \tag{2.87}$$

with $\theta_{\mathrm{ref},l} = (\theta_{\mathrm{T},l} + \theta_{\mathrm{R},l})/2$ and $\Delta\theta_l = \theta_{\mathrm{R},l} - \theta_{\mathrm{T},l}$. For single-bounce reflections $\boldsymbol{u}(\theta_{\mathrm{ref},l})$ is the normal vector to the reflecting surface. The information loss due to the synchronization error is described by

$$\boldsymbol{J}_{\epsilon_{\mathrm{clk}}}^{(\mathrm{s})} = \boldsymbol{z}_{\epsilon_{\mathrm{clk}}}\boldsymbol{z}_{\epsilon_{\mathrm{clk}}}^{\mathrm{T}}/K_{\epsilon_{\mathrm{clk}}}, \tag{2.88}$$

where

$$\boldsymbol{z}_{\epsilon_{\mathrm{clk}}} = \begin{cases} i_{\tau_0}\boldsymbol{z}_{\tau_0} + \sum_{l=1}^{L}\sin\left(\Delta\theta_l/2\right)i_l\boldsymbol{z}_l, & \text{if LOS exists,} \\ \sum_{l=0}^{L}\sin\left(\Delta\theta_l/2\right)i_l\boldsymbol{z}_l, & \text{otherwise,} \end{cases} \tag{2.89}$$

$$K_{\epsilon_{\mathrm{clk}}} = \begin{cases} i_{\epsilon_{\mathrm{clk}}} + i_{\tau_0} + \sum_{l'=1}^{L-1}\sin^2\left(\Delta\theta_{l'}/2\right)i_{l'}, & \text{if LOS exists,} \\ i_{\epsilon_{\mathrm{clk}}} + \sum_{l'=0}^{L-1}\sin^2\left(\Delta\theta_{l'}/2\right)i_{l'}, & \text{otherwise,} \end{cases} \tag{2.90}$$

with $i_{\epsilon_{\mathrm{clk}}} = \frac{1}{c^2\sigma_{\mathrm{clk}}^2}$. □

Proof: See Appendix A6. ■

Some interesting remarks are to be made based on Theorem 2.1. Similar to [21], we find that the EFIM of each of the single-bounce NLOS paths is rank-1. The intensity of position information is given by (2.86), whereby we can conclude that

$$i_l \leq \min\left(\frac{i_{\tau_l}}{\sin^2(\Delta\theta_l/2)}, \frac{i_{\theta_{\mathrm{T},l}}}{\cos^2(\Delta\theta_l/2)}, \frac{i_{\theta_{\mathrm{R},l}}}{\cos^2(\Delta\theta_l/2)}\right). \tag{2.91}$$

We can also see from (2.85) and (2.87) that the direction of the position information offered by a single-bounce NLOS path is determined solely by the geometry and is independent of the system parameters. The direction is orthogonal to the average of the AOD and AOA of the path, which in the case of single-bounce reflections is parallel to the reflecting surface. A geometric interpretation of this result is provided in Sec. 2.5

We observe that, in the LOS-only case, where the derived expressions (2.77),(2.78), (2.88)-(2.90) are exact, for an imperfectly synchronized system ($0 < \sigma_{\mathrm{clk}}^2 < \infty$) positioning is possible. However, the ranging information provided by the TOA of the LOS path decreases with increasing σ_{clk} and the achievable positioning accuracy is lower bounded by the synchronization error-induced ranging error $\sigma_{\mathrm{clk}}c$. Hence, large values of σ_{clk} may lead to poor position estimation accuracy. For an asynchronous system ($\sigma_{\mathrm{clk}}^2 \to \infty$), the ranging information from the TOA of the LOS path vanishes entirely and at least one NLOS path in addition to the LOS path is required. The NLOS path(s), combined with the LOS path, enables us to resolve the clock offset and compute the position.

When there is no LOS path, at least three NLOS paths are required for positioning [21]. Similarly to the LOS-only case, the achievable accuracy is lower bounded by $\sigma_{\mathrm{clk}}c$ and for an asynchronous system an additional NLOS path is required for positioning.

Similar results can be obtained for unknown Tx position and orientation:

Theorem 2.2. *(Static transmitter localization)* The EFIM for the position $\boldsymbol{p}_{\mathrm{T}}$ and the orientation α_{T} of an imperfectly synchronized transmitter, when the position $\boldsymbol{p}_{\mathrm{R}}$ and orientation α_{R} of the receiver are known, can be asymptotically expressed as in (2.77), (2.78), (2.85) and (2.88), with $\boldsymbol{z}_{\tau_0} = [-\boldsymbol{u}^{\mathrm{T}}(\theta_{\mathrm{T},0}),\ 0]^{\mathrm{T}} \in \mathbb{R}^3$, $\boldsymbol{z}_{\theta_{\mathrm{T},0}} = [\boldsymbol{u}_{\perp}^{\mathrm{T}}(\theta_{\mathrm{T},0}),\ -d_{\mathrm{T,R}}]^{\mathrm{T}}$, $\boldsymbol{z}_{\theta_{\mathrm{R},0}} = [\boldsymbol{u}_{\perp}^{\mathrm{T}}(\theta_{\mathrm{T},0}),\ 0]^{\mathrm{T}}$, and $\boldsymbol{z}_l = [\boldsymbol{u}_{\perp}^{\mathrm{T}}(\theta_{\mathrm{ref},l}),\ -\cos(\Delta\theta_l/2)d_{\mathrm{T,s},l}]^{\mathrm{T}}$. □

Proof: Similar to the proof of Theorem 2.1. ■

Theorems 2.1 and 2.2 can be used for the analysis of the effect of the geometry and the system parameters on the DL and UL positioning accuracy, respectively. Theorem 2.2 can also be used for the analysis of sidelink (SL) positioning, where a UE estimates another UE's relative position.

2.4.2 Dynamic Scenario

We are interested in the EFIM $\boldsymbol{J}_{\mathrm{pov}}$ of the position, orientation and velocity parameters:

$$\boldsymbol{J}_{\mathrm{pov}} = \boldsymbol{T}_{\mathrm{pov}}\boldsymbol{J}_{\boldsymbol{\phi}}\boldsymbol{T}_{\mathrm{pov}}^{\mathrm{T}} - \boldsymbol{T}_{\mathrm{pov}}\boldsymbol{J}_{\boldsymbol{\phi}}\boldsymbol{T}_{\mathrm{np}}^{\mathrm{T}}\left(\boldsymbol{T}_{\mathrm{np}}\boldsymbol{J}_{\boldsymbol{\phi}}\boldsymbol{T}_{\mathrm{np}}^{\mathrm{T}}\right)^{-1}\boldsymbol{T}_{\mathrm{np}}\boldsymbol{J}_{\boldsymbol{\phi}}\boldsymbol{T}_{\mathrm{pov}}^{\mathrm{T}}, \tag{2.92}$$

where we have split $\boldsymbol{T}$ as $\boldsymbol{T} = \left[\boldsymbol{T}_{\mathrm{pov}}^{\mathrm{T}},\ \boldsymbol{T}_{\mathrm{np}}^{\mathrm{T}}\right]^{\mathrm{T}}$, with $\boldsymbol{T}_{\mathrm{pov}}$ consisting of the first 5 rows of $\boldsymbol{T}$.

In order to keep the expressions relatively simple and gain insight on the effect of the movement of the receiver or the transmitter, apart from the assumptions made for the static scenario, we additionally assume that

1) the signal vectors on different subcarriers are (approximately) uncorrelated:

$$\sum_{b=0}^{N_{\mathrm{B}}-1} \boldsymbol{x}[p,b]\boldsymbol{x}^{\mathrm{H}}[q,b] \approx \mathbf{0},\ p \neq q. \tag{2.93}$$

2) $B/f_{\mathrm{c}} \ll \lambda_{\mathrm{c}}/D_{\max}$, where $B \approx \Delta f(\max(\mathcal{P}) - \min(\mathcal{P}))$ is the signal bandwidth and $D_{\max}$ is the largest of the Tx and Rx array apertures, in other words, that the system under consideration is narrowband.

Again, before presenting the results, we define a couple of useful quantities.

Definition 4. The *effective baseband bandwidth* of the signal arriving from the l-th path is

$$\beta_l = \sqrt{\sum\nolimits_{q\in\mathcal{P}} \xi_{l,q}\gamma[q]\omega_q^2/\xi_l - \left(\sum\nolimits_{q\in\mathcal{P}} \xi_{l,q}\gamma[q]\omega_p/\xi_l\right)^2}, \tag{2.94}$$

where

$$\xi_{l,q} = \sum\nolimits_{p\in\mathcal{P}} \left|Q_N\left(\Phi_{p,q,l}\right)\right|^2 \tag{2.95}$$

describes the intensity effect of the Doppler shift for the l-th path on the q-th subcarrier and $\xi_l = \sum_{q\in\mathcal{P}} \gamma[q]\xi_{l,q}$, with $\Phi_{p,q,l} = \left(\omega_p - \omega_q - v_l\omega_{\mathrm{c}}/c\right)T_{\mathrm{s}}/2$. Similar to what is reported in [17], the intensity effect for mm-Wave systems with large bandwidth is very small and can be neglected, i.e. $\xi_{l,q} \approx 1,\ \forall l, q$. Then, (2.94) falls back to (2.74) $\forall l$. □

Definition 5. The *root mean square (rms) duration* of the reference signal arriving from the l-th path is

$$t_{\mathrm{rms},l} = T_{\mathrm{s}}\sqrt{M^2\left(N_{\mathrm{B}}^2 - 1\right)/12 + n_{\mathrm{B,rms},l}^2}, \tag{2.96}$$

where

$$n_{\mathrm{B,rms},l}^2 = \frac{\sum_{q\in\mathcal{P}} \gamma[q] \sum_{p\in\mathcal{P}} \left|Q_N\left(\Phi_{p,q,l}\right)\right|^2 X_{p,q,l}^2}{\xi_l} - \left(\frac{\sum_{q\in\mathcal{P}} \gamma[q] \sum_{p\in\mathcal{P}} \left|Q_N\left(\Phi_{p,q,l}\right)\right|^2 X_{p,q,l}}{\xi_l}\right)^2, \tag{2.97}$$

with $X_{p,q,l} = \left(\cot\left(\Phi_{p,q,l}\right) - N\cot\left(N\Phi_{p,q,l}\right)\right)/2$. It can be shown that for practical scenarios with $\|\boldsymbol{v}_{\mathrm{R}}\|_2/c \ll 1$

$$n_{\mathrm{B,rms},l}^2 \approx n_{\mathrm{B,rms}}^2 = \frac{1}{4}\sum_{q\in\mathcal{P}} \gamma[q] \sum_{p\in\mathcal{P},\ p\neq q} \sin^{-2}\left(\pi(p-q)/N\right). \tag{2.98}$$

□

We now present the main result for the dynamic scenario:

Theorem 2.3. *(Mobile receiver localization)* The EFIM for the position $\boldsymbol{p}_{\mathrm{R}}$, orientation α_{R} and velocity $\boldsymbol{v}_{\mathrm{R}}$ of an imperfectly synchronized mobile receiver, when the position $\boldsymbol{p}_{\mathrm{T}}$ and orientation α_{T} of the static transmitter are known, can be asymptotically expressed as

$$\boldsymbol{J}_{\mathrm{pov}}^{(\mathrm{d})} \rightarrow \begin{cases} \sum_{l=1}^{L-1} \boldsymbol{J}_{\mathrm{NLOS},l}^{(\mathrm{d})} - \boldsymbol{J}_{\epsilon_{\mathrm{clk}}}^{(\mathrm{d})} + \boldsymbol{J}_{\mathrm{LOS}}^{(\mathrm{d})}, & \text{if LOS exists,} \\ \sum_{0=1}^{L-1} \boldsymbol{J}_{\mathrm{NLOS},l}^{(\mathrm{d})} - \boldsymbol{J}_{\epsilon_{\mathrm{clk}}}^{(\mathrm{d})}, & \text{otherwise,} \end{cases} \tag{2.99}$$

where the information from the LOS path is described by

$$\boldsymbol{J}_{\mathrm{LOS}}^{(\mathrm{d})} = i_{\tau_0}\boldsymbol{z}_{\tau_0}\boldsymbol{z}_{\tau_0}^{\mathrm{T}} + i_{\theta_{\mathrm{T},0}}\boldsymbol{z}_{\theta_{\mathrm{T},0}}\boldsymbol{z}_{\theta_{\mathrm{T},0}}^{\mathrm{T}} + i_{\theta_{\mathrm{R},0}}\boldsymbol{z}_{\theta_{\mathrm{R},0}}\boldsymbol{z}_{\theta_{\mathrm{R},0}}^{\mathrm{T}} + i_{v_0}\boldsymbol{z}_{v_0}\boldsymbol{z}_{v_0}^{\mathrm{T}}, \tag{2.100}$$

with

$$\boldsymbol{z}_{\tau_l} = [-\boldsymbol{u}^{\mathrm{T}}(\theta_{\mathrm{R},l}),\ 0,\ 0,\ 0]^{\mathrm{T}} \in \mathbb{R}^5, \tag{2.101}$$
$$\boldsymbol{z}_{\theta_{\mathrm{T},l}} = [\boldsymbol{u}_{\perp}^{\mathrm{T}}(\theta_{\mathrm{R},l}),\ 0,\ 0,\ 0]^{\mathrm{T}} \in \mathbb{R}^5, \tag{2.102}$$
$$\boldsymbol{z}_{\theta_{\mathrm{R},l}} = [\boldsymbol{u}_{\perp}^{\mathrm{T}}(\theta_{\mathrm{R},l}),\ -d_{\mathrm{R,s},l},\ 0,\ 0]^{\mathrm{T}} \in \mathbb{R}^5, \tag{2.103}$$
$$\boldsymbol{z}_{v_l} = [-\boldsymbol{u}_{\perp}^{\mathrm{T}}(\theta_{\mathrm{R},l}),\ 0,\ d_{\mathrm{R,s},l}\boldsymbol{u}^{\mathrm{T}}(\theta_{\mathrm{R},l})/\rho_l]^{\mathrm{T}} \in \mathbb{R}^5, \tag{2.104}$$

and $\rho_l = \boldsymbol{v}_{\mathrm{R}}^{\mathrm{T}}\boldsymbol{u}_{\perp}(\theta_{\mathrm{R},l}),\ l = 0, \ldots, L-1$, being the transverse velocity component. The information from the l-th NLOS path neglecting its coupling with other paths is described by

$$\boldsymbol{J}_{\mathrm{NLOS},l}^{(\mathrm{d})} = f_{\tau,\theta,l}\boldsymbol{z}_{\tau,\theta,l}\boldsymbol{z}_{\tau,\theta,l}^{\mathrm{T}} + f_{\theta,v,l}\boldsymbol{z}_{\theta,v,l}\boldsymbol{z}_{\theta,v,l}^{\mathrm{T}} + f_{\tau,v,l}\boldsymbol{z}_{\tau,v,l}\boldsymbol{z}_{\tau,v,l}^{\mathrm{T}}, \tag{2.105}$$

where

$$\boldsymbol{z}_{\tau,\theta,l} = [\boldsymbol{u}_{\perp}^{\mathrm{T}}(\theta_{\mathrm{ref},l}),\ -\cos(\Delta\theta_l/2)d_{\mathrm{R,s},l},\ 0,\ 0]^{\mathrm{T}} \in \mathbb{R}^5, \tag{2.106}$$
$$\boldsymbol{z}_{\theta,v,l} = [0,\ 0,\ -d_{\mathrm{R,s},l},\ d_{\mathrm{R,s},l}\boldsymbol{u}^{\mathrm{T}}(\theta_{\mathrm{R},l})/\rho_l]^{\mathrm{T}} \in \mathbb{R}^5, \tag{2.107}$$
$$\boldsymbol{z}_{\tau,v,l} = \boldsymbol{z}_{\tau,\theta,l} - \cos(\Delta\theta_l/2)\boldsymbol{z}_{\theta,v,l}, \tag{2.108}$$

and

$$f_{\tau,\theta,l} = \frac{i_{\tau_l}i_{\theta_{\mathrm{R},l}}i_{\theta_{\mathrm{T},l}}}{\chi_l}, \tag{2.109}$$
$$f_{\theta,v,l} = \frac{i_{\theta_{\mathrm{R},l}}i_{v_l}}{\chi_l}\Big(i_{\tau_l}\cos^2(\Delta\theta_l/2) + i_{\theta_{\mathrm{T},l}}\sin^2(\Delta\theta_l/2)\Big), \tag{2.110}$$
$$f_{\tau,v,l} = \frac{i_{\tau_l}i_{v_l}i_{\theta_{\mathrm{T},l}}}{\chi_l}, \tag{2.111}$$
$$\chi_l = \cos^2(\Delta\theta_l/2)i_{\tau_l}\Big(i_{\theta_{\mathrm{T},l}} + i_{\theta_{\mathrm{R},l}} + i_{v_l}\Big) + \sin^2(\Delta\theta_l/2)i_{\theta_{\mathrm{T},l}}\Big(i_{\theta_{\mathrm{R},l}} + i_{v_l}\Big), \tag{2.112}$$

with

$$i_{\tau_l} = \delta_{\mathrm{R,T}}|h_l|^2\xi_l\frac{\beta_l^2}{c^2}, \quad i_{\theta_{\mathrm{T},l}} = \delta_{\mathrm{R,T}}|h_l|^2\xi_l\frac{\omega_{\mathrm{c}}^2 S_{\mathrm{T}}(\tilde{\theta}_{\mathrm{T},l})}{c^2 d_{\mathrm{T,s},l}^2},$$
$$i_{\theta_{\mathrm{R},l}} = \delta_{\mathrm{R,T}}|h_l|^2\xi_l\frac{\omega_{\mathrm{c}}^2 S_{\mathrm{R}}(\tilde{\theta}_{\mathrm{R},l})}{c^2 d_{\mathrm{R,s},l}^2}, \quad i_{v_l} = \delta_{\mathrm{R,T}}|h_l|^2\xi_l\frac{\omega_{\mathrm{c}}^2\rho_l^2 t_{\mathrm{rms},l}^2}{c^2 d_{\mathrm{R,s},l}^2}. \tag{2.113}$$

The information loss due to the synchronization error is described by

$$\boldsymbol{J}_{\epsilon_{\mathrm{clk}}}^{(\mathrm{d})} = \boldsymbol{z}_{\epsilon_{\mathrm{clk}}}\boldsymbol{z}_{\epsilon_{\mathrm{clk}}}^{\mathrm{T}}/K_{\epsilon_{\mathrm{clk}}}, \tag{2.114}$$

where

$$\boldsymbol{z}_{\epsilon_{\mathrm{clk}}} = \begin{cases} \sum_{l=1}^{L}\sin(\Delta\theta_l/2)\big(f_{\tau,\theta,l}\boldsymbol{z}_{\tau,\theta,l} + f_{\tau,v,l}\boldsymbol{z}_{\tau,v,l}\big) + i_{\tau_0}\boldsymbol{z}_{\tau_0}, & \text{if LOS exists,} \\ \sum_{l=0}^{L}\sin\left(\Delta\theta_l/2\right)(f_{\tau,\theta,l}\boldsymbol{z}_{\tau,\theta,l} + f_{\tau,v,l}\boldsymbol{z}_{\tau,v,l}), & \text{otherwise,} \end{cases} \tag{2.115}$$

$$K_{\epsilon_{\mathrm{clk}}} = \begin{cases} i_{\epsilon_{\mathrm{clk}}} + i_{\tau_0} + \sum_{l'=1}^{L-1}\sin^2\left(\Delta\theta_{l'}/2\right)\big(f_{\tau,\theta,l} + f_{\tau,v,l}\big), & \text{if LOS exists,} \\ i_{\epsilon_{\mathrm{clk}}}\sum_{l'=0}^{L-1}\sin^2\left(\Delta\theta_{l'}\right)\big(f_{\tau,\theta,l} + f_{\tau,v,l}\big), & \text{otherwise.} \end{cases} \tag{2.116}$$

□

Proof: Similar to the proof of Theorem 2.1. ■

Some remarks on the theorem above should be made. From (2.104), we see that the Doppler shift of the LOS offers velocity information in the radial direction. In addition, it provides position information in the transverse direction, which corresponds to angle information. The intuition behind this is that, as an antenna array provides angle information by sampling the space at different locations *simultaneously*, the movement of the receiver also provides angle information by allowing every single antenna element to sample the space at different locations *over time*. The intensity of the position information is proportional to $\rho_0^2 t_{\mathrm{rms},0}^2$. As explained in [17], $\rho_0 t_{\mathrm{rms},0}$ can be interpreted as the *synthetic array aperture* for the LOS path, which is generated by the movement of the receiver.

For the l-th single-bounce NLOS path the synthetic array aperture is $\rho_l t_{\mathrm{rms},l}$. From (2.105)-(2.108) we conclude that, from rank-1 EFIM in $\mathbb{R}^3$ in the static scenario, the single-bounce NLOS paths now offer a rank-2 EFIM in $\mathbb{R}^5$. This results from the fact that $\boldsymbol{z}_{\tau,v,l}$ is a linear combination of $\boldsymbol{z}_{\tau,\theta,l}$ and $\boldsymbol{z}_{\theta,v,l}$. The EFIM from the l-th path is composed by the three rank-1 matrices determined by $\boldsymbol{z}_{\tau,\theta,l}$, $\boldsymbol{z}_{\tau,v,l}$ and $\boldsymbol{z}_{\theta,v,l}$. Only the first two matrices offer position information, in the same direction as in the static scenario. More specifically, the first matrix offers position and orientation information and the second matrix position and velocity information. The third matrix contains information only about the orientation and the velocity of the receiver.

In case the LOS path exists, at least one NLOS path is additionally required to have a full rank $\boldsymbol{J}_{\mathrm{pov}}$, i.e., in order to be able to estimate the position, orientation and velocity. When only the LOS path is available, the transverse velocity cannot be estimated. Writing $\boldsymbol{v}_{\mathrm{R}} = v_{\mathrm{r}}\boldsymbol{u}\big(\theta_{\mathrm{R},0}\big) + v_{\perp}\boldsymbol{u}\big(\theta_{\mathrm{R},0}\big)$, where v_r and $v_{\perp}$ are the radial and transverse velocity components, and plugging it into the dynamic signal model (2.29), (2.30), we can see that only the radial velocity is observable. This could also be seen from (2.104), where we observe that the LOS path offers velocity information only in the radial direction. Therefore, the LOS path allows us to estimate the position and the radial velocity v_r, but the NLOS paths enable us to obtain the missing orthogonal component $v_{\perp}$ of the velocity vector. This could be very important in the prediction step of position tracking algorithms. In the NLOS-only case three paths are required to obtain the position, orientation and velocity of the receiver, even in asynchronous operation.

Similar results, which are omitted for brevity, can be obtained in the case with a moving transmitter with unknown orientation and a static receiver *(mobile transmitter localization)*.

2.5 Geometric Interpretation of Position Information from Single-Bounce Non-Line-of-Sight (NLOS) paths With and Without Prior Information

For paths corresponding to reflections, the path and its parameters τ_l', $\theta_{\mathrm{T},l}$ and $\theta_{\mathrm{R},l}$ can be equivalently described using the concept of VAs [58]. The VAs have a physical interpretation, as they are mirror images of the physical anchor (PA) with respect to the reflecting surfaces, where the PA is the device whose position is considered to be known. In Fig. 2.2, which is the same as that of Fig. 2.1, but including also VAs. With $\boldsymbol{u}(\theta_{\mathrm{ref},l})$ denoting the normal vector to the reflecting surface corresponding to the l-th path, the position of the VA is

$$\boldsymbol{p}_{\mathrm{VA},l} = \boldsymbol{p}_{\mathrm{T}} + 2\boldsymbol{u}(\theta_{\mathrm{ref},l})\boldsymbol{u}^{\mathrm{T}}(\theta_{\mathrm{ref},l})\big(\boldsymbol{p}_{\mathrm{s},l} - \boldsymbol{p}_{\mathrm{T}}\big). \tag{2.117}$$

$(\pi - \theta_{\mathrm{T},l}) + 2\phi + \theta_{\mathrm{R},l} - \pi = \pi \Rightarrow \phi = \frac{\pi - \Delta\theta_l}{2}$, where ϕ is the angle between the AOD line and the surface line. Then, $\theta_{\mathrm{ref},l} = \theta_{\mathrm{R},l} - \pi + \phi + \pi/2 = \frac{\theta_{\mathrm{T},l} + \theta_{\mathrm{R},l}}{2}$. With simple geometric arguments we can

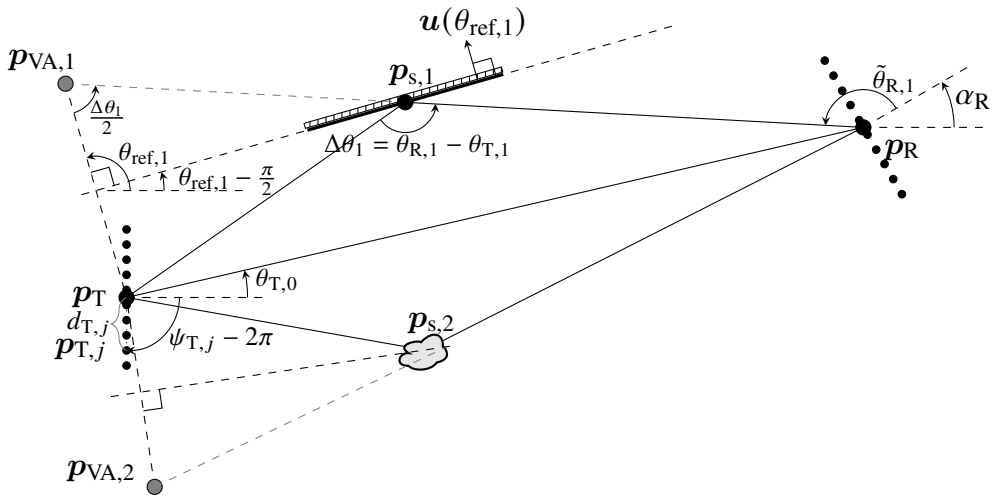

Fig. 2.2. Geometric model, example with ULAs at the Tx and Rx.

see that for a single-bounce path

$$\theta_{\text{ref},l} = \frac{\theta_{\text{T},l} + \theta_{\text{R},l}}{2}. \tag{2.118}$$

Given that $\theta_{\text{T},l}$ and $\theta_{\text{R},l}$ can be expressed as functions of $\boldsymbol{p}_{\text{T}}$, $\boldsymbol{p}_{\text{R}}$ and $\boldsymbol{p}_{\text{s},l}$ via (2.11), (2.12), (2.13) and (2.14), the concept of the virtual anchor can be used also in the case of a single-bounce scattered path, although without having a physical interpretation in this case. In fact, while for a reflected path $p_{\text{VA},l}$ is fixed, as it depends on the position of the PA and the reflecting surface, for a scattered path it can change as the UE moves. Hence, in this case, the term "anchor" is slightly abused, but it serves the purpose of having an alternative common mathematical description of single-bounce paths.

We can rewrite the relations connecting the parameters of the NLOS paths with the underlying geometry (2.8), (2.11) and (2.12) using $\boldsymbol{p}_{\text{VA},l}$ instead of $\boldsymbol{p}_{\text{s},l}$. The delay of the l-th NLOS path can be expressed as

$$\tau_l = \|\boldsymbol{p}_{\text{R}} - \boldsymbol{p}_{\text{VA},l}\|_2/c. \tag{2.119}$$

The expressions for the AOD and AOA depend on the scenario. When the Tx is the PA and the Rx is the UE, i.e., in a DL scenario, we have

$$\tilde{\theta}_{\text{R},l} = \text{atan2}\Big(p_{\text{VA},l,\text{y}} - p_{\text{R,y}}, p_{\text{VA},l,\text{x}} - p_{\text{R,x}}\Big) - \alpha_{\text{R}}. \tag{2.120}$$

From (2.118), (2.120) and

$$\theta_{\text{ref},l} = \text{atan2}(p_{\text{VA},l,\text{y}} - p_{\text{T,y}}, p_{\text{VA},l,\text{x}} - p_{\text{T,x}}), \tag{2.121}$$

we get the following expression for the AOD

$$\tilde{\theta}_{\text{T},l} = 2\,\text{atan2}(p_{\text{VA},l,\text{y}} - p_{\text{T,y}}, p_{\text{VA},l,\text{x}} - p_{\text{T,x}}) - \text{atan2}(p_{\text{VA},l,\text{y}} - p_{\text{R,y}}, p_{\text{VA},l,\text{x}} - p_{\text{R,x}}) - \alpha_{\text{T}}. \tag{2.122}$$

In this section, we consider the case when no prior knowledge on the VAs' locations is available, as in Sec. 2.4, but we also extend the analysis to the case of perfect and imperfect prior

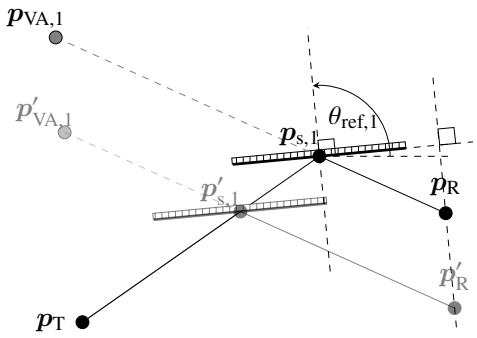

Fig. 2.3. Potential solutions for p_{R}, $p_{\mathrm{s},l}$ and $p_{\mathrm{VA},l}$ explaining the measurements for a single-bounce reflection.

knowledge on the VAs' locations. The parameter vector now contains the location of the VAs instead of the locations of the POIs:

$$\boldsymbol{\nu} = \begin{cases} [\boldsymbol{p}_{\mathrm{R}}^{\mathrm{T}}, \alpha_{\mathrm{R}}, \epsilon_{\mathrm{clk}}, \boldsymbol{h}_0^{\mathrm{T}}, \boldsymbol{p}_{\mathrm{VA},1}^{\mathrm{T}}, \boldsymbol{h}_1^{\mathrm{T}}, \ldots, \boldsymbol{p}_{\mathrm{VA},L-1}^{\mathrm{T}}, \boldsymbol{h}_{L-1}^{\mathrm{T}}]^{\mathrm{T}} \in \mathbb{R}^{4L+2}, & \text{0-th path is LOS,} \\ [\boldsymbol{p}_{\mathrm{R}}^{\mathrm{T}}, \alpha_{\mathrm{R}}, \epsilon_{\mathrm{clk}}, \boldsymbol{p}_{\mathrm{VA},0}^{\mathrm{T}}, \boldsymbol{h}_0^{\mathrm{T}}, \boldsymbol{p}_{\mathrm{VA},1}^{\mathrm{T}}, \boldsymbol{h}_1^{\mathrm{T}}, \ldots, \boldsymbol{p}_{\mathrm{VA},L-1}^{\mathrm{T}}, \boldsymbol{h}_{L-1}^{\mathrm{T}}]^{\mathrm{T}} \in \mathbb{R}^{4L+4}, & \text{otherwise.} \end{cases} \tag{2.123}$$

In the case of no knowledge on the VAs' location, the intensity and direction of position information from a single-bounce reflection are given by (2.86) and (2.87), respectively. As discussed in Sec. 2.4, the direction of position information is always parallel to the reflecting surface and independent of the Tx and Rx location. At first glance, this is a surprising result, since for LOS paths the direction of position information depends on $\boldsymbol{p}_{\mathrm{R}}$ and $\boldsymbol{p}_{\mathrm{T}}$. A geometrically intuitive explanation of this result can be obtained from Fig. 2.3. In Fig. 2.3 we consider a single-bounce reflection and plot two potential geometries $\{\boldsymbol{p}_{\mathrm{R}}, \boldsymbol{p}_{s,1}, \boldsymbol{p}_{\mathrm{VA},1}\}$ and $\{\boldsymbol{p}'_{\mathrm{R}}, \boldsymbol{p}'_{s,1}, \boldsymbol{p}'_{\mathrm{VA},1}\}$ that would produce the same TOA, AOD and AOA. In fact, there are infinitely many such geometries, parametrized as

$$\begin{aligned} \boldsymbol{p}_{\mathrm{R}} &= \boldsymbol{p}_{\mathrm{T}} + \lambda \boldsymbol{u}(\theta_{\mathrm{T},l}) - (c \cdot \tau_l - \lambda)\boldsymbol{u}(\theta_{\mathrm{R},l}) \\ &= \boldsymbol{p}_{\mathrm{T}} - c \cdot \tau_l \boldsymbol{u}(\theta_{\mathrm{R},l}) + 2\lambda \cos(\Delta\theta_l/2)\boldsymbol{u}(\theta_{\mathrm{ref},l}), \qquad (2.124) \\ \boldsymbol{p}_{\mathrm{VA},l} &= \boldsymbol{p}_{\mathrm{T}} + 2\lambda \cos(\Delta\theta_l/2)\boldsymbol{u}(\theta_{\mathrm{ref},l}), \qquad (2.125) \\ \boldsymbol{p}_{\mathrm{s},l} &= \boldsymbol{p}_{\mathrm{T}} + \lambda \boldsymbol{u}(\theta_{\mathrm{T},l}), \qquad (2.126) \end{aligned}$$

with $0 < \lambda < c \cdot \tau_l$. As can be seen in (2.124), the locus of $\boldsymbol{p}_{\mathrm{R}}$ is a line segment normal to the reflecting surface. Hence, the NLOS path associated with the reflection provides position information only in the direction that is perpendicular to this line segment, i.e., in the direction parallel to the reflecting surface. An implication of this result is that information from single-bounce paths from parallel (or close to parallel) reflecting surfaces may not suffice for target localization.

We then examine the case where the Rx has prior information on the VAs' location. Here, we derive the EFIM and corresponding CRLB treating $\boldsymbol{\nu}$ as a deterministic parameter vector, for the estimation of which two sources of information are used: the received signal and the prior information [32]. In this case the FIM is defined as in (2.39), but for the observation-related FIM, instead of averaging over the prior pdf, we use the true value of $\boldsymbol{\nu}$, as usual for the FIM of deterministic parameter vectors:

$$\boldsymbol{J}_{\boldsymbol{\nu}}^{(\mathrm{o})} = \mathbb{E}_{\boldsymbol{Y}|\boldsymbol{\nu}_r}\left[\frac{\partial \ln p(\boldsymbol{Y}|\boldsymbol{\nu})}{\partial \boldsymbol{\nu}} \frac{\partial \ln p(\boldsymbol{Y}|\boldsymbol{\nu})}{\partial \boldsymbol{\nu}^{\mathrm{T}}}\right] = -\mathbb{E}_{\boldsymbol{Y}|\boldsymbol{\nu}_r}\left[\frac{\partial^2 \ln p(\boldsymbol{Y}|\boldsymbol{\nu})}{\partial \boldsymbol{\nu} \partial \boldsymbol{\nu}^{\mathrm{T}}}\right] \tag{2.127}$$

We note that the results in the previous section would remain unchanged, regardless of whether $\boldsymbol{\nu}$ is treated as a deterministic or random vector, as the observation-related part of the FIM is independent of the value of ϵ_{clk}.

The prior information on the location of the l-th VA is encoded by the pdfs $\mathcal{N}(\boldsymbol{p}_{\text{VA},l}, \boldsymbol{\Sigma}_{\text{VA,pr},l})$. We express the covariance matrix $\Sigma_{\text{VA,pr},l}$ as

$$\boldsymbol{\Sigma}_{\text{VA,pr},l} = [\boldsymbol{u}(\theta_{\text{R},l})\ \boldsymbol{u}_{\perp}(\theta_{\text{R},l})] \begin{bmatrix} \sigma_{l,\parallel}^2 & s_l \sigma_{l,\parallel}\sigma_{l,\perp} \\ s_l \sigma_{l,\parallel}\sigma_{l,\perp} & \sigma_{l,\perp}^2 \end{bmatrix} \begin{bmatrix} \boldsymbol{u}^{\text{T}}(\theta_{\text{R},l}) \\ \boldsymbol{u}_{\perp}^{\text{T}}(\theta_{\text{R},l}) \end{bmatrix}. \tag{2.128}$$

The FIM then reads as

$$\boldsymbol{J}_{\boldsymbol{\nu}} = \boldsymbol{T}\boldsymbol{J}_{\tilde{\boldsymbol{\nu}}}^{(\text{o})}\boldsymbol{T}^{\text{T}} + \begin{bmatrix} \boldsymbol{0} & \boldsymbol{0} \\ \boldsymbol{0} & \boldsymbol{J}_{\text{VA,pr}} \end{bmatrix} + \frac{1}{\sigma_{\text{clk}}^2}\boldsymbol{e}_4\boldsymbol{e}_4^{\text{T}}, \tag{2.129}$$

where in the case where the LOS path exists

$$\boldsymbol{J}_{\text{VA,pr}} = \begin{bmatrix} \boldsymbol{0}_{2\times2} & \boldsymbol{0}_{2\times2} & \boldsymbol{0}_{2\times2} & \dots & \boldsymbol{0}_{2\times2} & \boldsymbol{0}_{2\times2} \\ \boldsymbol{0}_{2\times2} & \boldsymbol{\Sigma}_{\text{VA,pr},1}^{-1} & \boldsymbol{0}_{2\times2} & \dots & \boldsymbol{0}_{2\times2} & \boldsymbol{0}_{2\times2} \\ \boldsymbol{0}_{2\times2} & \boldsymbol{0}_{2\times2} & \boldsymbol{0}_{2\times2} & \dots & \boldsymbol{0}_{2\times2} & \boldsymbol{0}_{2\times2} \\ \vdots & \vdots & \vdots & \ddots & \vdots & \vdots \\ \boldsymbol{0}_{2\times2} & \boldsymbol{0}_{2\times2} & \boldsymbol{0}_{2\times2} & \dots & \boldsymbol{\Sigma}_{\text{VA,pr},L-1}^{-1} & \boldsymbol{0}_{2\times2} \\ \boldsymbol{0}_{2\times2} & \boldsymbol{0}_{2\times2} & \boldsymbol{0}_{2\times2} & \dots & \boldsymbol{0}_{2\times2} & \boldsymbol{0}_{2\times2} \end{bmatrix} \in \mathbb{R}^{2+4(L-1)\times 2+4(L-1)}. \tag{2.130}$$

If the LOS path does not exist, (2.130) is adjusted accordingly.

The position and orientation EFIM has the form of (2.77), with $\boldsymbol{J}_{\text{NLOS},l}^{(\text{s})}$ and $\boldsymbol{J}_{\epsilon_{\text{clk}}}^{(\text{s})}$ given by

$$\boldsymbol{J}_{\text{NLOS},l}^{(\text{s})} = [\boldsymbol{z}_{\tau_l},\ \boldsymbol{z}_{\theta_{\text{T},l}},\ \boldsymbol{z}_{\theta_{\text{R},l}}]\boldsymbol{M}_l[\boldsymbol{z}_{\tau_l},\ \boldsymbol{z}_{\theta_{\text{T},l}},\ \boldsymbol{z}_{\theta_{\text{R},l}}]^{\text{T}}, \tag{2.131}$$

$$\boldsymbol{J}_{\epsilon_{\text{clk}}}^{(\text{s})} = \boldsymbol{z}_{\epsilon_{\text{clk}}}\boldsymbol{z}_{\epsilon_{\text{clk}}}^{\text{T}}/K_{\epsilon_{\text{clk}}}, \tag{2.132}$$

$$\boldsymbol{z}_{\epsilon_{\text{clk}}} = i_{\tau_0}\boldsymbol{z}_{\tau_0} + \sum_l [\boldsymbol{z}_{\tau_l},\ \boldsymbol{z}_{\theta_{\text{T},l}},\ \boldsymbol{z}_{\theta_{\text{R},l}}]\boldsymbol{M}_{l,:,1}, \tag{2.133}$$

$$K_{\epsilon_{\text{clk}}} = i_{\tau_0} + i_{\epsilon_{\text{clk}}} + \sum_l M_{l,1,1}, \tag{2.134}$$

with the entries of $\boldsymbol{M}_l$ given in Appendix A7. The obtained expressions are quite involved, but are useful in examining how the position and orientation information from single-bounce NLOS paths changes when the prior information on the locations of the VAs changes from perfect to none. With perfectly known VAs' locations, i.e., $\sigma_{l,\parallel}, \sigma_{l,\perp} \to 0$, we have

$$\boldsymbol{J}_{\text{NLOS},l}^{(\text{s})} = i_{\tau_l}\boldsymbol{z}_{\tau_l}\boldsymbol{z}_{\tau_l}^{\text{T}} + i_{\theta_{\text{T},l}}\boldsymbol{z}_{\theta_{\text{T},l}}\boldsymbol{z}_{\theta_{\text{T},l}}^{\text{T}} + i_{\theta_{\text{R},l}}\boldsymbol{z}_{\theta_{\text{R},l}}\boldsymbol{z}_{\theta_{\text{R},l}}^{\text{T}}, \tag{2.135}$$

$$\boldsymbol{z}_{\epsilon_{\text{clk}}} = i_{\tau_0}\boldsymbol{z}_{\tau_0} + \sum_l i_{\tau_l}\boldsymbol{z}_{\tau_l}, \tag{2.136}$$

$$K_{\epsilon_{\text{clk}}} = i_{\tau_0} + i_{\epsilon_{\text{clk}}} + \sum_l i_{\tau_l}. \tag{2.137}$$

It is evident that, when their locations are perfectly known, the VAs act as PAs, offering rank-3 position and orientation information. In other words, the single-bounce NLOS paths behave as LOS paths between the corresponding VA and the Rx. We also note that, for $\sigma_{l,\parallel}, \sigma_{l,\perp} \to \infty$, (2.135)-(2.137) fall back to (2.85)-(2.90). In Sec. 2.6 we examine how the transition from no to perfect prior knowledge affects the ability of the Rx to localize itself.

2.6 Numerical Results

In this section, we numerically evaluate the expressions derived above. After defining the simulation parameters, we first conduct a comparison of DL and UL positioning with orthonormal and random beamformers. We then evaluate the accuracy of the asymptotic expressions derived in Sec. 2.4. We also study the effect of synchronization errors on the achievable positioning accuracy. Furthermore, we investigate the impact of mobility on the PEB for different channel types (LOS-only, NLOS-only, LOS + NLOS) and different levels of synchronization error variance.

2.6.1 Simulation Parameters

We consider a setup where the transmitter and the receiver are equipped with UCAs with $\lambda_c/2$-spaced elements, where $\lambda_c = c/f_c$ with $f_c = 38\,\text{GHz}$. The orientation of the arrays is irrelevant as the SAAF of a UCA is independent of the angle. Unless otherwise specified, we set $N_T = 32$, $N_R = 16$ and fix the position of the transmitter at $\boldsymbol{p}_T = [0\,\text{m},\ 0\,\text{m}]^T$. The receiver lies in a 60 m×60 m area with the transmitter at its center, i.e., $-30\,\text{m} \le p_{R,x} \le 30\,\text{m}$, $-30\,\text{m} \le p_{R,y} \le 30\,\text{m}$. The sampling frequency is set to $f_s = 122.88$ MHz, the number of subcarriers is $N = 64$ and $N_B = 10$ OFDM symbols are transmitted. The set of loaded subcarriers is $\mathcal{P} = \{-31, -30, \ldots, -1, 1, 2, \ldots, 31\}$ and $\gamma[p] = 1/|\mathcal{P}|,\ \forall p \in \mathcal{P}$, with $|\mathcal{P}| = 62$. We set the average transmit energy per time domain sample E_T to be such that $E_T f_s = 37\,\text{dBm}$. The noise spectral density is $N_0 = -174\,\text{dBm}\,\text{Hz}^{-1}$ and the Rx noise figure is NF = 13 dB, with the variance of the discrete time noise being $\sigma_{\eta,R} = N_0 \cdot \text{NF}$.

For the path gains we follow [21]: the magnitude of the coefficient of the LOS path is $|h_0| = \lambda_c/(4\pi d_{T,R})$, the magnitude of the NLOS paths is

$$|h_l| = \frac{\lambda_c}{4\pi} \begin{cases} \frac{\sqrt{\Gamma_{\text{refl},l}}}{d_{T,s,l}+d_{R,s,l}}, & \text{for a reflector,} \\ \sqrt{\frac{\sigma^2_{\text{RCS},l}}{4\pi}}\frac{1}{d_{T,s,l}d_{R,s,l}}, & \text{for a scatterer} \end{cases} \tag{2.138}$$

and the phase of all the paths is uniformly distributed.

2.6.2 Accuracy of the Asymptotic Expressions

We evaluate the accuracy of the asymptotic expressions derived in Sec. 2.4 for the FIM and, consequently, for the position and orientation CRLB, comparing them with the exact expressions from Sec. 2.2. The Tx's reference point is located at the origin, i.e., $\boldsymbol{p}_T = [0,\ 0]^T$. The receiver and two POIs, which correspond to scattering events, with $\sigma^2_{\text{RCS},l} = 50\,\text{m}^2$, are randomly placed in a $60\,\text{m} \times 60\,\text{m}$ square area according to a uniform distribution, with the following two restrictions:

- The Rx is in the far field of the Tx and the POIs are in the far field of the Tx and the Rx, i.e., $\{d_{T,s,l}\}_{l=0}^{L-1} > d_{f,T}$ and $\{d_{R,s,l}\}_{l=0}^{L-1} > d_{f,R}$, where $d_{f,T} = 2D^2_{\text{max},T}/\lambda_c$ and $d_{f,R} = 2D^2_{\text{max},R}/\lambda_c$ are the Fraunhofer distances of the Tx and Rx arrays.
- The angular separation of the resulting propagation paths both at the transmitter and the receiver is above a minimum value $\Delta\theta_{\min}$. The threshold is chosen so as to let the asymptotic orthogonality "kick in" for a reasonable number of antennas; the smaller the minimum angular separation is, the more antennas are required for the asymptotic bounds to approach the exact bounds.

Referring to the exact PEB as PEB_{ex} and to the asymptotic PEB as PEB_{as}, we define the relative error ε_{as} of the asymptotic expressions as

$$\varepsilon_{\text{as}} = \frac{\text{PEB}_{\text{as}} - \text{PEB}_{\text{ex}}}{\text{PEB}_{\text{ex}}}. \tag{2.139}$$

We assume no time synchronization between the Tx and Rx. In Fig. 2.4 we plot ε_{as} as a function of N_{T} and N_{R}, for minimum angular separation $\Delta\theta_{\min} = 5°$ (Fig. 2.4(a)) and $\Delta\theta_{\min} = 1°$ (Fig. 2.4(b)) averaging over 10000 random realizations of the geometry and the reference signal, whose entries are chosen as random quadrature phase shift keying (QPSK) symbols. In order to keep the geometry fixed with varying number of antennas and satisfy the far field assumption, we use the Fraunhofer distance of the largest considered array, i.e., UCA with 50 elements, which is equal to 0.25 mm, to obtain valid geometry realizations according to the aforementioned restrictions. We can see in Fig. 2.4 that, as the number of Tx and Rx antennas increases, the relative error of the asymptotic expressions decreases as well. Comparing Figs. 2.4(a) and (b) we observe that the relative error for minimum angular separation is slightly larger for the same number of antennas. As explaned above, this is due to the fact the further apart the angles (AOD and/or AOA) of the paths are, the more accurate the asymptotic orthogonality conditions (2.68)-(2.70) are.

2.6.3 Comparison of Uplink and Downlink Positioning

In Section 2.3, we studied the relation of the PEB in the DL and the UL when the same set of orthonormal beamforming vectors are used by each device for transmission and reception. We found that, under the same pseudo-SNR, DL and UL positioning are equivalent. Here, we conduct a numerical comparison of DL and UL positioning when the devices employ random beamforming vectors for transmission and reception. We consider the same setup as before: the BS is located at the origin and the UE and POIs are randomly placed in a 60 m × 60 m square area according to a uniform distribution, with restrictions stated in Sec. 2.6.2 and minimum angular separation 3°. We set $M_{\text{BS}} = 16$, which is M_{T} in the DL and M_{R} in the UL. Similarly, we set $M_{\text{UE}} = 4$, which is M_{R} in the DL and M_{T} in the UL. For each geometry realization, a random realization of the analog beamforming matrix of the BS (UE) is obtained, with its elements having constant modulus $1/\sqrt{N_{\text{BS}}}$ ($1/\sqrt{N_{\text{UE}}}$) with random phase uniformly distributed in $[-\pi, \pi)$. The available transmit energy is uniformly allocated to the beamforming vectors and the subcarriers, i.e.,

$$\sum_{b=0}^{N_{\text{B}}-1} \boldsymbol{x}[p,b]\boldsymbol{x}^{\text{H}}[p,b] = \frac{E_{\text{tot}}}{N_{\text{P}}} \frac{\boldsymbol{I}_{M_{\text{T}}}}{M_{\text{T}}}. \tag{2.140}$$

To conduct a realistic and fair comparison between the DL and the UL, we refer to [59, Tables 6.1.1-1 and 6.1.1-4] to set appropriate values for the Tx and the noise figure of the BS and the UE. For $f_{\text{c}} = 38$ GHz, which corresponds to frequency range (FR) 2 of 3GPP standards, and an urban micro scenario we set the Tx energy of the BS and the UE such that $E_{\text{T,BS}} f_{\text{s}} = 37$ dBm and $E_{\text{T,UE}} f_{\text{s}} = 23$ dBm and for their corresponding noise figures we use $\text{NF}_{\text{BS}} = 7$ dB and $\text{NF}_{\text{UE}} = 13$ dB.

In Fig. 2.5, using the expressions for the exact CRLB (2.39)-(2.45), we plot the cumulative distribution function (cdf) for the PEB in the DL and UL for $\alpha_{\text{UE}} = 180°$ for perfect synchronization and imperfect synchronization with $\sigma_{\text{clk}} = 0.5T_{\text{s}}$. We can see in Fig. 2.5 that the positioning accuracy in the DL is higher than in the UL. With perfect synchronization, the PEB at the 95-th percentile being 0.04 m in the DL and 0.11 m in the UL. With imperfect synchronization the PEB

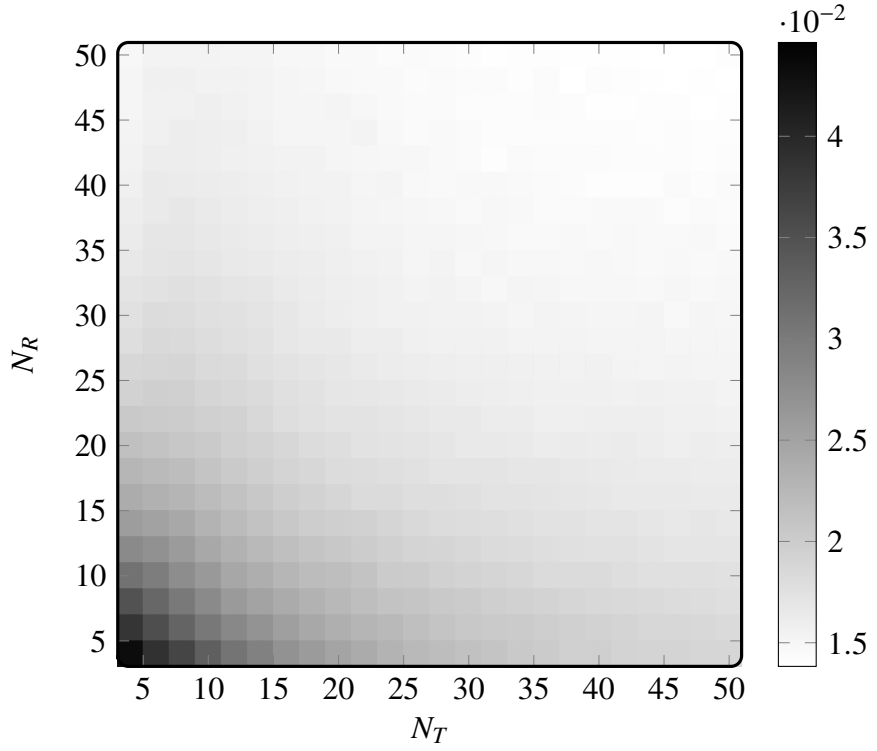

(a) Minimum angular separation $\Delta\theta_{\text{min}} = 5°$

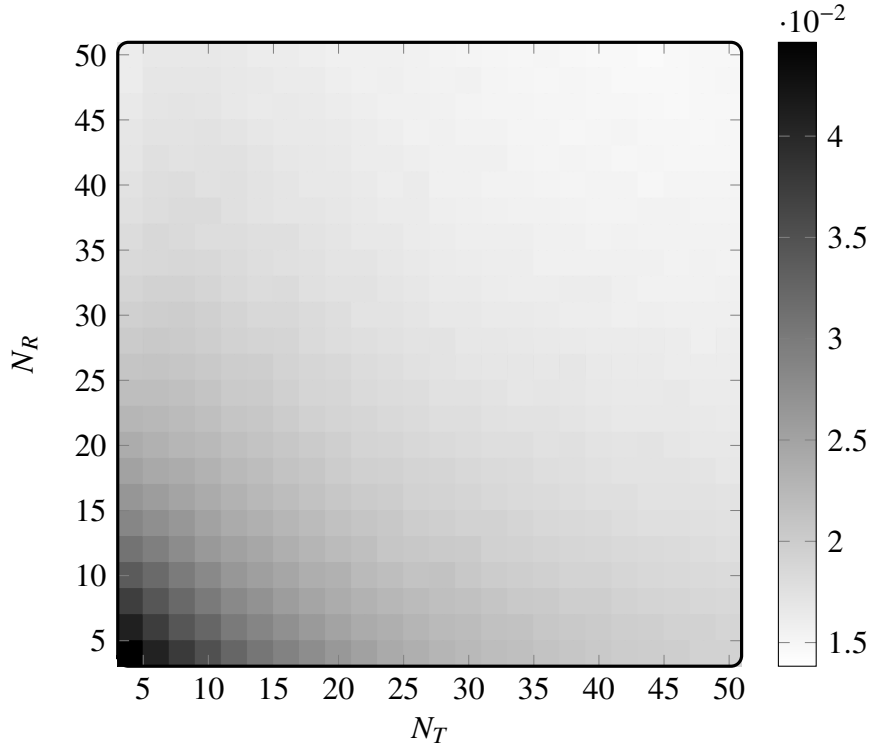

(b) Minimum angular separation $\Delta\theta_{\text{min}} = 1°$

Fig. 2.4. Relative error ε_{as} of the asymptotic PEB as a function of the number of Tx and Rx antennas for different minimum angular separations.

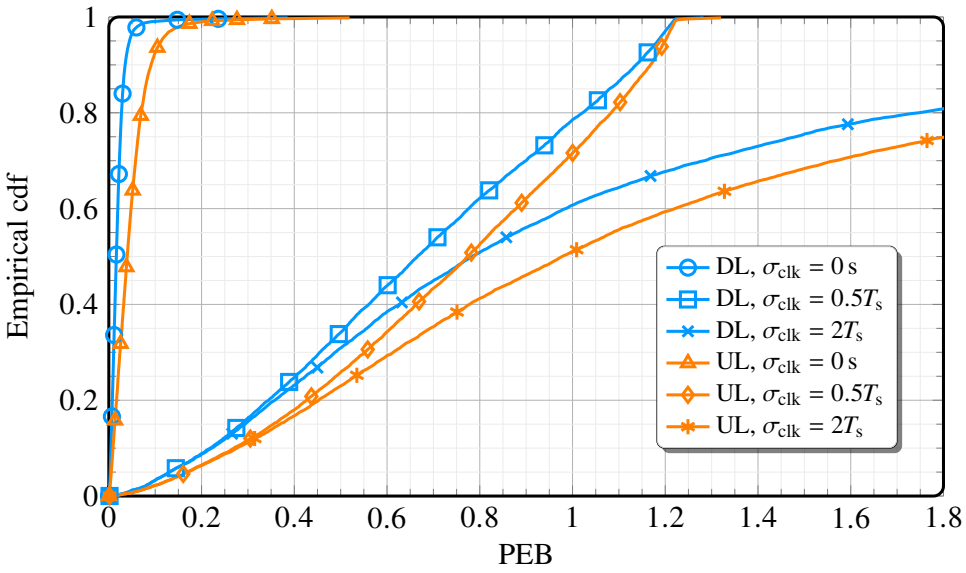

Fig. 2.5. DL and UL positioning comparison with random beamforming vectors for transmission and reception.

at the 95-th percentile is 1.07 m and 1.12 m for $\sigma_{\text{clk}} = 0.5T_\text{s}$ and 2.05 m and 2.44 m for $\sigma_{\text{clk}} = 2T_\text{s}$ in the DL and the UL, respectively. The superior performance of the DL is attributed to its higher pseudo-SNR, as $\delta_{\text{DL}}/\delta_{\text{UL}} = 2\,\text{dB}$. Furthermore, we can observe that the synchronization accuracy has a significant impact on the achievable positioning accuracy, due to the drastic decrease of range information obtained from the LOS path. Nevertheless, we can see that the presence of the single-bounce NLOS paths allows us to obtain good positioning accuracy under imperfect synchronization compared to the LOS-only case, where the PEB would be lower bounded by $\sigma_{\text{clk}}c_0$, which is equal to 1.22 m and 4.88 m for $\sigma_{\text{clk}} = 0.5T_\text{s}$ and $\sigma_{\text{clk}} = 2T_\text{s}$, respectively. In the following section, we examine the effect of synchronization in more detail.

2.6.4 The Importance of Synchronization

As seen in the last section, we saw that the time synchronization error can have a significant impact on the achievable localization accuracy. In this section, we have a closer look at the impact of the synchronization error and how the exploitation of single-bounce NLOS paths can help to mitigate it.

We first consider a setup with parameters as described in Sec. 2.6.1, with one POI with fixed position at $\boldsymbol{p}_{\text{s},1} = [10\,\text{m},\ 0\,\text{m}]^\text{T}$, and compute the asymptotic PEB for all possible Rx locations in the considered rectangular area. In Fig. 2.8 we plot the asymptotic PEB for a receiver with perfect synchronization (Fig. 2.8(a)) and with imperfect synchronization with $\sigma_{\text{clk}} = 0.5T_\text{s} \approx 4\,\text{ns}$ (Fig. 2.8(b)). In Fig. 2.6 we see that, under perfect Tx-Rx synchronization, the PEB is below 4 cm for all considered Rx locations. In addition, since the contour lines are concentric circles with the Tx at their center, the PEB depends only on the Tx-Rx distance. In this case, the range and angle Fisher information from the LOS path are dominant compared to the Fisher information provided by the NLOS paths. With the Tx being equipped with a UCA, the Fisher information on the AOD is independent of the AOD and depends on the Tx-Rx distance through the SNR. This, together with the fact that the range information also depends only on the distance through the SNR, explains the shape of the contour lines.

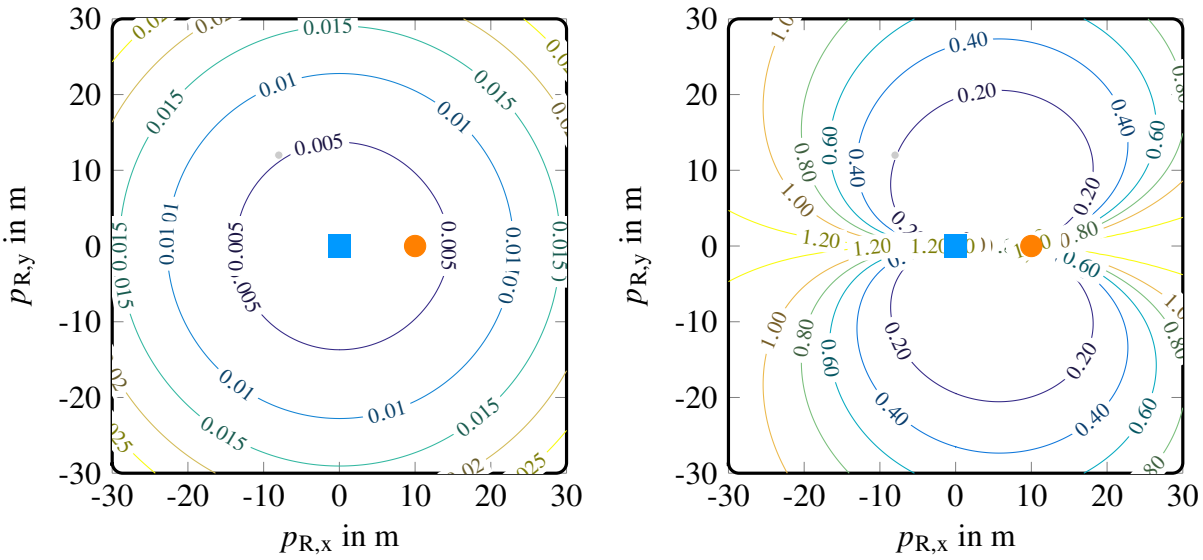

(a) Perfect synchronization.

(b) Imperfect synchronization: $\sigma_{\mathrm{clk}} = 0.5T_{\mathrm{s}} \approx 4\,\mathrm{ns}$.

Fig. 2.6. PEB in m for Rx localization with $\boldsymbol{p}_{\mathrm{T}} = [0\,\mathrm{m},\ 0\,\mathrm{m}]^{\mathrm{T}}, \boldsymbol{p}_{\mathrm{s},1} = [10\,\mathrm{m},\ 0\,\mathrm{m}]^{\mathrm{T}}$ under different levels of synchronization error variance. The position of the Tx is shown with a square and the position of the POI with a circle.

We can see in Fig. 2.6(b) that clock synchronization errors with standard deviation as small as $0.5T_{\mathrm{s}} \approx 4\,\mathrm{ns}$, corresponding to $c\sigma_{\mathrm{clk}} = 1.22\,\mathrm{m}$, can severely degrade the achievable positioning accuracy, compared to the case with perfect synchronization. It is evident that the shape of the contour lines is different and the PEB depends not only on the range, but also on the angular component of the Rx's position. When the receiver lies near the line between the Tx and the POI ($p_{\mathrm{R,x}}$ close to 0) the PEB reaches its maximum value ($c \approx \sigma_{\mathrm{clk}} = 1.22\,\mathrm{m}$), which is approximately that of a LOS-only setup (see also the discussion after Theorem 2.1). To better understand this result and link it to our theoretical analysis in Sec. 2.4 we consider two regions near the line $p_{\mathrm{R,x}} = 0$ separately:

- $p_{\mathrm{T,x}} < p_{\mathrm{R,x}} < p_{\mathrm{s},1,\mathrm{x}}$: In this area the Rx lies between the Tx and the POI. Since $\theta_{\mathrm{R},1} \approx \theta_{\mathrm{T},1}$, from (2.87) we conclude that the path offers information in the direction which is orthogonal to the radial direction, hence it offers information only on the angular component of the position. Thus, it cannot counteract the loss of range information due to imperfect synchronization.
- $p_{\mathrm{R,x}} < p_{\mathrm{T,x}}$ or $p_{\mathrm{R,x}} > p_{\mathrm{s},1,\mathrm{x}}$: In this area the POI lies between the Tx and Rx, with $\theta_{\mathrm{R},1} \approx \theta_{\mathrm{T},1} \pm \pi$. In this case, the path offers information in the radial direction, with intensity $i_1 = i_{\tau_1}$. Nevertheless, from (2.89) and (2.90), with $\sin(\Delta\theta_1/2) \approx 1$ much of this information is lost due to imperfect synchronization. As $\sigma_{\mathrm{clk}} \to \infty$ all available range information is lost. Intuitively, this result makes sense, as the single-bounce NLOS path is almost indistinguishable from the LOS path, when the Rx lies in this area. It is, therefore, difficult for the Rx to extract any additional information from it that would help resolving the synchronization error.

To also examine the effect of the synchronization error on the orientation estimation accuracy, in Fig. 2.7 we plot the OEB for the same setup with $\sigma_{\mathrm{clk}} = 0.5T_{\mathrm{s}}$. It is evident that the OEB depends only on the Tx-Rx distance and not on the angular component of the Rx's position. The information from the LOS path is sufficient for the Rx to reliably estimate the orientation and it is not affected by the synchronization error. For example, the Rx can get an estimate $\hat{\alpha}_{\mathrm{R}}$ of the

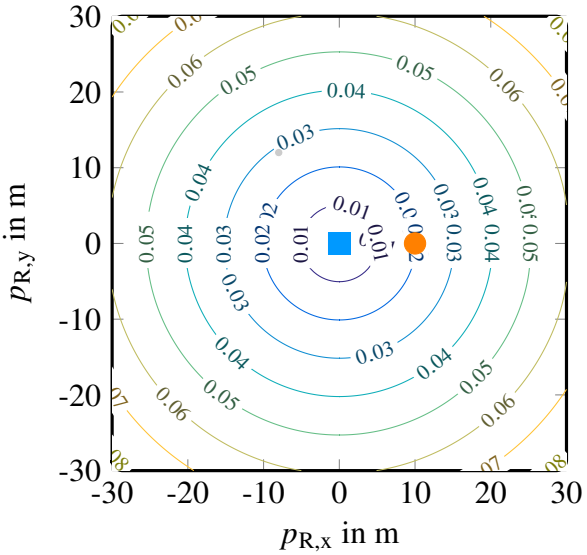

Fig. 2.7. OEB in ° for Rx localization with $\boldsymbol{p}_T = [0\,\text{m},\ 0\,\text{m}]^T, \boldsymbol{p}_{s,1} = [10\,\text{m},\ 0\,\text{m}]^T$ with $\sigma_{clk} = 0.5T_s$. The position of the Tx is shown with a square and the position of the POI with a circle.

orientation by $\hat{\alpha}_R = \tilde{\theta}_{T,0} + \alpha_T + \pi - \tilde{\theta}_{R,0}$. The additional information on the orientation offered by the NLOS path is insignificant compared to that of the LOS path. Hence, the contour plots for any level of synchronization are almost identical and therefore not shown here.

We then consider an additional POI at $\boldsymbol{p}_{s,2} = [-8\,\text{m},\ 12\,\text{m}]^T$ and in Fig. 2.8 we plot the asymptotic PEB for a receiver with imperfect synchronization with $\sigma_{clk} = 0.5T_s \approx 4\,\text{ns}$ (Fig. 2.8(b)) and $\sigma_{clk} = 2T_s \approx 16\,\text{ns}$ (Fig. 2.8(c)), and without synchronization (Fig. 2.8(d)). For perfect synchronization the result is identical to Fig. 2.6(a) We can see in Fig. 2.8(a) that the PEB is significantly improved compared to Fig. 2.8(b) due to the information offered by the additional POI, especially near the line $p_{R,x} = 0$, and it is much lower than that of the LOS-only setup almost for the entire considered region. Furthermore, the PEB reaches its maximum value in the areas behind the POIs. As explained in the discussion of Fig. 2.8(b), in the area behind a POI, this POI can hardly help resolving the synchronization error and the Rx relies mainly on the other POI, whose information intensity naturally decreases with increased propagation distance. This explains the curvature of the contour lines in these regions. Also, the PEB is much lower than that of the LOS-only setup ($\approx 4.88\,\text{m}$) for the entire considered region.

In Fig. 2.8(c) we see that an increase of σ_{clk} results in deterioration of the achievable positioning accuracy, mainly in the regions which are far from the POIs (close to the corners of the box). With increasing σ_{clk}, the system relies more on the weak NLOS components to obtain range information and, therefore, the PEB is increased. This effect is even more pronounced in the asynchronous case shown in Fig. 2.8(d). Nevertheless, we can conclude that, even in the asynchronous case, the exploitation of single-bounce NLOS allows us to obtain good positioning accuracy.

In order to further study the effect of synchronization on positioning accuracy, in Fig. 2.9 we plot the PEB as a function of σ_{clk}/T_s with the receiver's position fixed at $\boldsymbol{p}_R = [25\,\text{m},\ 10\,\text{m}]^T$. To also evaluate the performance of NLOS-only positioning, which requires at least 4 paths in the asynchronous case, we add extra reflectors at $\boldsymbol{p}_{s,3} = [12\,\text{m},\ 8\,\text{m}]^T$ and $\boldsymbol{p}_{s,4} = [7\,\text{m},\ -6\,\text{m}]^T$. The following 5 cases are considered: (i) *LOS-only*: only the LOS path is available; (ii) *3 NLOS-only*: only 3 NLOS paths (corresponding to $\boldsymbol{p}_{s,1}, \boldsymbol{p}_{s,2}$ and $\boldsymbol{p}_{s,3}$) are available; (iii) *LOS + 3 NLOS*: the LOS and the 3 NLOS paths are available; (iv) *4 NLOS-only*: only 4 NLOS paths are available; (v)

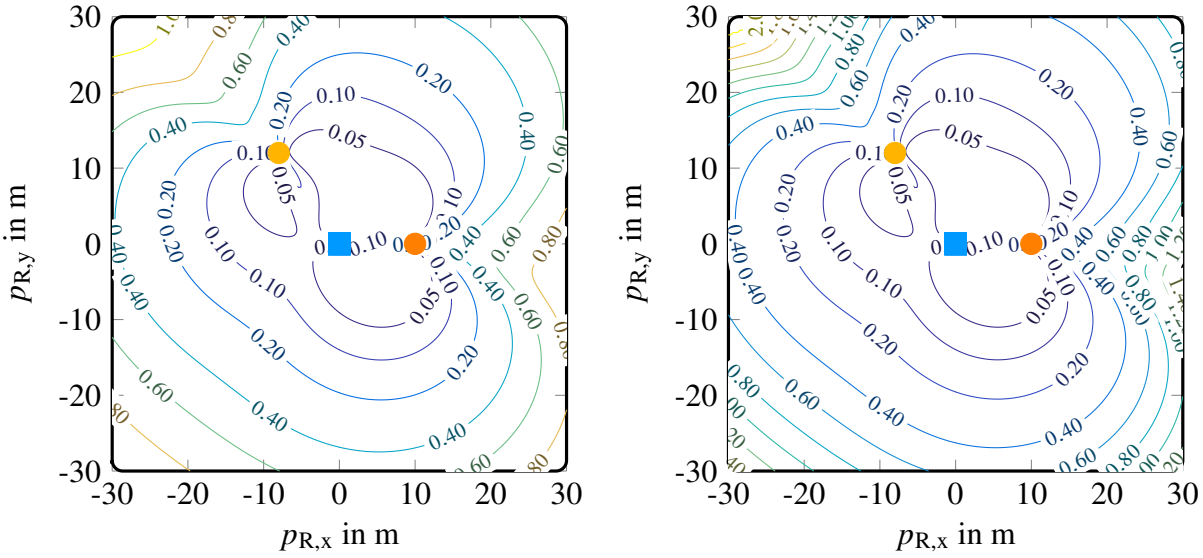

(a) Imperfect synchronization: $\sigma_{\mathrm{clk}} = 0.5T_{\mathrm{s}} \approx 4\,\mathrm{ns}$.

(b) Imperfect synchronization: $\sigma_{\mathrm{clk}} = 2T_{\mathrm{s}} \approx 16\,\mathrm{ns}$.

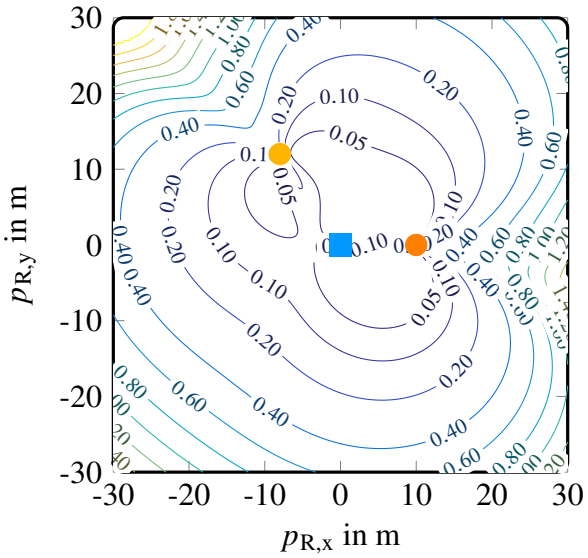

(c) No synchronization.

Fig. 2.8. PEB in m for Rx localization with $\boldsymbol{p}_{\mathrm{T}} = [0\,\mathrm{m},\ 0\,\mathrm{m}]^{\mathrm{T}}, \boldsymbol{p}_{\mathrm{s},1} = [10\,\mathrm{m},\ 0\,\mathrm{m}]^{\mathrm{T}}$ and $\boldsymbol{p}_{\mathrm{s},2} = [-8\,\mathrm{m},\ 12\,\mathrm{m}]^{\mathrm{T}}$ under different levels of synchronization error variance. The position of the Tx is shown with a square and the positions of the POIs with circles.

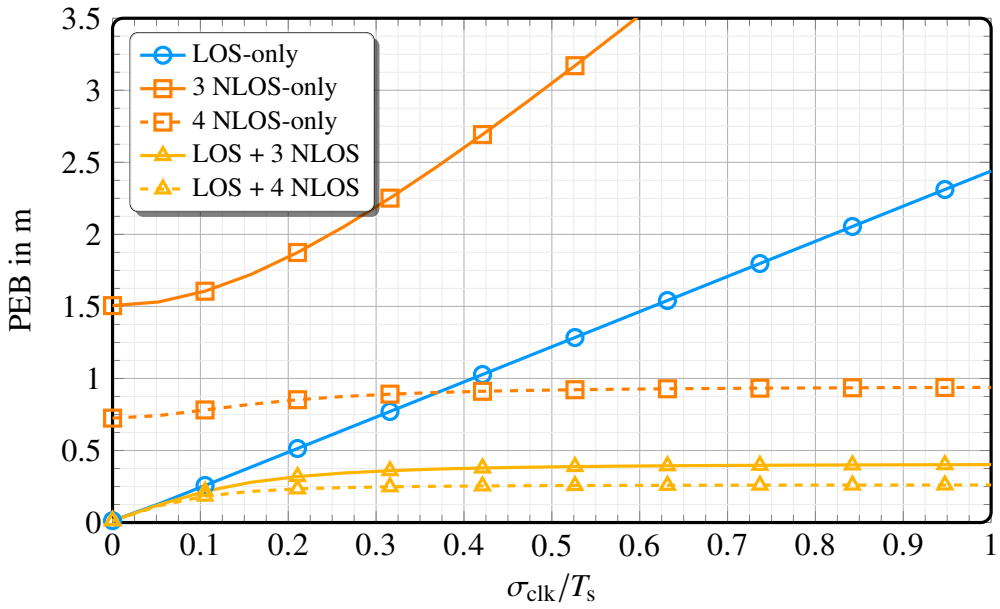

Fig. 2.9. PEB vs σ_{clk} for LOS and NLOS static Rx localization with $\boldsymbol{p}_{\mathrm{T}} = [0\,\mathrm{m},\ 0\,\mathrm{m}]$, $\boldsymbol{p}_{\mathrm{R}} = [25\,\mathrm{m},\ 10\,\mathrm{m}]^{\mathrm{T}}$, $\boldsymbol{p}_{\mathrm{s},1} = [10\,\mathrm{m},\ 0\,\mathrm{m}]^{\mathrm{T}}$, $\boldsymbol{p}_{\mathrm{s},2} = [-8\,\mathrm{m},\ 12\,\mathrm{m}]^{\mathrm{T}}$, $\boldsymbol{p}_{\mathrm{s},3} = [12\,\mathrm{m},\ 8\,\mathrm{m}]^{\mathrm{T}}$, $\boldsymbol{p}_{\mathrm{s},4} = [7\,\mathrm{m},\ -6\,\mathrm{m}]^{\mathrm{T}}$.

LOS + 4 NLOS: the LOS and the 4 NLOS paths are available. In the LOS-only case and in the NLOS-only case with 3 NLOS paths, the accuracy is significantly degraded with increasing σ_{clk}, as the performance of these cases is lower-bounded by the standard deviation of the ranging error caused by the synchronization error. On the other hand, with 4 NLOS paths, the PEB of NLOS-only positioning saturates with increasing σ_{clk}, as the synchronization error can be resolved using the paths. Similarly, when both LOS and NLOS paths are present, the PEB saturates, with the saturation value improving with increasing number of paths.

We note here that this result is relevant even for two-way localization schemes [60], which lift the requirement for tight Tx and Rx synchronization by employing transmission and reception of reference signals from both devices. In such schemes, each device has to measure and report to the position estimating entity the time difference between reception and transmission. These measurements include timing errors, which are induced by the time delay from the time when the signal is generated/digitized at baseband and the time when the RF signal is transmitted/received at the Tx/Rx antenna [5, Sec. 3.1]. The effect of these timing errors on the positioning accuracy is the same as that of the synchronization errors considered in this work and their values in cellular positioning accuracy studies are assumed to be in the order of a few nanoseconds [61], which, as shown by numerical results in Chapter 2, have a severe impact on accuracy. Therefore, such schemes would also benefit from exploiting NLOS paths and even optimize the reference signal to this end, as demonstrated in Chapter 4.

2.6.5 The Effect of Doppler Shifts

We consider the setup described in Section 2.6.1, with two POIs at $\boldsymbol{p}_{\mathrm{s},1} = [10\,\mathrm{m},\ 0\,\mathrm{m}]^{\mathrm{T}}$ and $\boldsymbol{p}_{\mathrm{s},2} = [-8\,\mathrm{m},\ 12\,\mathrm{m}]^{\mathrm{T}}$, and $\sigma_{\mathrm{clk}} = 2T_{\mathrm{s}}$. The receiver is now moving with velocity $\boldsymbol{v}_{\mathrm{R}} = \boldsymbol{u}(\pi/2)100\,\mathrm{km\,h^{-1}}$. The number of CP samples is set to $N_{CP} = 12$, so that the CP duration can accommodate the maximum delay spread for the given setup. Instead of $N_{\mathrm{B}} = 10$ OFDM symbols, we now transmit $N_{\mathrm{B}} = 200$ OFDM symbols to make the synthetic array aperture comparable to the

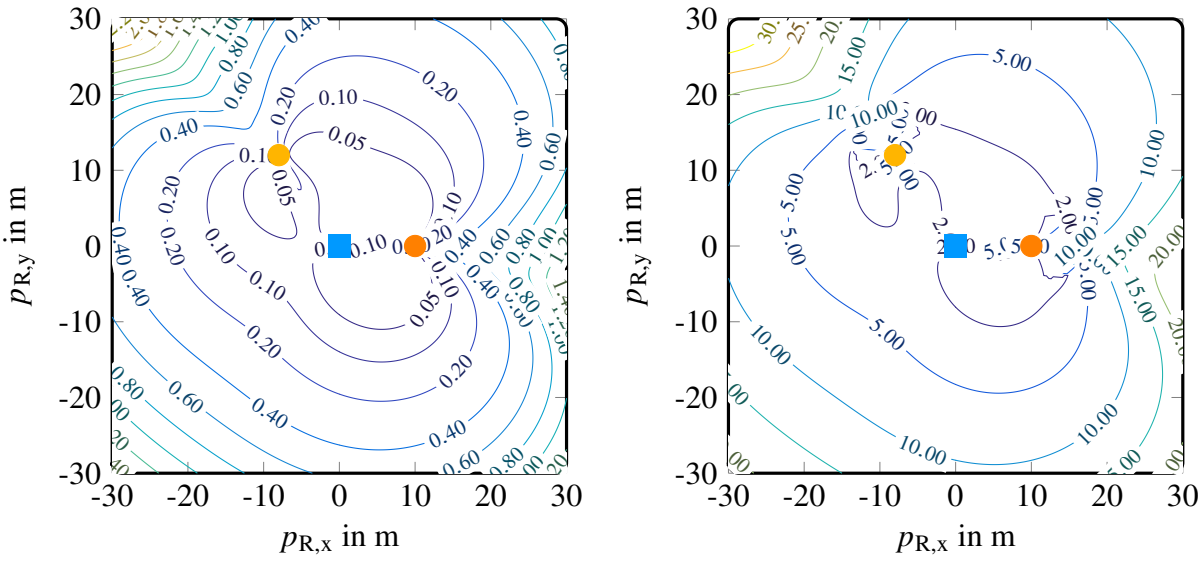

(a) PEB in m. (b) VEB in m/sec.

Fig. 2.10. Mobile Rx localization with $\boldsymbol{p}_{\mathrm{T}} = [0\,\mathrm{m},\ 0\,\mathrm{m}]^{\mathrm{T}}$, $\boldsymbol{p}_{\mathrm{s},1} = [10\,\mathrm{m},\ 0\,\mathrm{m}]^{\mathrm{T}}$ and $\boldsymbol{p}_{\mathrm{s},2} = [-8\,\mathrm{m},\ 12\,\mathrm{m}]^{\mathrm{T}}$, Rx velocity $\boldsymbol{v}_{\mathrm{R}} = \boldsymbol{u}(\pi/2)60\,\mathrm{km\,h^{-1}}$ and $\sigma_{\mathrm{clk}} = 2T_{\mathrm{s}} \approx 16\,\mathrm{ns}$. The position of the Tx is shown with a square and the positions of the POIs with circles.

physical aperture of the Rx antenna array, with the corresponding transmission duration being $T_{\mathrm{Tx}} = N_B(N + N_{CP})T_{\mathrm{s}} \approx 0.12\,\mathrm{ms}$ and an rms duration of $t_{\mathrm{rms}} = 0.036\,\mathrm{ms}$. The distance traveled by the Rx during transmission is $\|\boldsymbol{v}_{\mathrm{R}}\|_2 T_{\mathrm{T}} = 3.4\,\mathrm{mm}$, which is smaller than the wavelength $\lambda_{\mathrm{c}} = 7.9\,\mathrm{mm}$. The maximum synthetic array aperture is $\|\boldsymbol{v}_{\mathrm{R}}\|_2 t_{\mathrm{rms}} \approx 1\,\mathrm{mm}$, while the physical array aperture is $\sqrt{S_{\mathrm{R}}(\theta_{R,l})} = 7.1\,\mathrm{mm}^2$. To keep the total transmit energy the same as in the last section, we scale down the Tx energy such that $E_{\mathrm{T}} f_{\mathrm{s}} = 37\,\mathrm{dBm} - 10\log_{10}(200/10) \approx 24\,\mathrm{dBm}$, so as to observe the effect of the Rx's movement for the same Rx SNR.

In Fig. 2.10(a) we plot the PEB and in Fig. 2.10(b) the VEB for the considered rectangular area. It is evident from Fig. 2.10(a) that in the considered setup the additional information offered by the movement of the Rx through the Doppler shifts is insignificant compared to the information offered by other channel parameters. The same result is obtained when assuming known Rx velocity. We note here that a longer transmission duration would make the impact of the Doppler shifts stronger, but in such a case the Rx displacement during transmission might exceed the wavelength and the assumption that the channel parameters, more particularly the channel gains, remain constant becomes rather unrealistic. A possible remedy for this situation would be to assume that all other parameters remain constant during the transmission and the channel gains remain constant only for a given number of OFDM symbols. One could then consider a parameter vector including a series of gains for each path (instead of one channel gain for each path), but this is out of the scope of this work.

Although mobility does not have a significant impact on the achievable positioning accuracy, the estimation of the velocity itself is of interest. In addition, an accurate estimate of the velocity might be very useful in the prediction step of tracking methods. We can see in Fig. 2.10(b) that the presence of NLOS single-bounce paths makes the estimation of the instantaneous velocity possible, unlike the LOS-only case, where only the radial velocity can be estimated. Nevertheless,

[2]Not to be confused with the largest dimension of the Rx array (2.6), which in this case is $D_{\mathrm{max,R}} \approx 2\,\mathrm{cm}$.

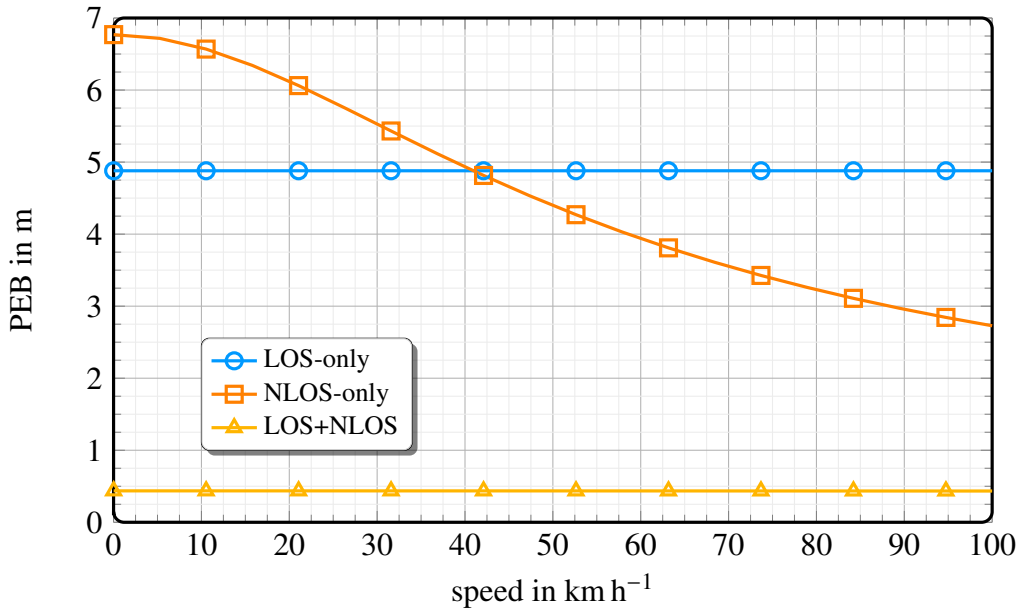

Fig. 2.11. PEB vs speed for LOS and NLOS receiver localization for imperfect synchronization ($\sigma_{\text{clk}} = 2T_{\text{s}}$) with $\boldsymbol{p}_{\text{T}} = [0\,\text{m},\ 0\,\text{m}]$, $\boldsymbol{p}_{\text{R}} = [18\,\text{m},\ 3\,\text{m}]^{\text{T}}$, $\boldsymbol{p}_{\text{s},1} = [10\,\text{m},\ 0\,\text{m}]^{\text{T}}$ and $\boldsymbol{p}_{\text{s},2} = [-8\,\text{m},\ 12\,\text{m}]^{\text{T}}$, $\boldsymbol{p}_{\text{s},3} = [12\,\text{m},\ 8\,\text{m}]^{\text{T}}$, velocity direction $\boldsymbol{v}_{\text{R}}/\|\boldsymbol{v}_{\text{R}}\|_2 = \boldsymbol{u}(\pi/2)$.

we can observe that the attained is VEB quite high for a large fraction of the considered area and it is lower than $5\,\text{km}\,\text{h}^{-1}$ only for an area close to the Tx and POIs.

To gain further insight on the effect of velocity, in Fig. 2.11 we plot the PEB as a function of the speed, i.e., $\|\boldsymbol{v}_{\text{R}}\|_2$, for a system with imperfect ($\sigma_{\text{clk}} = 2T_{\text{s}}$) synchronization, considering the cases where the velocity is known or unknown. Again, we fix the receiver's position at $\boldsymbol{p}_{\text{R}} = [25\,\text{m},\ 10\,\text{m}]^{\text{T}}$ and add an extra reflector at $\boldsymbol{p}_{\text{s},3} = [12\,\text{m},\ 8\,\text{m}]^{\text{T}}$. We consider three different cases: (i) *LOS-only*: only the LOS path is available; (ii) *NLOS-only*: only the 3 NLOS paths are available; (iii) *LOS+NLOS*: the LOS and the 3 NLOS paths are available. A few interesting observations can be made from Fig. 2.11. The accuracy of the LOS-only case is lower bounded by the standard deviation $c\sigma_{\text{clk}} \approx 2.44\,\text{m}$ of the ranging error induced by the synchronization error. From the LOS+NLOS curves, we first observe that the information from the NLOS paths is very important as it allows the receiver to resolve the synchronization error, as discussed before. Similarly to Fig. 2.10, we can see that the movement of the receiver has a small impact on the PEB, when the LOS path is present. On the contrary, in the NLOS-only case, mobility has a strong impact, with the PEB decreasing significantly with increasing speed. This can be understood by comparing (2.85)-(2.87) with (2.105)-(2.108): the additional sources of position and orientation information (2nd and 3rd matrices in (2.105)), whose intensities are proportional to ρ_l^2, allow the receiver to better resolve the synchronization error, while in the static scenario its accuracy is lower bounded by $c\sigma_{\text{clk}}$.

2.6.6 The Effect of Prior Information on Single-Bounce NLOS Paths

In this section, we study the effect of prior information on single-bounce NLOS paths, more particularly on the location of their corresponding VAs. To this end, we consider the setup depicted in Fig.2.12, where the Tx lies at the origin and the Rx at $\boldsymbol{p}_{\text{R}} = [12.5, 5]^{\text{T}}\text{m}$. The VAs resulting from single-bounce reflections at the room's walls are located at $\boldsymbol{p}_{\text{VA},1} = [0, 25]^{\text{T}}\text{m}$, $\boldsymbol{p}_{\text{VA},2} = [0, -25]^{\text{T}}\text{m}$

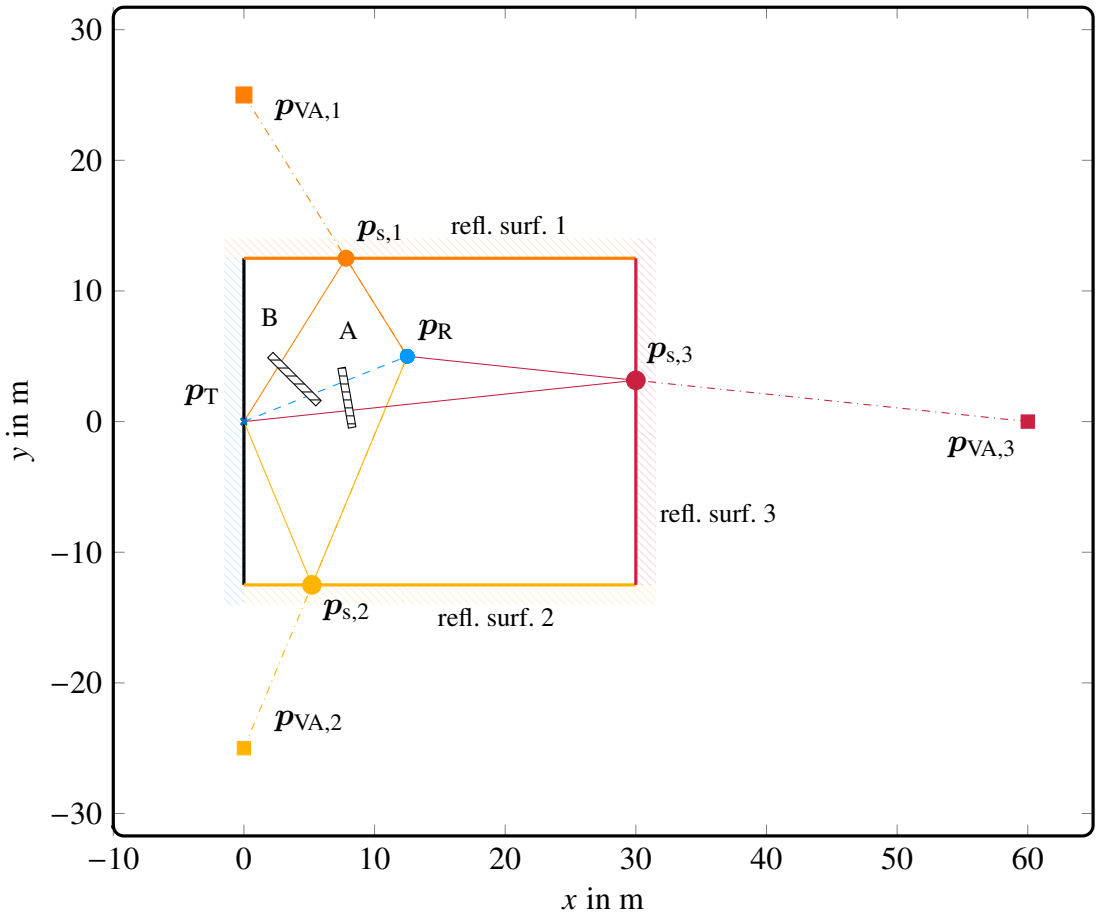

Fig. 2.12. Geometric setup for the evaluation of the effect of prior information on the location of VAs.

and $\boldsymbol{p}_{\mathrm{VA},3} = [60, 0]^{\mathrm{T}}$m. In order to concentrate on the potential implications of the results presented in Sec. 2.5, we assume that the Rx orientation α_{R} is known and the Tx and Rx are perfectly synchronized. We consider two NLOS-only cases:

- *case A*: the paths corresponding to the 1st and 2nd VAs are received;
- *case B*: the paths corresponding to the 2nd and 3rd VAs are received.

The amplitude of the complex path gain of the l-th path is $|h_l| = \sqrt{\gamma_l}\lambda/(4\pi d_l)$, where $\gamma_l = 0.1\ \forall l$, is the reflection coefficient, and the phase is uniformly distributed.

From the analysis in Sec. 2.5 we have a clear picture about the position information offered by single-bounce NLOS paths under perfect or no prior knowledge of their corresponding VAs locations. To gain more insight about the intermediate cases, setting $s_2 = 0$ and $\sigma_{2,\parallel} = \sigma_{2,\perp} = \sigma_{\mathrm{ref}}/\sqrt{2}$, we plot the eigenvalues and the directions of the eigenvectors for varying σ_{ref} in Fig. 2.13. We see that, as expected, when knowledge about the VA's position is accurate ($\sigma_{\mathrm{ref}} \to 0$), for known orientation and perfect synchronization (in this case $\boldsymbol{z}_{\theta_{\mathrm{T},l}} = \boldsymbol{z}_{\theta_{\mathrm{R},l}} = \boldsymbol{u}_{\perp}^{\mathrm{T}}(\theta_{\mathrm{R},l})$), $\boldsymbol{J}_2$ has two strong eigenvalues, with the eigenvectors pointing in the radial and the tangential direction. As σ_{ref} increases, the strongest eigenvalue decreases, starting from J_{τ_2}/c^2 and converges to j_2, while the second eigenvalue vanishes, resulting in a rank-1 $\boldsymbol{J}_2$. The direction of the eigenvector corresponding to the strongest eigenvalue gradually changes from $\theta_{\mathrm{R},2} + \pi$ (radial direction), to $\theta_{\mathrm{ref},2} + \pi/2$, that is parallel to the reflecting surface.

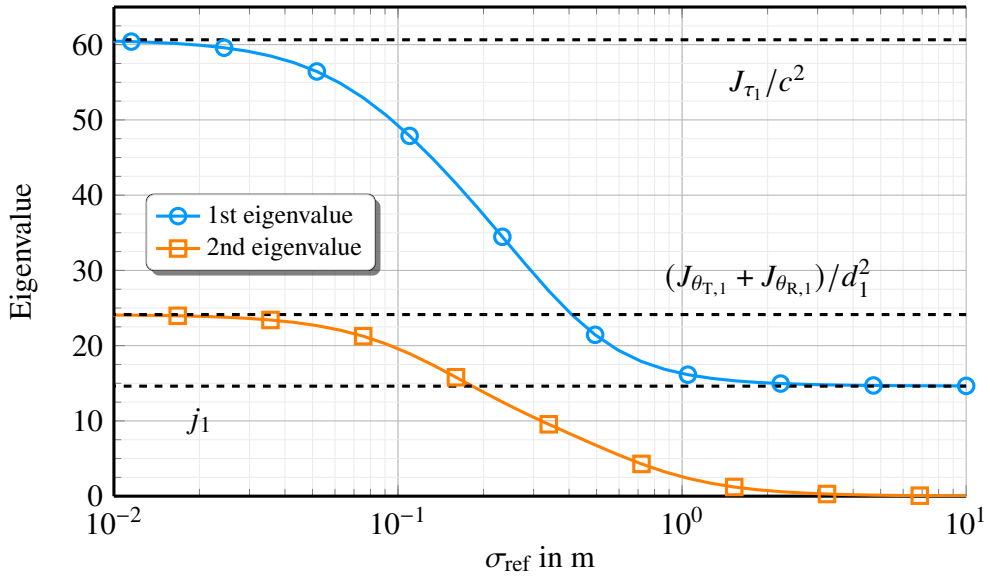

(a) Eigenvalues of $\boldsymbol{J}_2$.

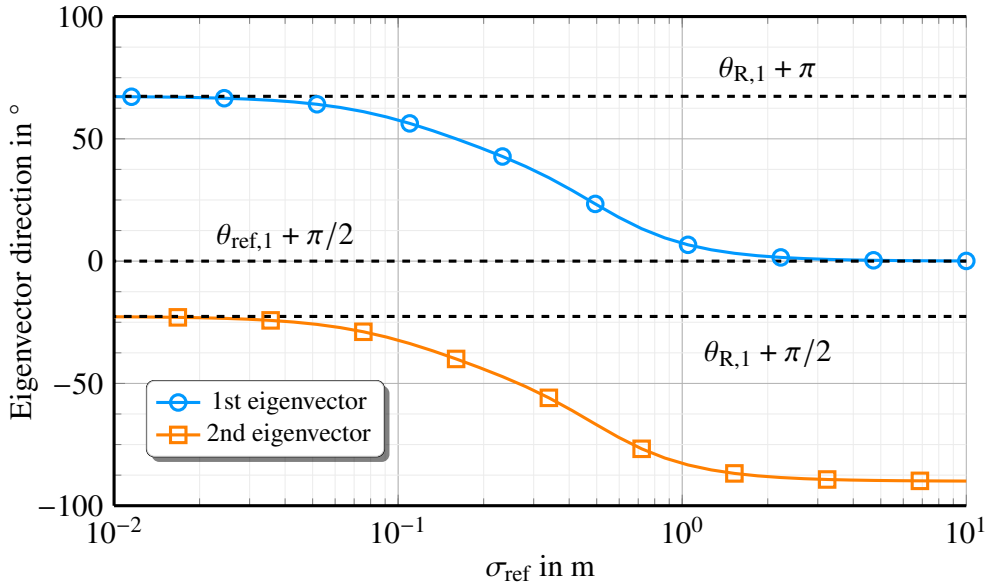

(b) Direction of eigenvectors of $\boldsymbol{J}_2$.

Fig. 2.13. Eigenvalues and directions of eigenvectors of the EFIM $\boldsymbol{J}_2$ of VA 2 as function of the prior VA position error σ_{ref}.

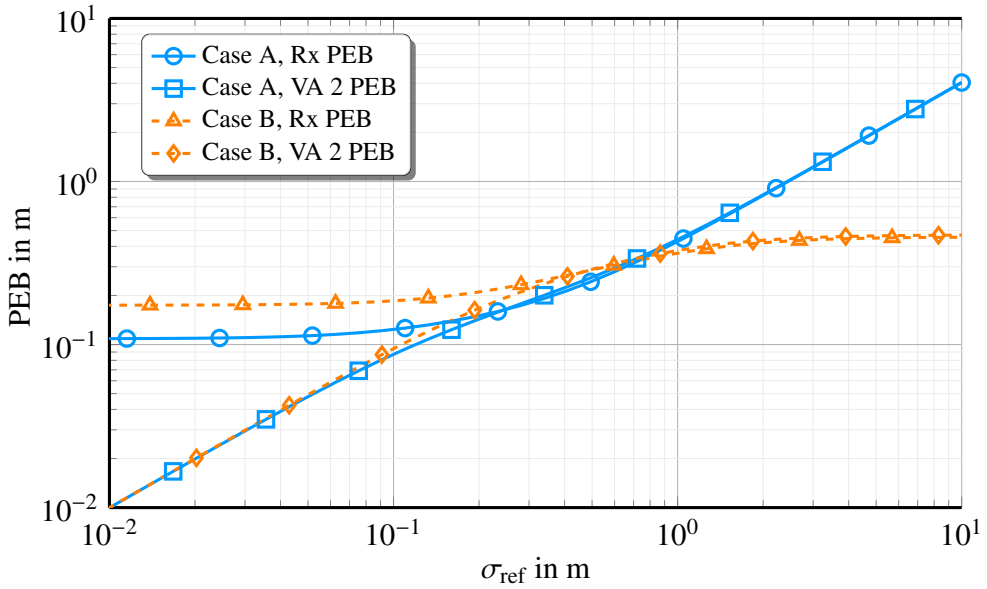

Fig. 2.14. Rx and VA 2 PEB as function of the prior VA position error σ_{ref}.

In Fig. 2.14 we plot the PEB of the Rx and VA 2 for the two considered cases as functions of σ_{ref}. We set again $s_l = 0$ and $\sigma_{l,\parallel} = \sigma_{l,\perp} = \sigma_{\text{ref}}/\sqrt{2}$, $l = 1, 2, 3$. We see that for $\sigma_{\text{ref}} \to 0$ the PEB of VA 2 converges to 0, while the Rx PEB converges to its lowest value as the two paths behave as LOS paths, providing position information in independent directions. In case A, as σ_{ref} increases, the two paths provide position information in almost the same direction, as they arise from parallel reflecting surfaces, with the available information in the orthogonal direction decreasing with increasing σ_{ref}. As a result, for high values of σ_{ref} (i.e., less accurate prior) the PEB of the Rx and VA 2 grows linearly with σ_{ref}. For moderate values of σ_{ref} (< 1 m), good positioning accuracy is achievable, as the directions of the strongest eigenvectors of $\boldsymbol{J}_1$ and $\boldsymbol{J}_2$ are sufficiently distinct. On the contrary, in case B, the PEB of the Rx and VA 2 saturates for high values of σ_{ref}, as the two paths provide position information in different directions, resulting from the two perpendicular walls. Therefore, combining the two NLOS paths, the Rx and VA positions can be resolved.

3. Parameter Estimation for Single-Anchor Positioning

In this chapter we present a novel algorithm for Rx position, orientation and clock offset estimation. We consider a static setup and a narrowband signal model, with $\boldsymbol{W}_{\mathrm{T}} = \boldsymbol{I}_{N_{\mathrm{T}}}$ and $\boldsymbol{W}_{\mathrm{R}} = \boldsymbol{I}_{N_{\mathrm{R}}}$, i.e., no analog precoding or Rx combining applied. In the first step of the algorithm an off-grid parameter estimation algorithm based on [48] is employed to recover the number paths and their respective TOAs, AODs and AOAs. In the second step, the recovered channel parameters are mapped to the position parameter vector $\boldsymbol{\nu}$.

3.1 Off-grid Compressed Sensing-based Channel Parameters Estimation

We first rewrite the signal model (2.22) by stacking the observations over subcarriers $\mathcal{P} = \{p_1, \ldots, p_{N_{\mathrm{P}}}\} = \{-N_{\mathrm{P}}/2, \ldots, -1, 1, \ldots, N_{\mathrm{P}}/2\}$

$$\begin{aligned}\boldsymbol{Y}_b &= \sum_{l=0}^{L-1} h_l \boldsymbol{a}_{\mathrm{R}}(\tilde{\theta}_{\mathrm{R},l}) \boldsymbol{a}_{\mathrm{T}}^{\mathrm{T}}(\tilde{\theta}_{\mathrm{T},l}) \boldsymbol{X}_b \operatorname{diag}(\boldsymbol{a}_\tau(\tau'_l)) + \boldsymbol{N}_b \\ &= \sum_{l=0}^{L-1} h_l \boldsymbol{C}_b(\tau'_l, \tilde{\theta}_{\mathrm{T},l}, \tilde{\theta}_{\mathrm{R},l}) + \boldsymbol{N}_b, \end{aligned} \tag{3.1}$$

where

$$\boldsymbol{C}_b(\tau', \tilde{\theta}_{\mathrm{T}}, \tilde{\theta}_{\mathrm{R}}) = \boldsymbol{a}_{\mathrm{R}}(\tilde{\theta}_{\mathrm{R}}) \boldsymbol{a}_{\mathrm{T}}^{\mathrm{T}}(\tilde{\theta}_{\mathrm{T}}) \boldsymbol{X}_b \operatorname{diag}(\boldsymbol{a}_\tau(\tau')) \in \mathbb{C}^{N_{\mathrm{R}} \times N_{\mathrm{P}}}, \tag{3.2}$$

$$\boldsymbol{a}_\tau(\tau') = [\mathrm{e}^{-\mathrm{j}\omega_{p_1}\tau'}, \ldots, \mathrm{e}^{-\mathrm{j}\omega_{p_{N_{\mathrm{P}}}}\tau'}]^{\mathrm{T}} \in \mathbb{C}^{N_{\mathrm{P}}}, \tag{3.3}$$

$$\boldsymbol{Y}_b = [\boldsymbol{y}[p_1, b], \ldots, \boldsymbol{y}[p_{N_{\mathrm{P}}}, b]] \in \mathbb{C}^{N_{\mathrm{R}} \times N_{\mathrm{P}}}, \tag{3.4}$$

$$\boldsymbol{X}_b = [\boldsymbol{x}[p_1, b], \ldots, \boldsymbol{x}[p_{N_{\mathrm{P}}}, b]] \in \mathbb{C}^{N_{\mathrm{T}} \times N_{\mathrm{P}}}, \tag{3.5}$$

$$\boldsymbol{N}_b = [\boldsymbol{\eta}[p_1, b], \ldots, \boldsymbol{\eta}[p_{N_{\mathrm{P}}}, b]] \in \mathbb{C}^{N_{\mathrm{R}} \times N_{\mathrm{P}}}. \tag{3.6}$$

By stacking the observations over N_{B} OFDM symbols, we get

$$\boldsymbol{Y} = \sum_{l=0}^{L-1} h_l \boldsymbol{C}(\tau'_l, \tilde{\theta}_{\mathrm{T},l}, \tilde{\theta}_{\mathrm{R},l}) + \boldsymbol{N} \tag{3.7}$$

where

$$\boldsymbol{Y} = [\boldsymbol{Y}_0^{\mathrm{T}}, \ldots, \boldsymbol{Y}_{N_{\mathrm{B}}-1}^{\mathrm{T}}]^{\mathrm{T}} \in \mathbb{C}^{N_{\mathrm{R}} N_{\mathrm{B}} \times N_{\mathrm{P}}}, \tag{3.8}$$

$$\boldsymbol{C}(\tau', \tilde{\theta}_{\mathrm{T}}, \tilde{\theta}_{\mathrm{R}}) = [\boldsymbol{C}_0^{\mathrm{T}}(\tau', \tilde{\theta}_{\mathrm{T}}, \tilde{\theta}_{\mathrm{R}}), \ldots, \boldsymbol{C}_{N_{\mathrm{B}}-1}^{\mathrm{T}}(\tau', \tilde{\theta}_{\mathrm{T}}, \tilde{\theta}_{\mathrm{R}})]^{\mathrm{T}} \in \mathbb{C}^{N_{\mathrm{R}} N_{\mathrm{B}} \times N_{\mathrm{P}}}, \tag{3.9}$$

$$\boldsymbol{N} = [\boldsymbol{N}_0^{\mathrm{T}}, \ldots, \boldsymbol{N}_{N_{\mathrm{B}}-1}^{\mathrm{T}}]^{\mathrm{T}} \in \mathbb{C}^{N_{\mathrm{R}} N_{\mathrm{B}} \times N_{\mathrm{P}}}. \tag{3.10}$$

For our positioning purposes, we would like to recover the number of paths, along with their respective gains, TOAs, AODs and AOAs. Hence, we aim to solve the following optimization problem

$$\min_{L',\{\tau'_l,\tilde{\theta}_{\mathrm{T},l},\tilde{\theta}_{\mathrm{R},l},h_l\}_{l=0}^{L'-1}} \Lambda(\boldsymbol{R}(\{\tau'_l,\tilde{\theta}_{\mathrm{T},l},\tilde{\theta}_{\mathrm{R},l},h_l\}_{l=0}^{L'-1})), \tag{3.11}$$

where

$$\Lambda(\boldsymbol{R}) = \frac{1}{2}\|\boldsymbol{R}\|_F^2 \tag{3.12}$$

is the loss function and

$$\boldsymbol{R}(\{\tau'_l,\tilde{\theta}_{\mathrm{T},l},\tilde{\theta}_{\mathrm{R},l},h_l\}_{l=0}^{L'-1}) = \boldsymbol{Y} - \sum_{l=0}^{L'-1} h_l \boldsymbol{C}(\tau'_l,\tilde{\theta}_{\mathrm{T},l},\tilde{\theta}_{\mathrm{R},l}) \tag{3.13}$$

is the residual. The problem (3.11) is non-convex in all optimization variables. Furthermore, with noisy observations $\boldsymbol{Y}$, in order to minimize the objective, the number of detected paths L' can grow arbitrarily large. Therefore, a constraint or a penalty term to limit L' is required to make the representation more parsimonious. As usual in sparse recovery setups, instead of using the L0 norm $\|\boldsymbol{h}\|_0$ of $\boldsymbol{h} = [h_0,\ldots,h_{L-1}]^{\mathrm{T}}$, which is non-convex, we use the convex L1 norm $\|\boldsymbol{h}\|_1$. Hence, we set up the following optimization problem:

$$\min_{L',\{\tau'_l,\tilde{\theta}_{\mathrm{T},l},\tilde{\theta}_{\mathrm{R},l},h_l\}_{l=0}^{L'-1}} \Lambda(\boldsymbol{R}(\{\tau'_l,\tilde{\theta}_{\mathrm{T},l},\tilde{\theta}_{\mathrm{R},l},h_l\}_{l=0}^{L'-1})) + \chi\|\boldsymbol{h}\|_1, \tag{3.14}$$

where χ is the regularization parameter. Larger values of χ promote sparser solutions, i.e., smaller values of L' at the expense of less accurate explanation of the measurements.

We solve problem (3.14) using the algorithmic framework of [48], termed as Alternating Descent Conditional Gradient Method (ADCGM), which is described in Alg. 1. Alg. 1 takes the following inputs:

- The reference signal $\boldsymbol{X} = [\boldsymbol{X}_1^{\mathrm{T}},\ldots,\boldsymbol{X}_{N_{\mathrm{B}}}^{\mathrm{T}}]^{\mathrm{T}}$.
- The observations $\boldsymbol{Y}$.
- The noise variance $\sigma^2_{\eta,\mathrm{R}}$.
- The maximum number of detected paths $L_{\max}$, which limits the amount of algorithmic iterations that can be performed.
- The probability of false alarm P_{fa}, which describes the probability that noise is falsely detected as a path of the channel. Given P_{fa}, along with $\boldsymbol{X}$ and $\sigma^2_{\eta,\mathrm{R}}$, we can compute the appropriate value of the threshold ζ_1 that results in the desired P_{fa}. The choice of probability of false alarm controls a trade-off between false alarms and missed detections. For our numerical results, we avoid an analytic computation of ζ_1, as it is rather complicated for an arbitrary reference signal $\boldsymbol{X}$, and compute it numerically.
- The parameter ζ_2 which is used in the path pruning step, to discard paths whose gain is effectively zero. We provide more details in Sec. 3.1.4.2.
- The number of inner coordinate descent iterations N_{cd}.

The output of the algorithm is the rank of the channel L' and the path parameters $\{\tau'_l,\tilde{\theta}_{\mathrm{T},l},\tilde{\theta}_{\mathrm{R},l},h_l\}_{l=0}^{L'-1}$. The number of detected paths at the start of the i-th iteration is denoted as $L^{(i)}$. The TOAs of the detected paths at the start of the i-th iteration are stacked in the sequence $\boldsymbol{\tau}'^{(i)} = (\tau_0'^{(i)},\ldots,\tau'^{(i)}_{L^{(i)}-1})^{\mathrm{T}} \in \mathbb{R}^{L^{(i)}}$ and $\tilde{\boldsymbol{\theta}}_{\mathrm{T}}^{(i)}, \tilde{\boldsymbol{\theta}}_{\mathrm{R}}^{(i)}$ and $\boldsymbol{h}^{(i)}$ are defined accordingly. In the following, we describe the steps of the algorithm in detail.

Algorithm 1 Channel parameter estimation with ADCGM

Input: $\{\boldsymbol{X}_b\}_{b=1}^{N_\mathrm{B}},\ \boldsymbol{Y},\ \sigma_{\eta,\mathrm{R}}^2,\ L_{\max},\ N_{\mathrm{cd}},\ P_{\mathrm{fa}},\ \zeta_2$

Initialize: $\boldsymbol{\tau}'^{(0)}, \tilde{\boldsymbol{\theta}}_{\mathrm{T}}^{(0)}, \tilde{\boldsymbol{\theta}}_{\mathrm{R}}^{(0)}, \boldsymbol{h}^{(0)} = (\ ), i = 0$

do

1. Compute residual $\boldsymbol{R}_i$

2. Detect next potential path according to (3.18) or (3.21) and (3.22) to get $\tau'^{(i)}$, $\tilde{\theta}_{\mathrm{T}}^{(i)}$ and $\tilde{\theta}_{\mathrm{R}}^{(i)}$

if $\left|\mathrm{tr}(\boldsymbol{R}_i^{\mathrm{H}}\boldsymbol{C}(\tau^{(i)}, \tilde{\theta}_{\mathrm{T}}^{(i)}, \tilde{\theta}_{\mathrm{R}}^{(i)})\right| < \zeta_1(\boldsymbol{X}, \sigma_{\eta,\mathrm{R}}^2, P_{\mathrm{fa}})$ **then**

stop program

end if

3. Update support, adding the new potential path to the existing ones according to (3.23)-(3.25) to obtain $\boldsymbol{\tau}'^{(i+1)}, \tilde{\boldsymbol{\theta}}_{\mathrm{T}}^{(i+1)}, \tilde{\boldsymbol{\theta}}_{\mathrm{R}}^{(i+1)}$

4. Coordinate descent on non-convex objective:

for $j = 1$ to N_{cd} **do**

(a) Compute gains:

$$\boldsymbol{h}^{(i+1)} = \mathrm{argmin}_{\boldsymbol{h}}\, \Lambda(\boldsymbol{R}(\{\tau_l'^{(i+1)}, \tilde{\theta}_{\mathrm{T},l}^{(i+1)}, \tilde{\theta}_{\mathrm{R},l}^{(i+1)}, h_l\}_{l=0}^{L^{(i)}})) + \chi\|\boldsymbol{h}\|_1$$

(b) Prune support:

$$\boldsymbol{\tau}'^{(i+1)}, \tilde{\boldsymbol{\theta}}_{\mathrm{T}}^{(i+1)}, \tilde{\boldsymbol{\theta}}_{\mathrm{R}}^{(i+1)}, \boldsymbol{h}^{(i+1)} \leftarrow \mathrm{prune}(\boldsymbol{\tau}'^{(i+1)}, \tilde{\boldsymbol{\theta}}_{\mathrm{T}}^{(i+1)}, \tilde{\boldsymbol{\theta}}_{\mathrm{R}}^{(i+1)}, \boldsymbol{h}^{(i+1)}; \zeta_2)$$

(c) Locally improve support:

$$\boldsymbol{\tau}'^{(i+1)}, \tilde{\boldsymbol{\theta}}_{\mathrm{T}}^{(i+1)}, \tilde{\boldsymbol{\theta}}_{\mathrm{R}}^{(i+1)}, \boldsymbol{h}^{(i+1)} \leftarrow \mathrm{local\_descent}(\boldsymbol{\tau}'^{(i+1)}, \tilde{\boldsymbol{\theta}}_{\mathrm{T}}^{(i+1)}, \tilde{\boldsymbol{\theta}}_{\mathrm{R}}^{(i+1)}, \boldsymbol{h}^{(i+1)})$$

end for

$i = i + 1$

while $i < L_{\max}$

3.1.1 Step 1: Residual Computation

In the first step of the algorithm, the current residual $\boldsymbol{R}_i$ is computed according to (3.13) employing $\boldsymbol{\tau}'^{(i)}$, $\tilde{\boldsymbol{\theta}}_{\mathrm{T}}^{(i)}$, $\tilde{\boldsymbol{\theta}}_{\mathrm{R}}^{(i)}$ and $\boldsymbol{h}^{(i)}$, with

$$\boldsymbol{R}_i = [\boldsymbol{R}_{i,0}^{\mathrm{T}}, \ldots, \boldsymbol{R}_{i,N_{\mathrm{B}}-1}^{\mathrm{T}}]^{\mathrm{T}}, \tag{3.15}$$

$$\boldsymbol{R}_{i,b} = [\boldsymbol{r}_i[p_1, b], \ldots, \boldsymbol{r}_i[p_{N_{\mathrm{P}}}, b]] = \boldsymbol{Y}_b - \sum_{l=0}^{L^{(i)}-1} h_l \boldsymbol{C}_b(\tau_l'^{(i)}, \tilde{\theta}_{\mathrm{T},l}^{(i)}, \tilde{\theta}_{\mathrm{R},l}^{(i)}) \in \mathbb{C}^{N_{\mathrm{R}} \times N_{\mathrm{P}}}. \tag{3.16}$$

3.1.2 Step 2: Detection of a New Potential Path

In order to get the next potential path, we have to solve the following optimization problem

$$\tau'^{(i)}, \tilde{\theta}_{\mathrm{T}}^{(i)}, \tilde{\theta}_{\mathrm{R}}^{(i)} = \underset{(\tau', \tilde{\theta}_{\mathrm{T}}, \tilde{\theta}_{\mathrm{R}}) \in \Omega}{\operatorname{argmax}} \left| \operatorname{tr}(\boldsymbol{R}_i^{\mathrm{H}} \boldsymbol{C}(\tau', \tilde{\theta}_{\mathrm{T}}, \tilde{\theta}_{\mathrm{R}})) \right|, \tag{3.17}$$

where $\Omega = [0, T_{\mathrm{CP}}] \times [-\pi, \pi) \times [-\pi, \pi)$ is the 3D parameter space.

A detailed mathematical justification of this step can be found in [48] and in Appendix A8, but we briefly provide an explanation here: Conditional gradient descent methods are based on successive linearizations of the convex objective and minimization of the linearized objective over the feasible set. Problem (3.14) can be expressed as a convex optimization problem with respect to the sparse atomic measure $\mu = \sum_{l=0}^{L-1} h_l \delta_{\tau', \tilde{\theta}_{\mathrm{T}}, \tilde{\theta}_{\mathrm{R}}}$. The solution of (3.17) corresponds to the minimization of the linearized objective. Intuitively, for our specific choice of the loss function, in this step we identify the potential path whose contribution to the observations $\boldsymbol{C}(\tau', \tilde{\theta}_{\mathrm{T}}, \tilde{\theta}_{\mathrm{R}})$ has the maximum correlation with the current residual $\boldsymbol{R}_i$.

The problem at hand (3.17) is non-convex with respect to (w.r.t.) all optimization variables. It can be solved approximately by discretizing the 3D parameter space Ω to get an $N_\tau \times N_{\theta_{\mathrm{T}}} \times N_{\theta_{\mathrm{R}}}$-dimensional grid $\Omega_{\mathcal{G}} = \mathcal{G}_\tau \times \mathcal{G}_{\theta_{\mathrm{T}}} \times \mathcal{G}_{\theta_{\mathrm{R}}}$, where $\mathcal{G}_\tau$, $\mathcal{G}_{\theta_{\mathrm{T}}}$ and $\mathcal{G}_{\theta_{\mathrm{R}}}$ are the TOA, AOD and AOA grids and N_τ, $N_{\theta_{\mathrm{T}}}$ and $N_{\theta_{\mathrm{R}}}$ are their corresponding sizes. We maximize the objective over $\Omega_{\mathcal{G}}$ as

$$\tau'^{(i)}, \tilde{\theta}_{\mathrm{T}}^{(i)}, \tilde{\theta}_{\mathrm{R}}^{(i)} = \underset{(\tau', \tilde{\theta}_{\mathrm{T}}, \tilde{\theta}_{\mathrm{R}}) \in \Omega_{\mathcal{G}}}{\operatorname{argmax}} \left| \operatorname{tr}(\boldsymbol{R}_i^{\mathrm{H}} \boldsymbol{C}(\tau', \tilde{\theta}_{\mathrm{T}}, \tilde{\theta}_{\mathrm{R}})) \right|, \tag{3.18}$$

At this point, it is instructive to consider the computational complexity that such a solution entails.

3.1.2.1 Computational Complexity of New Potential Path Detection

As a measure of computational complexity, we consider the number of complex multiplications, which is sufficient for an approximate evaluation. Although we do not consider optimal algorithms for matrix multiplications, we do avoid obvious repetitions of computations where appropriate. The first step is to rewrite the objective of (3.17) as

$$\begin{aligned}
g_s(\tau', \tilde{\theta}_{\mathrm{T}}, \tilde{\theta}_{\mathrm{R}}) &= \left| \operatorname{tr}(\boldsymbol{R}_i^{\mathrm{H}} \boldsymbol{C}(\tau', \tilde{\theta}_{\mathrm{T}}, \tilde{\theta}_{\mathrm{R}})) \right| \\
&\overset{(a)}{=} \left| \operatorname{tr}\Big(\sum_{b=0}^{N_{\mathrm{B}}-1} \boldsymbol{R}_{i,b}^{\mathrm{H}} \boldsymbol{C}_b(\tau', \tilde{\theta}_{\mathrm{T}}, \tilde{\theta}_{\mathrm{R}}) \Big) \right| \\
&\overset{(b)}{=} \left| \operatorname{tr}\Big(\sum_{b=0}^{N_{\mathrm{B}}-1} \boldsymbol{R}_i^{\mathrm{H}} \boldsymbol{a}_{\mathrm{R}}(\tilde{\theta}_{\mathrm{R},l}) \boldsymbol{a}_{\mathrm{T}}^{\mathrm{T}}(\tilde{\theta}_{\mathrm{T},l}) \boldsymbol{X}_b \operatorname{diag}(\boldsymbol{a}_\tau(\tau_l')) \Big) \right| \\
&\overset{(c)}{=} \left| \boldsymbol{a}_{\mathrm{T}}^{\mathrm{T}}(\tilde{\theta}_{\mathrm{T}}) \Big(\sum_{b=0}^{N_{\mathrm{B}}-1} \boldsymbol{X}_b \operatorname{diag}(\boldsymbol{a}_\tau(\tau')) \boldsymbol{R}_{i,b}^{\mathrm{H}} \Big) \boldsymbol{a}_{\mathrm{R}}(\tilde{\theta}_{\mathrm{R}}) \right|,
\end{aligned} \tag{3.19}$$

where (a) follows from (3.9) and (3.15), (b) follows from (3.2) and (c) follows from the property of the trace operator $\mathrm{tr}(\boldsymbol{AB}) = \mathrm{tr}(\boldsymbol{BA})$.

For a given value τ' on the defined grid, we count the complex multiplications required for the computation of the matrix in the parentheses. The product of $\boldsymbol{X}_b$ and $\mathrm{diag}(\boldsymbol{a}_\tau(\tau'))$ requires $N_\mathrm{T}N_\mathrm{P}$. For the product of the resulting matrix with $\boldsymbol{R}_{i,b}$, $N_\mathrm{T}N_\mathrm{R}N_\mathrm{P}$ multiplications are required. Hence, for the computation of the matrix in the parentheses, $N_\mathrm{B}N_\mathrm{T}N_\mathrm{P}(N_\mathrm{R}+1)$ multiplications are required. For our purposes, considering only the dominant term $N_\mathrm{B}N_\mathrm{T}N_\mathrm{P}N_\mathrm{R}$ is sufficient. Then, the product of the resulting $N_\mathrm{T} \times N_\mathrm{R}$ matrix with $\boldsymbol{a}_\mathrm{T}^\mathrm{T}(\tilde{\theta}_\mathrm{T})$ for all values $\tilde{\theta}_\mathrm{T}$ on the grid is computed, requiring $N_{\theta_\mathrm{T}}N_\mathrm{T}N_\mathrm{R}$. Each of the N_{θ_T} resulting vectors is multiplied with $\boldsymbol{a}_\mathrm{R}(\tilde{\theta}_\mathrm{R})$ for each value $\tilde{\theta}_\mathrm{R}$ on the grid, resulting in $N_{\theta_\mathrm{T}}N_\mathrm{R}N_{\theta_\mathrm{R}}$ multiplications Therefore, for a single value τ', $N_\mathrm{R}(N_\mathrm{T}N_\mathrm{P}N_\mathrm{B}+N_{\theta_\mathrm{T}}N_\mathrm{T}+N_{\theta_\mathrm{T}}N_{\theta_\mathrm{R}})$ multiplications are required. Hence, the computational complexity for detecting the new potential path is $O(N_\tau N_\mathrm{R}(N_\mathrm{T}N_\mathrm{P}N_\mathrm{B}+N_{\theta_\mathrm{T}}N_\mathrm{T}+N_{\theta_\mathrm{T}}N_{\theta_\mathrm{R}}))$. The resulting expression corresponds to a specific order of computation and slightly different expressions may be obtained for an alternative computation order, but the conclusions remain intact.

3.1.2.2 Reduction of the Computational Complexity of New Potential Path Detection

The computational complexity of the search on the 3D grid is high, and, in fact, it is the one dominating the computational complexity of Alg. 1. It is possible to reduce the 3D search to a 2D and a one-dimensional (1D) search as follows

$$
\begin{aligned}
g_s(\tau', \tilde{\theta}_\mathrm{T}, \tilde{\theta}_\mathrm{R}) &= \Big|\boldsymbol{a}_\mathrm{T}^\mathrm{T}(\tilde{\theta}_\mathrm{T})\Big(\sum_{b=0}^{N_\mathrm{B}-1} \boldsymbol{X}_b \,\mathrm{diag}(\boldsymbol{a}_\tau(\tau'))\boldsymbol{R}_{i,b}^\mathrm{H}\Big)\boldsymbol{a}_\mathrm{R}(\tilde{\theta}_\mathrm{R})\Big| \\
&= \Bigg|\sum_{b=0}^{N_\mathrm{B}-1} [\boldsymbol{a}_\mathrm{T}^\mathrm{T}(\tilde{\theta}_\mathrm{T})\boldsymbol{x}[p_1, b], \ldots, \boldsymbol{a}_\mathrm{T}^\mathrm{T}(\tilde{\theta}_\mathrm{T})\boldsymbol{x}[p_{N_\mathrm{P}}, b]] \\
&\qquad \times \begin{bmatrix} \mathrm{e}^{-\mathrm{j}\,\omega_{p_1}\tau'} & \ldots & 0 \\ \vdots & \ddots & \vdots \\ 0 & \ldots & \mathrm{e}^{-\mathrm{j}\,\omega_{p_{N_\mathrm{P}}}\tau'} \end{bmatrix} \begin{bmatrix} \boldsymbol{r}_i^\mathrm{H}[p_1, b]\boldsymbol{a}_\mathrm{R}(\tilde{\theta}_\mathrm{R}) \\ \vdots \\ \boldsymbol{r}_i^\mathrm{H}[p_{N_\mathrm{P}}, b]\boldsymbol{a}_\mathrm{R}(\tilde{\theta}_\mathrm{R}) \end{bmatrix}\Bigg| \\
&= \Big|\sum_{p\in\mathcal{P}}\sum_{b=0}^{N_\mathrm{B}-1} \boldsymbol{r}_i^\mathrm{H}[p, b]\boldsymbol{a}_\mathrm{R}(\tilde{\theta}_\mathrm{R})\boldsymbol{a}_\mathrm{T}^\mathrm{T}(\tilde{\theta}_\mathrm{T})\boldsymbol{x}[p, b]\,\mathrm{e}^{-\mathrm{j}\,\omega_p\tau'}\Big| \\
&\overset{(a)}{\leq} \sum_{p\in\mathcal{P}}\Big|\sum_{b=0}^{N_\mathrm{B}-1} \boldsymbol{r}_i^\mathrm{H}[p, b]\boldsymbol{a}_\mathrm{R}(\tilde{\theta}_\mathrm{R})\boldsymbol{a}_\mathrm{T}^\mathrm{T}(\tilde{\theta}_\mathrm{T})\boldsymbol{x}[p, b]\,\mathrm{e}^{-\mathrm{j}\,\omega_p\tau'}\Big| \\
&= \sum_{p\in\mathcal{P}}\Big|\sum_{b=0}^{N_\mathrm{B}-1} \boldsymbol{r}_i^\mathrm{H}[p, b]\boldsymbol{a}_\mathrm{R}(\tilde{\theta}_\mathrm{R})\boldsymbol{a}_\mathrm{T}^\mathrm{T}(\tilde{\theta}_\mathrm{T})\boldsymbol{x}[p, b]\Big| \\
&= \sum_{p\in\mathcal{P}}\Big|\boldsymbol{a}_\mathrm{T}^\mathrm{T}(\tilde{\theta}_\mathrm{T})\boldsymbol{X}_p\boldsymbol{R}_{i,p}^\mathrm{H}\boldsymbol{a}_\mathrm{R}(\tilde{\theta}_\mathrm{R})\Big|, \qquad (3.20)
\end{aligned}
$$

where $\boldsymbol{X}_p = [\boldsymbol{x}[p, 0], \ldots, \boldsymbol{x}[p, N_\mathrm{B}-1]] \in \mathbb{C}^{N_\mathrm{T}\times N_\mathrm{B}}$, $\boldsymbol{R}_{i,p} = [\boldsymbol{r}_i[p, 0], \ldots, \boldsymbol{r}_i[p, N_\mathrm{B}-1]] \in \mathbb{C}^{N_\mathrm{R}\times N_\mathrm{B}}$ and (a) follows from the triangle inequality. The upper bound (3.20) depends only on the AOD and

AOA and can be used instead as a surrogate function for the detection of a new potential path as

$$\tilde{\theta}_{\mathrm{T}}^{(i)}, \tilde{\theta}_{\mathrm{R}}^{(i)} = \underset{(\tilde{\theta}_{\mathrm{T}}, \tilde{\theta}_{\mathrm{R}}) \in \mathcal{G}_{\theta_{\mathrm{T}}} \times \mathcal{G}_{\theta_{\mathrm{R}}}}{\operatorname{argmax}} \sum_{p \in \mathcal{P}} \left| \boldsymbol{a}_{\mathrm{T}}^{\mathrm{T}}(\tilde{\theta}_{\mathrm{T}}) \boldsymbol{X}_p \boldsymbol{R}_p^{\mathrm{H}} \boldsymbol{a}_{\mathrm{R}}(\tilde{\theta}_{\mathrm{R}}) \right|. \tag{3.21}$$

After obtaining $\tilde{\theta}_{\mathrm{T}}^{(i)}$ and $\tilde{\theta}_{\mathrm{R}}^{(i)}$, we plug them in (3.19) and maximize it over the TOA grid

$$\tau'^{(i)} = \underset{\tau' \in \mathcal{G}_\tau}{\operatorname{argmax}} \left| \boldsymbol{a}_\tau^{\mathrm{T}}(\tau') \Big(\sum\nolimits_{b=0}^{N_{\mathrm{B}}-1} \operatorname{diag}(\boldsymbol{X}_b^{\mathrm{T}} \boldsymbol{a}_{\mathrm{T}}(\tilde{\theta}_{\mathrm{T}}^{(i)})) \boldsymbol{R}_b^{\mathrm{H}} \boldsymbol{a}_{\mathrm{R}}(\tilde{\theta}_{\mathrm{R}}^{(i)}) \Big) \right|. \tag{3.22}$$

Using similar arguments as those for the 3D search, the complexity of this approach is $\mathcal{O}(N_{\mathrm{P}}(N_{\mathrm{T}}N_{\mathrm{R}}N_{\mathrm{B}} + N_{\theta_{\mathrm{T}}}N_{\mathrm{T}}N_{\mathrm{R}} + N_{\theta_{\mathrm{T}}}N_{\mathrm{T}}N_{\theta_{\mathrm{R}}}))$. Naturally, the complexity reduction comes with a cost. From (3.21) it is evident that the observations on different subcarriers are processed incoherently. This should incur an SNR loss in the detection of paths, which we will quantify in the numerical results. Finally, we note that a similar procedure can be followed to conduct the 2D search over TOA-AOA or TOA-AOD.

3.1.3 Step 3: Update Support

After computing the new potential path, we add it to the existing ones:

$$\boldsymbol{\tau}'^{(i+1)} = (\tau'^{(i)}_0, \ldots, \tau'^{(i)}_{L^{(i)}-1}, \tau'^{(i)}), \tag{3.23}$$

$$\tilde{\boldsymbol{\theta}}_{\mathrm{T}}^{(i+1)} = (\tilde{\theta}_{\mathrm{T},0}^{(i)}, \ldots, \tilde{\theta}_{\mathrm{T},L^{(i)}-1}^{(i)}, \tilde{\theta}_{\mathrm{R}}^{(i)}), \tag{3.24}$$

$$\tilde{\boldsymbol{\theta}}_{\mathrm{R}}^{(i+1)} = (\tilde{\theta}_{\mathrm{R},0}^{(i)}, \ldots, \tilde{\theta}_{\mathrm{R},L^{(i)}-1}^{(i)}, \tilde{\theta}_{\mathrm{R}}^{(i)}). \tag{3.25}$$

3.1.4 Step 4: Coordinate Descent

The aim of this algorithmic step is two-fold, namely to refine the parameters of detected paths and to remove potentially redundant paths. We iteratively perform 3 sub-steps for a fixed number of N_{cd} iterations.

3.1.4.1 Path Gain Computation

We update the gains solving (3.26), keeping the other path parameters fixed:

$$\boldsymbol{h}^{(i+1)} = \operatorname{argmin}_{\boldsymbol{h}} \Lambda(\boldsymbol{R}(\{\tau'^{(i+1)}_l, \tilde{\theta}^{(i+1)}_{\mathrm{T},l}, \tilde{\theta}^{(i+1)}_{\mathrm{R},l}, h_l\}_{l=0}^{L^{(i)}})) + \chi \|\boldsymbol{h}\|_1. \tag{3.26}$$

The regularization parameter χ determines the accuracy-sparsity trade-off. Due to the presence of the L1-norm penalty, the gain of previously detected paths, which may have become redundant after the subsequent detection and refinement of other paths, may be set to (approximately) zero.

3.1.4.2 Prune Support

In this step we prune the paths that have become redundant according to their gain computed in (3.26). We consider a path to be redundant when its gain is much smaller than the gain of the strongest path. More formally, the l-th path is pruned if

$$\frac{|h_l^{(i+1)}|^2}{\max_{l=0,\ldots,L^{(i)}-1} |h_l^{(i+1)}|^2} < \zeta_2, \tag{3.27}$$

where $0 < \zeta_2 \ll 1$ and the resulting sequence of TOAs if the l-th path is pruned is

$$\boldsymbol{\tau}'^{(i+1)} \leftarrow (\tau'^{(i+1)}_0, \ldots, \tau'^{(i+1)}_{l-1}, \tau'^{(i+1)}_{l+1}, \ldots, \tau'^{(i+1)}_{L^{(i)}}), \tag{3.28}$$

with the resulting AODs and AOAs sequences obtained accordingly. The threshold ζ_2 quantifies how low the gain of a path must be for it to be considered essentially zero. We use the ratio of the gain of a path to the maximum gain, because this is what decides whether a path is significant or essentially non-existent. For example, when the LOS path exists, an NLOS path with a gain 35 dB lower than that of the LOS may be irrelevant, whereas the same path might be relevant in the absence of LOS.

3.1.4.3 Local Descent

We perform local descent over all parameters of all detected paths, for each path and each parameter sequentially, as follows

$$\tau'^{(i+1)}_l \leftarrow \tau'^{(i+1)}_l - \mathrm{sgn}(\partial\Lambda/\partial\tau'^{(i+1)}_l)s^{(i+1)}_{\tau,l}, \tag{3.29}$$

$$\theta^{(i+1)}_{\mathrm{T},l} \leftarrow \theta^{(i+1)}_{\mathrm{T},l} - \mathrm{sgn}(\partial\Lambda/\partial\theta^{(i+1)}_{\mathrm{T},l})s^{(i+1)}_{\theta_\mathrm{T},l}, \tag{3.30}$$

$$\theta^{(i+1)}_{\mathrm{R},l} \leftarrow \theta^{(i+1)}_{\mathrm{R},l} - \mathrm{sgn}(\partial\Lambda/\partial\theta^{(i+1)}_{\mathrm{R},l})s^{(i+1)}_{\theta_\mathrm{R},l}, \tag{3.31}$$

$$h^{(i+1)}_l \leftarrow \frac{\mathrm{tr}\left(\boldsymbol{C}^{\mathrm{H}}(\tau'^{(i+1)}_l, \tilde{\theta}^{(i+1)}_{\mathrm{T},l}, \tilde{\theta}^{(i+1)}_{\mathrm{R},l})\left(\boldsymbol{Y} - \sum_{l'\neq l} h^{(i+1)}_{l'}\boldsymbol{C}(\tau'^{(i+1)}_{l'}, \tilde{\theta}^{(i+1)}_{\mathrm{T},l'}, \tilde{\theta}^{(i+1)}_{\mathrm{R},l'})\right)\right)}{\|\boldsymbol{C}^{\mathrm{H}}(\tau'^{(i+1)}_l, \tilde{\theta}^{(i+1)}_{\mathrm{T},l}, \tilde{\theta}^{(i+1)}_{\mathrm{R},l})\|^2_F}, \tag{3.32}$$

where

$$s^{(i+1)}_{\tau,l} = \min\left(\left|\left(\partial^2\Lambda/(\partial\tau'^{(i+1)}_l)^2\right)^{-1}\partial\Lambda/\partial\tau'^{(i+1)}_l\right|, \frac{N_{\mathrm{CP}}T_\mathrm{s}}{2(N_\tau - 1)}\right), \tag{3.33}$$

$$s^{(i+1)}_{\theta_\mathrm{T},l} = \min\left(\left|\left(\partial^2\Lambda/(\partial\theta^{(i+1)}_{\mathrm{T},l})^2\right)^{-1}\partial\Lambda/\partial\theta^{(i+1)}_{\mathrm{T},l}\right|, \frac{\pi}{N_{\theta_\mathrm{T}-1}}\right), \tag{3.34}$$

$$s^{(i+1)}_{\theta_\mathrm{R},l} = \min\left(\left|\left(\partial^2\Lambda/(\partial\theta^{(i+1)}_{\mathrm{R},l})^2\right)^{-1}\partial\Lambda/\partial\theta^{(i+1)}_{\mathrm{R},l}\right|, \frac{\pi}{N_{\theta_\mathrm{R}-1}}\right) \tag{3.35}$$

are the step sizes. We note that, for the geometry-related parameters, we use truncated Newton steps, where, instead of just using Newton steps, we limit the maximum step size to be equal to half of the corresponding grid bin size so as to avoid convergence problems near inflection points of the loss function. The steps are always in the negative gradient direction. For the update of the path gains, (3.32) provides the loss-minimizing $h^{(i+1)}_l$ with all other parameters fixed to their current value.

As pointed out in [48], the local refinement of the parameters of all detected paths is very important for the convergence of the algorithm and the identification of sparse solutions. The effective off-grid parameter estimation enables the algorithm to avoid detecting artificial paths arising due to grid mismatch. Also, through the refinement of the parameters of all paths, some of them may become obsolete and be removed, leading to sparser solutions.

A slight difference compared to [48] is that we also update the path gains in the local descent step, a choice also made in [62], where it is shown that this step is essential to prove convergence of the algorithm in a finite number of iteration.

3.1.5 Termination Condition

The algorithm is terminated either when the maximum number of paths is detected or when the following condition is satisfied

$$\left|\mathrm{tr}(\boldsymbol{R}_i^{\mathrm{H}}\boldsymbol{C}(\tau^{(i)},\tilde{\theta}_{\mathrm{T}}^{(i)},\tilde{\theta}_{\mathrm{R}}^{(i)})\right| < \zeta_1(\boldsymbol{X},\sigma_{\eta,\mathrm{R}},P_{\mathrm{fa}}). \tag{3.36}$$

Intuitively, this condition means that any new path is not (sufficiently) correlated with the residual, namely it corresponds to noise. Therefore, it should be ignored and the process should stop.

3.1.6 A Note about Global Optimality

A natural question that arises is whether we have any guarantees about the recovery of the true parameters from Alg. 1. There are two points to consider here:

- Whether the solution of (3.14) recovers the true parameters.
- Whether Alg. 1 recovers the globally optimal solution of (3.14).

Regarding the first point, in the noiseless case and given a minimum angular separation, the true parameters are the unique solution of (3.14) [62], [63]. In the noisy case, under the non-degenerate source condition [64] (roughly speaking, sufficiently separated paths), the unique solution of (3.14) has the same number of paths as the true channel, provided that χ and $\|\boldsymbol{h}\|_2/\chi$ are small enough, and with decreasing noise the solution converges to the true parameters.

Regarding the second point, Alg. 1 is based on ADCGM [48] and, regardless of the implementation details of the individual steps, the algorithmic framework of ADCGM does not provide guarantees about the recovery of the true parameters. Nevertheless, it has been shown to provide state of the art performance in a wide range of sparse inverse problems [48], [65].

3.2 Channel to Position Parameters Mapping with Path Rejection

Let $\hat{\tilde{\boldsymbol{\nu}}}$ be the estimate of the channel parameter vector $\tilde{\boldsymbol{\nu}}$, defined as

$$\hat{\tilde{\boldsymbol{\nu}}} = [\tau_0', \hat{\tilde{\theta}}_{\mathrm{T},0}, \hat{\tilde{\theta}}_{\mathrm{R},0}, \hat{h}_0, \ldots, \hat{\tau}_{\hat{L}-1}', \hat{\tilde{\theta}}_{\mathrm{T},\hat{L}-1}', \hat{\tilde{\theta}}_{\mathrm{R},\hat{L}-1}, \hat{h}_{\hat{L}-1}]^{\mathrm{T}}, \tag{3.37}$$

where $\hat{L}$ is the estimated number of paths. We would like to obtain an estimate $\hat{\boldsymbol{\nu}}$ of the position parameter vector $\boldsymbol{\nu}$. In the following, we assume that the LOS path exists and we identify it as strongest path. We note that this is a simplistic choice, as LOS detection is out of the scope of this work. More details on LOS/NLOS detection can be found in [66]. We estimate the position parameter vector $\boldsymbol{\nu}$ employing the EXIP as in [22], with a slight modification to include the prior information on the clock offset. To this end, we intend to solve

$$\hat{\boldsymbol{\nu}} = \underset{\boldsymbol{\nu}}{\mathrm{argmin}} \left((\hat{\tilde{\boldsymbol{\nu}}} - f(\boldsymbol{\nu}))^{\mathrm{T}} \boldsymbol{J}_{\hat{\tilde{\boldsymbol{\nu}}}} (\hat{\tilde{\boldsymbol{\nu}}} - f(\boldsymbol{\nu})) + (\epsilon_{\mathrm{clk}}/\sigma_{\mathrm{clk}})^2 \right), \tag{3.38}$$

where $\boldsymbol{J}_{\hat{\tilde{\boldsymbol{\nu}}}}$ is the channel parameter FIM, which is computed using the estimated channel parameters, and $f : \mathbb{R}^{4\hat{L}+2} \to \mathbb{R}^{5\hat{L}}$ is the mapping from position to channel parameters, determined by (2.8), (2.11)-(2.12) (or (2.119), (2.120) and (2.122) with a VA parametrization of NLOS components).

We note that false alarms, that is, falsely detected paths, can have severe impact on position estimation, as the additional erroneous terms in the optimization (3.38) may drive the position estimate away from the true value. Therefore, we apply the following two criteria to filter them out:

- A single-bounce NLOS path and a LOS path always form a triangle, as can be seen in Fig. 2.1. Therefore, for the formation of a triangle to be possible, a single-bounce NLOS path must satisfy

$$\Delta\hat{\tilde{\theta}}_{\mathrm{T},l} \cdot \Delta\hat{\tilde{\theta}}_{\mathrm{R},l} < 0,\ l = 1, \ldots, \hat{L} - 1, \tag{3.39}$$

  where $\Delta\hat{\tilde{\theta}}_{\mathrm{T},l} = \hat{\tilde{\theta}}_{\mathrm{T},l} - \hat{\tilde{\theta}}_{\mathrm{T},0}$ and $\Delta\hat{\tilde{\theta}}_{\mathrm{R},l} = \hat{\tilde{\theta}}_{\mathrm{R},l} - \hat{\tilde{\theta}}_{\mathrm{R},0}$, with $\Delta\hat{\tilde{\theta}}_{\mathrm{T},l}$ and $\Delta\hat{\tilde{\theta}}_{\mathrm{R},l} \in [-\pi, \pi)$. Hence, if the l-th path, $l = 1, \ldots, \hat{L} - 1$, does not satisfy (3.39), it is dropped.
- Combined with the LOS path, each NLOS path can provide an estimate $\hat{\epsilon}_{\mathrm{clk},l}$ of ϵ_{clk} as

$$\hat{\epsilon}_{\mathrm{clk},l} = \frac{\hat{\tau}'_l \sin(\Delta\hat{\tilde{\theta}}_{\mathrm{R},l} - \Delta\hat{\tilde{\theta}}_{\mathrm{T},l}) - \hat{\tau}'_0(\sin(\Delta\hat{\tilde{\theta}}_{\mathrm{R},l}) - \sin(\Delta\hat{\tilde{\theta}}_{\mathrm{T},l}))}{\sin(\Delta\hat{\tilde{\theta}}_{\mathrm{R},l} - \Delta\hat{\tilde{\theta}}_{\mathrm{T},l}) - (\sin(\Delta\hat{\tilde{\theta}}_{\mathrm{R},l}) - \sin(\Delta\hat{\tilde{\theta}}_{\mathrm{T},l}))}. \tag{3.40}$$

  With $\zeta_{3,a} > 0$ and $\zeta_{3,b} > 0$ being predefined probability thresholds for ϵ_{clk} values, if

$$p(\hat{\epsilon}_{\mathrm{clk},l}) < \zeta_{3,a} \text{ or } p(\hat{\epsilon}_{\mathrm{clk},l}) < \zeta_{3,b} p_{\mathrm{clk,max}}, \tag{3.41}$$

  the path is filtered out, with $p_{\mathrm{clk,max}} = \max_{l=1,\ldots,\hat{L}-1} p(\hat{\epsilon}_{\mathrm{clk},l})$.

Replacing $\hat{\tilde{\boldsymbol{\nu}}}$ with $\hat{\tilde{\boldsymbol{\nu}}}'$, which contains only the remaining paths, we solve (3.38) with the Levenberg-Marquardt algorithm [67], [68]. For the initial point $\boldsymbol{\nu}^{(0)}$ we compute

$$\hat{\epsilon}^{(0)}_{\mathrm{clk}} = \frac{\sum_l |\hat{h}_l|^2 \hat{\epsilon}_{\mathrm{clk},l}}{\sum_l |\hat{h}_l|^2}, \tag{3.42}$$

$$\hat{\boldsymbol{p}}^{(0)}_{\mathrm{R}} = c(\hat{\tau}'_0 - \hat{\epsilon}^{(0)}_{\mathrm{clk}})\boldsymbol{u}(\hat{\tilde{\theta}}_{\mathrm{T},0}), \tag{3.43}$$

$$\hat{\alpha}^{(0)}_{\mathrm{R}} = \hat{\tilde{\theta}}_{\mathrm{T},0} + \pi - \hat{\tilde{\theta}}_{\mathrm{R},0}, \tag{3.44}$$

$$\hat{\boldsymbol{p}}^{(0)}_{\mathrm{s},l} = \frac{\tan(\hat{\tilde{\theta}}_{\mathrm{R},l} + \hat{\alpha}^{(0)}_{\mathrm{R}})\hat{p}^{(0)}_{\mathrm{R},x} - \hat{p}^{(0)}_{\mathrm{R},y}}{\tan(\hat{\tilde{\theta}}_{\mathrm{R},l} + \hat{\alpha}^{(0)}_{\mathrm{R}})\cos\hat{\tilde{\theta}}_{\mathrm{T},l} - \sin\hat{\tilde{\theta}}_{\mathrm{T},l}}\boldsymbol{u}(\hat{\tilde{\theta}}_{\mathrm{T},l}), l = 1, \ldots, \hat{L}', \tag{3.45}$$

where $\hat{L}'$ is the number of remaining estimated paths.

3.3 Numerical Results

The geometric setup used for the evaluation of the positioning algorithm is depicted in Fig. 3.1. We consider a 60 m × 50 m room. The Tx is located at the left wall of the room, at origin of the coordinate system, i.e., $\boldsymbol{p}_{\mathrm{T}} = [0,\ 0]^{\mathrm{T}}$ m and is equipped with a ULA with $N_{\mathrm{T}} = 32$ elements. The Rx is located at $\boldsymbol{p}_{\mathrm{T}} = [25,\ 10]^{\mathrm{T}}$ m and has a UCA with $N_{\mathrm{R}} = 16$. There is a LOS path between the Tx and Rx, as well as three single-bounce reflections from the wall's room, with $\boldsymbol{p}_{\mathrm{s},1} = [15.63,\ 25]^{\mathrm{T}}$ m, $\boldsymbol{p}_{\mathrm{s},2} = [10.42,\ -25]^{\mathrm{T}}$ m and $\boldsymbol{p}_{\mathrm{s},3} = [60,\ 6.32]^{\mathrm{T}}$ m. The path gains are computed according to (2.138), with $\Gamma_{\mathrm{refl},l} = -10\,\mathrm{dB}, \forall l$. The carrier frequency is set to $f_{\mathrm{c}} = 38\,\mathrm{GHz}$, the sampling frequency is $f_{\mathrm{s}} = 122.88\,\mathrm{MHz}$, the number of subcarriers is $N = 64$ and $N_{\mathrm{B}} = 10$ OFDM symbols are transmitted. The entries of the reference signal $\boldsymbol{X}$ are QPSK symbols. The set of loaded subcarriers is $\mathcal{P} = \{-31, -30, \ldots, -1, 1, 2, \ldots, 31\}$ and $\gamma_p = 1/|\mathcal{P}|,\ \forall p \in \mathcal{P}$, with $|\mathcal{P}| = 62$. The noise spectral density is $N_0 = -174\,\mathrm{dBm}$ and the Rx noise figure is $\mathrm{NF} = 13\,\mathrm{dB}$. The Tx and Rx are imperfectly synchronized with $c\sigma_{\mathrm{clk}} = 2cT_{\mathrm{s}} \approx 4.88\,\mathrm{m}$.

The algorithm is parameterized as follows: the number of iterations in the coordinate descent step is set to $N_{\mathrm{cd}} = 3$ and the false alarm rate to $P_{\mathrm{fa}} = 0.05$, with the appropriate value

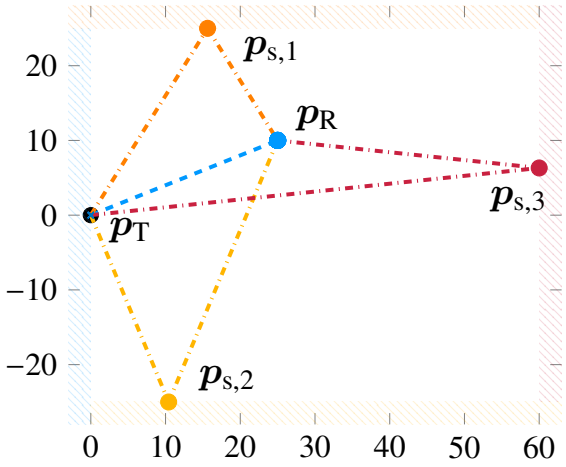

Fig. 3.1. Geometric setup for evaluation of the position estimation algorithm.

of ζ_1 for the desired P_{fa} being computed numerically using 10000 random noise and reference signal realizations. The pruning threshold is $\zeta_2 = 30\,\text{dB}$. The grid parameters are $N_\tau = 64$, $N_{\theta_\text{T}} = 32$ and $N_{\theta_\text{R}} = 64$ and we consider both 2D and 3D grid search in step 2 (new potential path detection). The maximum number of paths is $L_{\max} = 10$, the regularization parameter $\chi = \sigma_\eta\sqrt{2(N_\text{T}+N_\text{R})|\mathcal{P}|N_\text{B}E_\text{RE}/N_\text{T}}$ (chosen according to [69]) and the path filtering thresholds $\zeta_{3,a} = 10^{-4}$ and $\zeta_{3,b} = 10^{-2}$.

For the comparison, we consider the single-anchor positioning algorithm from [22], which, due to its performance, is taken as the benchmark in many related works, and is the most cited single-anchor positioning algorithm. In the first stage of the approach proposed in [22], a compressed sensing-based algorithm, called distributed compressed sensing-simultaneous orthogonal matching pursuit (DCS-SOMP) is used to obtain coarse estimates of the multipath parameters (number of paths, TOAs, AODs, AOAs and gains), with the coarse estimates refined in the second stage using space-alternating generalized expectation maximization (SAGE). In the third stage, the refined estimates are mapped to the Rx position and orientation and the scatterer/reflector positions using the EXIP. The parameterization of the algorithm is as follows: false alarm rate $P_{\text{fa}} = 0.05$, 3 SAGE iterations, and the number of Tx and Rx angular domain bins (analogous to N_{θ_T} and N_{θ_R}) is 64 and 32, respectively. As will become evident with the following results, in the medium to high SNR region, this algorithm overestimates the model order. Therefore, for the maximimum number of detected paths $L_{\max}$, we will consider different values to gain insight on the influence of the different characteristics of the algorithm on its performance. In addition, similar to our approach, we will study the effect of path filtering after the refinement of the paths' parameters with SAGE.

We list the algorithmic variations that will be considered in the following results with their corresponding label:

1) "3D + F": the method proposed in the current work with a 3D grid search;
2) "2D + F": the method proposed in the current work with a 2D grid search;
3) "2D - F": the method proposed in the current work with a 2D grid search, but without the path filtering step in (3.39) and in the sentence after (3.41), before the mapping from channel to position parameters;
4) "B": the algorithm proposed in [22];
5) "B + F": the algorithm proposed in [22], but applying the path filtering step proposed in our work after refinement of the path parameters with SAGE;

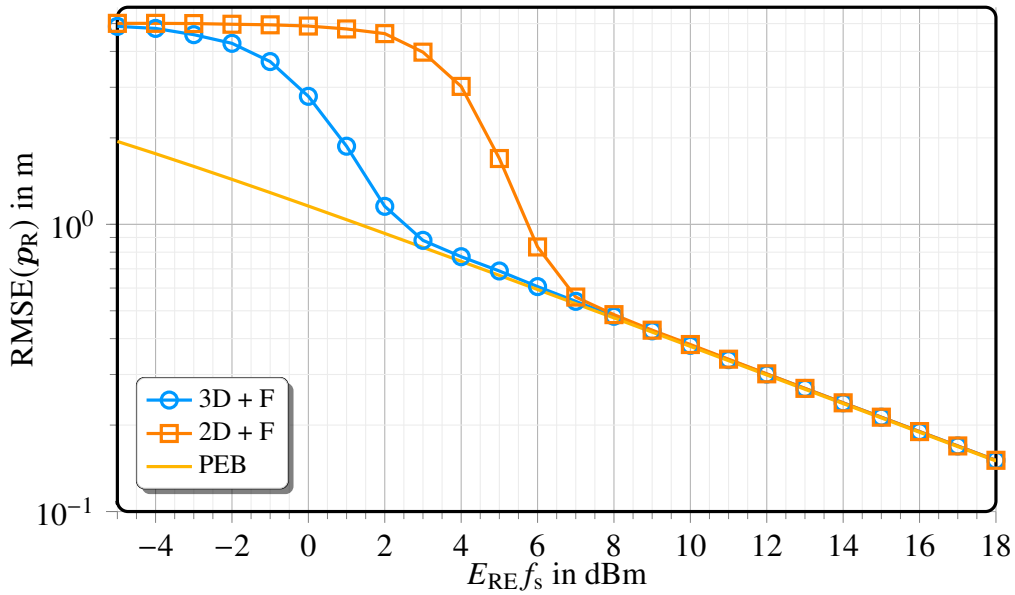

Fig. 3.2. Position RMSE of the proposed algorithm with 2D and 3D grid search as a function of E_{RE}.

3.3.1 The Effect of Grid Search Dimensionality

In order to evaluate our proposed approach, we plot in Fig. 3.2 the position RMSE RMSE($\boldsymbol{p}_R$) of the proposed algorithm with 2D and 3D grid search for path detection as a function of the average energy per resource element E_{RE}, where the RMSE of a parameter ν is defined as

$$\mathrm{RMSE}(\nu) = \sqrt{\mathbb{E}_{\hat{\nu}}[(\hat{\nu} - \nu)^2]} \tag{3.46}$$

and $\hat{\nu}$ is the estimated parameter. For each E_{RE} value, we average over (the same) 1000 random noise and reference signal realizations. The PEB is also plotted for the evaluation of the algorithm's performance. Furthermore, to more effectively explain and better understand the trends of the RMSE curves as functions of E_{RE}, we also plot in Figs. 3.3, 3.4, 3.5 and 3.6 the RMSE of the parameters of all paths (TOA, AOD and AOA) as a function of E_{RE}. For the NLOS components, we also plot the RMSE of the corresponding POI and detection rate for each path. For these, as well as the following figures in the chapter, each data point is generated by averaging over 2000 noise realizations.

At this point, it is necessary to mention that their computation is not as straightforward as RMSE($\boldsymbol{p}_R$), due to the fact that it inherently involves a data association problem: an estimated path might correspond to any of the true paths or even to none of them (false alarm), while a true path might result in zero, one or multiple path detections. Data association is a well-studied problem within the framework of multi-target tracking [70]. Since tracking is out of the scope of this work and we deal with the data association problem only for the evaluation of multipath parameter estimation, we use a simple Euclidean distance-based rule to associate estimated and true paths. For the l-th true path and its corresponding POI we find the index of the potentially associated estimated path by

$$m = \underset{l'=1,\ldots,\hat{L}'}{\operatorname{argmin}} \|\hat{\boldsymbol{p}}_{s,l'} - \boldsymbol{p}_{s,l}\|_2. \tag{3.47}$$

We then associate the l-th true path with the m-th estimated path if

$$\|\hat{\boldsymbol{p}}_{s,m} - \boldsymbol{p}_{s,l}\|_2 < a_{th}, \tag{3.48}$$

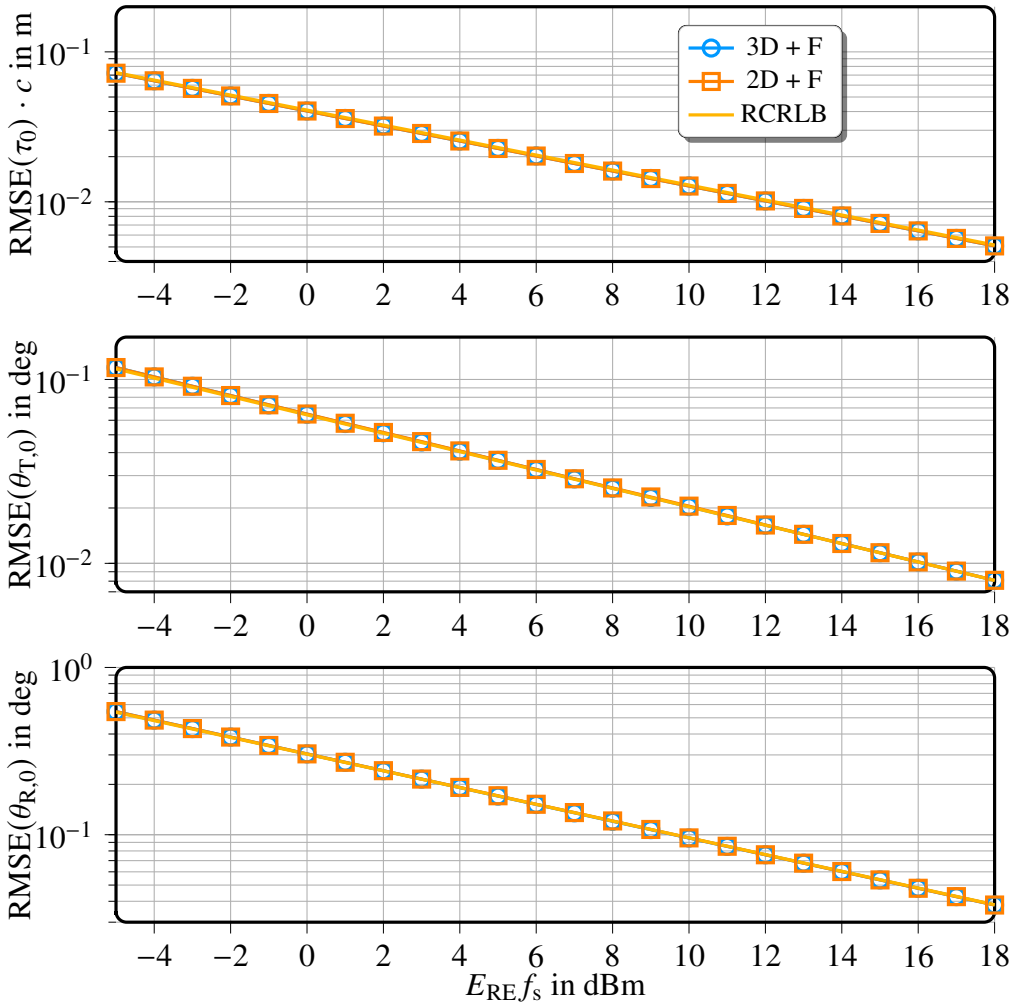

Fig. 3.3. Estimation performance for the LOS (0-th path) as a function of E_{RE}.

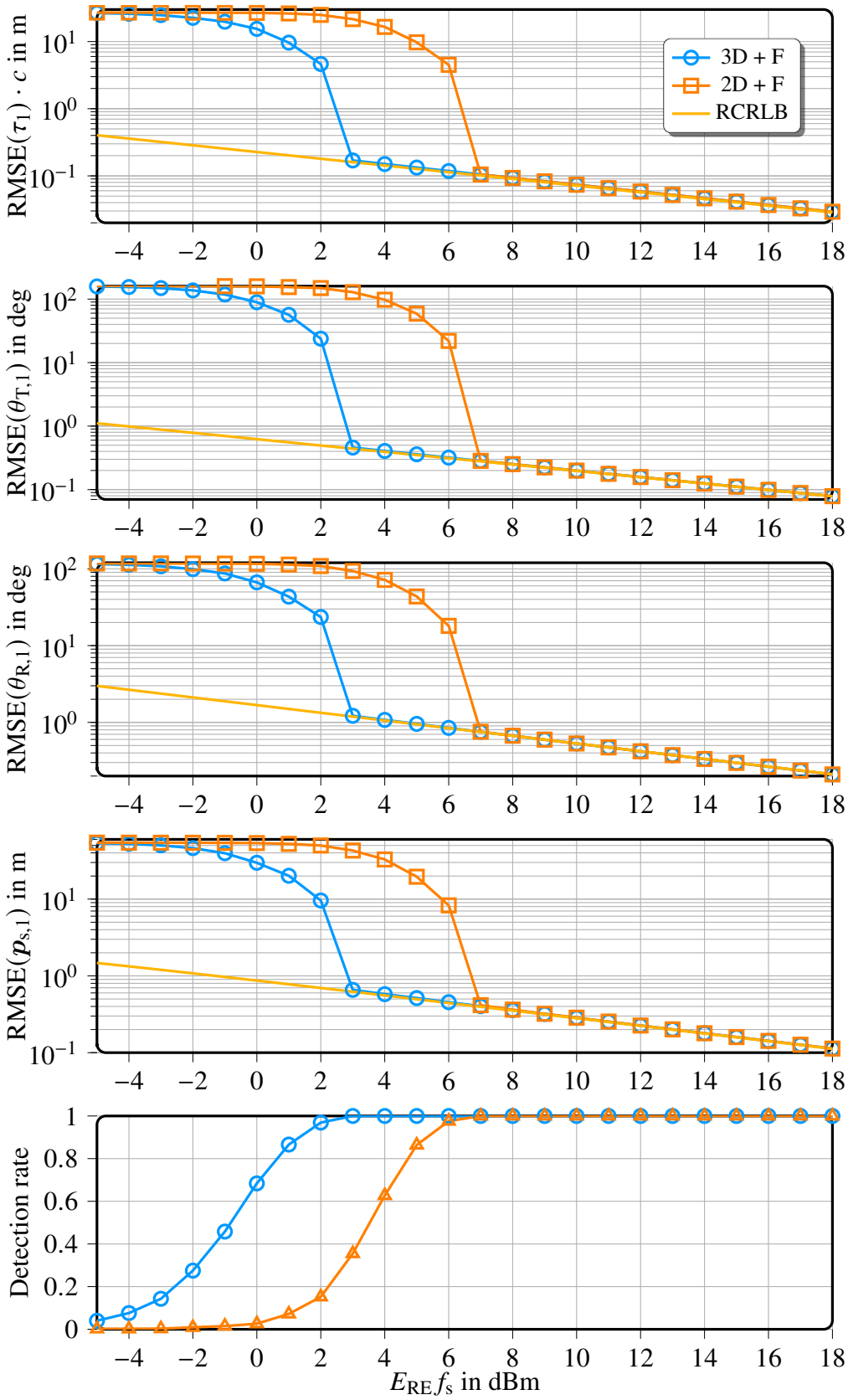

Fig. 3.4. Estimation performance for the 1st NLOS path as a function of E_{RE}.

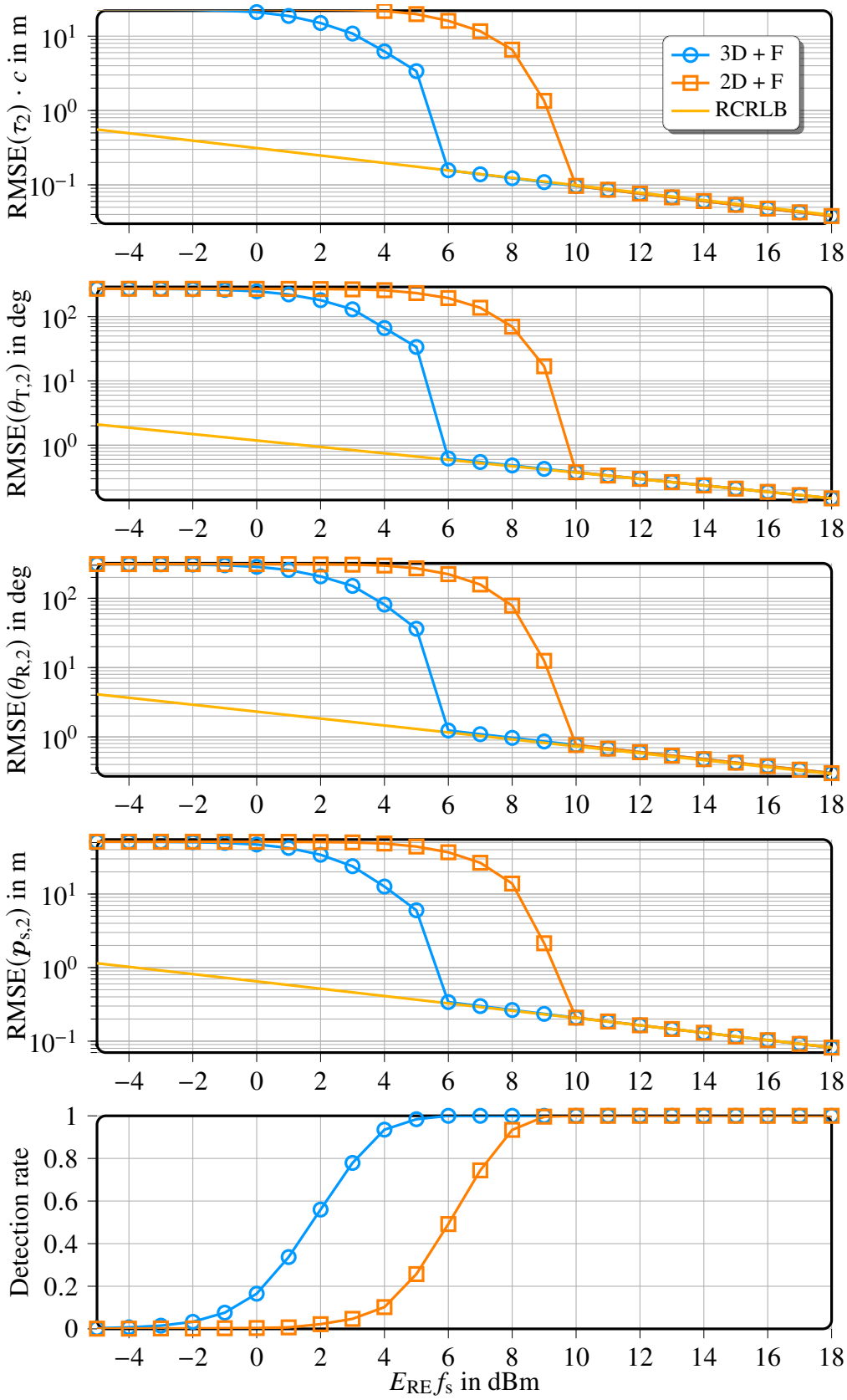

Fig. 3.5. Estimation performance for the 2nd NLOS path as a function of E_{RE}.

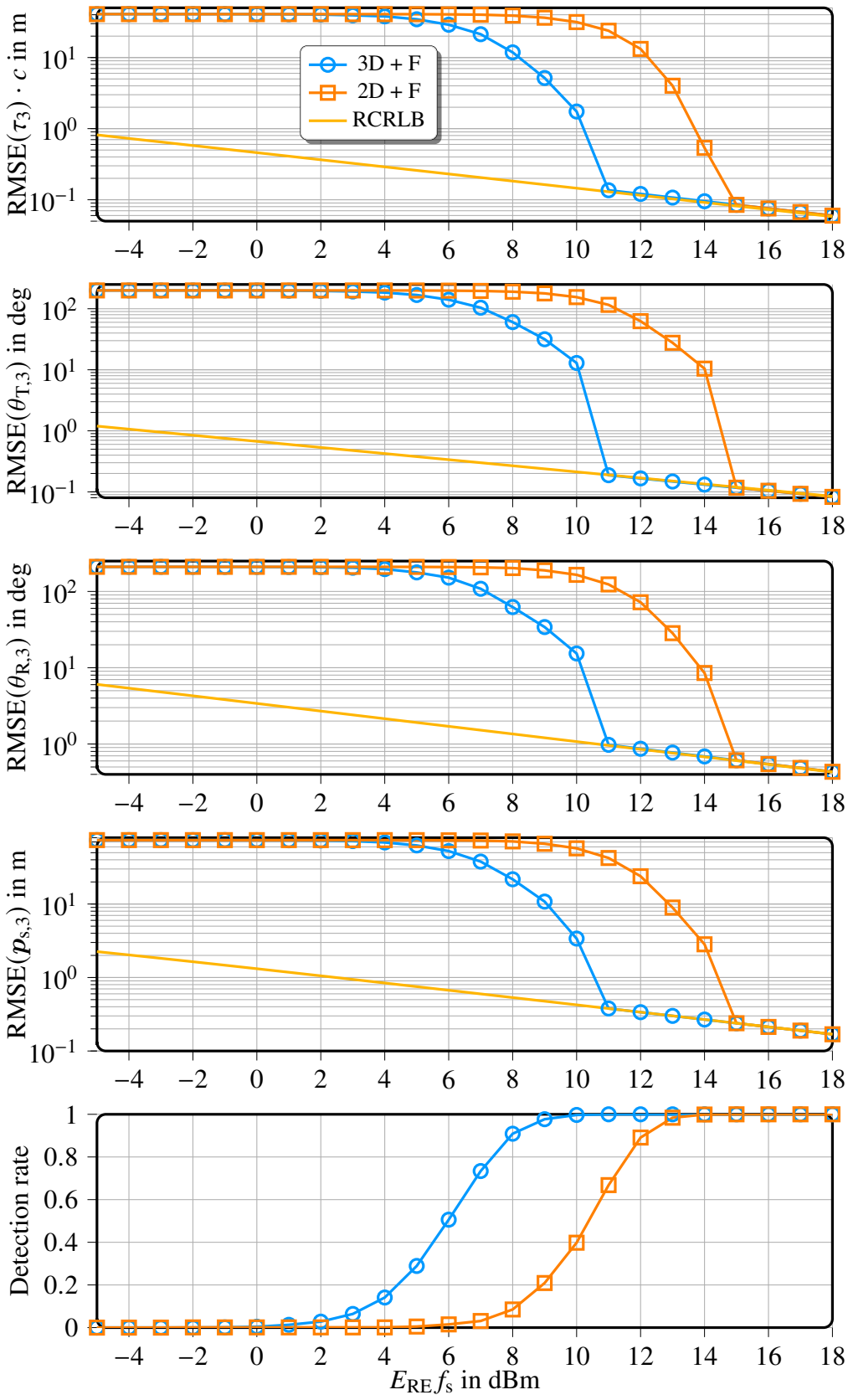

Fig. 3.6. Estimation performance for the 3rd NLOS path as a function of E_{RE}.

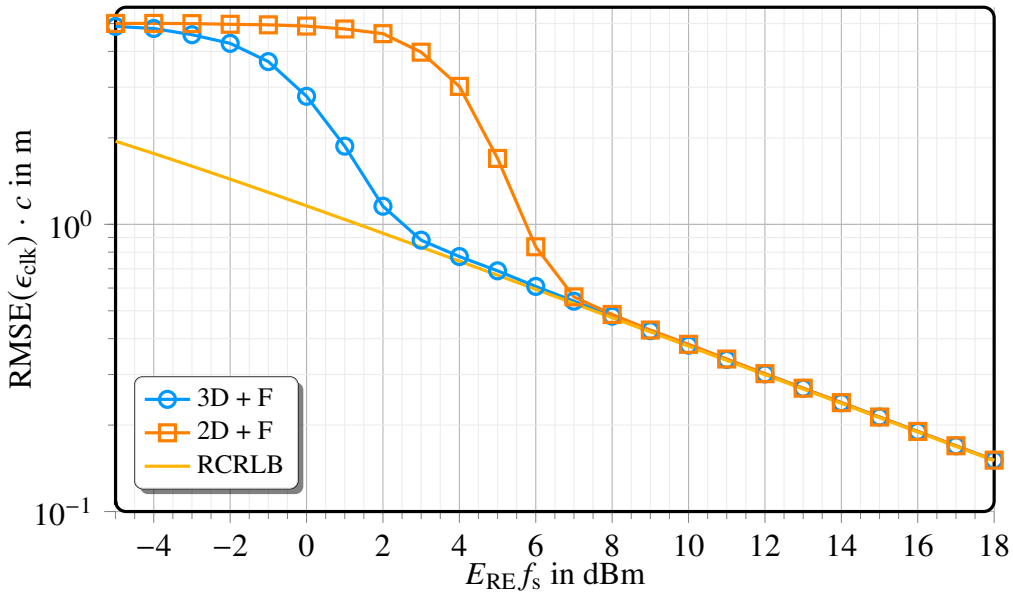

Fig. 3.7. RMSE(ϵ_{clk}) · c of the proposed algorithm with 2D and 3D grid search as a function of E_{RE}.

where a_{th} is the association threshold which we set as $a_{\text{th}} = 5\,\text{m}$. If (3.48) does not hold, we count a missed detection.

We can now go back to the discussion of Fig. 3.2. We can see that for the lower SNR (i.e., E_{RE}) considered in the plot, RMSE($\boldsymbol{p}_{\text{R}}$) is lower bounded by $c\sigma_{\text{clk}} \approx 4.88\,\text{m}$. In particular for "2D + F", there is a wider rage of E_{RE} values for which improvement of the SNR does not result in improvement of the RMSE. This can be understood by examining the estimation performance of the multipath parameters. In Fig. 3.3 we observe that both "3D + F" and "2D + F" attain the CRLB for all considered E_{RE} values, that is, the parameters of the LOS path are estimated accurately. On the other hand, in Fig 3.4 we observe that the RMSE of the parameters of the 1st NLOS path approaches the root CRLB (RCRLB) for $E_{\text{RE}} \geq 4\,\text{dBm}$ with "3D + F" and for $E_{\text{RE}} \geq 9\,\text{dBm}$ with "2D + F". From Figs. 3.5 and 3.6 we can see that, for the other two paths, the estimators converge to the bound for higher E_{RE} values, due to their higher attenuation, which results from their larger propagation distance. Hence, we can conclude that until the parameters of an NLOS path can be reliably estimated, RMSE($\boldsymbol{p}_{\text{R}}$) is driven by $c\sigma_{\text{clk}}$. Due to the synchronization error, the distance component of $\boldsymbol{p}_{\text{R}} - \boldsymbol{p}_{\text{T}}$ cannot be accurately estimated using the TOA of the LOS path. As the detection rate of the 1st NLOS path increases, the performance of the estimators converges to the bound, as the NLOS path allows the estimators to resolve the clock offset and obtain accurate distance information of the Rx.

To better illustrate this, in Fig. 3.7 we plot the RMSE of the estimated clock offset $c\hat{\epsilon}_{\text{clk}}$ as a function of E_{RE}, as well as the corresponding RCRLB. It is evident that the curves are almost identical to those in Fig. 3.2. Therefore, it is verified that the error in the estimation of the clock offset, and, consequently, the error in the distance component of the estimated Rx position is dominating RMSE($\boldsymbol{p}_{\text{R}}$).

Comparing "3D + F" and "2D + F" in all RMSE plots, we can see that the reduction of the 3D grid search to the 2D grid search by non-coherent processing of the observations over different subcarriers results in an increase of approximately 3 dB of the E_{RE} value required for convergence of the estimator to the bound.

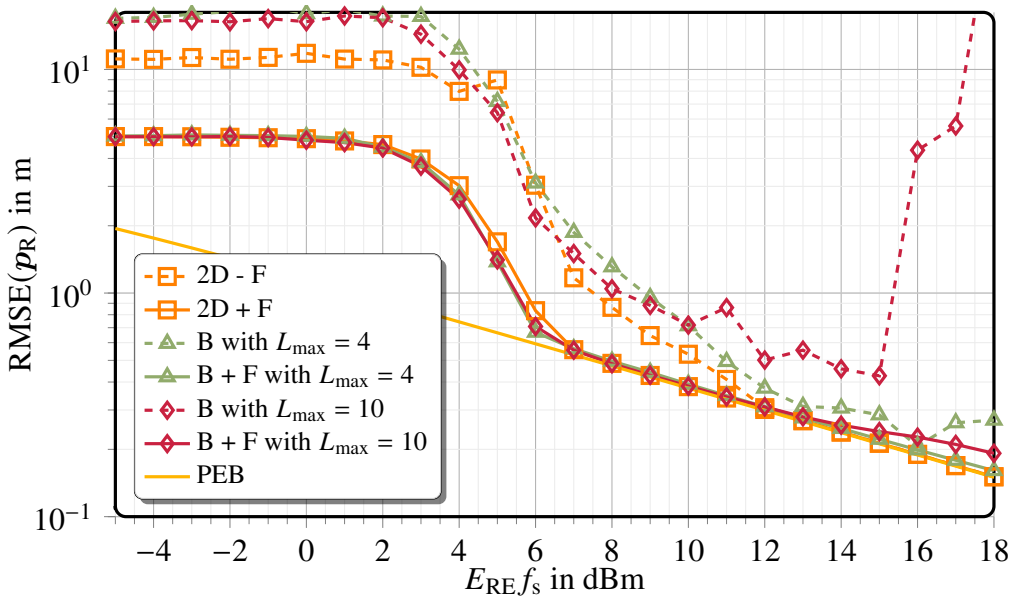

Fig. 3.8. Position RMSE of the proposed algorithm with 2D grid search and SotA approach from [22] with and without path filtering as a function of E_{RE}.

3.3.2 The Effect of Path Filtering and Off-Grid Parameter Estimation

We next study the effect of path filtering and off-grid parameter estimation on the performance of the positioning algorithm. To this end, we consider the SotA approach "B", which employs a 2D grid search and, unlike our work, does not refine the paths' parameters before searching for a new path. In addition, we consider "B + F" to examine the effect of path filtering on the SotA approach. As will become evident in the following, the fact that "B"/"B + F" use on-grid parameter estimation for the discovery of the paths has a negative impact on the model order estimation, as well as on the position estimation. Therefore, we consider different L_{max} values for "B"/"B + F", including the true model order L. For a fair evaluation, we compare the aforementioned methods with our proposed approach using a 2D grid search, with and without path filtering, i.e., "2D + F" and "2D - F".

In Fig. 3.8 we plot RMSE($\boldsymbol{p}_R$) of these methods as a function of E_{RE}. We can observe that "2D + F", "B + F with $L_{max} = 4$" and "B + F with $L_{max} = 10$" achieve the best performance, as their RMSEs approach the bound at the lowest E_{RE} value compared to the others. It should be noted here that "B + F with $L_{max} = 4$" achieves this performance by limiting the maximum number of detected paths to the true model order. We see that "B + F with $L_{max} = 10$" has a slight performance degradation for high SNR. This can be attributed to the false detection of additional paths, caused by the on-grid parameter estimation during the discovery of new paths. In "B"/"B + F", when a new path is detected, only a coarse on-grid estimation of the path's parameters takes place and the contribution of the path to the observations $\boldsymbol{Y}$ is imperfectly removed (in the computation of the residual). Therefore, the remaining contribution of the true path on neighboring bins might be above the detection threshold (which is computed taking only noise into account) and lead to a false detection, especially in the medium to high SNR region. Such false detections that correspond to the LOS path may be rejected by the first condition (3.39) in the subsequent path filtering step. On the contrary, such false detections corresponding to single-bounce NLOS paths are unlikely to be rejected.

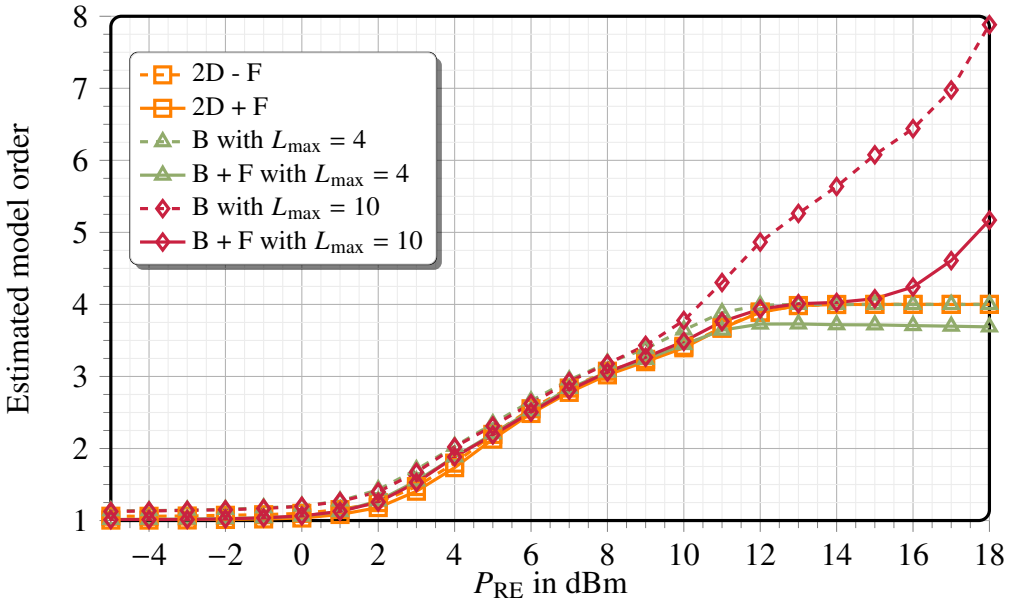

Fig. 3.9. Estimated model order of the proposed algorithm with 2D grid search and SotA approach from [22] with and without path filtering as a function of E_{RE}.

Another source of erroneous paths is noise. When noise is falsely detected as a path of the channel, additional (erroneous) elements are included in $\hat{\tilde{\boldsymbol{\nu}}}$, $f(\boldsymbol{\nu})$ and $\boldsymbol{J}_{\hat{\tilde{\boldsymbol{\nu}}}}$ in (3.38) and this leads to accuracy degradation, as the algorithm tries to match the position of the receiver to these false measurements to minimize the cost function. The number of falsely detected noisy paths is controlled through the probability of false alarm P_{fa}. Lower values of P_{fa} result in less false alarms, but also result in less detections of the true paths.

The approaches that do not employ path filtering exhibit worse performance. "2D - F" converges to the bound 5 dB later than its filtered counterpart "B + F". Owing to off-grid parameter estimation, it avoids the detection of spurious paths and maintains optimal performance for high SNR. The absence of path filtering has a more detrimental effect on the SotA approach "B" in the high SNR region, especially when $L_{\max} = 10$.

To facilitate understanding, in Fig. 3.9 we plot the estimated model order for the different approaches as a function of E_{RE}. We can observe that "B with $L_{\max} = 10$" and "B + F with $L_{\max} = 10$" overestimate the model order as E_{RE} increases, with the path filtering mitigating the issue, but not completely eliminating it. Looking back to Fig. 3.8, these additional erroneous paths have a severe impact on the position estimation performance. The proposed approach accurately estimates the model order at high SNR with or without path filtering.

To sum up, we can make the following observations from Fig. 3.8, which help us understand the importance of off-grid channel parameter estimation and path filtering proposed in our work:

- Considering our proposed approach, we can see that path filtering results in much faster convergence of the position estimation algorithm to the bound. When not filtered, the noisy paths result in additional terms in the optimization objective in (3.38), which drive the solution to erroneous values. Nevertheless, for sufficiently high SNR both alternatives (i.e., with and without filtering of the paths) converge to the PEB.
- Considering the approach in [22], we can see that it can also benefit from path filtering. Additionally, we can observe that even with path filtering, when the true rank of the channel is not

known (as is practically the case) they do not attain the bound for high SNR. This is attributed to the gridded path detection and coarse parameter estimation in the first step (DCS-SOMP) of the algorithm in [22]. Especially in the high SNR region, due to grid mismatch, a real path can lead to the detection of multiple paths. Unlike random noisy paths, which can be successfully rejected by the path filtering step, these spurious paths may not be filtered out, as their parameters may correspond to a single-bounce path. Therefore, off-grid parameter estimation, which avoids this issue, is important for accurate multipath-based parameter estimation.

4. Multi-beam Reference Signal Optimization

In this chapter, we study the optimization of the reference signal with the aim of improving the Rx's position estimation accuracy, when the Tx has perfect or imperfect knowledge of the position parameters. For the reference signal optimization, we assume a narrowband signal model and $\boldsymbol{W}_{\mathrm{T}} = \boldsymbol{I}_{N_{\mathrm{T}}}$ and $\boldsymbol{W}_{\mathrm{R}} = \boldsymbol{I}_{N_{\mathrm{R}}}$, as in Chapter 3, and that, with large bandwidth and number of antennas, the paths are asymptotically orthogonal. We note that the SPEB, which is the square of the PEB (2.48) and will be used in the following for reference signal optimization, is a function of

$$\boldsymbol{\nu}' = [\boldsymbol{p}_{\mathrm{R}}^{\mathrm{T}}, \alpha_{\mathrm{R}}, |h_0|, \boldsymbol{p}_{\mathrm{s},1}^{\mathrm{T}}, |h_1|, \ldots, \boldsymbol{p}_{\mathrm{s},L-1}^{\mathrm{T}}, |h_{L-1}|]^{\mathrm{T}} \in \mathbb{R}^{3L+1}, \tag{4.1}$$

that is, it is independent of the values of $\arg(h_l)$, $l = 1, \ldots, L-1$, (due to the asymptotic orthogonality of the paths) and ϵ_{clk} (it depends only on its variance). Also, due to the inner product of the derivatives in (2.45), we can observe (see (2.18), (2.17) and (2.23)) that $\boldsymbol{J}_{\boldsymbol{\nu}}$ is independent of $\beta_k[p, b]$. In the following, we write $\boldsymbol{J}_{\boldsymbol{\nu}} = \boldsymbol{J}_{\boldsymbol{\nu}}(\boldsymbol{F}, \boldsymbol{q}, \boldsymbol{\nu}')$, with $\boldsymbol{q} = [q_1, \ldots, q_{M_{\mathrm{T}}}] \in \mathbb{R}^{M_{\mathrm{T}}}$, to stress that $\boldsymbol{J}_{\boldsymbol{\nu}}$ is the hybrid FIM of $\boldsymbol{\nu}$, whose value depends on the beam codebook $\boldsymbol{F}$, the energy allocation vector $\boldsymbol{q}$ over the beamforming vectors of the codebook and $\boldsymbol{\nu}'$. Similarly, we write $\mathrm{SPEB} = \mathrm{SPEB}(\boldsymbol{F}, \boldsymbol{q}, \boldsymbol{\nu}')$. Under perfect prior knowledge of $\boldsymbol{\nu}'$, we use the SPEB as the performance metric and under imperfect prior knowledge the expected SPEB (ESPEB), which is defined as

$$\mathrm{ESPEB}(\boldsymbol{F}, \boldsymbol{q}) = \mathbb{E}_{\boldsymbol{\nu}'}[\mathrm{SPEB}(\boldsymbol{F}, \boldsymbol{q}, \boldsymbol{\nu}')]. \tag{4.2}$$

The following proposed methods can be easily adapted for other objectives, such as $\max_{\boldsymbol{\nu}'} \mathrm{SPEB}(\boldsymbol{F}, \boldsymbol{q}, \boldsymbol{\nu}')$.

4.1 Transmit Strategies with Perfect Channel Knowledge

In this section, we study the optimization of the reference signal under the assumption that the Tx has perfect knowledge of the parameter vector $\boldsymbol{\nu}'$. This is an unrealistic assumption that is never true in practice, but can provide useful insights about the form of the optimal solutions in the more practical case of imperfect knowledge of $\boldsymbol{\nu}'$. We first consider the LOS-only channel and then a multipath channel.

4.1.1 Line-of-Sight-Only Channel

We distinguish between the case where the Tx is allowed to optimize both $\boldsymbol{F}$ and $\boldsymbol{q}$, and the case where it uses a fixed set of beamforming vectors $\boldsymbol{F}$, which we refer to as the beam codebook, and optimizes only $\boldsymbol{q}$. In this subsection, we drop the path index in the subscript of involved parameters as there is a single path.

4.1.1.1 Optimal Beamforming Vectors

In this case the optimization problem is

$$\min_{\boldsymbol{F},\boldsymbol{q}} \mathrm{SPEB}(\boldsymbol{F},\boldsymbol{q},d,\tilde{\theta}_\mathrm{T},|h|) \quad \text{s.t. } \boldsymbol{q} \geqslant \boldsymbol{0}, \quad \mathbf{1}^\mathrm{T}\boldsymbol{q} \leq 1, \\ \|\boldsymbol{f}_k\|_2 = 1,\ k = 1,\ldots,M_\mathrm{T}, \tag{4.3}$$

where $\geqslant$ denotes element-wise inequality. We have expressed the SPEB as a function of the channel parameters $d = c\tau$ and $\tilde{\theta}_\mathrm{T}$, instead of the position parameters. We note that the SPEB is independent of α_R in the LOS-only case. We define a couple of quantities that are useful for the presentation of the result: The effective bandwidth β_k of the signal transmitted through the k-th beamforming direction is defined as

$$\beta_k = \sqrt{\sum\nolimits_{p\in\mathcal{P}_k} \gamma_k[p]\omega_p^2 - \Big(\sum\nolimits_{p\in\mathcal{P}_k} \gamma_k[p]\omega_p\Big)^2}, \tag{4.4}$$

where

$$\gamma_k[p] = \sum_b \gamma_k[p,b], \tag{4.5}$$

and the array aperture function $\Xi_\mathrm{T}(\tilde{\theta}_\mathrm{T})$ of the Tx array is defined as the square root of the SAAF (2.76)

$$\Xi_\mathrm{T}(\tilde{\theta}_\mathrm{T}) = \sqrt{S_\mathrm{T}(\tilde{\theta}_\mathrm{T})}. \tag{4.6}$$

Theorem 4.1. The optimal beamforming directions for SPEB minimization are the normalized array steering vector and its normalized derivative w.r.t. to $\tilde{\theta}_\mathrm{T}$:

$$\boldsymbol{f}_{\mathrm{opt},1}(\tilde{\theta}_\mathrm{T}) = \frac{1}{\sqrt{N_\mathrm{T}}}\boldsymbol{a}_\mathrm{T}^*(\tilde{\theta}_\mathrm{T}), \tag{4.7}$$

$$\boldsymbol{f}_{\mathrm{opt},2}(\tilde{\theta}_\mathrm{T}) = \frac{c}{\omega_\mathrm{c}\Xi_\mathrm{T}(\tilde{\theta}_\mathrm{T})\sqrt{N_\mathrm{T}}}\boldsymbol{D}_\mathrm{T}^*(\tilde{\theta}_\mathrm{T})\boldsymbol{a}_\mathrm{T}^*(\tilde{\theta}_\mathrm{T}), \tag{4.8}$$

where $\boldsymbol{D}_\mathrm{T}(\tilde{\theta}_\mathrm{T})$ is a diagonal matrix with $\big[\boldsymbol{D}_\mathrm{T}(\tilde{\theta}_\mathrm{T})\big]_{j,j} = -\mathrm{j}\,\frac{\omega_\mathrm{c}}{c}d_{\mathrm{T},j}\boldsymbol{u}_\perp^\mathrm{T}(\tilde{\theta}_\mathrm{T})\boldsymbol{u}(\psi_{\mathrm{T},j})$, $j = 1,\ldots,N_\mathrm{T}$. The optimal energy allocation is

$$q_1(d,\tilde{\theta}_\mathrm{T}) = \frac{\omega_\mathrm{c}\Xi_\mathrm{T}(\tilde{\theta}_\mathrm{T})}{\beta_1 d + \omega_\mathrm{c}\Xi_\mathrm{T}(\tilde{\theta}_\mathrm{T})}, \tag{4.9}$$

$$q_2(d,\tilde{\theta}_\mathrm{T}) = 1 - q_1(d,\tilde{\theta}_\mathrm{T}), \tag{4.10}$$

and the attained minimum is

$$\mathrm{SPEB}_\mathrm{min}(d,\tilde{\theta}_\mathrm{T},|h|) = \frac{1}{g}\left(\frac{c}{\beta_1} + \frac{cd}{\omega_\mathrm{c}\Xi_\mathrm{T}(\tilde{\theta}_\mathrm{T})}\right)^2, \tag{4.11}$$

where $g = 2N_\mathrm{R}N_\mathrm{T}\Delta f E_\mathrm{tot}|h|^2/\sigma_{\eta,\mathrm{R}}^2$ is the Rx SNR. □

Proof: See Appendix A9. ■

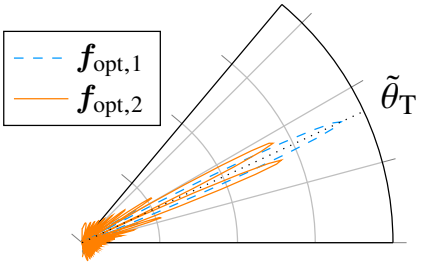

Fig. 4.1. Optimal beamforming directions for a ULA with 32 elements: $|\boldsymbol{a}_{\text{T}}^{\text{T}}(\tilde{\theta}_{\text{T}})\boldsymbol{f}_{\text{opt},k}|$, $k = 1, 2$, as a function of $\tilde{\theta}_{\text{T}}$.

Remark 1. In Fig. 4.1 we plot $|\boldsymbol{a}_{\text{T}}^{\text{T}}(\tilde{\theta}_{\text{T}})\boldsymbol{f}_{\text{opt},k}|$, $k = 1, 2$, as a function of $\tilde{\theta}_{\text{T}}$. As $\boldsymbol{f}_{\text{opt},1}$ is the normalized steering vector, it is no surprise that it forms a beam with $\tilde{\theta}_{\text{T}}$ at its center. More interestingly, $\boldsymbol{f}_{\text{opt},2}(\tilde{\theta}_{\text{T}})$ forms two equally strong lobes surrounding the beam formed by $\boldsymbol{f}_{\text{opt},1}(\tilde{\theta}_{\text{T}})$ and has a null at $\tilde{\theta}_{\text{T}}$. Theorem 4.1 tells us that this pair of beamforming vectors, which is used in monopulse radar for direction tracking [71], is optimal for positioning with a LOS path and provides the optimal energy allocation between them. □

Remark 2. From (4.11) we can observe that SPEB_{min} is a monotonically decreasing function of β_1, which depends on the fractions $\gamma_1[p]$ of q_1 allocated to the subcarriers in $\mathcal{P}_1$, that determine the waveform of the signal transmitted through $\boldsymbol{f}_{\text{opt},1}$. It can be shown that it is optimal to use only the edge subcarriers, i.e., $\mathcal{P}_1 = \{\min_{p\in\mathcal{P}} p,\ \max_{p\in\mathcal{P}} p\}$, with the energy equally shared. However, as discussed in [72], this waveform choice results in higher sidelobes of the autocorrelation function of the signal transmitted through $\boldsymbol{f}_{\text{opt},1}$, which can degrade the delay estimation accuracy at low to medium SNR. Since this topic is outside of the scope of the current work, we assume $\mathcal{P}_k$ and $\gamma_k[p, b]$ to be given. □

As discussed above, the assumption of perfect prior knowledge at the Tx is unrealistic. Nevertheless, the resulting solution can be applied in scenarios where the prior knowledge is sufficiently accurate, i.e., when the uncertainty region about the Rx location, especially in the angular domain, is covered by the derived optimal beamforming vectors.

4.1.1.2 Fixed Beam Codebook

The Tx has to use a predefined beam codebook $\boldsymbol{F}$ and optimize the energy allocation $\boldsymbol{q}$ among the beamfrming vectors, which can lead to the selection of just a subset of them. Using (2.45) and (2.43), we find that $\boldsymbol{J}_{\boldsymbol{\nu}}(\boldsymbol{q}, d, \tilde{\theta}_{\text{T}}, |h|)$ depends linearly on $\boldsymbol{q}$, i.e., $\boldsymbol{J}_{\boldsymbol{\nu}}(\boldsymbol{q}, d, \tilde{\theta}_{\text{T}}, |h|) = \sum_{k=1}^{M_{\text{T}}} q_k \boldsymbol{J}_{\boldsymbol{\nu}}(\boldsymbol{e}_k, d, \tilde{\theta}_{\text{T}}, |h|)$, where $\boldsymbol{e}_k$ is the vector of appropriate size whose k-th entry is equal to 1 and the rest of its entries are 0. Hence, $\boldsymbol{J}_{\boldsymbol{\nu}}(\boldsymbol{q}, d, \tilde{\theta}_{\text{T}}, |h|)$ is a linear transformation of $\boldsymbol{q}$. The optimization problem can be expressed as

$$\text{(G0)}: \min_{\boldsymbol{q}} \text{SPEB}(\boldsymbol{q}, d, \tilde{\theta}_{\text{T}}, |h|) \quad \text{s.t. } \boldsymbol{q} \succcurlyeq \boldsymbol{0},\ \boldsymbol{1}^{\text{T}}\boldsymbol{q} \leq 1. \tag{4.12}$$

(G0) is a convex optimization problem. To see this we write

$$\begin{aligned} \text{SPEB}(\boldsymbol{q}, d, \tilde{\theta}_{\text{T}}, |h|) &= \text{tr}(\boldsymbol{E}^{\text{T}}\boldsymbol{J}_{\boldsymbol{\nu}}^{-1}(\boldsymbol{q}, d, \tilde{\theta}_{\text{T}}, |h|)\boldsymbol{E}) \\ &= \sum_{i=1}^{2} \boldsymbol{e}_i^{\text{T}}\boldsymbol{J}_{\boldsymbol{\nu}}^{-1}(\boldsymbol{q}, d, \tilde{\theta}_{\text{T}}, |h|)\boldsymbol{e}_i, \end{aligned} \tag{4.13}$$

where $\boldsymbol{E} = [\boldsymbol{e}_1, \boldsymbol{e}_2] \in \mathbb{R}^{5\times 2}$. The matrix fractional function $\boldsymbol{e}_i^{\mathrm{T}} \boldsymbol{J}_{\boldsymbol{\nu}}^{-1}(\boldsymbol{q}, d, \tilde{\theta}_{\mathrm{T}}, |h|)\boldsymbol{e}_i$ is a convex function of $\boldsymbol{J}_{\boldsymbol{\nu}}^{-1}(\boldsymbol{q}, d, \tilde{\theta}_{\mathrm{T}}, |h|)$, hence it is also a convex function of $\boldsymbol{q}$ as a composition of a convex and a linear function. Therefore, the SPEB is a convex function of $\boldsymbol{q}$ as a sum of convex functions.

Proposition 1. (G0) is equivalent to the following semidefinite program (SDP):

$$\text{(G1)}: \min_{\boldsymbol{q},\boldsymbol{B}} \operatorname{tr}(\boldsymbol{B}) \ \text{ s.t. } \begin{bmatrix} \boldsymbol{B} & \boldsymbol{E}^{\mathrm{T}} \\ \boldsymbol{E} & \boldsymbol{J}_{\boldsymbol{\nu}}(\boldsymbol{q}, d, \tilde{\theta}_{\mathrm{T}}, |h|) \end{bmatrix} \succeq \boldsymbol{0}, \quad \boldsymbol{q} \geqslant \boldsymbol{0},\ \boldsymbol{1}^{\mathrm{T}}\boldsymbol{q} \leq 1, \tag{4.14}$$

where $\boldsymbol{B} \in \mathbb{R}^{2\times 2}$ and $\operatorname{tr}(\cdot)$ is the trace operator. □

Proof: We write (G0) in its epigraph form:

$$\min_{\boldsymbol{q}} t \quad \text{s.t. } \operatorname{tr}(\boldsymbol{E}^{\mathrm{T}} \boldsymbol{J}_{\boldsymbol{\nu}}^{-1}(\boldsymbol{q}, d, \tilde{\theta}_{\mathrm{T}}, |h|)\boldsymbol{E}) \leq t, \quad \boldsymbol{q} \geqslant \boldsymbol{0},\ \boldsymbol{1}^{\mathrm{T}}\boldsymbol{q} \leq 1. \tag{4.15}$$

We then replace t by the trace of a positive semidefinite matrix $\boldsymbol{B}$:

$$\min_{\boldsymbol{q},\boldsymbol{B}} \operatorname{tr}(\boldsymbol{B}) \quad \text{s.t. } \operatorname{tr}(\boldsymbol{E}^{\mathrm{T}} \boldsymbol{J}_{\boldsymbol{\nu}}^{-1}(\boldsymbol{q}, d, \tilde{\theta}_{\mathrm{T}}, |h|)\boldsymbol{E}) \leq \operatorname{tr}(\boldsymbol{B}), \quad \boldsymbol{q} \geqslant \boldsymbol{0},\ \boldsymbol{1}^{\mathrm{T}}\boldsymbol{q} \leq 1, \quad \boldsymbol{B} \succeq \boldsymbol{0}. \tag{4.16}$$

Problem 4.16, which is identical to (G0), is not identical to (G1), but it is equivalent: Let $(\boldsymbol{q}_0, \boldsymbol{B}_0)$ and $(\boldsymbol{q}_1, \boldsymbol{B}_1)$ be the solutions of 4.16 and (G1). The feasible region of (4.16) is larger than that of (G1), as $\boldsymbol{B} - \boldsymbol{E}^{\mathrm{T}} \boldsymbol{J}_{\boldsymbol{\nu}}^{-1}(\boldsymbol{q}, d, \tilde{\theta}_{\mathrm{T}}, |h|)\boldsymbol{E} \succeq \boldsymbol{0} \Rightarrow \operatorname{tr}(\boldsymbol{B}) \geq \operatorname{tr}(\boldsymbol{E}^{\mathrm{T}} \boldsymbol{J}_{\boldsymbol{\nu}}^{-1}(\boldsymbol{q}, d, \tilde{\theta}_{\mathrm{T}}, |h|)\boldsymbol{E})$, but the reverse direction is not necessarily true. Hence, $\operatorname{tr}(\boldsymbol{B}_0) \leq \operatorname{tr}(\boldsymbol{B}_1)$. The first constraint of (4.16) is necessarily active at the optimum, i.e., $\operatorname{tr}(\boldsymbol{E}^{\mathrm{T}} \boldsymbol{J}_{\boldsymbol{\nu}}^{-1}(\boldsymbol{q}_0, d, \tilde{\theta}_{\mathrm{T}}, |h|)\boldsymbol{E}) = \operatorname{tr}(\boldsymbol{B}_0)$. To see this, let us assume that $\operatorname{tr}(\boldsymbol{E}^{\mathrm{T}} \boldsymbol{J}_{\boldsymbol{\nu}}^{-1}(\boldsymbol{q}_0, d, \tilde{\theta}_{\mathrm{T}}, |h|)\boldsymbol{E}) < \operatorname{tr}(\boldsymbol{B}_0)$. Then, there is another feasible solution $(\boldsymbol{q}_0, \boldsymbol{B}_0')$ with $\operatorname{tr}(\boldsymbol{B}_0') < \operatorname{tr}(\boldsymbol{B}_0)$, e.g., $\boldsymbol{B}_0' = a\boldsymbol{B}_0$, where $a = \operatorname{tr}(\boldsymbol{E}^{\mathrm{T}} \boldsymbol{J}_{\boldsymbol{\nu}}^{-1}(\boldsymbol{q}_0, d, \tilde{\theta}_{\mathrm{T}}, |h|)\boldsymbol{E})/\operatorname{tr}(\boldsymbol{B}_0)$. Furthermore, $(\boldsymbol{q}_0, \boldsymbol{E}^{\mathrm{T}} \boldsymbol{J}_{\boldsymbol{\nu}}^{-1}(\boldsymbol{q}_0, d, \tilde{\theta}_{\mathrm{T}}, |h|)\boldsymbol{E})$ belongs to the feasible set of (G1). Therefore, we have $\operatorname{tr}(\boldsymbol{B}_1) \leq \operatorname{tr}(\boldsymbol{E}^{\mathrm{T}} \boldsymbol{J}_{\boldsymbol{\nu}}^{-1}(\boldsymbol{q}_0, d, \tilde{\theta}_{\mathrm{T}}, |h|) = \operatorname{tr}(\boldsymbol{B}_0)$. We can then conclude that $\operatorname{tr}(\boldsymbol{B}_0) = \operatorname{tr}(\boldsymbol{B}_1)$ and the two problems are equivalent. ■

The formulation (G1) is important as it allows us to find the optimal energy allocation in a computationally efficient way. The solution of (G0)/(G1) gives the optimal energy allocation $\boldsymbol{q}$ over the beam codebook, while for the reasons explained in Remark 1 of Theorem 4.1, we assume that $\mathcal{P}_k$ and $\gamma_k[p, b]$ are given.

4.1.2 Multipath Channel

For the case of a multipath channel, a reasonable conjecture, based on the result about the optimal beamforming vectors for the LOS-only case, would be that the array steering vector and its derivative, evaluated at the AOD of the path, should be used for each of the paths in the channel. In fact, work published after our relevant work for the LOS-case [73], proved that this is indeed the case [74]. Therefore, hereafter, we consider only the case of a fixed beam codebook.

The optimization problem to be solved in order to obtain the optimal energy allocation is almost identical to (G1), with $\boldsymbol{J}_{\boldsymbol{\nu}}(\boldsymbol{q}, d, \tilde{\theta}_{\mathrm{T}}, |h|)$ being replaced by $\boldsymbol{J}_{\boldsymbol{\nu}}(\boldsymbol{q}, \boldsymbol{\nu}')$.

4.2 Energy Allocation for a Fixed Beam Codebook with Imperfect Channel Knowledge

Under imperfect prior knowledge, we restrict the reference signal optimization to the optimization of the energy allocation over the beamforming vectors of a fixed beam codebook. We note that, after the publication of this work [75], the optimization of the reference signal, including codebook optimization, was studied in [74].

The optimization problem in hand reads as:

$$\min_{\boldsymbol{q}} \mathbb{E}_{\boldsymbol{\nu}'}[\mathrm{SPEB}(\boldsymbol{q},\boldsymbol{\nu}')] \;\; \text{s.t. } \boldsymbol{q} \succcurlyeq \mathbf{0},\; \mathbf{1}^{\mathrm{T}}\boldsymbol{q} \leq 1, \tag{4.17}$$

where $\succcurlyeq$ denotes element-wise inequality. In order to solve (4.17), one can employ a cubature rule [76], [77] with positive weights to approximate the expectation integral with a sum:

$$\mathbb{E}_{\boldsymbol{\nu}'}[\mathrm{SPEB}(\boldsymbol{q},\boldsymbol{\nu}')] \approx \sum\nolimits_{j=1}^{N'_{\nu}} p_j \mathrm{SPEB}(\boldsymbol{q},\boldsymbol{\nu}'_j), \tag{4.18}$$

where $\boldsymbol{\nu}'_j$ and $p_j > 0,\;\; j = 1,\ldots,N_{\boldsymbol{\nu}'}$ are the cubature points and their corresponding weights, with $N_{\boldsymbol{\nu}'}$ being the number of cubature points. $N_{\boldsymbol{\nu}'}$ is determined by the dimension of $\boldsymbol{\nu}'$ and the degree r of the cubature[1]. The cubature points and their weights are determined by the pdf of $\boldsymbol{\nu}'$ and r. Then, (4.17) becomes

$$\min_{\boldsymbol{q}} \sum\nolimits_{j=1}^{N_{\boldsymbol{\nu}'}} p_j \mathrm{SPEB}(\boldsymbol{q},\boldsymbol{\nu}'_j) \;\; \text{s.t. } \boldsymbol{q} \succcurlyeq \mathbf{0},\; \mathbf{1}^{\mathrm{T}}\boldsymbol{q} \leq 1. \tag{4.19}$$

4.2.1 Optimal Solution

In a similar fashion to (G0), using the epigraph form of (4.19), we can show that it is equivalent to the following SDP:

$$\begin{aligned} \min_{\boldsymbol{q},\boldsymbol{B}_1,\ldots,\boldsymbol{B}_{N_{\boldsymbol{\nu}'}}} \sum\nolimits_{j=1}^{N_{\boldsymbol{\nu}'}} p_j \,\mathrm{tr}(\boldsymbol{B}_j) \quad \text{s.t.} \begin{bmatrix} \boldsymbol{B}_j & \boldsymbol{E}^{\mathrm{T}} \\ \boldsymbol{E} & \boldsymbol{J}_{\boldsymbol{\nu}}(\boldsymbol{q},\boldsymbol{\nu}'_j) \end{bmatrix} \succeq \mathbf{0},\; j = 1,\ldots,N_{\boldsymbol{\nu}'} \\ \boldsymbol{q} \succcurlyeq \mathbf{0},\; \mathbf{1}^{\mathrm{T}}\boldsymbol{q} \leq 1, \end{aligned} \tag{4.20}$$

where $\boldsymbol{B}_j \in \mathbb{R}^{2\times 2},\;\; j = 1,\ldots,N_{\boldsymbol{\nu}}$ are auxiliary variables of the SDP and $\succeq$ denotes positive semidefiniteness. The positivity requirement on the cubature weights is imposed to ensure convexity of the objective in (4.20). In the numerical results (Sec. 4.3), we refer to the solution of (4.20) as "opt. unconstr.", indicating that it corresponds to the optimal solution without any further constraints.

The optimal vector $\boldsymbol{q}$ obtained with (4.20) may indicate that very low energy should be allocated in the direction of the LOS path, which may lead to a missed detection of the LOS path at the Rx. This can be avoided by ensuring that the excitation of directions around the LOS path is at least a fraction q_{th} of the excitation in any other direction. To this end, for a given confidence level κ, we define $\tilde{\theta}^{(\kappa)}_{\mathrm{T},l,\min}$ and $\tilde{\theta}^{(\kappa)}_{\mathrm{T},l,\max}$ as the minimum and maximum AODs corresponding to the 2D Rx locations ($l = 0$) or scatterer/reflector locations ($l = 1,\ldots,L-1$) in the κ-confidence ellipse of the respective marginal. With a uniform grid of N_θ possible AODs $\tilde{\theta}_{\mathrm{T},l,m}$ within the interval $[\tilde{\theta}^{(\kappa)}_{\mathrm{T},l,\min}, \tilde{\theta}^{(\kappa)}_{\mathrm{T},l,\max}]$

$$\tilde{\theta}^{(\kappa)}_{\mathrm{T},l,m} = \tilde{\theta}^{(\kappa)}_{\mathrm{T},l,\min} + \frac{m-1}{N_\theta - 1}(\tilde{\theta}^{(\kappa)}_{\mathrm{T},l,\max} - \tilde{\theta}^{(\kappa)}_{\mathrm{T},l,\min}),\; m = 1,\ldots,N_\theta, \tag{4.21}$$

[1] A cubature rule has degree r if it is exact for a (multivariate) polynomial of degree r.

we define the excitation matrix $\boldsymbol{A}_l \in \mathbb{R}^{N_\theta \times M_\mathrm{T}}$ for the l-th path as

$$[\boldsymbol{A}_l]_{m,k} = |\boldsymbol{a}_\mathrm{T}^\mathrm{T}(\tilde{\theta}_{\mathrm{T},l,m}^{(\kappa)})\boldsymbol{f}_k|^2. \tag{4.22}$$

Finally, the vector with the excitation of the possible AODs associated with the l-th path is $\boldsymbol{A}_l\boldsymbol{q}$. We augment (4.20) with the following linear constraints:

$$\boldsymbol{A}_0\boldsymbol{q} \succcurlyeq q_\mathrm{th}\|\boldsymbol{A}\boldsymbol{q}\|_\infty \mathbf{1}_{N_\theta}, \tag{4.23}$$

where $\boldsymbol{A} = [\boldsymbol{A}_0^\mathrm{T}, \ldots, \boldsymbol{A}_{L-1}^\mathrm{T}]^\mathrm{T}$. We note that the constraints (4.23) can be equivalently expressed as

$$\boldsymbol{A}_0\boldsymbol{q} \succcurlyeq q_\mathrm{th} e_\mathrm{max}\mathbf{1}_{N_\theta}, \quad \boldsymbol{A}\boldsymbol{q} \preccurlyeq e_\mathrm{max}\mathbf{1}_{LN_\theta}, \tag{4.24}$$

with e_max being an auxiliary optimization variable. In the numerical results (Sec. 4.3), we refer to the solution of (4.20) with the additional constraints (4.23) as "opt. constr.".

The main challenge with the approach described above is that $p_{\boldsymbol{\nu}}$ is a multidimensional pdf. The number of auxiliary matrices $\boldsymbol{B}_j$ and corresponding positive semidefiniteness (PSD) constraints in (4.20) is equal to the number of cubature points. For known cubature rules [76], the number of points is lower bounded by $(3L+1)^{(r-1)/2}$, which could result in very high complexity for our optimization task, as the integrand is highly non-linear and a rule with $r \geq 5$ (as observed from numerical results) is required for an accurate approximation.

4.2.2 Low-complexity Sub-optimal Solution

4.2.2.1 Dimensionality Reduction

A way to circumvent the dimensionality challenge is to use a surrogate function which involves the expectation over a smaller set of parameters. To this end, we first note that $\boldsymbol{e}_i^\mathrm{T}\boldsymbol{J}_{\boldsymbol{\nu}}^{-1}\boldsymbol{e}_i,\ i = 1, 2$, is a convex function of $\boldsymbol{J}_{\boldsymbol{\nu}}$ and so is the SPEB as a sum of convex functions. Splitting $\boldsymbol{\nu}'$ into any couple of vectors $\boldsymbol{\nu}_1$ and $\boldsymbol{\nu}_2$, we can write

$$\begin{aligned}\mathbb{E}_{\boldsymbol{\nu}'}[\mathrm{SPEB}(\boldsymbol{q},\boldsymbol{\nu}')] &= \mathbb{E}_{\boldsymbol{\nu}'}\big[\mathrm{tr}(\boldsymbol{E}^\mathrm{T}\boldsymbol{J}_{\boldsymbol{\nu}}^{-1}(\boldsymbol{q},\boldsymbol{\nu}')\boldsymbol{E})\big] = \mathbb{E}_{\boldsymbol{\nu}_1}\Big[\mathbb{E}_{\boldsymbol{\nu}_2|\boldsymbol{\nu}_1}\big[\mathrm{tr}(\boldsymbol{E}^\mathrm{T}\boldsymbol{J}_{\boldsymbol{\nu}}^{-1}(\boldsymbol{q},\boldsymbol{\nu}_1,\boldsymbol{\nu}_2)\boldsymbol{E})\big]\Big] \\ &\overset{(a)}{\geq} \mathbb{E}_{\boldsymbol{\nu}_1}\big[\mathrm{tr}(\boldsymbol{E}^\mathrm{T}(\mathbb{E}_{\boldsymbol{\nu}_2|\boldsymbol{\nu}_1}[\boldsymbol{J}_{\boldsymbol{\nu}}(\boldsymbol{q},\boldsymbol{\nu}_1,\boldsymbol{\nu}_2)])^{-1}\boldsymbol{E})\big],\end{aligned} \tag{4.25}$$

where (a) follows from Jensen's inequality. We choose $\boldsymbol{\nu}_1 = [\boldsymbol{p}_\mathrm{R}^\mathrm{T}, \boldsymbol{p}_{\mathrm{s},1}^\mathrm{T}, \ldots, \boldsymbol{p}_{\mathrm{s},L-1}^\mathrm{T}]^\mathrm{T}$ and $\boldsymbol{\nu}_2 = [\alpha_\mathrm{R}, |h_0|, \ldots, |h_{L-1}|]^\mathrm{T}$, as the position parameters are the ones determining the AODs, which in turn determine which beamforming vectors are relevant or not. One could optimize the lower bound on the ESPEB in (4.25)

$$\begin{aligned}\min_{\boldsymbol{q},\boldsymbol{B}_1,\ldots,\boldsymbol{B}_{N_{\boldsymbol{\nu}_1}}} \sum_{j=1}^{N_{\boldsymbol{\nu}_1}} p_j\,\mathrm{tr}(\boldsymbol{B}_j) \quad \text{s.t.} \begin{bmatrix}\boldsymbol{B}_j & \boldsymbol{E}^\mathrm{T} \\ \boldsymbol{E} & \mathbb{E}_{\boldsymbol{\nu}_2|\boldsymbol{\nu}_{1,j}}[\boldsymbol{J}_{\boldsymbol{\nu}}(\boldsymbol{q},\boldsymbol{\nu}_{1,j},\boldsymbol{\nu}_2)]\end{bmatrix} \succcurlyeq \mathbf{0},\ j = 1,\ldots,N_{\boldsymbol{\nu}_1} \\ \boldsymbol{q} \succcurlyeq \mathbf{0},\ \mathbf{1}^\mathrm{T}\boldsymbol{q} \leq 1, \\ \boldsymbol{A}_0\boldsymbol{q} \succcurlyeq q_\mathrm{th}\|\boldsymbol{A}\boldsymbol{q}\|_\infty \mathbf{1}_{N_\theta}.\end{aligned} \tag{4.26}$$

In the numerical results (Sec. 4.3), we refer to the solution of (4.26) with the additional constraints (4.23) as "opt. reduced". We note that the number of cubature points $N_{\boldsymbol{\nu}_1'}$ is still lower bounded by $(2L)^{(r-1)/2}$.

4.2.2.2 Energy allocation as a Weighted Sum of Per-Path Energy Allocation Vectors

Our aim is to reduce the complexity of the optimization problem in hand. We accomplish this by taking the following heuristic approach: we compute a energy allocation vector $\boldsymbol{q}_l,\ l = 0, \ldots, L-1$, considering the uncertainty regarding each path separately and then weight the resulting energy allocation vectors in order to minimize a lower bound on the ESPEB.

More specifically, for the energy allocation vector $\boldsymbol{q}_0$ we consider only the LOS path and neglect the NLOS paths and solve

$$\begin{aligned}\boldsymbol{q}_0 = \underset{\boldsymbol{q}}{\operatorname{argmin}}\ & \mathbb{E}_{\boldsymbol{p}_\mathrm{R}}\big[\operatorname{tr}(\boldsymbol{E}^\mathrm{T}(\mathbb{E}_{|h_0|,\alpha_\mathrm{R}|\boldsymbol{p}_\mathrm{R}}[\boldsymbol{J}_{\boldsymbol{\nu}_\mathrm{LOS}}(\boldsymbol{q},\boldsymbol{p}_\mathrm{R},\alpha_\mathrm{R},|h_0|)])^{-1}\boldsymbol{E})\big] \\ & \text{s.t. } \boldsymbol{A}_0\boldsymbol{q} \succcurlyeq q_{\mathrm{th,LOS}}\|\boldsymbol{A}_0\boldsymbol{q}\|_\infty \mathbf{1}_{N_\theta}, \\ & \quad \boldsymbol{q} \succcurlyeq \mathbf{0},\ \mathbf{1}^\mathrm{T}\boldsymbol{q} \le 1,\end{aligned} \tag{4.27}$$

where $\boldsymbol{J}_{\boldsymbol{\nu}_\mathrm{LOS}}$ represents the FIM for the parameter vector $\boldsymbol{\nu}_\mathrm{LOS} = [\boldsymbol{p}_\mathrm{R}^\mathrm{T}, \alpha_\mathrm{R}, \epsilon_\mathrm{clk}, \boldsymbol{h}_0^\mathrm{T}]^\mathrm{T}$. Similarly to (4.23), the first constraint in (4.27) limits the ratio of energy spent among possible LOS directions, with $q_\mathrm{th,LOS}$ being the corresponding minimum ratio. For the gain of the LOS path it is natural that $p(\boldsymbol{h}_0|\boldsymbol{p}_\mathrm{R}) = p(\boldsymbol{h}_0|d_0)$, with $d_0 = \|\boldsymbol{p}_\mathrm{R}\|_2$, i.e., the distribution of the gain depends only on the Tx-Rx distance, and the integration over the radial component d_0 and the angular component $\tilde{\theta}_{\mathrm{T},0}$ of $\boldsymbol{p}_\mathrm{R}$ can be carried out separately. Then, as shown in Appendix A10, we can reformulate (4.27) as an SDP using a 1D quadrature rule for the approximation of the expectation integral over $\tilde{\theta}_{\mathrm{T},0}$:

$$\begin{aligned}\min_{\boldsymbol{q},\boldsymbol{B}_1,\ldots,\boldsymbol{B}_{N_{\theta_{\mathrm{T},0}}}}\ & \sum\nolimits_{j=1}^{N_{\theta_{\mathrm{T},0}}} p_j \operatorname{tr}(\boldsymbol{B}_j) \\ & \text{s.t. } \boldsymbol{A}_0\boldsymbol{q} \succcurlyeq q_{\mathrm{th,LOS}}\|\boldsymbol{A}_0\boldsymbol{q}\|_\infty \mathbf{1}_{N_\theta}, \\ & \quad \boldsymbol{q} \succcurlyeq \mathbf{0},\ \mathbf{1}^\mathrm{T}\boldsymbol{q} \le 1, \\ & \quad \begin{bmatrix} \boldsymbol{B}_j & \boldsymbol{E}^\mathrm{T} \\ \boldsymbol{E} & \boldsymbol{J}_{\boldsymbol{\nu}_\mathrm{LOS}}(\boldsymbol{q}, \bar{d}_0(\tilde{\theta}_{\mathrm{T},0,j}), \tilde{\theta}_{\mathrm{T},0,j}, \breve{\alpha}_\mathrm{R}, \sqrt{\bar{g}_0(\tilde{\theta}_{\mathrm{T},0,j})}\,\mathrm{e}^{\mathrm{j}\beta_g}) \end{bmatrix} \succcurlyeq \mathbf{0},\ j = 1, \ldots, N_{\theta_{\mathrm{T},0}},\end{aligned} \tag{4.28}$$

where the definitions of $\bar{d}_0(\tilde{\theta}_{\mathrm{T},0})$, $\breve{\alpha}_\mathrm{R}$, $\bar{g}_0(\tilde{\theta}_{\mathrm{T},0,j})$ and β_g are provided in Appendix A10.

For the energy allocation vector $\boldsymbol{q}_l$ we consider only the l-th NLOS path and assume that the Rx position and orientation are known and equal to their mean values $\bar{\boldsymbol{p}}_\mathrm{R}$ and $\bar{\alpha}_\mathrm{R}$. This is basically a bistatic radar setup, where the goal is the estimation of the point of incidence. Therefore, we obtain $\boldsymbol{q}_l$ by solving

$$\boldsymbol{q}_l = \underset{\boldsymbol{q}}{\operatorname{argmin}}\ \mathbb{E}_{\boldsymbol{p}_{\mathrm{s},l}}\big[\operatorname{tr}(\boldsymbol{E}^\mathrm{T}(\mathbb{E}_{|h_l||\boldsymbol{p}_{\mathrm{s},l}}[\boldsymbol{J}_{\mathrm{NLOS},l}(\boldsymbol{q},\boldsymbol{p}_{\mathrm{s},l},|h_l|)])^{-1}\boldsymbol{E})\big] \quad \text{s.t. } \boldsymbol{q} \succcurlyeq \mathbf{0},\ \mathbf{1}^\mathrm{T}\boldsymbol{q} \le 1, \tag{4.29}$$

where $\boldsymbol{J}_{\mathrm{NLOS},l}$ represent the FIM for the parameter vector $\boldsymbol{\nu}_{\mathrm{NLOS},l} = [\boldsymbol{p}_{\mathrm{s},l}^\mathrm{T}, \epsilon_\mathrm{clk}, \boldsymbol{h}_l^\mathrm{T}]^\mathrm{T}$. Problem (4.29) can be solved employing a 2D cubature on $\boldsymbol{p}_{\mathrm{s},l}$.

Finally, we compute the optimal weights $\boldsymbol{w} \in \mathbb{R}^L$ of $\boldsymbol{q}_l, l = 0, \ldots, L-1$, by minimizing an approximate lower bound on the ESPEB, obtained similarly to (4.25):

$$\begin{aligned}\boldsymbol{w} = \underset{\boldsymbol{w}'}{\operatorname{argmin}}\ & \mathbb{E}_{\boldsymbol{p}_\mathrm{R}}[\operatorname{tr}(\boldsymbol{E}^\mathrm{T}\boldsymbol{J}_{\boldsymbol{\nu}}^{-1}(\boldsymbol{Q}\boldsymbol{w}', \bar{\boldsymbol{\nu}})\boldsymbol{E})] \quad \text{s.t. } \boldsymbol{A}_0\boldsymbol{Q}\boldsymbol{w}' \succcurlyeq q_\mathrm{th}\|\boldsymbol{A}\boldsymbol{Q}\boldsymbol{w}'\|_\infty \mathbf{1}_{N_\theta} \\ & \qquad\qquad \boldsymbol{Q}\boldsymbol{w}' \succcurlyeq \mathbf{0},\ \mathbf{1}^\mathrm{T}\boldsymbol{Q}\boldsymbol{w}' \le 1,\end{aligned} \tag{4.30}$$

where, in order to further reduce the computational load, we have replaced $\mathbb{E}_{\boldsymbol{\nu}|\boldsymbol{p}_\mathrm{R}}[\boldsymbol{J}_{\boldsymbol{\nu}}(\boldsymbol{Q}\boldsymbol{w}', \boldsymbol{\nu})]$ with its approximation $\boldsymbol{J}_{\boldsymbol{\nu}}(\boldsymbol{Q}\boldsymbol{w}', \bar{\boldsymbol{\nu}})$, with $\bar{\boldsymbol{\nu}} = \mathbb{E}_{\boldsymbol{\nu}|\boldsymbol{p}_\mathrm{R}}[\boldsymbol{\nu}]$ and $\boldsymbol{Q} = [\boldsymbol{q}_0, \ldots, \boldsymbol{q}_{L-1}]$. Finally, the energy allocation vector is $\boldsymbol{q} = \boldsymbol{Q}\boldsymbol{w}$.

4.3 Numerical Results

4.3.1 System Parameters

As in Chapters 2 and 3, for the waveform we set $f_\mathrm{s} = 122.88\,\mathrm{MHz}$, $f_\mathrm{c} = 38\,\mathrm{GHz}$, $N = 64$, $N_\mathrm{B} = 10$, $\mathcal{P} = \{-31, \ldots, -1, 1 \ldots, 31\}$ and $\Delta f(\max(\mathcal{P}) - \min(\mathcal{P})) \approx 120\,\mathrm{MHz}$. The noise spectral density is $N_0 = -174\,\mathrm{dBm\,Hz^{-1}}$ and the Rx noise figure is $\mathrm{NF} = 13\,\mathrm{dB}$. The average transmit energy per resource element is set such that $E_\mathrm{RE} f_\mathrm{s} = 10\,\mathrm{dBm}$, unless otherwise specified.

The Tx is equipped with a ULA with $N_\mathrm{T} = 32$ antennas. In order to be able to discriminate all possible AOAs, the Rx has a UCA with $N_\mathrm{R} = 16$ antennas. With the Rx being equipped with a UCA, the SPEB is independent of the orientation α_R. Hence, α_R will not be considered in the optimization of the energy allocation strategies in the following numerical results.

As discussed in Remark 1 of Theorem 4.1, the optimization of the resources $\mathcal{R}_k$ assigned to each beamforming vector is out of the scope of this work and is assumed to be given. The energy of each beamforming vector is distributed uniformly among its resources, i.e., $\gamma_k[p, b] = 1/|\mathcal{R}_k|$ and the resources are assigned to the beamforming vectors in an interleaved and staggered manner, i.e., $\mathcal{R}_k = \{(k + b + iM_\mathrm{T}, b) | i \in \mathbb{Z}, b = 1, \ldots, N_\mathrm{B} : k + b + iM_\mathrm{T} \in \mathcal{P}\}$. This choice is made with the following aspects in mind:

- All beamforming vectors have approximately the same effective bandwidth β_k.
- Robust TOA estimation performance is ensured for all SNR values. Alternatively, one could consider allocations $\gamma_k[p, b]$, where all energy would be allocated to the edge resources of $\mathcal{R}_k$, as dictated by the CRLB. But, this would lead to poor TOA estimation at medium SNR values.
- Given the two aforementioned aspects, we would like to have as large effective bandwidth β_k as possible. Alternatively, one could consider contiguous subcarrier allocations to the beamforming vectors, but this could lead to lower β_k.

After the optimization of $\boldsymbol{q}$, very low or even no energy may be allocated to some of the beamforming vectors. In order to avoid leaving empty resources, for the position estimation algorithm, we reallocate the resources among the activated beamforming vectors in the same manner as described above. The impact of this reallocation on the resulting effective bandwidths and, consequently, the PEB is negligible.

We use the DFT codebook

$$\boldsymbol{f}_k = \left[1, \mathrm{e}^{\mathrm{j}\frac{2\pi}{N_\mathrm{T}}(k-1)}, \ldots, \mathrm{e}^{\mathrm{j}\frac{2\pi}{N_\mathrm{T}}(N_\mathrm{T}-1)(k-1)}\right], \; k = 1, \ldots, M_\mathrm{T} = N_\mathrm{T}, \tag{4.31}$$

but note that other codebooks could also be considered, like the one in [73]. There, motivated by Theorem 4.1 and observing that, for a ULA, the k-th beamforming vector of the DFT codebook is collinear with $\boldsymbol{a}_\mathrm{T}^*(\theta_k)$, where $\sin(\theta_k) = (k-1)/N_\mathrm{T}$, the DFT codebook is augmented with the unit-norm beamforming vectors that are collinear with the derivative of the steering vector $\boldsymbol{D}_\mathrm{T}^*(\theta_k)\boldsymbol{a}_\mathrm{T}^*(\theta_k)$, $k = 1, \ldots, N_\mathrm{T}$. Such a codebook was shown in [73] to offer an improved positioning performance in terms of the PEB. Nevertheless, numerical evaluations not included in thesis have shown that, when used with optimized energy allocation, it may result in an autocorrelation function in the AOD domain with high sidelobes. This, in turn, may impose great challenges on the position estimation algorithm and it may lead to erroneous AOD estimation and, consequently, poor positioning accuracy, even for high SNR, with this effect not being captured by the PEB. Therefore, in the following results, we stick to the DFT codebook.

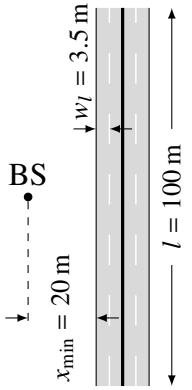

Fig. 4.2. V2X scenario for beam energy allocation.

4.3.2 Line-of-sight (LOS)-only Channel

We first deal with the simpler case of the LOS-only channel and consider the following setup, which is depicted in Fig. 4.2. An BS serves vehicles in a $l = 100\,\mathrm{m}$ long road segment with 4 lanes, which have a width of $w_l = 3.5\,\mathrm{m}$. The BS is located midway of the segment, $x_{\min} = 20\,\mathrm{m}$ away from its left edge. The vehicles are uniformly distributed on the road, resulting in a p_{D,Θ_T} with bounded support. The resulting maximum and minimum AOD are $\tilde{\theta}_{\mathrm{T,max}} = -\tilde{\theta}_{\mathrm{T,max}} = 69.2°$. We use a deterministic relation between the amplitude of the channel gain and the distance, using the free space path loss model $|h|c/(4\pi f_\mathrm{c} d)$ and discretize p_{Θ_T} using a trapezoidal rule with $N_\theta = 127$. We assume perfect synchronization between the Tx and Rx, i.e., $\sigma_\mathrm{clk} = 0$, so as to be able to examine the performance differences between the energy allocation strategies, as in this case, in the absence of NLOS components, the clock offset cannot be estimated and it would dominate the estimation error.

For the energy allocation strategies, since only the LOS path is available, we consider the solution of (4.19), which can be solved as (4.28) (without the constraint on the ratio of energy spent among possible LOS directions), and refer to it in this section as "minexp". In addition, with the prior distribution having a bounded support, it is also reasonable to consider a different objective, where instead of the expected SPEB, the maximum SPEB is minimized. We refer to this solution as "minmax". Apart from "minexp" and "minmax", we also consider a heuristic scheme as a baseline ("uni"), where the available energy is uniformly allocated to the subset $\mathcal{B}_\mathrm{uni}$ of the DFT beamforming vectors maximizing the projection to $\boldsymbol{f}_{\mathrm{opt},1}$:

$$\mathcal{B}_\mathrm{uni} = \cup_{l=1}^{N_\theta} \left\{ \underset{k=1,\ldots,N_\mathrm{T}}{\mathrm{argmax}} \, |\boldsymbol{f}_{\mathrm{opt},1}^\mathrm{T}(\tilde{\theta}_{\mathrm{T},l})\boldsymbol{f}_k| \right\}. \tag{4.32}$$

We note that we do not consider the optimal beamforming directions (4.7)-(4.8), as it would be meaningless for the wide range of angles involved. The resulting radiation patterns of the different energy allocation strategies are depicted in Fig. 4.3, along with their corresponding PEB over the considered road segment. We can see that for both optimization strategies, and especially for minmax, the edge beamforming vectors get most of the available energy. This is explained as follows: first, the locations illuminated by the edge beamforming vectors have the largest distance from the Tx, hence more transmit energy is required to combat the higher path loss. Furthermore, for a ULA, as the angle to be estimated moves away from the array's boresight, the accuracy of the estimation decreases. Therefore, more energy is required to counter the AOD estimation accuracy loss at these locations.

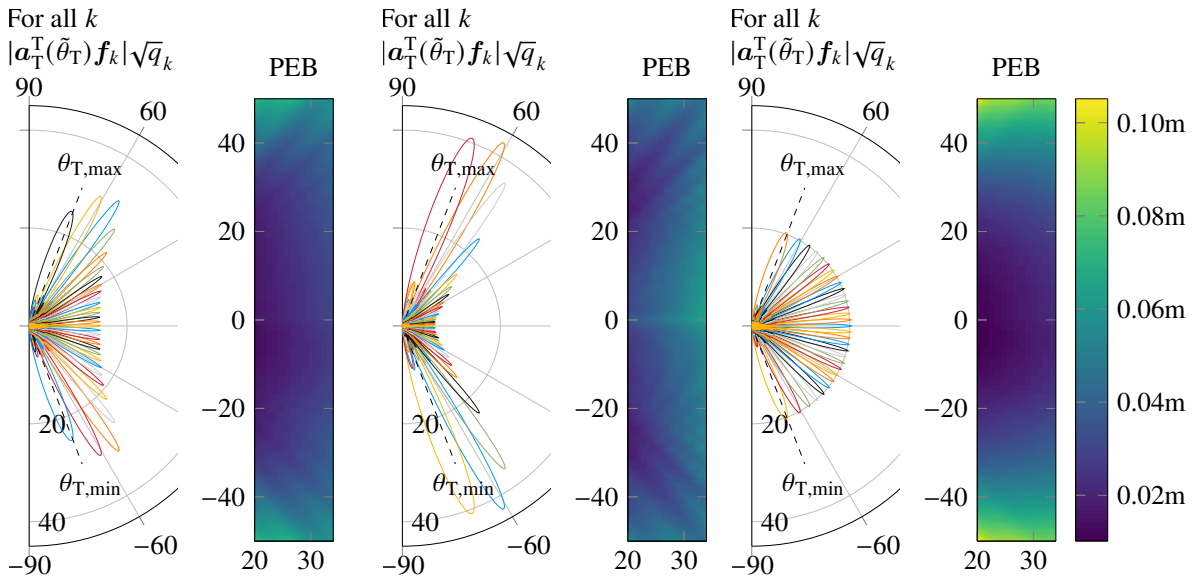

(a) minexp:
$\mathbb{E}[\mathrm{PEB}] = 0.03\,\mathrm{m}$
$\max \mathrm{PEB} = 0.08\,\mathrm{m}$

(b) minmax:
$\mathbb{E}[\mathrm{PEB}] = 0.04\,\mathrm{m}$
$\max \mathrm{PEB} = 0.07\,\mathrm{m}$

(c) uni:
$\mathbb{E}[\mathrm{PEB}] = 0.04\,\mathrm{m}$
$\max \mathrm{PEB} = 0.11\,\mathrm{m}$

Fig. 4.3. Beam patterns $|\boldsymbol{a}_{\mathrm{T}}^{\mathrm{T}}(\tilde{\theta}_{\mathrm{T}})\boldsymbol{f}_k\sqrt{q_k}|, k = 1, \ldots, M_{\mathrm{T}}$, of energy allocation strategies "minexp", "minmax" and "uni" over the DFT codebook and corresponding performance in terms of the PEB over the considered road segment.

The comparison of the optimized energy allocation with the uniform allocation over useful directions ("uni") shows that, even in this scenario with coarse prior knowledge about the UE's location (the UEs may lie anywhere in the considered 14 m × 100 m road segment), optimization of the energy allocation over the codebook beamforming vectors can result in performance gains, especially in terms of the maximum PEB. The largest PEB for "minexp" and "uni" is observed at the upper left corner of the road segment, whereas, for "minmax", the PEB attains its maximum value at the center right part of the road segment.

For further evaluation of the energy allocation strategies, we make use of the position estimation algorithm presented in Chapter 3. In Fig. 4.4 we plot $\mathrm{RMSE}(\boldsymbol{p}_{\mathrm{R}})$ and the PEB as functions of $E_{\mathrm{RE}} f_{\mathrm{s}}$ for all considered energy allocation strategies, for a fixed Rx position at $\boldsymbol{p}_{\mathrm{R}} = [32.25,\ 0]^{\mathrm{T}}$ (Fig. 4.4(a)), which corresponds to the center of the rightmost lane of the road segment, and $\boldsymbol{p}_{\mathrm{R}} = [21.75,\ 50]^{\mathrm{T}}$ (Fig. 4.4(b)), which corresponds to the top position of the leftmost lane. Each RMSE point is generated by averaging over 1000 noise realizations. In Fig. 4.4(a), with the Rx position fixed at $\boldsymbol{p}_{\mathrm{R}} = [32.25,\ 0]^{\mathrm{T}}$, we can see that, as expected from Fig. 4.3, "uni" results in the lowest PEB. Its RMSE converges to the PEB for $E_{\mathrm{RE}} f_{\mathrm{s}} > -4\,\mathrm{dBm}$, faster than the other two considered energy allocation strategies. The RMSE has a similar behavior, with the Tx energy required for convergence to the PEB being approximately 3 dB higher than that of "uni", which corresponds to the difference in energy allocation to the Rx-illuminating beamforming vector between the two strategies. Regarding "minmax", although the energy allocated to the Rx-illuminating beamforming vector is about 10 dB lower than that of "uni", its RMSE converges to the PEB for $E_{\mathrm{RE}} f_{\mathrm{s}} > 12.5\,\mathrm{dBm}$, i.e., 16.5 dB higher than that of "uni". This can be attributed to the fact that the shape of the autocorrelation function, which is not taken into account in the design, makes it more difficult for the positioning algorithm to reliably detect the LOS path.

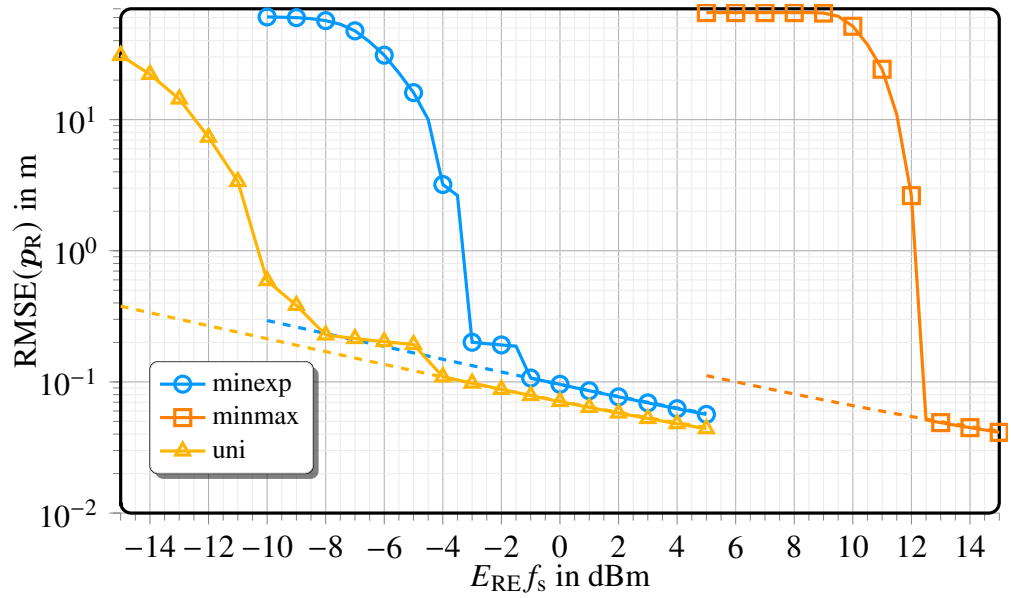

(a) Rx position fixed at $\boldsymbol{p}_R = \begin{bmatrix} 32.25, & 0 \end{bmatrix}^T$.

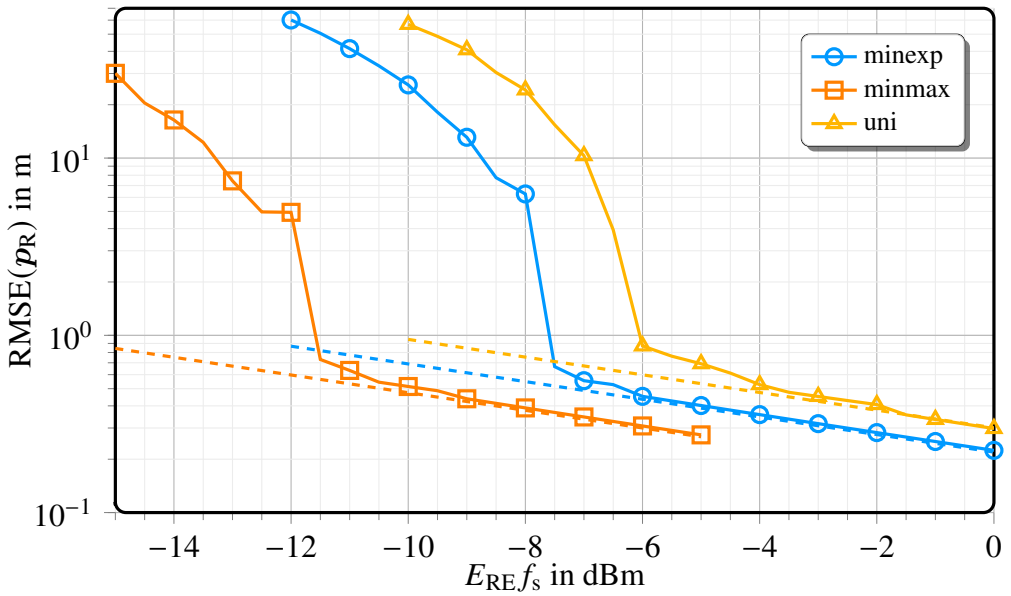

(b) Rx position fixed at $\boldsymbol{p}_R = \begin{bmatrix} 21.75, & 50 \end{bmatrix}^T$.

Fig. 4.4. Position RMSE and PEB of the energy allocation strategies "minexp", "minmax" and "uni" as a function of $E_{RE} f_s$ for fixed Rx position.

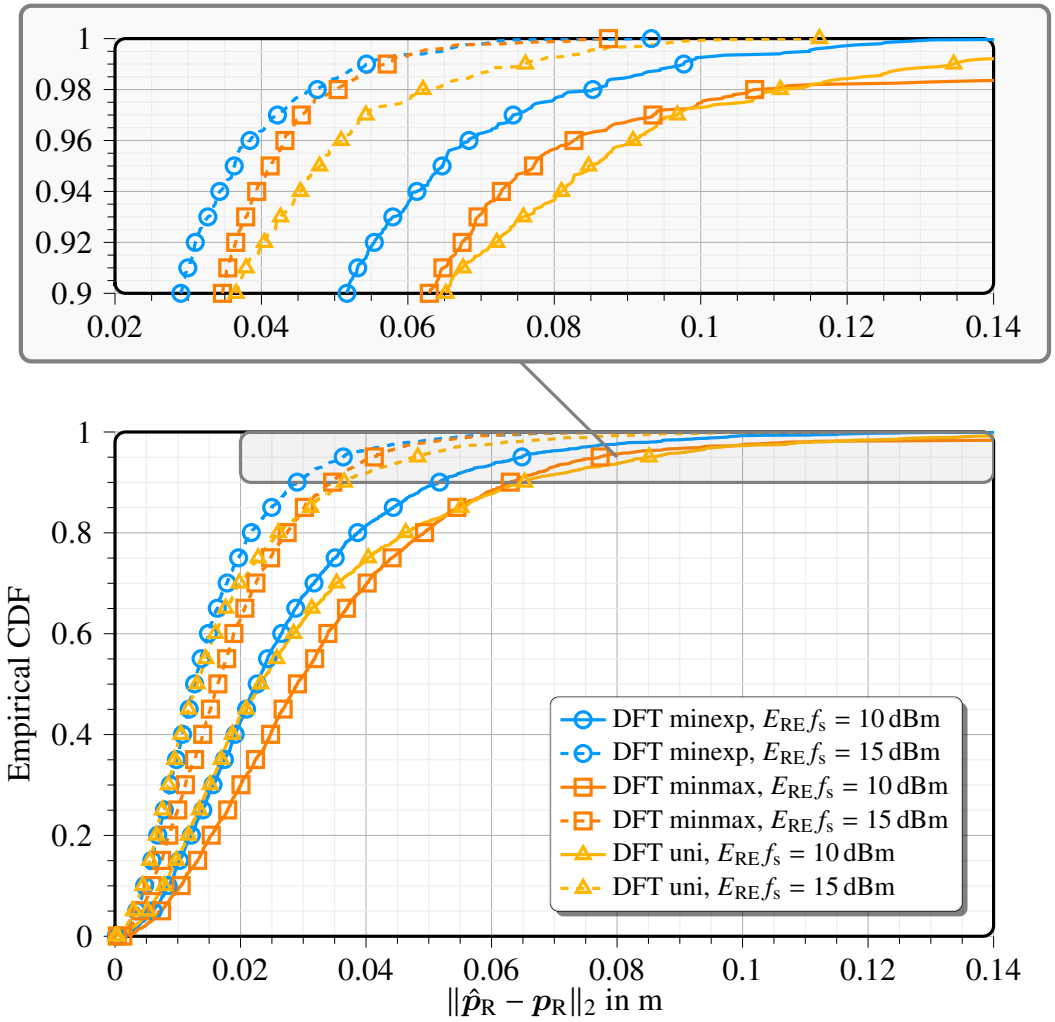

Fig. 4.5. Empirical cdf of $\|\hat{p}_R - p_R\|_2$ for different energy allocation strategies on the road segment of Fig. 4.2.

The observations from Fig. 4.4(b) are similar. With the Rx position fixed at $p_R = [21.75,\ 50]^T$, we observe that, as expected, "minmax" offers the best performance and its RMSE converges to the PEB for $E_{RE} f_s > -9$ dBm. The amount of additional energy required for the other two strategies to converge to their PEBs corresponds approximately to the deficit of energy allocated to the LOS-illuminating beamforming vector.

Using again the position estimation algorithm of Chapter 3, we compare the performance of the energy allocation strategies, with the position of the Rx being uniformly distributed over the road segment. For 2000 random realizations of the Rx position p_R, in Fig. 4.5, we plot the empirical cdf of the position error $\|\hat{p}_R - p_R\|_2$, where $\hat{p}_R$ is the estimated position for the considered energy allocation strategies and for two different Tx energy values, i.e., $E_{RE} f_s = 10$ dBm and $E_{RE} f_s = 15$ dBm. A summary of the percentiles of the distribution of the position error is provided in Table 4.1. For $E_{RE} f_s = 10$ dBm, we can see that "minexp" is the best-performing strategy for cdf values greater than 50%, whereas for lower cdf values, "uni" offers the best performance. We would expect "minmax" to outperform the other two for higher cdf values, since it is the one minimizing the maximum PEB, but this is not the case, as can be observed in Table 4.1, with the 99% position error being 36.16 m. This is due to the fact that, for some locations, $E_{RE} f_s = 10$ dBm is

Table 4.1. Percentiles of the cdf of the position error in m for different energy allocation strategies.

	$E_{\mathrm{RE}} f_{\mathrm{s}} = 10\,\mathrm{dBm}$				$E_{\mathrm{RE}} f_{\mathrm{s}} = 15\,\mathrm{dBm}$			
	50%	90%	95%	99%	50%	90%	95%	99%
minexp	**0.023**	**0.052**	**0.065**	**0.098**	**0.013**	**0.029**	**0.036**	**0.054**
minmax	0.029	0.063	0.077	36.16	0.016	0.035	0.041	0.057
uni	**0.023**	0.065	0.085	0.135	**0.013**	0.037	0.048	0.076

not sufficient for the position estimation algorithm to detect the LOS path reliably, leading to large position errors, as can be seen, for example, in Fig. 4.4(a) for $\boldsymbol{p}_{\mathrm{R}} = [21.75,\ 50]^{\mathrm{T}}$.

For $E_{\mathrm{RE}} f_{\mathrm{s}} = 15\,\mathrm{dBm}$, "minexp" outperforms "uni" for cdf values higher than 50%, while "minmax" outperforms "uni" for cdf values higher than 85%, with the LOS path now being reliably detected, as suggested by the absence of outliers. Interestingly, "minmax" outperforms "minexp" only for some cdf values greater than 99.5%. As a conclusion, for the given geometric setup and system configuration, "minexp" seems to be the best strategy, as it offers performance improvement for the majority of considered locations, while being sufficiently reliable for any location.

4.3.3 Multipath Channel

4.3.3.1 Geometric Setup, Prior Information at the Transmitter (Tx) and Synchronization Accuracy

For the evaluation of the energy allocation algorithm, using also the position estimation algorithm from Chapter 3, we consider again the geometric setup of Sec. 3.3, shown in Fig. 3.1.

We consider NLOS paths resulting from single-bounce reflections. The phases of the complex path gains are uniformly distributed over $[-\pi, \pi)$ and their magnitudes are given by

$$|h_l| = \begin{cases} c/(4\pi f_{\mathrm{c}} \|\boldsymbol{p}_{\mathrm{R}}\|_2), & l = 0, \\ \sqrt{\rho_l}\, c/(4\pi f_{\mathrm{c}} (\|\boldsymbol{p}_{\mathrm{s},l}\|_2 + \|\boldsymbol{p}_{\mathrm{R}} - \boldsymbol{p}_{\mathrm{s},l}\|_2)), & l \neq 0, \end{cases} \tag{4.33}$$

where ρ_l is the reflection coefficient.

The standard deviation of the clock offset is equal to the 2 sample intervals, i.e., $\sigma_{\mathrm{clk}} = 2/(N\Delta f)$, so that $c\sigma_{\mathrm{clk}} \approx 4.88\,\mathrm{m}$.

Regarding prior knowledge at the Tx, we consider two cases, with the first one being an artifically generated distribution that will allow us to highlight the differences between the various energy allocation strategies, and the second one resulting from the CRLB, assuming a prior transmission.

1) In the first case, we assume that the prior knowledge about the Rx location is encoded by $\mathcal{N}(\mu_{\boldsymbol{p}_{\mathrm{R}}}, \boldsymbol{C}_{0,0})$, with $\mu_{\boldsymbol{p}_{\mathrm{R}}} = [25,\ 10]^{\mathrm{T}}$ and $\boldsymbol{C}_{0,0} = 3/\sqrt{2}\boldsymbol{I}_2\mathrm{m}^2$. We also assume that the Tx has imperfect knowledge about the environment encoded by the distributions of the locations of the VAs $\boldsymbol{p}_{\mathrm{VA},l}$, $l = 1, 2, 3$, which are assumed to be $\mathcal{N}(\mu_{\boldsymbol{p}_{\mathrm{VA},l}}, \boldsymbol{C}_{\mathrm{VA}})$, with

$$\mu_{\boldsymbol{p}_{\mathrm{VA},1}} = [0,\ 50]\mathrm{m}, \tag{4.34}$$
$$\mu_{\boldsymbol{p}_{\mathrm{VA},2}} = [0,\ -50]\mathrm{m}, \tag{4.35}$$
$$\mu_{\boldsymbol{p}_{\mathrm{VA},3}} = [120,\ 0]\mathrm{m}, \tag{4.36}$$
$$\boldsymbol{C}_{\mathrm{VA}} = 3/\sqrt{2}\boldsymbol{I}_2. \tag{4.37}$$

For the reflection coefficient ρ_l, $l = 1, 2, 3$, we assume $\rho_l \sim \mathcal{N}(\mu_\rho, \sigma_\rho^2)$, with $\mu_\rho = -10\,\mathrm{dB}$ and $\sigma_\rho = -4\,\mathrm{dB}$. In order to compute the distributions of the POIs $\boldsymbol{p}_{\mathrm{s},l}$, $l = 1, 2, 3$, which

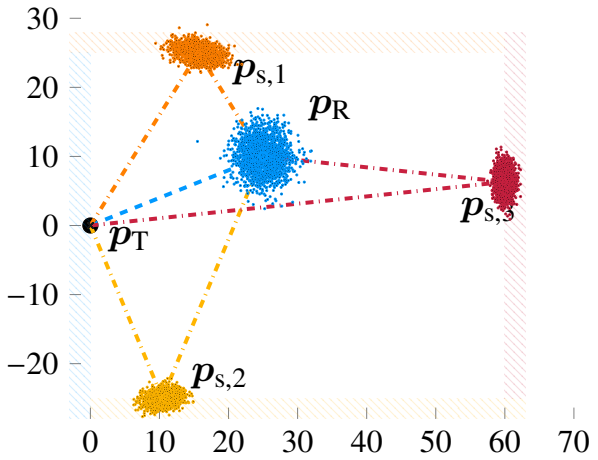

Fig. 4.6. Samples from the distribution of the 1st case of prior knowledge at the Tx.

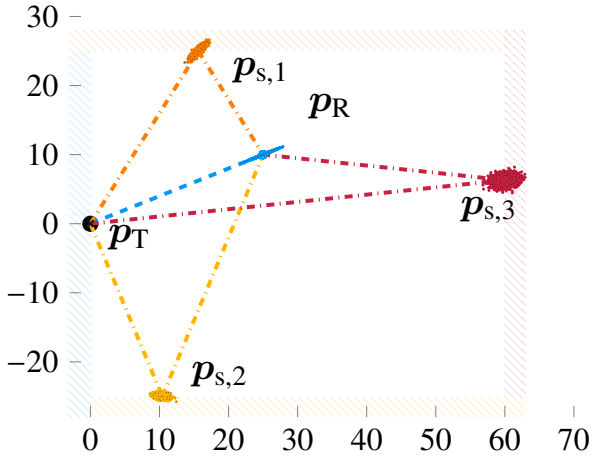

Fig. 4.7. Samples from the distribution of the 2nd case of prior knowledge at the Tx.

are functions of $\boldsymbol{p}_{\mathrm{R}}$ and $\boldsymbol{p}_{\mathrm{VA},l}$, we draw 2000 random samples from the distributions of $\boldsymbol{p}_{\mathrm{R}}$ and $\boldsymbol{p}_{\mathrm{VA},l}$. Using these samples, we compute the mean of $\boldsymbol{p}_{\mathrm{s},l}$, as well as its covariance and cross-covariances with $\boldsymbol{p}_{\mathrm{R}}$ and $\boldsymbol{p}_{\mathrm{s},l'}$, $l' \neq l$, and assume that $\boldsymbol{p}_{\mathrm{R}}$ and $\boldsymbol{p}_{\mathrm{s},l}$, $l = 1, 2, 3$, are jointly Gaussian distributed. Samples from this distribution are depicted in Fig. 4.6. Such a distribution may result, for example, from information about the Rx location from another positioning technology (e.g., GNSS) and imperfect knowledge about the location of the walls from positioning other devices.

2) In the second case, we assume that prior knowledge about the location of the Rx and the POIs has been obtained through a prior transmission in the UL and the covariance matrix of $\boldsymbol{\nu}'$ is set according to the CRLB, with its mean set as in the first case. For the computation of the CRLB, all parameters are set as described in Sec. 4.3.1, except for the transmit energy and the noise figure at the UL Rx. Similar to Sec. 2.6.3, we set the transmit energy of the UE to be 13 dB lower than that of the BS, i.e., we set $E_{\mathrm{RE,UE}}$ such that $E_{\mathrm{RE,UE}} f_{\mathrm{s}} = -3$ dBm and the noise figure is set 6 dB lower, i.e., $\mathrm{NF}_{\mathrm{BS}} = 7$ dB. Assuming that the parameters are jointly Gaussian distributed, samples from the resulting distribution are depicted in Fig. 4.7.

4.3.3.2 Benchmark for Beam Energy Allocation

In order to fairly evaluate our energy allocation strategies, we set as a benchmark the uniform energy allocation to beamforming vectors exciting useful directions. For a given confidence level κ we get a grid of AODs for each path as in (4.21) and compute the set of useful beamforming vectors as

$$\mathcal{B}_{\text{uni}}^{(\kappa)} = \cup_{l=0}^{L-1} \cup_{m=0}^{N_\theta} \left\{ \underset{k=1,\ldots,N_{\text{T}}}{\text{argmax}} \, |\boldsymbol{a}_{\text{T}}^{\text{T}}(\tilde{\theta}_{\text{T},l,m}^{(\kappa)}) \boldsymbol{f}_k| \right\}. \tag{4.38}$$

The energy allocation vector $\boldsymbol{q}$ is

$$q_k = \begin{cases} 1/|\mathcal{B}_{\text{uni}}^{(\kappa)}|, & k \in \mathcal{B}_{\text{uni}}^{(\kappa)}, \\ 0, & k \notin \mathcal{B}_{\text{uni}}^{(\kappa)}. \end{cases} \tag{4.39}$$

4.3.3.3 Power Allocation Strategies and Position Estimation Algorithm Parameters

The energy allocation strategies and their corresponding parametrizations that we consider for our simulation results are as follows:

- *opt. unconstr.*: The energy allocation is obtained by the solution of (4.20). Assuming that the amplitude of the gain of the LOS path is deterministically related to the geometry (4.33), the dimension of the integral that has to be numerically approximated is $n = 2L + (L-1) = 11$. The minimum number of points of known cubatures of 5th degree (in order to ensure a sufficiently dense sampling of the support of the distribution) with positive weights and dimension $n > 7$ is $2^n + 2n$ [76], [78]. Therefore, a minimum of 4118 points would be required, which incurs prohibitive computational complexity. Instead, we draw $N_{\boldsymbol{\nu}'} = n^2 = 121$ random samples from the joint 11-dimensional distribution, which is a lower bound for the number of points of any known cubature of 5th degree [78].
- *opt. constr.*: Similar to "opt. unconstr.", the energy allocation is obtained by the solution of (4.20) with $N_{\boldsymbol{\nu}'} = n^2 = 121$ random samples from the joint 11-dimensional distribution and additional constraints (4.23), with $\kappa = 0.995$, $q_{\text{th}} = -10\,\text{dB}$ and $N_\theta = 15$.
- *opt. reduced*: Due to the dimensionality reduction (4.25), in this case $n = 2L = 8$. Similar to "opt. unconstr." and "opt. constr.", the energy allocation is obtained by the solution of the minimization of the lower bound on ESPEB (4.25) with $N_{\boldsymbol{\nu}'} = n^2 = 8^2 = 64$ random samples from the joint 8-dimensional distribution and additional constraints (4.23), with $\kappa = 0.995$, $q_{\text{th}} = -10\,\text{dB}$ and $N_\theta = 15$.
- *subopt.*: The energy allocation is obtained by the solution of (4.27)-(4.30), with 9-point cubatures for the involved 2D marginals, $\kappa = 0.995$, $q_{\text{th,LOS}} = -3\,\text{dB}$, $q_{\text{th}} = -10\,\text{dB}$ and $N_\theta = 15$.
- *uni* κ: The energy allocation is obtained by uniform energy allocation to useful directions, according to (4.38)-(4.39), with $\kappa = \{0.50,\ 0.90\}$ and $N_\theta = 15$. We note that choosing $\kappa = 0.995$ as for the other strategies results in performance degradation; hence, results for this value are not included.

For the 1st case of prior knowledge, the beampatterns of the energy allocation strategies for the considered prior knowledge are shown in Fig. 4.8. We observe in Figs. 4.8(a)-(d) that for the optimized energy allocation strategies, most of the available energy is spent on beamforming vectors illuminating NLOS paths. When σ_{clk} is very small (i.e., when the synchronization error is very small), having only the delay measurement of the LOS suffices to determine the distance between the BS and the UE. However, as σ_{clk} increases, neither the LOS nor the NLOS provide individually

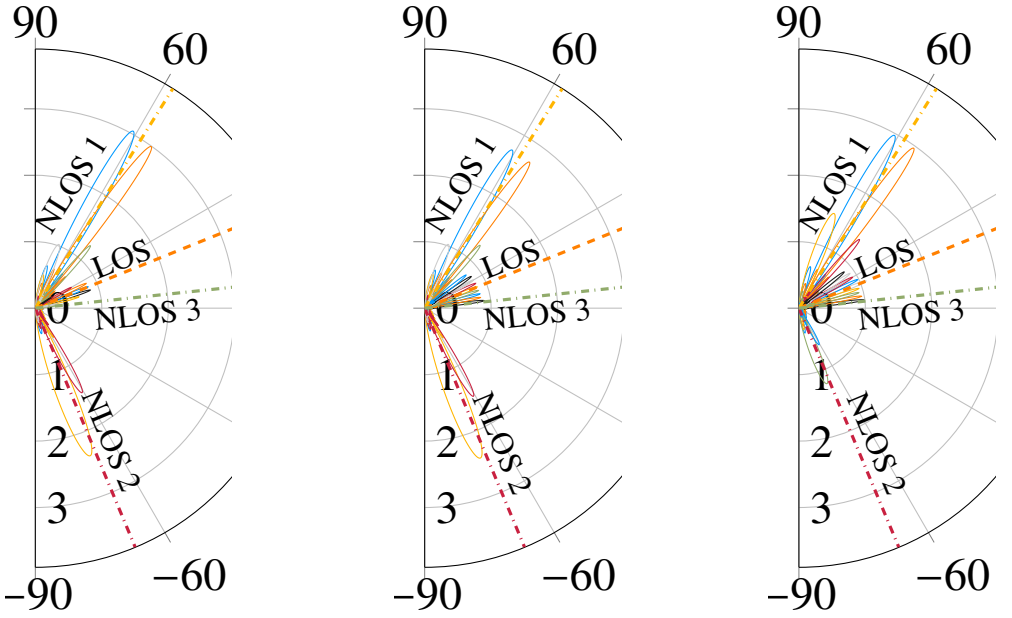

(a) opt. unconstr.:
$\mathbb{E}[\mathrm{PEB}] = 0.18\,\mathrm{m}$
max PEB = 0.61 m

(b) opt. constr.:
$\mathbb{E}[\mathrm{PEB}] = 0.19\,\mathrm{m}$
max PEB = 0.62 m

(c) opt. reduced:
$\mathbb{E}[\mathrm{PEB}] = 0.19\,\mathrm{m}$
max PEB = 0.76 m

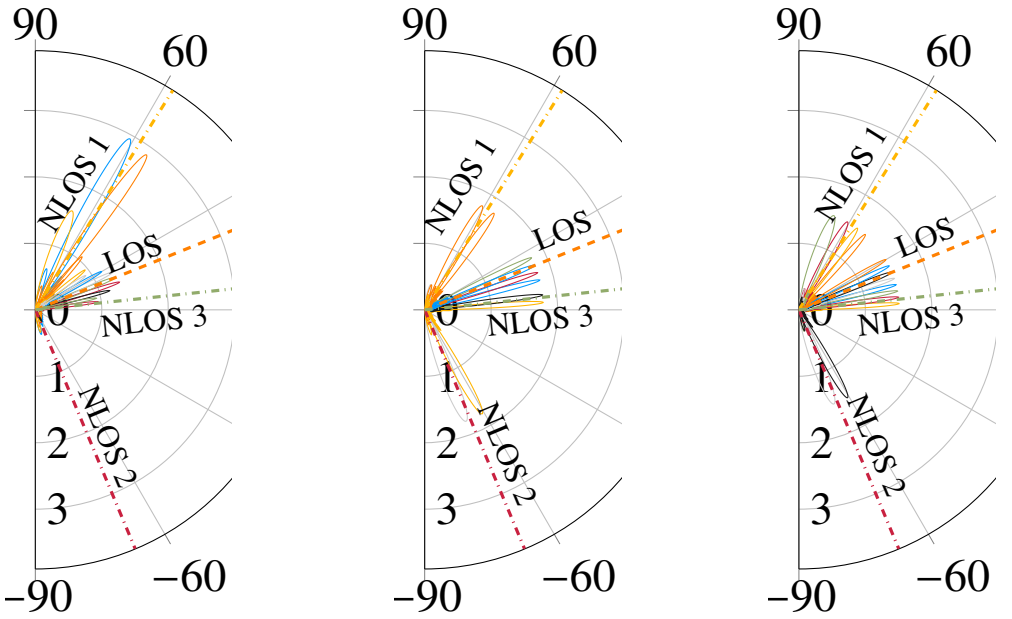

(d) subopt.:
$\mathbb{E}[\mathrm{PEB}] = 0.20\,\mathrm{m}$
max PEB = 1.00 m

(e) uni 0.50:
$\mathbb{E}[\mathrm{PEB}] = 0.28\,\mathrm{m}$
max PEB = 3.13 m

(f) uni 0.90:
$\mathbb{E}[\mathrm{PEB}] = 0.27\,\mathrm{m}$
max PEB = 2.72 m

Fig. 4.8. Beam patterns $|\boldsymbol{a}_{\mathrm{T}}^{\mathrm{T}}(\tilde{\theta}_{\mathrm{T}})\boldsymbol{f}_k\sqrt{q_k}|$, $k = 1, \ldots, M_{\mathrm{T}}$, for different energy allocation strategies for the 1st case of prior knowledge.

information about the BS-UE distance. In these cases, the information about the BS-UE distance comes from the delay differences, and this implies that several paths (not only one) have to be illuminated with sufficient energy. If there is a large energy unbalance between rays, then the delay differences will be estimated less precisely. Comparing Fig. 4.8(a) with Figs. 4.8(b)-(d), we see that when the constraints (4.23) are not applied, the energy allocation to NLOS components is more significant, with the energy spent on less likely LOS directions being very low. From Figs. 4.8(b) and (c), we can see that the impact of the dimensionality reduction (4.25) is the reduction of the energy spent on the 2nd NLOS path. This is explained by the fact that the fading of the path gains is not taken into account; hence, for the mean values of the path gains, more energy is spent on the paths that offer more useful position information. Also, in Fig. 4.8(d) we observe that our suboptimal approach allocates almost no energy to the 2nd NLOS path, as in the last step where all paths are considered jointly, only the receiver's location uncertainty and the mean positions of scatterers/reflectors are taken into account; for this setup, the information offered by the 1st NLOS path is more useful and, therefore, most of the available energy is allocated for its illumination. For the uniform allocation, higher confidence values lead to activation of more beamforming vectors and spreading of the available energy to more directions.

For the 2nd case of prior knowledge, "opt. unconstr.", "opt. constr." and "opt. reduced" result in the same energy allocation. Therefore, in the following results about this case, we omit results about "opt. unconstr." and "opt. constr.". The beampatterns of the energy allocation strategies prior knowledge are shown in Fig. 4.9. Both optimized energy allocation strategies ("opt. reduced" and "subopt.") allocate energy only on beamforming vectors illuminating the LOS and the 1st NLOS path. The difference between them is the energy allocation on the LOS-illuminating beamforming vectors. Regarding the "uni" energy allocation strategies, we observe that, compared to "uni 0.50", only one additional beamforming vector is activated for "uni 0.90", due to the shape of the prior and the width of the beamforming vectors.

Regarding the position estimation algorithm parameters, we set $N_\tau = 2N_\mathrm{P}$, $N_{\theta_\mathrm{T}} = 2N_\mathrm{T}$, $N_{\theta_\mathrm{R}} = 2N_\mathrm{R}$, $P_\mathrm{fa} = 0.05$, ζ_1 is pre-trained for the given P_fa and energy allocation strategy, $\zeta_2 = -35\,\mathrm{dB}$, $N_\mathrm{cd} = 3$, $L_\mathrm{max} = 10$, $\chi = \sigma_\eta\sqrt{2(N_\mathrm{T}+N_\mathrm{R})|\mathcal{P}|N_\mathrm{B}P_\mathrm{RE}/N_\mathrm{T}}$ (chosen according to [69]), $\zeta_{3,a} = 10^{-4}$ and $\zeta_{3,b} = 10^{-2}$.

4.3.3.4 Performance vs Signal-to-Noise Ratio (SNR) for Fixed Geometry

We fix the geometry and the reflection coefficients to their mean value, as described in Sec. 4.3.3.1, to examine the performance of the position estimation algorithm as a function of the Tx energy.

Considering the 1st case of prior knowledge, for the energy allocation strategies described in Sec. 4.3.3.3, in Fig. 4.10, we plot the position RMSE $\mathbb{E}_{\boldsymbol{\eta},\epsilon_\mathrm{clk}}[\|\hat{\boldsymbol{p}}_\mathrm{R} - \boldsymbol{p}_\mathrm{R}\|_2^2]$ and PEB as functions of $E_\mathrm{RE}f_\mathrm{s}$, with $\hat{\boldsymbol{p}}_\mathrm{R}$ being the position estimate.

We can see that the bound is attained for all energy allocation strategies. Regarding uniform energy allocation, the distance of the RMSE from the bound for low Tx energy is attributed to the fact that, although the LOS path is detected, the probability of detection for the NLOS is small. With only the LOS path being detected, the clock offset cannot be resolved and the resulting position RMSE approaches the standard deviation of the clock offset $c \cdot \sigma_\mathrm{clk} \approx 4.88\,\mathrm{m}$. Among the two considered configurations ($\kappa = 0.60$ and $\kappa = 0.90$), the former has slightly better performance, as the available energy is more concentrated to the true location of the Rx and the reflectors. But, as we will see later on, this comes with a cost, when the uncertainty about the geometry is considered.

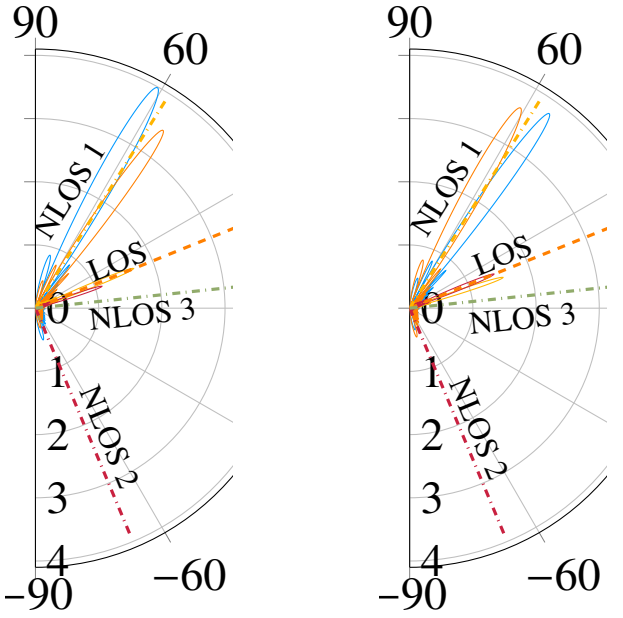

(a) opt. reduced:
$\mathbb{E}[\mathrm{PEB}] = 0.13\,\mathrm{m}$
$\max \mathrm{PEB} = 0.16\,\mathrm{m}$

(b) subopt.:
$\mathbb{E}[\mathrm{PEB}] = 0.14\,\mathrm{m}$
$\max \mathrm{PEB} = 0.17\,\mathrm{m}$

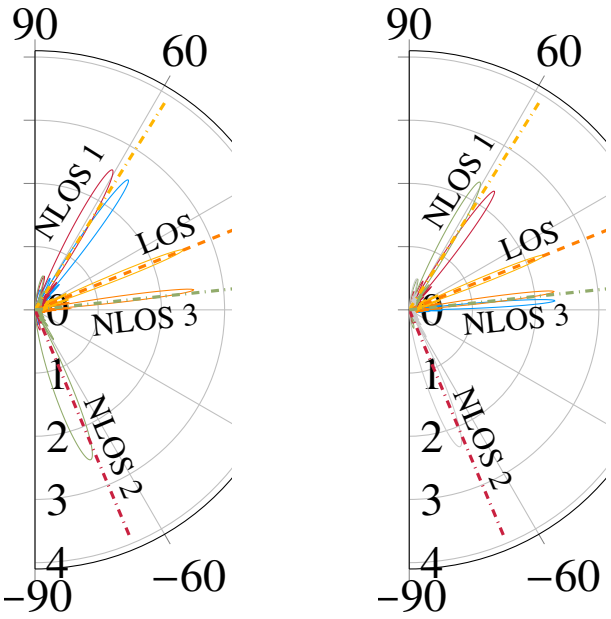

(c) uni 0.50:
$\mathbb{E}[\mathrm{PEB}] = 0.19\,\mathrm{m}$
$\max \mathrm{PEB} = 0.22\,\mathrm{m}$

(d) uni 0.90:
$\mathbb{E}[\mathrm{PEB}] = 0.20\,\mathrm{m}$
$\max \mathrm{PEB} = 0.24\,\mathrm{m}$

Fig. 4.9. Beam patterns $|\boldsymbol{a}_{\mathrm{T}}^{\mathrm{T}}(\tilde{\theta}_{\mathrm{T}})\boldsymbol{f}_k\sqrt{q_k}|, k = 1,\ldots,M_{\mathrm{T}}$, for different energy allocation strategies for the 2nd case of prior knowledge.

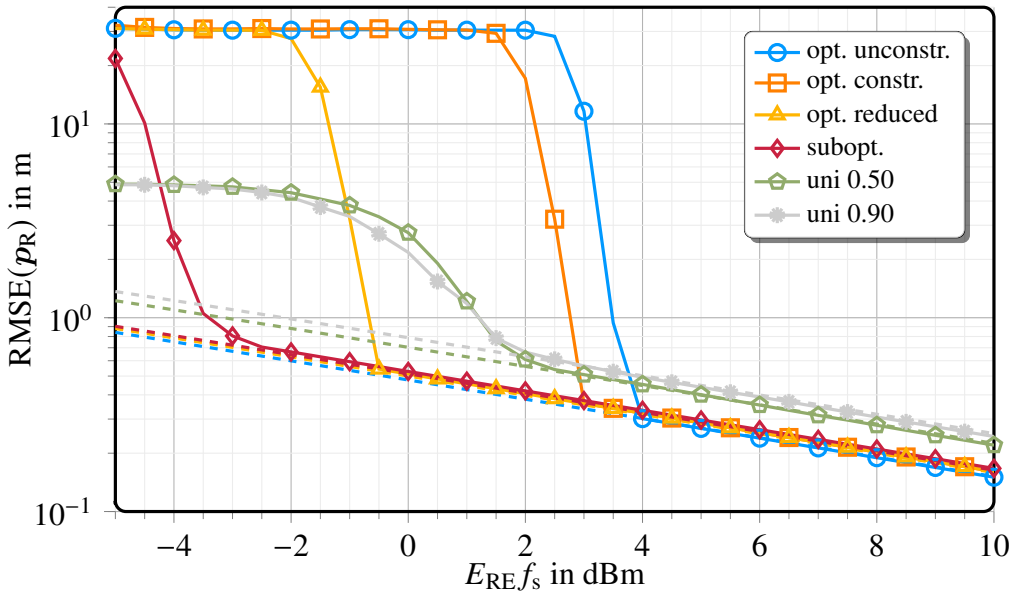

Fig. 4.10. Position RMSE (solid lines) and PEB (dashed lines) vs Tx energy for different energy allocation strategies for the 1st case of prior knowledge.

The optimized allocation strategies result in similar PEBs, with the lowest PEB obtained by "opt. unconstr.", and offer significant improvement compared to the uniform, with a gain of 3 to 4 dB for the same localization accuracy. Their convergence behavior varies and, depending on the specific strategy, their position RMSE converges to the PEB for lower or higher P_{RE} values compared to the uniform energy allocation strategies. Before convergence their RMSE is much higher than that of the uniform strategies and this can be explain as follows. For the RMSE to convergence to the bound, the LOS path and at least one NLOS path have to be reliably detected. All the optimized energy allocation strategies spent more energy on the 1st NLOS path (see Fig. 4.8), which is the first path that is detected and (falsely) used as the LOS path in the estimation algorithm. Only when the transmit energy is sufficiently high, so that the LOS path can be reliably detected, too, the RMSE converges to the PEB. As can be seen in Fig. 4.8, for "opt. unconstr." and "opt. constr.", only a small fraction of energy is spent on the LOS direction and the Tx energy required for the LOS path to be detected is larger. As we will see in subsequent numerical results, this issue is more pronounced for "opt. unconstr." when the geometry is not fixed, as considered here, but random. In this case, a slight deviation of the Rx position from its mean may result in much lower energy spent in the LOS direction.

The RMSE of "opt. reduced" converges slightly faster to the bound compared to "opt. constr.", as slightly more energy is allocated to the LOS path. The "subopt." allocation exhibits the most robust performance, as the LOS path can be detected for much lower Tx energy values, with only a small performance penalty in terms of PEB.

Considering next the 2nd case of prior knowledge, in Fig. 4.11, for the same setup as in Fig. 4.10, we plot again the position RMSE $\mathbb{E}_{\boldsymbol{\eta},\epsilon_{\text{clk}}}[\|\hat{\boldsymbol{p}}_R - \boldsymbol{p}_R\|_2^2]$ and PEB as functions of $E_{RE}f_s$. We can see that, compared to the 1st case of prior knowledge, the attained RMSE and PEB are lower for all considered energy allocations strategies, because the available energy is distributed to a smaller number of beamforming vectors, due to the shape of the prior. The RMSE of the energy allocation strategies "subopt.", "uni 0.50", and "uni 0.90" exhibit similar convergence behavior as for the 1st case of prior knowledge. On the contrary, we observe that the RMSE of "opt. reduced"

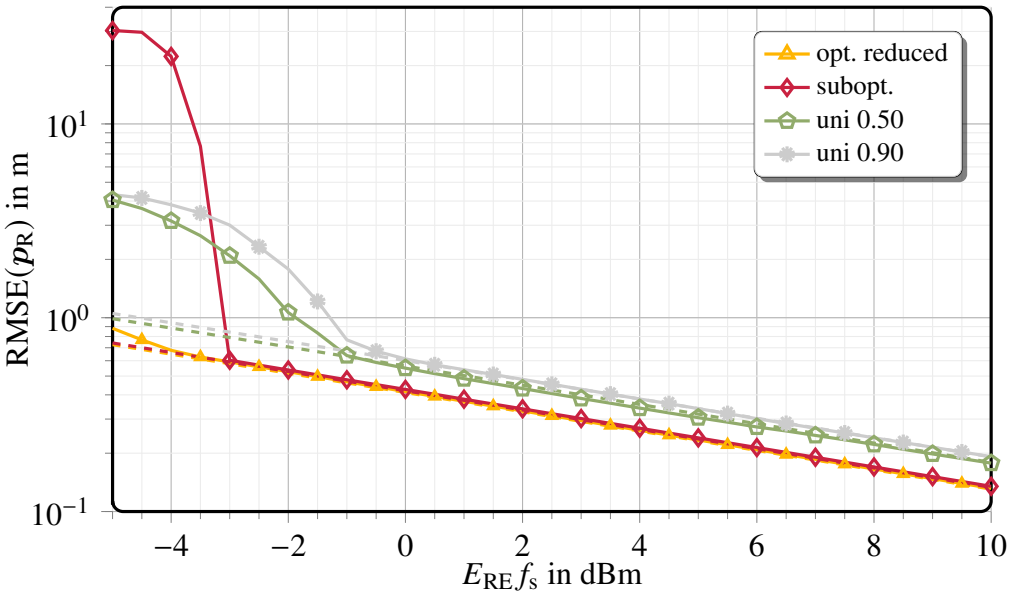

Fig. 4.11. Position RMSE (solid lines) and PEB (dashed lines) vs Tx energy for different energy allocation strategies for the 2nd case of prior knowledge.

Table 4.2. Percentiles of the cdf of the position error in m for different energy allocation strategies.

	50%	90%	95%	99%
opt. unconstr.	0.11	0.35	0.59	58.98
opt. constr.	0.12	0.32	0.42	0.64
opt. reduced	0.13	0.35	0.45	0.68
subopt.	0.12	0.36	0.49	0.77
uni 0.50	0.18	0.71	1.49	32.09
uni 0.90	0.16	0.49	0.61	1.09

converges to the PEB for a much lower energy value than in the 1st case. This is attributed to the fact that more energy is allocated to the LOS path-illuminating beamforming vectors in this case.

4.3.3.5 Performance with Random Geometry

The results in Fig. 4.10 and the corresponding discussion were useful in examining the behavior of the position estimation algorithm, but do not provide a complete characterization of the performance of the energy allocation strategies. Starting with the 1st case of prior knowledge, to better evaluate their performance, for $E_{RE}f_s = 10$ dBm and the rest of the system parameters as described in Sec. 4.3.1, we plot in Fig. 4.12 the cdf of the position error $\|\hat{\boldsymbol{p}}_R - \boldsymbol{p}_R\|_2$, which is computed by drawing 2000 random samples of $\boldsymbol{p}_R$, $\boldsymbol{p}_{s,l}$, ρ_l, $l = 1, 2, 3$, from the prior distribution. A summary of the percentiles of the distribution of the position error is provided in Table 4.2.

We can observe in Fig. 4.12 and Table 4.2 that "opt. constr." achieves the best performance, followed by "opt. reduced" and "subopt.", which have similar performance. The fact that "opt. constr." takes into account the variability of the reflection coefficients leads to allocation of a larger fraction of energy to beamforming vectors illuminating the 2nd NLOS path and this turns out to be beneficial for specific realizations. It is worth noting that, in spite of the lower computational cost of the "subopt." allocation, its performance degradation is small. On the other hand, the "opt.

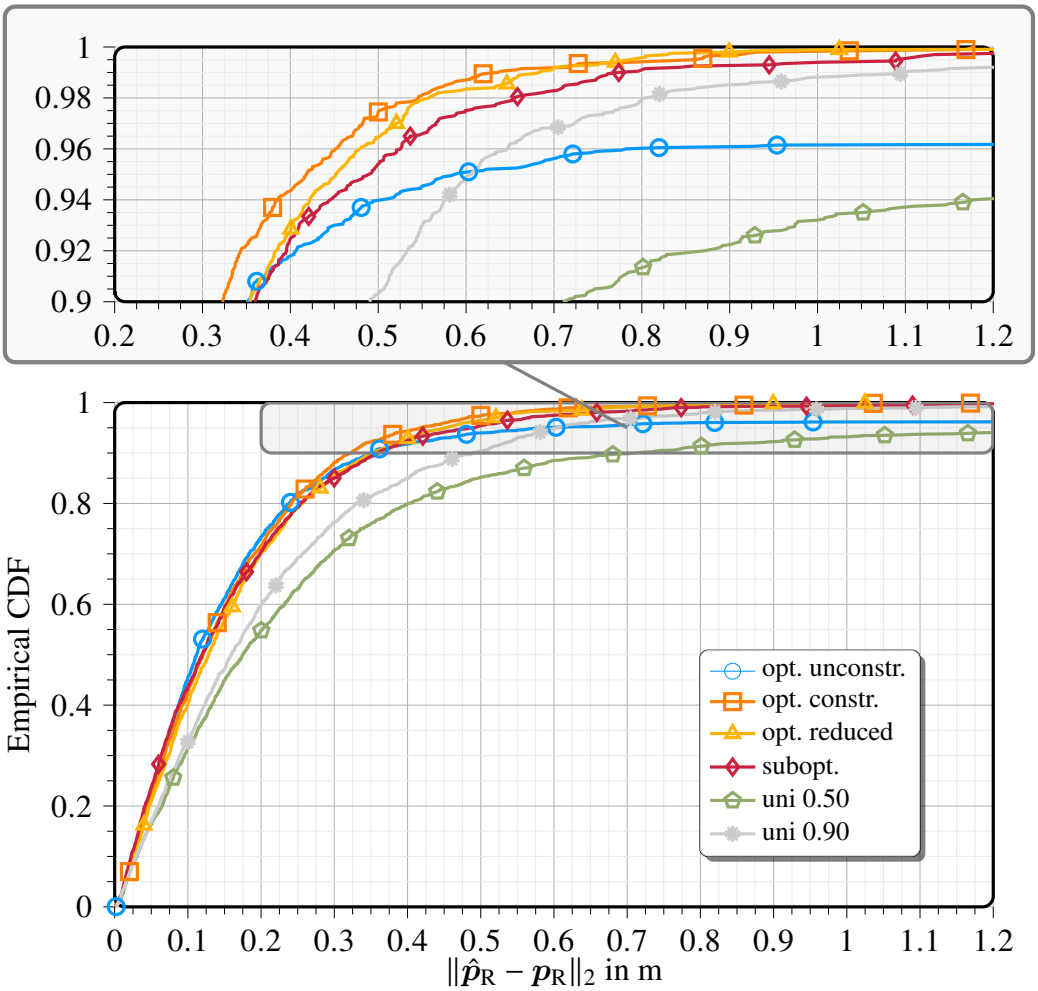

Fig. 4.12. Empirical cdf of $\|\hat{p}_R - p_R\|_2$ for different energy allocation strategies for the 1st case of prior knowledge.

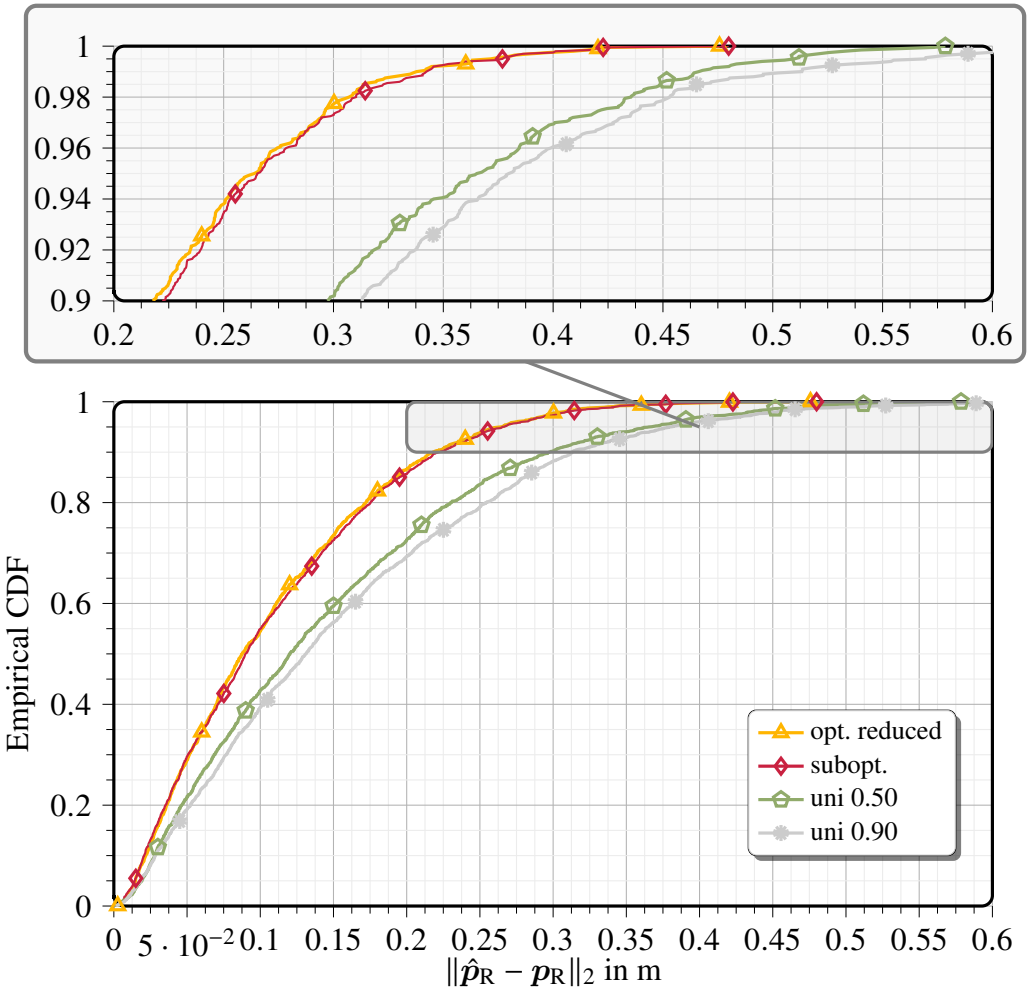

Fig. 4.13. Empirical cdf of $\|\hat{\boldsymbol{p}}_{\mathrm{R}} - \boldsymbol{p}_{\mathrm{R}}\|_2$ for different energy allocation strategies.

unconstr." approach, although attaining the same median error as "opt. constr.", has much lower accuracy for higher percentiles. This is attributed to the low energy spent on the direction around the LOS path, resulting in low probability of detection of the LOS. Compared to the best of the uniform allocations, the "opt. constr." energy allocation offers a position error reduction of 25%, 35%, 31% and 41% at the 50%, 90%, 95% and 99% percentile, respectively.

Regarding the uniform allocations, we can see that spreading the energy to a reduced set of beamforming vectors ("uni 0.50") might result in better positioning accuracy for some geometry realizations, as seen for example in Fig. 4.10, but it significantly deteriorates the performance for other possible realizations. This explains the higher values of position errors of "uni 0.5".

In Fig. 4.13, we plot again the cdf of the position error $\|\hat{\boldsymbol{p}}_{\mathrm{R}} - \boldsymbol{p}_{\mathrm{R}}\|_2$ for the different energy allocation strategies, with the random samples drawn from the distribution of the 2nd case of prior knowledge. We remind here that, in this case, we omit results for "opt. unconstr." and "opt. constr.", as the resulting energy allocation is identical to that of "opt. reduced". In Table 4.3 we provide a summary of the percentiles of the distribution of the position error. The optimized energy allocation strategies ("opt. reduced" and "subopt.") achieve the same performance. Hence, in this case, the lower complexity of "subopt." comes with no performance penalty. Furthermore, contrary to the 1st case, "uni 0.5" outerforms "uni 0.90", which can be explained as follows. Due to the shape of the prior and the width of the beams, increasing the required confidence level κ from 0.50 to

Table 4.3. Percentiles of the cdf of the position error in m for different energy allocation strategies.

	50%	90%	95%	99%
opt. reduced	0.09	0.22	0.26	0.34
subopt.	0.09	0.22	0.27	0.34
uni 0.50	0.12	0.30	0.37	0.47
uni 0.90	0.13	0.31	0.38	0.51

0.90 leads to the activation of only one additional beamforming vector illuminating the 3rd path, while the beamforming vectors illuminating the rest remain unchanged. Nevertheless, as we can deduce from the optimized energy allocations, the first two NLOS paths are more important for Rx localization. The activation of an additional beamforming vector illuminating the 3rd NLOS path results in less energy used on the beamforming vector illuminating the LOS path and the 1st and 2nd NLOS paths, leading to worse performance of "uni 0.90". Compared to the "uni 0.50", the "opt. reduced" energy allocation offers a position error reduction of 25%, 27%, 30% and 28% at the 50%, 90%, 95% and 99% percentile, respectively.

4.3.3.6 Energy Allocation as a Function of σ_{clk}

We now examine the effect of σ_{clk} on the energy allocation. First, similar to (4.38), we define the set of LOS-illuminating beamforming vectors as

$$\mathcal{B}_{\text{LOS}}^{(\kappa)} = \cup_{m=0}^{N_\theta} \left\{ \underset{k=1,\ldots,N_{\text{T}}}{\text{argmax}} \, |\boldsymbol{a}_{\text{T}}^{\text{T}}(\tilde{\theta}_{\text{T},0,m}^{(\kappa)}) \boldsymbol{f}_k| \cup \underset{k}{\text{argmax}} \left| \frac{\partial \boldsymbol{a}_{\text{T}}^{\text{T}}(\tilde{\theta}_{\text{T},0,m}^{(\kappa)})}{\partial \tilde{\theta}_{\text{T}}} \boldsymbol{f}_k \right| \right\} \tag{4.40}$$

and the fraction of energy spent on them as

$$q_{\text{LOS}} = \sum_{k \in \mathcal{B}_{\text{LOS}}^{(\kappa)}} q_k . \tag{4.41}$$

For the 1st case of prior knowledge, in Fig. 4.14(a) we plot q_{LOS} as a function of $c\sigma_{\text{clk}}$ for the energy allocation strategies "opt. unconstr.", "opt. constr.", "subopt" and "uni 0.90", for $N_{\text{R}} = \{4, \ 16\}$, $P_{\text{RE}} = 0\,\text{dBm}$, $\kappa = 0.995$ and the rest of the system parameters as described in Sec. 4.3.1; in Fig. 4.14(b) we plot the corresponding $\mathbb{E}[\text{PEB}]$. We can see in Fig. 4.14(a) that for very low values of σ_{clk}, equivalent to almost perfect Tx-Rx synchronization, it is optimal to spend almost all the available energy on LOS-illuminating beamforming vectors. As σ_{clk} increases, q_{LOS} decreases rapidly for both optimized allocation strategies, until it saturates at a relatively low value. This is explained as follows: The clock offset decreases the amount of range information provided by the LOS path and the larger the standard deviation of the clock offset, the more significant the decrease. Hence, as σ_{clk} increases, the ranging information provided by the NLOS paths becomes more significant and, therefore, more energy is spent on them. Nevertheless, the saturation occurs because the measurement of the LOS AOD offers significant information in the orthogonal direction, which is reduced when q_{LOS} is decreased. The saturation value for "opt. constr." is higher due to the additional constraints on LOS illumination. Also, we observe that the transition from high to low q_{LOS} values is slower for $N_{\text{R}} = 4$. This is attributed to the fact that NLOS paths offer rank-1 position information, whose intensity depends on the quality of the TOA, AOD and AOA measurements combined [79]. For $N_{\text{R}} = 4$, the quality of the AOA measurement is lower; therefore, the

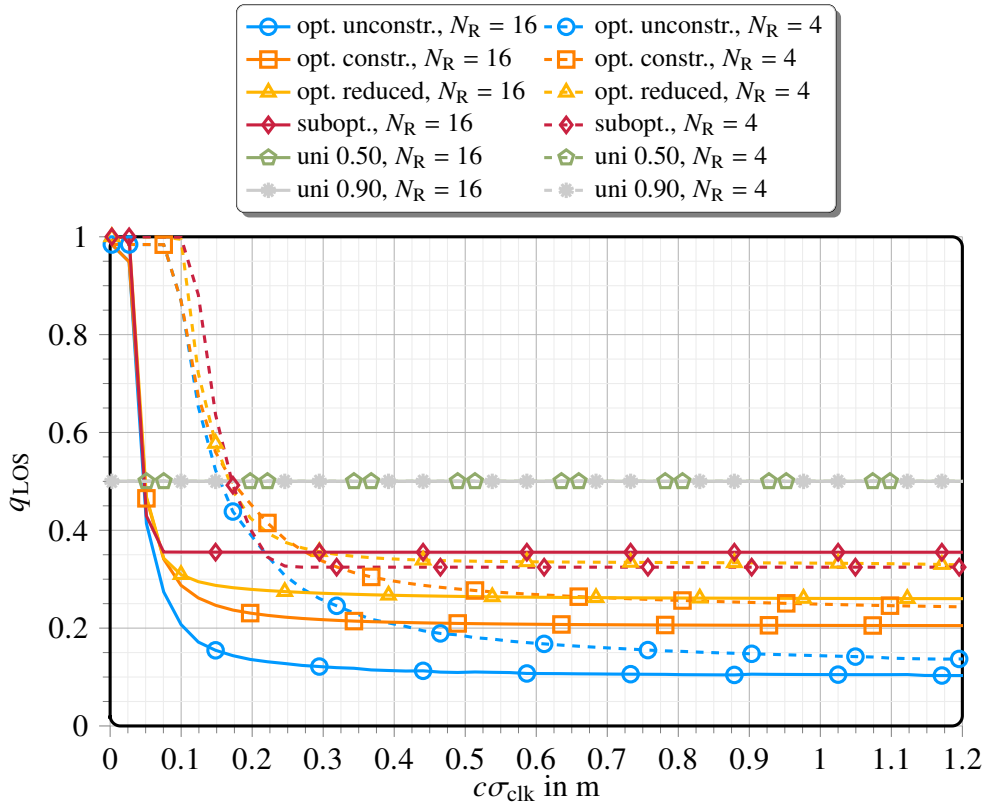

(a) Fraction of energy allocated to LOS-illuminating beamforming vectors q_{LOS} as a function of the clock offset standard deviation $c\sigma_{clk}$.

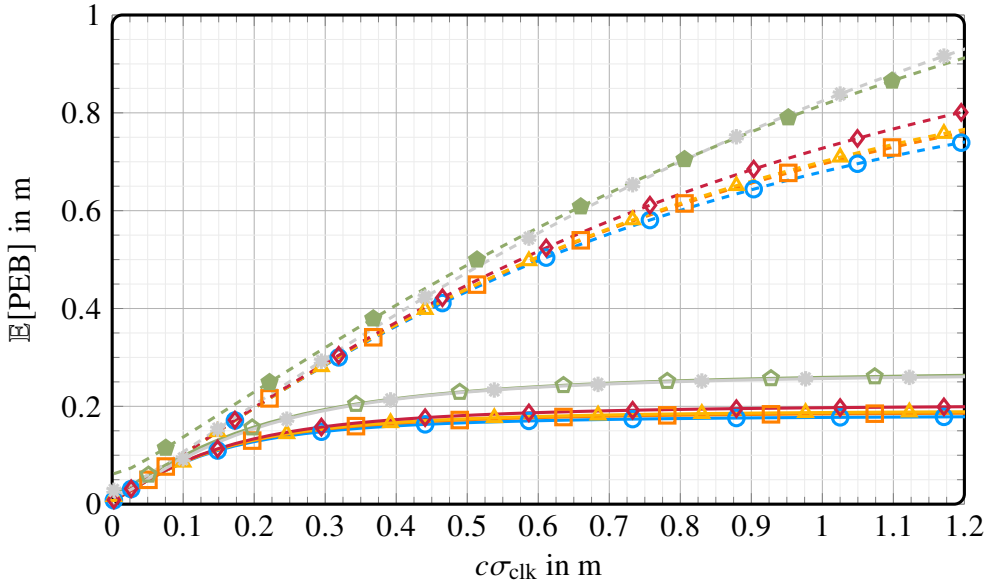

(b) Expected PEB $\mathbb{E}$[PEB] as a function of the clock offset standard deviation $c\sigma_{clk}$

Fig. 4.14. Fraction of energy allocated to LOS-illuminating beamforming vectors q_{LOS} and expected PEB $\mathbb{E}$[PEB] as functions of the clock offset standard deviation $c\sigma_{clk}$ for the 1st case of prior knowledge.

intensity of the ranging information from the NLOS paths is smaller, compared to $N_R = 16$, and it becomes significant for larger values of σ_{clk}.

In Fig. 4.14(b) we see that $\mathbb{E}[\text{PEB}]$ increases with increasing σ_{clk}, until it saturates at a value which depends on the energy allocation strategy and the system configuration ($N_R = \{4,\ 16\}$). As σ_{clk} increases the reduction of ranging information from the LOS path cannot be complemented by ranging information from the NLOS paths (even with optimized energy allocation), resulting in a larger error. In the saturation region the ranging information from the LOS path becomes negligible compared to the clock offset-independent part of ranging information offered by the combination of NLOS paths with the LOS path.

Considering now the 2nd case of prior knowledge, we plot again the fraction of energy allocated to the LOS path q_{LOS} and the resulting $\mathbb{E}[\text{PEB}]$ as functions of $c\sigma_{clk}$ in Figs. 4.15(a) and (b), respectively. The observations from Figs. 4.15 (a) and (b) are very similar to those from Figs 4.14 (a) and (b). In addition, we can see that, in this case, q_{LOS} converges to its asymptotic values for $N_R = 16$ for lower $c\sigma_{clk}$ values. Also, compared to the 1st case of prior knowledge, q_{LOS} is lower, even for $c\sigma_{clk} \to 0$.

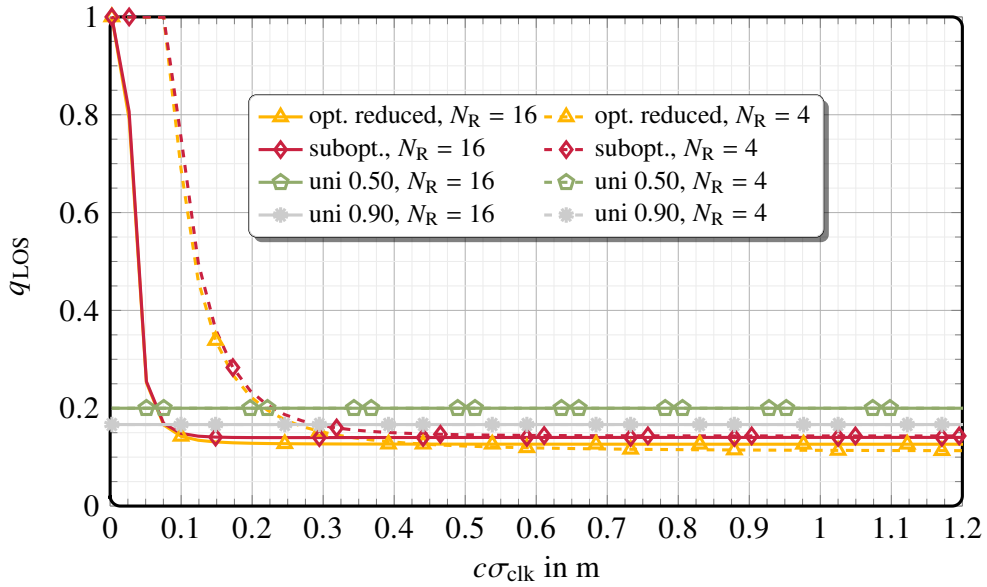

(a) Fraction of energy allocated to LOS-illuminating beamforming vectors q_{LOS} as a function of the clock offset standard deviation $c\sigma_{clk}$.

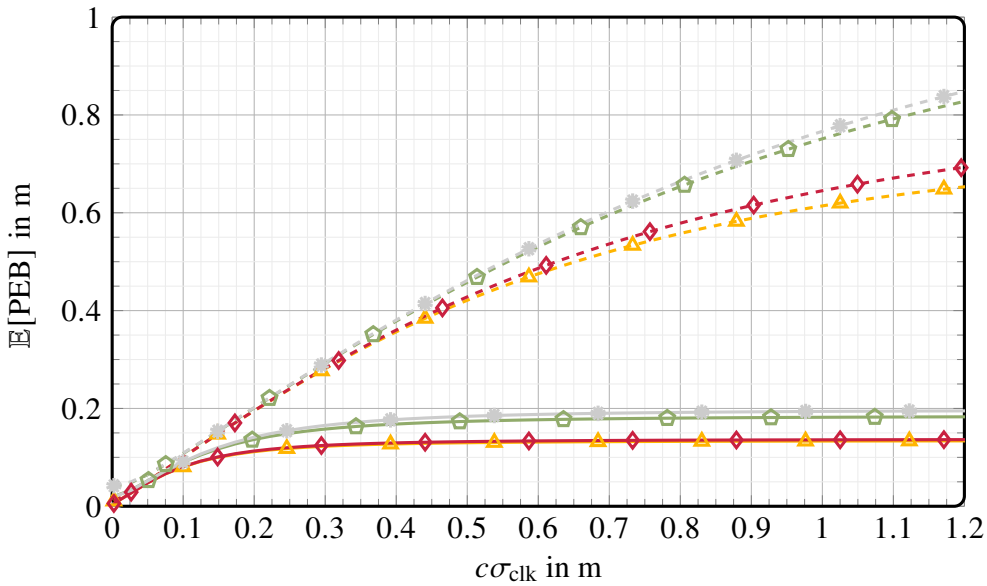

(b) Expected PEB $\mathbb{E}$[PEB] as a function of the clock offset standard deviation $c\sigma_{clk}$.

Fig. 4.15. Fraction of energy allocated to LOS-illuminating beamforming vectors q_{LOS} and expected PEB $\mathbb{E}$[PEB] as functions of the clock offset standard deviation $c\sigma_{clk}$ for the 2nd case of prior knowledge.

5. Conclusions and Recommendations for Future Work

5.1 Conclusions

Throughout the thesis, we studied several aspects of single-anchor positioning with multi-antenna transceivers in mm-Wave channels, investigating its theoretical accuracy limits, developing a CRLB-achieving positioning algorithm and optimizing reference signals for positioning. A central point of the thesis was the practical consideration of imperfect synchronization between the Tx and Rx and its impact on the three aforementioned aspects.

In Chapter 2, we derived asymptotic expressions for the Fisher information on position, orientation and velocity for single-anchor localization in a MIMO-OFDM setup, considering synchronization errors and mobility of the Tx or Rx, and showed analytically that the direction of position information from a single-bounce reflection is parallel to the reflecting surface, when no prior knowledge about the environment is available at the Rx. We studied the impact of synchronization errors and found that even small synchronization errors can significantly degrade the achievable positioning accuracy. Through analytical and numerical results, we showed that NLOS paths can help resolve the clock offset and drastically improve the PEB. In addition, we investigated the effect of mobility and proved that each single-bounce NLOS path contributes a rank-2 FIM on position, orientation and velocity. Our numerical results showed that, in the presence of the LOS path, mobility has no significant impact on the achievable positioning accuracy. However, for NLOS-only positioning, it can provide valuable information that can drastically improve the positioning accuracy of an imperfectly synchronized system. Finally, we compared DL and UL positioning with orthonormal or random beamforming, using 3GPP-compliant assumptions for the Tx power and the noise figure of BSs and UEs, and found that DL can offer superior performance, due to its higher SNR.

In Chapter 3, we developed and evaluated a novel single-anchor positioning algorithm for imperfectly synchronized Tx and Rx and compared it with a SotA algorithm to gain better insight on its characteristics that differentiates it from the SotA. We showed that our proposed path filtering step, where the geometry of single-bounce paths and the known variance of the synchronization error are exploited to reject falsely detected paths, has a significant impact on the algorithm's performance. Furthermore, the off-grid parameter estimation allows our approach to avoid detection of spurious paths and, thus, accurately estimate the model order. This is particularly important in the high SNR regime, where not only the computational burden of processing falsely detected paths is avoided, but also the resulting positioning accuracy is improved. Additionally, for the discover of new potential paths, apart from the full 3D search, we proposed an alternative lower dimensional (2D) grid search with lower complexity and showed with numerical evaluations that employing it the algorithm still converges to the CRLB, but at higher Tx energy values.

In Chapter 4, we discussed how prior knowledge of the Rx position and the position of POIs in the environment can be used to design the reference signal and enhance the performance of single-anchor positioning with imperfectly synchronized trasceivers. We analytically showed that under perfect prior knowledge, the optimal beams for Rx localization with a LOS path are the array steering vector and its derivative, which are used in monopulse radar, and computed the optimal energy allocation over them. Under imperfect prior knowledge, we considered a fixed beam codebook and optimized the energy allocation over the codebook beams. We derived energy allocation strategies with different levels of computational complexity and evaluated them under two different types of prior knowledge. both in terms of their theoretical performance and in terms of their performance using the positioning algorithm of Chapter 3. By comparing with a baseline, where energy is uniformly allocated to all relevant directions, we observed that optimization of the energy allocation can result in significant performance improvement, even if the prior knowledge is coarse. Our evaluations showed that our proposed sub-optimal solution, which is based on initially treating each path separately and computing an intra-path energy allocation vector, followed by an inter-path energy allocation considering all paths jointly and weighting the intra-path allocations, results in a small to no performance penalty (depending on the form of the prior), with a substantially lower computational complexity. We also observed that including constraints enforcing a minimum illumination of the possible LOS directions, despite incurring a small theoretical performance cost in terms of the ESPEB, results in superior performance when an actual positioning algorithm is used. This is due to the resulting higher probability of detection of the LOS, which is not captured by the CRLB and has a strong impact on the positioning accuracy. Finally, we observed that, even for low values synchronization error variance, most of the available energy is allocated to beams illuminating NLOS components to recover necessary range information. This result further confirms the importance of NLOS paths for single-anchor positioning under imperfect synchronization.

5.2 Recommendations for Future Work

Throughout this work, we have used the CRLB as the tool to analyze theoretical performance and optimize the reference signal for single-anchor positioning. Nevertheless, as discussed above, our results in Chapter 4 corroborated the fact that the CRLB, despite being a convenient mathematical tool, may not accurately represent the performance of an actual estimator, which may be improved by appropriately constraining the feasible set. The use of alternative performance metrics that better capture the behavior of practical estimators, like the Ziv-Zakai lower bound (ZZLB) [80], which has been used for waveform optimization for ranging [72], [81], is an interesting research direction. In the same spirit, as discussed in Sec. 4.3.1, a codebook including derivative beams, like the one proposed in [73], although theoretically offering improved accuracy compared to conventional DFT codebooks, when used with a practical estimator may result in performance degradation. Therefore, optimization of energy allocation over such codebooks employing alternative performance metrics, may prove beneficial in this case, too.

With research for 6G networks having already started, one of their main foreseen innovations is joint communications and sensing (JCS), where the objective is the design of signals appropriate for jointly transmitting data, estimating the location of UEs and sensing objects in the environment. A possible extension of the work conducted in this thesis would be the signal design for single-anchor JCS. In addition, in this work, we have assumed that the transmitters can generate any signals, having an arbitrary form, and, more specifically, an arbitrarily high peak-to-average power ratio (PAPR). In practice, due to the non-linearity of the PAs and to avoid distortion of the

signal, a power back-off must be used, so that the signal falls into the linear region of the PA, leading to reduced PA efficiency. Hence, for energy efficient communication, low-PAPR or even constant envelope signals are desired. Furthermore, low-PAPR signals are important for sensing, as they allow for higher estimation SNR for the parameters of interest. We note that traditional radar systems employ low PAPR waveforms, like frequency modulated continuous wave (FMCW) or OFDM with specially designed pilot sequences, but such waveforms are not suitable for data transmission. Therefore, an interesting research topic is the design of constant envelope, or, in general, low-PAPR signals for JCS, with the problem becoming even more interesting when considering multiplexing of beamformed reference signal transmissions with beamformed data transmissions.

Finally, in this work we have assumed that coupling among the antenna elements of the arrays can be neglected. As discussed in Sec. 2.3, this is accurate only for isotropic radiators placed at distances which are multiples of $\lambda_c/2$. Hence, this assumption will in general not hold in practical systems. In a similar fashion to the analysis conducted in [54] for MIMO communications, it would be useful to analyze the performance and design signals for positioning, taking mutual coupling into account. Alongside mutual coupling, one could also consider the effect and joint estimation of transceiver hardware imperfections.

Appendix

A1 Signal Model Derivation

A1.1 Static Scenario

The frequency-domain transmit signal vector at subcarrier p, $p \in \mathcal{P} = \{-N_\mathrm{P}/2, \ldots, N_\mathrm{P}/2-1\}$, of block b, $b = 0, \ldots, N_\mathrm{B}-1$ is $\boldsymbol{x}[p,b] \in \mathbb{C}^{N_\mathrm{T}}$, which is assumed to be a reference signal, and, assuming that the rest of the subcarriers are empty, the corresponding time-domain transmit signal vector is

$$\tilde{\boldsymbol{x}}[k,b] = \frac{1}{\sqrt{N}} \sum_{p\in\mathcal{P}} \boldsymbol{x}[p,b]\, \mathrm{e}^{\mathrm{j}\frac{2\pi}{N}p(k-N_\mathrm{CP})},\ k = 0\ldots, M-1, \tag{A1.1}$$

where $M = N + N_\mathrm{CP}$. The serialized time-domain transmit signal $\tilde{\boldsymbol{x}}_\mathrm{S}[n]$ is related to the k-th vector of the b-th time-domain OFDM symbol $\tilde{\boldsymbol{x}}[k,b]$ as

$$\tilde{\boldsymbol{x}}_\mathrm{S}[bM + k + n_\mathrm{T}] = \tilde{\boldsymbol{x}}[k,b], \tag{A1.2}$$

where $n_\mathrm{T}T_\mathrm{s}$ is the time instant when the signal transmission starts, i.e., the TOT.

The discrete time-domain channel from the j-th transmit antenna to the i-th receive antenna

$$c_{i,j}[m] = \sum_{l=0}^{L-1} h'_l \tilde{g}\left(mT_\mathrm{s} - \tau_{l,i,j}\right) \mathrm{e}^{-\mathrm{j}\,\omega_\mathrm{c}\tau_{l,i,j}}, \tag{A1.3}$$

where $h'_l \in \mathbb{C},\ l = 0, \ldots, L-1$, are the gains of the propagation paths. Let $\tau_\mathrm{min} = \min_{l,i,j} \tau_{l,i,j}$ and $\tau_\mathrm{max} = \max_{l,i,j} \tau_{l,i,j}$. Then, $c_{i,j}[m] = 0$ for $m \neq \lceil \tau_\mathrm{min}/T_\mathrm{s} \rceil, \ldots, \lfloor (\tau_\mathrm{max} + \tau_g)/T_\mathrm{s} \rfloor$. The received signal at the i-th antenna is

$$\begin{aligned}
\tilde{r}_{\mathrm{S},i}[n] &= \sum_{j=1}^{N_\mathrm{T}} \sum_{m=-\infty}^{\infty} c_{i,j}[m] \tilde{x}_{\mathrm{S},j}[n-m] + \tilde{\eta}_{\mathrm{S},i}[n] \\
&= \sum_{j=1}^{N_\mathrm{T}} \sum_{m=\lceil \tau_\mathrm{min}/T_\mathrm{s} \rceil}^{\lfloor (\tau_\mathrm{max}+\tau_g)/T_\mathrm{s} \rfloor} c_{i,j}[m] \tilde{x}_{\mathrm{S},j}[n-m] + \tilde{\eta}_{\mathrm{S},i}[n],
\end{aligned} \tag{A1.4}$$

where $\tilde{\boldsymbol{\eta}}_\mathrm{S}[n] \sim \mathcal{N}_\mathbb{C}(\boldsymbol{0}, \sigma^2_{\eta,\mathrm{R}} \boldsymbol{I}_{N_\mathrm{R}})$.

To keep the presentation simple, and since the multiplication with the analog beamforming matrix $\boldsymbol{W}_\mathrm{R}$ and the DFT are linear operations, we swap their order. In order to start processing the OFDM symbols, the receiver has to synchronize to the arrival of the first symbol. As can be seen from (A1.4), the symbol to which it should synchronize, i.e., the first symbol that should be fed to the subsequent DFT operation (discarding also the CP), is $\tilde{\boldsymbol{r}}_\mathrm{S}[\lceil \tau_\mathrm{min}/T_\mathrm{s} \rceil + N_\mathrm{CP} + n_\mathrm{T}]$. We assume that a coarse synchronization error $n_\epsilon \in \mathbb{N}$ exists, therefore the first symbol fed to the DFT will be $\tilde{\boldsymbol{r}}_\mathrm{S}[n_0]$, where

$$n_0 = \lceil \tau_\mathrm{min}/T_\mathrm{s} \rceil + N_\mathrm{CP} + n_\mathrm{T} - n_\epsilon. \tag{A1.5}$$

Hence, the synchronized received signal at the i-th antenna $\tilde{y}_{\mathrm{S},i}[n]$ is

$$\begin{aligned}
\tilde{y}_{\mathrm{S},i}[n] &= \tilde{r}_{\mathrm{S},i}[n+n_0] = \tilde{r}_{\mathrm{S},i}[n + \lceil \tau_\mathrm{min}/T_\mathrm{s} \rceil + N_\mathrm{CP} + n_\mathrm{T} - n_\epsilon] \\
&= \sum_{j=1}^{N_\mathrm{T}} \sum_{m=\lceil \tau_\mathrm{min}/T_\mathrm{s} \rceil}^{\lfloor (\tau_\mathrm{max}+\tau_g)/T_\mathrm{s} \rfloor} c_{i,j}[m] \tilde{x}_{\mathrm{S},j}[n + \lceil \tau_\mathrm{min}/T_\mathrm{s} \rceil + N_\mathrm{CP} + n_\mathrm{T} - n_\epsilon - m] + \tilde{\eta}'_{\mathrm{S},i}[n] \\
&= \sum_{j=1}^{N_\mathrm{T}} \sum_{m'=0}^{L_\mathrm{c}-1} c_{i,j}[m' + \lceil \tau_\mathrm{min}/T_\mathrm{s} \rceil] \tilde{x}_{\mathrm{S},j}[n + N_\mathrm{CP} + n_\mathrm{T} - n_\epsilon - m'] + \tilde{\eta}'_{\mathrm{S},i}[n],
\end{aligned} \tag{A1.6}$$

where

$$L_{\mathrm{c}} = \lfloor (\tau_{\max} + \tau_g)/T_{\mathrm{s}} \rfloor - \lceil \tau_{\min}/T_{\mathrm{s}} \rceil + 1, \tag{A1.7}$$

$$\tilde{\boldsymbol{\eta}}'_{\mathrm{S}}[n] = \tilde{\boldsymbol{\eta}}_{\mathrm{S}}[n + \lceil \tau_{\min}/T_{\mathrm{s}} \rceil + N_{\mathrm{CP}} + n_{\mathrm{T}} - n_\epsilon], \tag{A1.8}$$

and the last equality follows by the change of variables $m' = m - \lceil \tau_{\min}/T_{\mathrm{s}} \rceil$. The k-th sample of the b-th time-domain received OFDM symbol $\tilde{y}_i[k, b]$, $k = 0, \ldots, N-1$, at the i-th receive antenna is obtained as

$$\begin{aligned}\tilde{y}_i[k, b] &= \tilde{y}_{\mathrm{S},i}[bM + k] \\ &= \sum_{j=1}^{N_{\mathrm{T}}} \sum_{m'=0}^{L_{\mathrm{c}}-1} c_{i,j}[m' + \lceil \tau_{\min}/T_{\mathrm{s}} \rceil] \tilde{x}_{\mathrm{S},j}[bM + k + N_{\mathrm{CP}} + n_{\mathrm{T}} - n_\epsilon - m'] + \tilde{\eta}'_{\mathrm{S},i}[bM + k].\end{aligned} \tag{A1.9}$$

From (A1.9) we can observe that if

$$n_\epsilon \geq 0 \tag{A1.10}$$

and

$$N_{\mathrm{CP}} \geq L_{\mathrm{c}} - 1 + n_\epsilon \tag{A1.11}$$

the b-th received OFDM symbol contains only vectors from the b-th transmitted OFDM symbol. Hence, using (A1.2) we get

$$\tilde{y}_i[k, b] = \sum_{j=1}^{N_{\mathrm{T}}} \sum_{m'=0}^{L_{\mathrm{c}}-1} c_{i,j}[m' + \lceil \tau_{\min}/T_{\mathrm{s}} \rceil] \tilde{x}_j[k + N_{\mathrm{CP}} - n_\epsilon - m', b] + \tilde{\eta}'_{\mathrm{S},i}[bM + k]. \tag{A1.12}$$

Applying now an N-point DFT, we can obtain the received signal at the p-th subcarrier of the b-th OFDM symbol $\boldsymbol{y}'[p, b]$ at the i-th antenna

$$\begin{aligned}y'_i[p, b] &= \frac{1}{\sqrt{N}} \sum_{k=0}^{N-1} \tilde{y}_i[k, b] \, \mathrm{e}^{-\mathrm{j} \frac{2\pi}{N} kp} \\ &= \sum_{j=1}^{N_{\mathrm{T}}} \sum_{m'=0}^{L_{\mathrm{c}}-1} c_{i,j}[m' + \lceil \tau_{\min}/T_{\mathrm{s}} \rceil] \frac{1}{\sqrt{N}} \sum_{k=0}^{N-1} \tilde{x}_j[k + N_{\mathrm{CP}} - n_\epsilon - m', b] \, \mathrm{e}^{-\mathrm{j} \frac{2\pi}{N} kp} + \eta_i[p, b],\end{aligned} \tag{A1.13}$$

where

$$\boldsymbol{\eta}[p, b] = \frac{1}{\sqrt{N}} \sum_{k=0}^{N-1} \tilde{\boldsymbol{\eta}}'_{\mathrm{S}}[bM + k] \, \mathrm{e}^{-\mathrm{j} \frac{2\pi}{N} kp} \, . \tag{A1.14}$$

From (A1.14) it is straightforward that $\boldsymbol{\eta}[p, b] \sim \mathcal{N}(\mathbf{0}, \sigma^2_{\eta,\mathrm{R}} \boldsymbol{I}_{N_{\mathrm{R}}})$. Using (A1.1) we find that

$$\begin{aligned}\frac{1}{\sqrt{N}} \sum_{k=0}^{N-1} \tilde{\boldsymbol{x}}[k + N_{\mathrm{CP}} - n_\epsilon - m', b] \, \mathrm{e}^{-\mathrm{j} \frac{2\pi}{N} kp} &= \frac{1}{N} \sum_{k=0}^{N-1} \sum_{q \in \mathcal{P}} \boldsymbol{x}[q, b] \, \mathrm{e}^{\mathrm{j} \frac{2\pi}{N} ((k - n_\epsilon - m')q - kp)} \\ &= \frac{1}{N} \sum_{q \in \mathcal{P}} \boldsymbol{x}[q, b] \, \mathrm{e}^{-\mathrm{j} \frac{2\pi}{N} (n_\epsilon + m')q} \sum_{k=0}^{N-1} \mathrm{e}^{\mathrm{j} \frac{2\pi}{N} (q-p)k} \\ &= \boldsymbol{x}[p, b] \, \mathrm{e}^{-\mathrm{j} \frac{2\pi}{N} (n_\epsilon + m')p},\end{aligned} \tag{A1.15}$$

where the last equality follows from

$$\sum_{k=0}^{N-1} \mathrm{e}^{\mathrm{j}\frac{2\pi}{N}(q-p)k} = \begin{cases} N, & p = q, \\ 0, & p \neq q. \end{cases} \tag{A1.16}$$

Therefore, we can write (A1.13) as

$$\begin{aligned} y_i'[p,b] &= \mathrm{e}^{-\mathrm{j}\frac{2\pi}{N}n_\epsilon p} \sum_{j=1}^{N_\mathrm{T}} x_j[p,b] \sum_{m'=0}^{L_\mathrm{c}-1} c_{i,j}[m' + \lceil \tau_{\min}/T_\mathrm{s} \rceil] \, \mathrm{e}^{-\mathrm{j}\frac{2\pi}{N}m'p} + \eta_i[p,b] \\ &= \mathrm{e}^{-\mathrm{j}\frac{2\pi}{N}n_\epsilon p} \sum_{j=1}^{N_\mathrm{T}} x_j[p,b] \sum_{l=0}^{L-1} h_l' \, \mathrm{e}^{-\mathrm{j}\,\omega_\mathrm{c}\tau_{l,i,j}} \sum_{m'=0}^{L_\mathrm{c}-1} \tilde{g}\big((m' + \lceil \tau_{\min}/T_\mathrm{s} \rceil)T_\mathrm{s} - \tau_{l,i,j}\big) \, \mathrm{e}^{-\mathrm{j}\frac{2\pi}{N}m'p} \\ &\quad + \eta_i[p,b]. \end{aligned} \tag{A1.17}$$

With $\tilde{g}$ being time-limited and essentially band-limited and

$$g[p] = \sum_{m'=0}^{L_\mathrm{c}-1} \tilde{g}(m'T_\mathrm{s}) \, \mathrm{e}^{-\mathrm{j}\frac{2\pi}{N}m'p} \tag{A1.18}$$

being the DFT of the sampled pulse, the following approximate non-integer time-shift property of the DFT can be shown [82]:

$$g[p] \, \mathrm{e}^{-\mathrm{j}\frac{2\pi}{N}\frac{\tau}{T_\mathrm{s}}p} \approx \sum_{m'=0}^{L_\mathrm{c}-1} \tilde{g}(m'T_\mathrm{s} - \tau) \, \mathrm{e}^{-\mathrm{j}\frac{2\pi}{N}m'p}, \tag{A1.19}$$

where τ is the time-shift. To show this property, one has to consider the following Fourier transform pair

$$\tilde{g}(t-\tau) \, \mathrm{e}^{-\mathrm{j}\frac{2\pi}{N}p\frac{t}{T_\mathrm{s}}} \overset{\mathcal{F}}{\rightarrow} G\Big(f + \frac{p}{NT_\mathrm{s}}\Big) \, \mathrm{e}^{-\mathrm{j}\,2\pi\left(f+\frac{p}{NT_\mathrm{s}}\right)\tau} \tag{A1.20}$$

where $G(f)$ is the Fourier transform of $\tilde{g}(t)$, and apply the Poisson summation formula

$$\sum_{m'=-\infty}^{\infty} \tilde{g}(m'T_\mathrm{s} - \tau) \, \mathrm{e}^{-\mathrm{j}\frac{2\pi}{N}pm'} = \frac{1}{T_\mathrm{s}} \sum_{l=-\infty}^{\infty} G\Big(\frac{l}{T_\mathrm{s}} + \frac{p}{NT_\mathrm{s}}\Big) \, \mathrm{e}^{-\mathrm{j}\,2\pi\left(l+\frac{p}{N}\right)\frac{\tau}{T_\mathrm{s}}}. \tag{A1.21}$$

From (A1.17), (A1.7) and the fact that the time support of $\tilde{g}(t)$ is $[0, \tau_g)$, we can see that, for a time-shift $\tau \leq \tau_{\max}$, the non-zero terms of the sum on the left-hand side (LHS) of (A1.21) are for $m' = 0, \ldots, L_\mathrm{c} - 1$. Using now the assumption that the pulse is also (approximately) band-limited in $(-1/(2T_\mathrm{s}), 1/(2T_\mathrm{s}))$, the only non-zero term in the sum on the right-hand side (RHS) of (A1.21) is for $l = 0$, with $p = -N/2, \ldots, N/2$. Hence, we have

$$\begin{aligned} \sum_{m'=0}^{L_\mathrm{c}-1} \tilde{g}(m'T_\mathrm{s} - \tau) \, \mathrm{e}^{-\mathrm{j}\frac{2\pi}{N}pm'} &= \frac{1}{T_\mathrm{s}} G\Big(\frac{p}{NT_\mathrm{s}}\Big) \, \mathrm{e}^{-\mathrm{j}\,2\pi\frac{p\tau}{NT_\mathrm{s}}} \\ &= g[p] \, \mathrm{e}^{-\mathrm{j}\,2\pi\frac{p\tau}{NT_\mathrm{s}}}, \end{aligned} \tag{A1.22}$$

where the last equality follows by employing the Poisson summation formula for $g(t)$ and $G(f)$. Using this property in (A1.17) we get

$$y_i'[p,b] \approx \mathrm{e}^{-\mathrm{j}\,\omega_p(n_\epsilon - \lceil \tau_{\min}/T_\mathrm{s} \rceil)T_\mathrm{s}}\, g[p] \sum_{j=1}^{N_\mathrm{T}} x_j[p,b] \sum_{l=0}^{L-1} h_l' \,\mathrm{e}^{-\mathrm{j}(\omega_\mathrm{c}+\omega_p)\tau_{l,i,j}} + \eta_i[p,b]. \tag{A1.23}$$

Using (2.7), the definition of the Tx steering vector (2.25) and setting $\omega_p = 2\pi p f_\mathrm{s}/N$, we can write

$$y_i'[p,b] \approx g[p] \sum_{l=0}^{L-1} h_l'' \,\mathrm{e}^{-\mathrm{j}\,\omega_p(\tau_l - (\lceil \tau_{\min}/T_\mathrm{s} \rceil - n_\epsilon)T_\mathrm{s})}\, \mathrm{e}^{\mathrm{j}(\omega_\mathrm{c}+\omega_p)\tau_{\mathrm{R},i}(\tilde{\theta}_{\mathrm{R},l})}\, \boldsymbol{a}_{\mathrm{T},p}^\mathrm{T}(\tilde{\theta}_{\mathrm{T},l})\boldsymbol{x}[p,b] + \eta_i[p,b], \tag{A1.24}$$

where

$$h_l'' = h_l' \,\mathrm{e}^{-\mathrm{j}\,\omega_\mathrm{c}\tau_l}\,. \tag{A1.25}$$

Stacking the signals over different Rx antennas, the frequency-domain received signal vector at the p-th subcarrier of the b-th OFDM symbol is

$$\begin{aligned}\boldsymbol{y}'[p,b] &\approx g[p] \sum_{l=0}^{L-1} h_l'' \,\mathrm{e}^{-\mathrm{j}\,\omega_p(\tau_l - (\lceil \tau_{\min}/T_\mathrm{s} \rceil - n_\epsilon)T_\mathrm{s})}\, \boldsymbol{a}_{\mathrm{R},p}(\tilde{\theta}_{\mathrm{R},l})\boldsymbol{a}_{\mathrm{T},p}^\mathrm{T}(\tilde{\theta}_{\mathrm{T},l})\boldsymbol{x}[p,b] + \boldsymbol{\eta}[p,b] \\ &= g[p] \sum_{l=0}^{L-1} h_l'' \,\mathrm{e}^{-\mathrm{j}\,\omega_p(\tau_l - (n_0 - n_\mathrm{T} - N_\mathrm{CP})T_\mathrm{s})}\, \boldsymbol{a}_{\mathrm{R},p}(\tilde{\theta}_{\mathrm{R},l})\boldsymbol{a}_{\mathrm{T},p}^\mathrm{T}(\tilde{\theta}_{\mathrm{T},l})\boldsymbol{x}[p,b] + \boldsymbol{\eta}[p,b], \end{aligned} \tag{A1.26}$$

where the last equality follows from (A1.5). We can observe from (A1.26) that the per subcarrier rotations of the signal that the Rx observes depend, as expected, on the TOAs $\tau_l + n_\mathrm{T}T_\mathrm{s}$ of the paths, which in turn depend on the TOT $n_\mathrm{T}T_\mathrm{s}$. Hence, the Rx requires knowledge of the TOT to convert the TOAs to TOFs τ_l. We assume that the receiver has imperfect knowledge of the TOT due to the clock synchronization error, i.e., it operates under the premise that the signal was transmitted at $n_\mathrm{T}T_\mathrm{s} - \epsilon_\mathrm{clk}$, instead of $n_\mathrm{T}T_\mathrm{s}$. Applying a per-subcarrier rotation by $\mathrm{e}^{-\mathrm{j}\,\omega_p((n_0 - n_\mathrm{T} - N_\mathrm{CP})T_\mathrm{s} + \epsilon_\mathrm{clk})}$ to (A1.26) we get

$$\begin{aligned}\boldsymbol{y}''[p,b] &= \boldsymbol{y}'[p,b]\,\mathrm{e}^{-\mathrm{j}\,\omega_p((n_0 - n_\mathrm{T} - N_\mathrm{CP})T_\mathrm{s} + \epsilon_\mathrm{clk})} \\ &= g[p] \sum_{l=0}^{L-1} h_l'' \,\mathrm{e}^{-\mathrm{j}\,\omega_p(\tau_l + \epsilon_\mathrm{clk})}\, \boldsymbol{a}_{\mathrm{R},p}(\tilde{\theta}_{\mathrm{R},l})\boldsymbol{a}_{\mathrm{T},p}^\mathrm{T}(\tilde{\theta}_{\mathrm{T},l})\boldsymbol{x}[p,b] + \boldsymbol{\eta}[p,b] \\ &= g[p] \sum_{l=0}^{L-1} h_l'' \,\mathrm{e}^{-\mathrm{j}\,\omega_p\tau_l'}\, \boldsymbol{a}_{\mathrm{R},p}(\tilde{\theta}_{\mathrm{R},l})\boldsymbol{a}_{\mathrm{T},p}^\mathrm{T}(\tilde{\theta}_{\mathrm{T},l})\boldsymbol{x}[p,b] + \boldsymbol{\eta}[p,b], \end{aligned} \tag{A1.27}$$

where $\tau_l' = \tau_l + \epsilon_\mathrm{clk}$. In practical implementations the filter $\tilde{g}$ has a flat frequency response over the used spectrum, i.e., $g[p] = g,\ \forall p \in \mathcal{P}$. In this case, after multiplication with the analog beamforming matrix $\boldsymbol{W}_\mathrm{R}^\mathrm{H}$, we get

$$\begin{aligned}\boldsymbol{y}[p,b] &= \boldsymbol{W}_\mathrm{R}^\mathrm{H}\boldsymbol{y}''[p,b] \\ &= \boldsymbol{W}_\mathrm{R}^\mathrm{H} \sum_{l=0}^{L-1} h_l \,\mathrm{e}^{-\mathrm{j}\,\omega_p\tau_l'}\, \boldsymbol{a}_{\mathrm{R},p}(\tilde{\theta}_{\mathrm{R},l})\boldsymbol{a}_{\mathrm{T},p}^\mathrm{T}(\tilde{\theta}_{\mathrm{T},l})\boldsymbol{x}[p,b] + \boldsymbol{W}_\mathrm{R}^\mathrm{H}\boldsymbol{\eta}[p,b], \end{aligned} \tag{A1.28}$$

with $h_l = g h_l''$.

A1.2 Dynamic Scenario

As described in Sec. 2.1.2, we define $\boldsymbol{p}_{\mathrm{R}}$ to be the Rx's position at time $n_0 T_{\mathrm{s}}$, which is the TOA of the first sample of the Rx signal fed to the DFT, i.e., the sample to which the Rx synchronizes. The position of the receiver at time nT_{s} is $\boldsymbol{p}_{\mathrm{R}}(nT_{\mathrm{s}}) = \boldsymbol{p}_{\mathrm{R}} + \boldsymbol{v}_{\mathrm{R}} \cdot (n - n_0)T_{\mathrm{s}}$. Then, the propagation delay of the l-th path from the Tx to the Rx reference point for a signal transmitted at time nT_{s} can be approximated as $\tau_l - (n - n_0)T_{\mathrm{s}} v_l / c$, with $v_l = \boldsymbol{v}_{\mathrm{R}}^{\mathrm{T}} \boldsymbol{u}\big(\theta_{\mathrm{R},l}\big)$ being the speed of the receiver in the direction of the AOA. The discrete time-domain channel from the j-th transmit antenna to the i-th receive antenna is

$$c_{i,j}[m,n] = \sum_{l=0}^{L-1} h'_l \tilde{g}\big(mT_{\mathrm{s}} - \tau_{l,i,j} + v_l(n-n_0)T_{\mathrm{s}}/c\big)\, \mathrm{e}^{-\mathrm{j}\,2\pi f_{\mathrm{c}}\left(\tau_{l,i,j} - v_l(n-n_0)T_{\mathrm{s}}/c\right)}. \tag{A1.29}$$

Then, $c_{i,j}[m,n] = 0$ for $m \neq \lceil \tau_{\min}/T_{\mathrm{s}} - (n-n_0)v_l/c \rceil, \ldots, \lfloor (\tau_{\max} + \tau_g)/T_{\mathrm{s}} - (n-n_0)v_l/c \rfloor$. Since $v_l/c \ll 1$ and in order to keep the notation simple, we assume $\lceil \tau_{\min}/T_{\mathrm{s}} - (n-n_0)v_l/c \rceil = \lceil \tau_{\min}/T_{\mathrm{s}} \rceil$ and $\lfloor (\tau_{\max}+\tau_g)/T_{\mathrm{s}} - (n-n_0)v_l/c \rfloor = \lfloor (\tau_{\max}+\tau_g)/T_{\mathrm{s}} \rfloor$, $\forall n$, that is, we assume that $|(n-n_0)v_l/c|$ is smaller than the distance of $\tau_{\min}/T_{\mathrm{s}}$ or $(\tau_{\max}+\tau_g)/T_{\mathrm{s}}$ from its next or previous integer. The received signal at the i-th antenna is

$$\begin{aligned}
\tilde{r}_{\mathrm{S},i}[n] &= \sum_{j=1}^{N_{\mathrm{T}}} \sum_{m=-\infty}^{\infty} c_{i,j}[m,n]\tilde{x}_{\mathrm{S},j}[n-m] + \tilde{\eta}_{\mathrm{S},i}[n] \\
&= \sum_{j=1}^{N_{\mathrm{T}}} \sum_{m=\lceil \tau_{\min}/T_{\mathrm{s}} \rceil}^{\lfloor (\tau_{\max}+\tau_g)/T_{\mathrm{s}} \rfloor} c_{i,j}[m,n]\tilde{x}_{\mathrm{S},j}[n-m] + \tilde{\eta}_{\mathrm{S},i}[n].
\end{aligned} \tag{A1.30}$$

The first sample of the transmit signal is transmitted at $n_{\mathrm{T}} T_{\mathrm{s}}$ and it arrives at the Rx at $\tau_l - (n_{\mathrm{T}} - n_0)T_{\mathrm{s}} v_l / c$. As in the static case, the Rx synchronizes to

$$\begin{aligned}
n_0 &= \lceil \tau_{\min}/T_{\mathrm{s}} - (n_{\mathrm{T}} - n_0)T_{\mathrm{s}} v_l / c \rceil + N_{\mathrm{CP}} + n_{\mathrm{T}} - n_\epsilon \\
&= \lceil \tau_{\min}/T_{\mathrm{s}} \rceil + N_{\mathrm{CP}} + n_{\mathrm{T}} - n_\epsilon,
\end{aligned} \tag{A1.31}$$

and following similar steps to the static case, we find that, analogously to (A1.12), using $n = bM + k + n_0$, the k-th sample of the b-th time-domain received OFDM symbol $\tilde{y}_i[k,b]$, $k = 0, \ldots, N-1$, at the i-th receive antenna can be expressed as

$$\tilde{y}_i[k,b] = \sum_{j=1}^{N_{\mathrm{T}}} \sum_{m'=0}^{L_{\mathrm{c}}-1} c_{i,j}[m' + \lceil \tau_{\min}/T_{\mathrm{s}} \rceil, bM + k + n_0]\tilde{x}_j[k + N_{\mathrm{CP}} - n_\epsilon - m', b] + \tilde{\eta}'_{\mathrm{S},i}[bM + k]. \tag{A1.32}$$

Applying the N-point DFT we get

$$\begin{aligned}
y'_i[p,b] &= \frac{1}{\sqrt{N}} \sum_{k=0}^{N-1} \tilde{y}_i[k,b]\, \mathrm{e}^{-\mathrm{j}\,\frac{2\pi}{N}kp} \\
&= \sum_{j=1}^{N_{\mathrm{T}}} \sum_{m'=0}^{L_{\mathrm{c}}-1} c_{i,j}[m' + \lceil \tau_{\min}/T_{\mathrm{s}} \rceil, bM + k + n_0] \frac{1}{\sqrt{N}} \sum_{k=0}^{N-1} \tilde{x}_j[k + N_{\mathrm{CP}} - n_\epsilon - m', b]\, \mathrm{e}^{-\mathrm{j}\,\frac{2\pi}{N}kp} \\
&\quad + \eta_i[p,b].
\end{aligned} \tag{A1.33}$$

Using (A1.29) and

$$\tilde{\boldsymbol{x}}[k+N_{\mathrm{CP}}-n_\epsilon-m',b]=\frac{1}{\sqrt{N}}\sum_{q\in\mathcal{P}}\boldsymbol{x}[q,b]\,\mathrm{e}^{\mathrm{j}\frac{2\pi}{N}(k-n_\epsilon-m')q} \tag{A1.34}$$

we get

$$\begin{aligned}y_i'[p,b]=\frac{1}{N}\sum_{q\in\mathcal{P}}\mathrm{e}^{-\mathrm{j}\frac{2\pi}{N}n_\epsilon q}\sum_{l=0}^{L-1}h_l'\sum_{j=1}^{N_{\mathrm{T}}}x_j[q,b]\,\mathrm{e}^{-\mathrm{j}\,2\pi f_{\mathrm{c}}\tau_{l,i,j}}\sum_{k=0}^{N-1}\mathrm{e}^{-\mathrm{j}\,2\pi f_{\mathrm{c}}\frac{v_l}{c}(bM+k)T_{\mathrm{s}}}\,\mathrm{e}^{-\mathrm{j}\frac{2\pi}{N}(p-q)k}\\ \times\sum_{m'=0}^{L_{\mathrm{c}}-1}\tilde{g}((m'+\lceil\tau_{\min}/T_{\mathrm{s}}\rceil)T_{\mathrm{s}}-\tau_{l,i,j}-(bM+k)T_{\mathrm{s}}v_l/c)\,\mathrm{e}^{-\mathrm{j}\frac{2\pi}{N}m'q}+\eta_i[p,b].\end{aligned} \tag{A1.35}$$

Employing the approximate non-integer time-shift property of the DFT (A1.19) for the last sum of (A1.35)

$$\begin{aligned}y_i'[p,b]=\sum_{q\in\mathcal{P}}g[q]\,\mathrm{e}^{-\mathrm{j}\,\omega_q(n_\epsilon-\lceil\tau_{\min}/T_{\mathrm{s}}\rceil)T_{\mathrm{s}}}\sum_{l=0}^{L-1}h_l'\,\mathrm{e}^{\mathrm{j}(\omega_{\mathrm{c}}+\omega_q)\frac{v_l}{c}bMT_{\mathrm{s}}}\sum_{j=1}^{N_{\mathrm{T}}}x_j[q,b]\,\mathrm{e}^{-\mathrm{j}(\omega_{\mathrm{c}}+\omega_q)\tau_{l,i,j}}\\ \times\frac{1}{N}\sum_{k=0}^{N-1}\mathrm{e}^{-\mathrm{j}\frac{2\pi}{N}(p-q-f_{\mathrm{c}}\frac{v_l}{c}NT_{\mathrm{s}}-\frac{v_l}{c}q)k}+\eta_i[p,b].\end{aligned} \tag{A1.36}$$

With

$$\frac{1}{N}\sum_{k=0}^{N-1}\mathrm{e}^{-\mathrm{j}\frac{2\pi}{N}(p-q-f_{\mathrm{c}}\frac{v_l}{c}NT_{\mathrm{s}}-\frac{v_l}{c}q)k}=Q_N\left(\left(\omega_p-\omega_q-\frac{\omega_{\mathrm{c}}+\omega_q}{c}v_l\right)\frac{T_{\mathrm{s}}}{2}\right), \tag{A1.37}$$

where

$$Q_N(x)=\mathrm{e}^{-\mathrm{j}(N-1)x}\,\frac{\sin(Nx)}{N\sin(x)}, \tag{A1.38}$$

and using (2.7), (A1.25) and the definition of the Tx steering vector (2.25), we write $\boldsymbol{y}'[p,b]$ as

$$\begin{aligned}\boldsymbol{y}'[p,b]&\approx\sum_{q\in\mathcal{P}}g[q]\sum_{l=0}^{L-1}h_l''\,\mathrm{e}^{-\mathrm{j}\,\omega_q(\tau_l-(\lceil\tau_{\min}/T_{\mathrm{s}}\rceil-n_\epsilon)T_{\mathrm{s}})}\,\mathrm{e}^{\mathrm{j}(\omega_{\mathrm{c}}+\omega_q)\frac{v_l}{c}bMT_{\mathrm{s}}}\,Q_N\left(\left(\omega_p-\omega_q-\frac{\omega_{\mathrm{c}}+\omega_q}{c}v_l\right)\frac{T_{\mathrm{s}}}{2}\right)\\ &\quad\times\mathrm{e}^{\mathrm{j}(\omega_{\mathrm{c}}+\omega_q)\tau_{\mathrm{R},i}(\tilde{\theta}_{\mathrm{R},l})}\,\boldsymbol{a}_{\mathrm{T},q}^{\mathrm{T}}(\tilde{\theta}_{\mathrm{T},l})\boldsymbol{x}[q,b]+\eta_i[p,b]\\ &=\sum_{q\in\mathcal{P}}g[q]\sum_{l=0}^{L-1}h_l''\,\mathrm{e}^{-\mathrm{j}\,\omega_p(\tau_l-n_0-n_{\mathrm{T}}-N_{\mathrm{CP}})T_{\mathrm{s}})}\,\mathrm{e}^{\mathrm{j}(\omega_{\mathrm{c}}+\omega_q)\frac{v_l}{c}bMT_{\mathrm{s}}}\,Q_N\left(\left(\omega_p-\omega_q-\frac{\omega_{\mathrm{c}}+\omega_q}{c}v_l\right)\frac{T_{\mathrm{s}}}{2}\right)\\ &\quad\times\mathrm{e}^{\mathrm{j}(\omega_{\mathrm{c}}+\omega_q)\tau_{\mathrm{R},i}(\tilde{\theta}_{\mathrm{R},l})}\,\boldsymbol{a}_{\mathrm{T},q}^{\mathrm{T}}(\tilde{\theta}_{\mathrm{T},l})\boldsymbol{x}[q,b]+\eta_i[p,b].\end{aligned} \tag{A1.39}$$

The last equality follows from (A1.31). Finally, as in the static scenario, applying a per-subcarrier rotation by $\mathrm{e}^{-\mathrm{j}\,\omega_p((n_0-n_{\mathrm{T}}-N_{\mathrm{CP}})T_{\mathrm{s}}+\epsilon_{\mathrm{clk}})}$ to (A1.26), assuming again that $g[q]\approx g$ for all used subcarriers and multiplying with the analog beamforming matrix $\boldsymbol{W}_{\mathrm{R}}^{\mathrm{H}}$, we get

$$\begin{aligned}\boldsymbol{y}[p,b]&=\boldsymbol{W}_{\mathrm{R}}^{\mathrm{H}}\sum_{q\in\mathcal{P}}\sum_{l=0}^{L-1}h_l\,\mathrm{e}^{-\mathrm{j}(\omega_q\tau_l'-(\omega_{\mathrm{c}}+\omega_q)\frac{v_l}{c}bMT_{\mathrm{s}})}\,Q_N\left(\left(\omega_p-\omega_q-\frac{\omega_{\mathrm{c}}+\omega_q}{c}v_l\right)\frac{T_{\mathrm{s}}}{2}\right)\\ &\quad\times\boldsymbol{a}_{\mathrm{R},q}(\tilde{\theta}_{\mathrm{R},l})\boldsymbol{a}_{\mathrm{T},q}^{\mathrm{T}}(\tilde{\theta}_{\mathrm{T},l})\boldsymbol{x}[q,b]+\boldsymbol{W}_{\mathrm{R}}^{\mathrm{H}}\eta_i[p,b]\\ &=\boldsymbol{W}_{\mathrm{R}}^{\mathrm{H}}\sum_{q\in\mathcal{P}}\boldsymbol{H}[p,q,b]\boldsymbol{x}[q,b]+\boldsymbol{W}_{\mathrm{R}}^{\mathrm{H}}\eta_i[p,b],\end{aligned} \tag{A1.40}$$

where

$$\boldsymbol{H}[p,q,b] = \sum_{l=0}^{L-1} h_l \, \mathrm{e}^{-\mathrm{j}(\omega_q \tau_l' - (\omega_\mathrm{c}+\omega_q)\frac{v_l}{c} bMT_\mathrm{s})} \, Q_N\left(\left(\omega_p - \omega_q - \frac{\omega_\mathrm{c}+\omega_q}{c} v_l\right)\frac{T_\mathrm{s}}{2}\right) \boldsymbol{a}_{\mathrm{R},q}(\tilde{\theta}_{\mathrm{R},l}) \boldsymbol{a}_{\mathrm{T},q}^{\mathrm{T}}(\tilde{\theta}_{\mathrm{T},l}). \tag{A1.41}$$

A2 Derivatives of $m[p,b]$ w.r.t. the Channel Parameter Vector

We provide the required derivatives of $\boldsymbol{m}[p,b]$ for the dynamic scenario; the required derivatives for the static scenario can be obtained from them by setting $\boldsymbol{v}_\mathrm{R} = \mathbf{0}$ (or equivalently $v_l = 0,\ \forall l$), bearing in mind that $\lim_{v_l \to 0} Q_N(\tilde{\Phi}_{p,p,l}) = 1$ and $\lim_{v_l \to 0} Q_N(\tilde{\Phi}_{p,q,l}) = 0,\ p \neq q$, where $\tilde{\Phi}_{p,q,l} = \Big(\omega_p - \omega_q - \big(\omega_\mathrm{c} + \omega_q\big)v_l/c\Big)T_\mathrm{s}/2$, and $Q_N(\cdot)$ is defined in (2.31). Setting $\tilde{\Psi}_{q,l,b} = \omega_q \tau_l' - \frac{\omega_\mathrm{c}+\omega_q}{c} v_l b M T_\mathrm{s}$, we compute the required derivatives as

$$\frac{\partial \boldsymbol{m}[p,b]}{\partial \tau_l'} = -\mathrm{j} \sum\nolimits_{q\in\mathcal{P}} \omega_q h_l \, \mathrm{e}^{-\mathrm{j}\,\tilde{\Psi}_{q,l,b}} \, Q_N(\tilde{\Phi}_{p,q,l}) \boldsymbol{W}_\mathrm{R}^\mathrm{H} \boldsymbol{a}_{\mathrm{R},q}(\tilde{\theta}_{\mathrm{R},l}) \boldsymbol{a}_{\mathrm{T},q}^\mathrm{T}(\tilde{\theta}_{\mathrm{T},l}) \boldsymbol{x}[q,b], \tag{A2.1}$$

$$\frac{\partial \boldsymbol{m}[p,b]}{\partial \tilde{\theta}_{\mathrm{T},l}} = \sum\nolimits_{q\in\mathcal{P}} h_l \, \mathrm{e}^{-\mathrm{j}\,\tilde{\Psi}_{q,l,b}} \, Q_N(\tilde{\Phi}_{p,q,l}) \boldsymbol{W}_\mathrm{R}^\mathrm{H} \boldsymbol{a}_{\mathrm{R},q}(\tilde{\theta}_{\mathrm{R},l}) \boldsymbol{a}_{\mathrm{T},q}^\mathrm{T}(\tilde{\theta}_{\mathrm{T},l}) \boldsymbol{D}_{\mathrm{T},q}^\mathrm{T}(\tilde{\theta}_{\mathrm{T},l}) \boldsymbol{x}[q,b], \tag{A2.2}$$

$$\frac{\partial \boldsymbol{m}[p,b]}{\partial \tilde{\theta}_{\mathrm{R},l}} = \sum\nolimits_{q\in\mathcal{P}} h_l \, \mathrm{e}^{-\mathrm{j}\,\tilde{\Psi}_{q,l,b}} \, Q_N(\tilde{\Phi}_{p,q,l}) \boldsymbol{W}_\mathrm{R}^\mathrm{H} \boldsymbol{D}_{\mathrm{R},q}(\tilde{\theta}_{\mathrm{R},l}) \boldsymbol{a}_{\mathrm{R},q}(\tilde{\theta}_{\mathrm{R},l}) \boldsymbol{a}_{\mathrm{T},q}^\mathrm{T}(\tilde{\theta}_{\mathrm{T},l}) \boldsymbol{x}[q,b], \tag{A2.3}$$

$$\frac{\partial \boldsymbol{m}[p,b]}{\partial |h_l|} = \sum\nolimits_{q\in\mathcal{P}} \mathrm{e}^{\arg(h_l)} \, \mathrm{e}^{-\mathrm{j}\,\tilde{\Psi}_{q,l,b}} \, Q_N(\tilde{\Phi}_{p,q,l}) \boldsymbol{W}_\mathrm{R}^\mathrm{H} \boldsymbol{a}_{\mathrm{R},q}(\tilde{\theta}_{\mathrm{R},l}) \boldsymbol{a}_{\mathrm{T},q}^\mathrm{T}(\tilde{\theta}_{\mathrm{T},l}) \boldsymbol{x}[q,b], \tag{A2.4}$$

$$\frac{\partial \boldsymbol{m}[p,b]}{\partial \arg(h_l)} = \mathrm{j} \sum\nolimits_{q\in\mathcal{P}} h_l \, \mathrm{e}^{-\mathrm{j}\,\tilde{\Psi}_{q,l,b}} \, Q_N(\tilde{\Phi}_{p,q,l}) \boldsymbol{W}_\mathrm{R}^\mathrm{H} \boldsymbol{a}_{\mathrm{R},q}(\tilde{\theta}_{\mathrm{R},l}) \boldsymbol{a}_{\mathrm{T},q}^\mathrm{T}(\tilde{\theta}_{\mathrm{T},l}) \boldsymbol{x}[q,b], \tag{A2.5}$$

$$\frac{\partial \boldsymbol{m}[p,b]}{\partial v_l} = \sum\nolimits_{q\in\mathcal{P}} h_l \, \mathrm{e}^{-\mathrm{j}\,\tilde{\Psi}_{q,l,b}} \, Q_N(\tilde{\Phi}_{p,q,l}) V_{b,p,q,l} \boldsymbol{W}_\mathrm{R}^\mathrm{H} \boldsymbol{a}_{\mathrm{R},q}(\tilde{\theta}_{\mathrm{R},l}) \boldsymbol{a}_{\mathrm{T},q}^\mathrm{T}(\tilde{\theta}_{\mathrm{T},l}) \boldsymbol{x}[q,b], \tag{A2.6}$$

where $\boldsymbol{D}_{\mathrm{T},q}(\tilde{\theta}_{\mathrm{T},l})$ is a diagonal matrix with $[\boldsymbol{D}_{\mathrm{T},q}(\tilde{\theta}_{\mathrm{T},l})]_{j,j} = -\mathrm{j}\,\frac{\omega_\mathrm{c}+\omega_q}{c} d_{\mathrm{T},j} \boldsymbol{u}_\perp^\mathrm{T}(\tilde{\theta}_{\mathrm{T},l}) \boldsymbol{u}(\psi_{\mathrm{T},j})$ and $\boldsymbol{D}_{\mathrm{R},p}(\tilde{\theta}_{\mathrm{R},l})$ is defined accordingly. Also

$$V_{b,p,q,l} = \big(\cot(\tilde{\Phi}_{p,q,l}) - N\cot(N\tilde{\Phi}_{p,q,l})\big)T_\mathrm{s}/2 + \mathrm{j}(bM + (N-1)/2)T_\mathrm{s}. \tag{A2.7}$$

A3 Entries of Transformation Matrix $\boldsymbol{T}$

The entries of $\boldsymbol{T}_{\mathrm{T}}$ ($\boldsymbol{T}_{\mathrm{R}}$) corresponding to identical parameters in $\tilde{\boldsymbol{\nu}}$ and $\boldsymbol{\nu}_{\mathrm{T}}$ ($\boldsymbol{\nu}_{\mathrm{R}}$) are equal to 1, e.g., $\partial h_{0,\Re}/\partial h_{0,\Re} = 1$. The rest non-zero entries are computed as follows:

$$\partial\tau_l/\partial\boldsymbol{p}_{\mathrm{R}} = -\boldsymbol{u}(\theta_{\mathrm{R},l})/c, \tag{A3.1}$$

$$\partial\tilde{\theta}_{\mathrm{T},l}/\partial\boldsymbol{p}_{\mathrm{R}} = \begin{cases} \boldsymbol{u}_{\perp}(\theta_{\mathrm{R},l})/d_{\mathrm{T,s},l}, & l\text{-th path is LOS}, \\ \boldsymbol{0}, & \text{otherwise}, \end{cases} \tag{A3.2}$$

$$\partial\tilde{\theta}_{\mathrm{R},l}/\partial\boldsymbol{p}_{\mathrm{R}} = \frac{\boldsymbol{u}_{\perp}(\theta_{\mathrm{R},l})}{d_{\mathrm{R,s},l}}, \tag{A3.3}$$

$$\partial\tilde{\theta}_{\mathrm{R},l}/\partial\alpha_{\mathrm{R}} = -1, \tag{A3.4}$$

$$\partial\tau_l/\partial\boldsymbol{p}_{\mathrm{T}} = -\boldsymbol{u}(\theta_{\mathrm{T},l})/c, \tag{A3.5}$$

$$\partial\tilde{\theta}_{\mathrm{T},l}/\partial\boldsymbol{p}_{\mathrm{T}} = \boldsymbol{u}_{\perp}(\theta_{\mathrm{T},l})/d_{\mathrm{T,s},l}, \tag{A3.6}$$

$$\partial\tilde{\theta}_{\mathrm{R},l}/\partial\boldsymbol{p}_{\mathrm{T}} = \begin{cases} \boldsymbol{u}_{\perp}(\theta_{\mathrm{T},l})/d_{\mathrm{R,s},l}, & l\text{-th path is LOS}, \\ \boldsymbol{0}, & \text{otherwise}, \end{cases} \tag{A3.7}$$

$$\partial\tilde{\theta}_{\mathrm{T},l}/\partial\alpha_{\mathrm{T}} = -1, \tag{A3.8}$$

$$\partial\tau_l/\partial\boldsymbol{p}_{\mathrm{s},l} = (\boldsymbol{u}(\theta_{\mathrm{T},l}) + \boldsymbol{u}(\theta_{\mathrm{R},l}))/c, \tag{A3.9}$$

$$\partial\tilde{\theta}_{\mathrm{T},l}/\partial\boldsymbol{p}_{\mathrm{s},l} = -\boldsymbol{u}_{\perp}(\theta_{\mathrm{T},l})/d_{\mathrm{T,s},l}, \tag{A3.10}$$

$$\partial\tilde{\theta}_{\mathrm{R},l}\partial\boldsymbol{p}_{\mathrm{s},l} = -\boldsymbol{u}_{\perp}(\theta_{\mathrm{R},l})/d_{\mathrm{R,s},l}. \tag{A3.11}$$

For a mobile receiver

$$\partial v_l/\partial\boldsymbol{p}_{\mathrm{R}} = -\rho_l\boldsymbol{u}_{\perp}(\theta_{\mathrm{R},l})/d_{\mathrm{R,s},l}, \tag{A3.12}$$

$$\partial v_l/\partial\boldsymbol{v}_{\mathrm{R}} = \boldsymbol{u}\big(\theta_{\mathrm{R},l}\big), \tag{A3.13}$$

$$\partial v_l/\partial\boldsymbol{p}_{\mathrm{s},l} = \rho_l\boldsymbol{u}_{\perp}\big(\theta_{\mathrm{R},l}\big)/d_{\mathrm{R,s},l}, \tag{A3.14}$$

where $\rho_l = \boldsymbol{v}_{\mathrm{R}}^{\mathrm{T}}\boldsymbol{u}_{\perp}\big(\theta_{\mathrm{R},l}\big)$. Similar expressions can be obtained for a mobile transmitter.

Table A1. BS and UE NF and Tx power values reported in 3GPP technical specification (TS) 38.855.

	FR 1	FR2
BS NF in dB	5	7
UE NF in dB	9	13
UE Tx power in dBm	23	23
indoor BS Tx power in dBm	24	24
urban micro BS Tx power in dBm	44	37
urban macro BS Tx power in dBm	49	–

A4 Choice of Noise Figure and Transmit Power for Base Stations (BSs) and User Equipments (UEs)

To get a realistic comparison of DL and UL positioning, we have to choose realistic values for the noise figure (NF) and the Tx power of the BS and the UE. We have identified some relevant values in the 3GPP technical report (TR) 38.855 [59], which is a study on new radio (NR) positioning support and describes a set of comment parameters agreed in 3GPP to be used in evaluations. The parameters for FR 1 (sub-6 GHz) and FR 2 (above 6 GHz) are shown in Table A1.

A5 Favorable Propagation Conditions for Uniform Linear Arrays (ULAs) and Uniform Circular Arrays (UCAs)

For ULAs with $\lambda_c/2$-spaced elements we have

$$d_{\mathrm{T},j} = \frac{\lambda_c}{2}|j-(N+1)/2| \tag{A5.1}$$

$$\psi_{\mathrm{T},j} = \begin{cases} \pi/2, & j < N/2 \\ -\pi/2, & j \geq N/2 \end{cases} \tag{A5.2}$$

$$\frac{1}{N_\mathrm{T}}\boldsymbol{a}_{\mathrm{T},p}^{\mathrm{H}}(\tilde{\theta}_{\mathrm{T},l})\boldsymbol{a}_{\mathrm{T},p}(\tilde{\theta}_{\mathrm{T},l'}) = \mathrm{psinc}_{N_\mathrm{T}}(x(\tilde{\theta}_{\mathrm{T},l},\tilde{\theta}_{\mathrm{T},l'})) \to 0, \tag{A5.3}$$

where

$$\mathrm{psinc}_N(x) = \frac{\sin(Nx)}{N\sin(x)} \tag{A5.4}$$

$$x(\tilde{\theta}_{\mathrm{T},l},\tilde{\theta}_{\mathrm{T},l'}) = \frac{\pi}{2}\frac{\omega_c+\omega_p}{\omega_c}(\sin(\tilde{\theta}_{\mathrm{T},l})-\sin(\tilde{\theta}_{\mathrm{T},l'})). \tag{A5.5}$$

We also compute

$$\begin{aligned}\frac{1}{N_\mathrm{T}^2}\frac{\partial}{\partial\tilde{\theta}_{\mathrm{T},l}}\boldsymbol{a}_{\mathrm{T},p}^{\mathrm{H}}(\tilde{\theta}_{\mathrm{T},l})\boldsymbol{a}_{\mathrm{T},p}(\tilde{\theta}_{\mathrm{T},l'}) &= \mathrm{psinc}_{N_\mathrm{T}}(x(\tilde{\theta}_{\mathrm{T},l},\tilde{\theta}_{\mathrm{T},l'}))\left(\cot(N_\mathrm{T}x(\tilde{\theta}_{\mathrm{T},l},\tilde{\theta}_{\mathrm{T},l'})) - \frac{\cot(x(\tilde{\theta}_{\mathrm{T},l},\tilde{\theta}_{\mathrm{T},l'}))}{N_\mathrm{T}}\right) \\ &\sim \frac{1}{x(\tilde{\theta}_{\mathrm{T},l},\tilde{\theta}_{\mathrm{T},l'})}\frac{\cos(N_\mathrm{T}x(\tilde{\theta}_{\mathrm{T},l},\tilde{\theta}_{\mathrm{T},l'}))}{N_\mathrm{T}} \to 0\end{aligned} \tag{A5.6}$$

$$\left\|\frac{\partial}{\partial\tilde{\theta}_{\mathrm{T},l}}\boldsymbol{a}_{\mathrm{T},p}(\tilde{\theta}_{\mathrm{T},l})\right\|_2^2 = \left(\frac{\omega_c+\omega_p}{\omega_c}\pi\sin(\tilde{\theta}_{\mathrm{T},l})\right)^2\frac{(N_\mathrm{T}-1)N_\mathrm{T}(N_\mathrm{T}+1)}{12}, \tag{A5.7}$$

where for any functions f, g of n, $f(n) \sim g(n)$ means that f is asymptotic to $g(n)$.

The radius of UCAs with $\lambda_c/2$-spaced elements is $\lambda_c/\big(4\sin(\pi/N_\mathrm{T})\big)$. We then have for large N_T [83]

$$\frac{1}{N_\mathrm{T}}\boldsymbol{a}_{\mathrm{T},p}^{\mathrm{H}}(\tilde{\theta}_{\mathrm{T},l})\boldsymbol{a}_{\mathrm{T},p}(\tilde{\theta}_{\mathrm{T},l'}) \sim J_0\left(\frac{\pi}{\sin(\pi/N_\mathrm{T})}\frac{\omega_c+\omega_p}{\omega_c}\sin\left(\frac{\tilde{\theta}_{\mathrm{T},l}-\tilde{\theta}_{\mathrm{T},l'}}{2}\right)\right) \to 0, \tag{A5.8}$$

where $J_0(\cdot)$ is the zero-th order Bessel function of the first kind. We also compute

$$\begin{aligned}\frac{1}{N_\mathrm{T}^2}\frac{\partial}{\partial\tilde{\theta}_{\mathrm{T},l}}\boldsymbol{a}_{\mathrm{T},p}^{\mathrm{H}}(\tilde{\theta}_{\mathrm{T},l})\boldsymbol{a}_{\mathrm{T},p}(\tilde{\theta}_{\mathrm{T},l'}) &\sim -\frac{\pi}{2N_\mathrm{T}\sin(\pi/N_\mathrm{T})}\frac{\omega_c+\omega_p}{\omega_c}\cos\left(\frac{\tilde{\theta}_{\mathrm{T},l}-\tilde{\theta}_{\mathrm{T},l'}}{2}\right)\times \\ &\quad J_1\left(\frac{\pi}{\sin(\pi/N_\mathrm{T})}\frac{\omega_c+\omega_p}{\omega_c}\sin\left(\frac{\tilde{\theta}_{\mathrm{T},l}-\tilde{\theta}_{\mathrm{T},l'}}{2}\right)\right) \to 0\end{aligned} \tag{A5.9}$$

$$\left\|\frac{\partial}{\partial\tilde{\theta}_{\mathrm{T},l}}\boldsymbol{a}_{\mathrm{T},p}(\tilde{\theta}_{\mathrm{T},l})\right\|_2^2 = \frac{1}{2}\left(\frac{\omega_c+\omega_p}{\omega_c}\frac{\pi}{2\sin(\pi/N_\mathrm{T})}\right)^2 N_\mathrm{T}, \tag{A5.10}$$

where $J_1(\cdot)$ is the first order Bessel function of the first kind.

A6 Proof of Theorem 2.1

We first have to compute the asymptotic expressions for the entries of the channel parameters FIM $\boldsymbol{J}_{\tilde{\boldsymbol{\nu}}}^{(\mathrm{o})}$. In order to facilitate readability and understanding, instead of referring to the entries of $\boldsymbol{J}_{\tilde{\boldsymbol{\nu}}}^{(\mathrm{o})}$ by their position in the matrix, e.g. $J_{\nu,1,2}^{(\mathrm{o})}$, we refer to them by using as indices the variables they correspond to, e.g., $J_{\tau_0'\tilde{\theta}_{\mathrm{T},0}}$. Using (2.45), (2.68) and (A2.1)-(A2.5) and the assumptions 1-2 of Section 2.4, we find that

$$J_{\tau_l'\tau_l'} = \delta_{\mathrm{R,T}}|h_l|^2 \sum_{p\in\mathcal{P}} \gamma[p]\omega_p^2, \tag{A6.1}$$

$$J_{\tilde{\theta}_{\mathrm{T},l}\tilde{\theta}_{\mathrm{T},l}} = \delta_{\mathrm{R,T}}|h_l|^2 \big(\bar{\omega}_c/c\big)^2 S_{\mathrm{T}}(\tilde{\theta}_{\mathrm{T},l}), \tag{A6.2}$$

$$J_{\tilde{\theta}_{\mathrm{R},l}\tilde{\theta}_{\mathrm{R},l}} = \delta_{\mathrm{R,T}}|h_l|^2 \big(\bar{\omega}_c/c\big)^2 S_{\mathrm{R}}(\tilde{\theta}_{\mathrm{R},l}), \tag{A6.3}$$

$$J_{|h_l||h_l|} = \delta_{\mathrm{R,T}}, \tag{A6.4}$$

$$J_{\arg(h_l)\arg(h_l)} = \delta_{\mathrm{R,T}}|h_l|^2, \tag{A6.5}$$

$$J_{\tau_l \arg(h_l)} = -\delta_{\mathrm{R,T}}|h_l|^2 \sum_{p\in\mathcal{P}} \gamma[p]\omega_p, \tag{A6.6}$$

where with some abuse of notation the equality sign is used to denote that the asymptotic values are equal. Using the notion of the EFIM, we can show that, as far as position and orientation information is concerned, we can exclude the channel gains from the parameter vectors, as long as we include the uncertainty they introduce to the model by replacing the time-related FIM entries $\left\{J_{\tau_l'\tau_l'}\right\}_{l=0}^{L-1}$ with $\left\{J'_{\tau_l'\tau_l'},\right\}_{l=0}^{L-1}$, where $J'_{\tau_l'\tau_l'} = \delta_{\mathrm{R,T}}\beta^2|h_l|^2$. Using the favorable propagation conditions (2.68)-(2.70) and following the Bachmann-Landau asymptotic notations[1] [84], we can show that all the diagonal entries of the FIM are $\Theta(x^3)$, where $x \in N_{\mathrm{T}}, N_{\mathrm{R}}, F_{\mathrm{s}}$, e.g., $J_{\tau_l\tau_l} = \Theta(N_{\mathrm{R}}F_{\mathrm{s}}^2)$, and the rest of the entries are $o(x^3)$, which means they can be ignored in the computation of the asymptotic position and orientation EFIM. For brevity, we only present the derivation for the case when the LOS path is available. In order to make the expressions more compact, when the same variable is used in both indices we write it only once; e.g., we write $J'_{\tau_0'}$ instead of $J'_{\tau_0'\tau_0'}$. Using the expressions from Appendix A3 for the entries of the Fisher information transformation matrices, we compute

$$\boldsymbol{T}_{\mathrm{po}}\boldsymbol{J}_{\tilde{\boldsymbol{\nu}}}\boldsymbol{T}_{\mathrm{po}}^{\mathrm{T}} = \frac{J'_{\tau_0}}{c^2}\boldsymbol{z}_{\tau_0}\boldsymbol{z}_{\tau_0}^{\mathrm{T}} + \frac{J_{\tilde{\theta}_{\mathrm{T},0}}}{d_{\mathrm{T,s},0}^2}\boldsymbol{z}_{\theta_{\mathrm{T},0}}\boldsymbol{z}_{\theta_{\mathrm{T},0}}^{\mathrm{T}} + \frac{J_{\tilde{\theta}_{\mathrm{R},0}}}{d_{\mathrm{R,s},0}^2}\boldsymbol{z}_{\theta_{\mathrm{R},0}}\boldsymbol{z}_{\theta_{\mathrm{R},0}}^{\mathrm{T}} + \sum_{l=1}^{L-1}\left(\frac{J'_{\tau_l}}{c^2}\boldsymbol{z}_{\tau_l}\boldsymbol{z}_{\tau_l}^{\mathrm{T}} + \frac{J_{\tilde{\theta}_{\mathrm{R},l}}}{d_{\mathrm{R,s},l}^2}\boldsymbol{z}_{\theta_{\mathrm{R},l}}\boldsymbol{z}_{\theta_{\mathrm{R},l}}^{\mathrm{T}}\right), \tag{A6.7}$$

where $\boldsymbol{z}_{\tau_l} = [-\boldsymbol{u}^{\mathrm{T}}\big(\theta_{\mathrm{R},l}\big),\ 0]^{\mathrm{T}}$ and $\boldsymbol{z}_{\theta_{\mathrm{R},l}} = [\boldsymbol{u}_{\perp}^{\mathrm{T}}\big(\theta_{\mathrm{R},l}\big),\ -d_{\mathrm{R,s},l}]^{\mathrm{T}}$. We also write

$$\boldsymbol{T}_{\mathrm{np}}\boldsymbol{J}_{\tilde{\boldsymbol{\nu}}}\boldsymbol{T}_{\mathrm{np}}^{\mathrm{T}} + \frac{1}{\sigma_{\mathrm{clk}}^2}\boldsymbol{e}_1\boldsymbol{e}_1^{\mathrm{T}} = \begin{bmatrix} \sum_{l=0}^{L-1} J'_{\tau_l'} + \frac{1}{\sigma_{\mathrm{clk}}^2} & \boldsymbol{b}^{\mathrm{T}} \\ \boldsymbol{b} & \boldsymbol{C} \end{bmatrix}, \tag{A6.8}$$

where $\boldsymbol{b} = [J'_{\tau_1'}\boldsymbol{\nu}_1^{\mathrm{T}}/c, \ldots, J'_{\tau_{L-1}'}\boldsymbol{\nu}_{L-1}^{\mathrm{T}}/c]^{\mathrm{T}}$, $\boldsymbol{\nu}_l = \boldsymbol{u}(\theta_{\mathrm{T},l}) + \boldsymbol{u}\big(\theta_{\mathrm{R},l}\big)$ and $\boldsymbol{C}$ is a block diagonal matrix with the following 2×2 matrices on its diagonal

$$\boldsymbol{J}_{s,l} = \frac{J'_{\tau_l'}}{c^2}\boldsymbol{\nu}_l\boldsymbol{\nu}_l^{\mathrm{T}} + \frac{J_{\tilde{\theta}_{\mathrm{T},l}}}{d_{\mathrm{T,s},l}^2}\boldsymbol{u}_{\perp}\big(\theta_{\mathrm{T},l}\big)\boldsymbol{u}_{\perp}^{\mathrm{T}}\big(\theta_{\mathrm{T},l}\big) + \frac{J_{\tilde{\theta}_{\mathrm{R},l}}}{d_{\mathrm{R,s},l}^2}\boldsymbol{u}_{\perp}\big(\theta_{\mathrm{R},l}\big)\boldsymbol{u}_{\perp}^{\mathrm{T}}\big(\theta_{\mathrm{R},l}\big). \tag{A6.9}$$

[1] $f(x) = o(g(x))$ means that $\lim_{x\to\infty}\left|\frac{f(x)}{g(x)}\right| = 0$ and $f(x) = \Theta(g(x))$ means that $0 < \liminf_{x\to\infty}\left|\frac{f(x)}{g(x)}\right| \leq \limsup_{x\to\infty}\left|\frac{f(x)}{g(x)}\right| < \infty$

In order to compute $\left(\boldsymbol{T}_{\mathrm{np}}\boldsymbol{J}_{\tilde{\boldsymbol{\nu}}}\boldsymbol{T}_{\mathrm{np}}^{\mathrm{T}}\right)^{-1}$ using block matrix inversion, we still need to compute $\boldsymbol{C}^{-1}$, which in turn, using block diagonal matrix inversion, requires the computation of $\boldsymbol{J}_{\mathrm{s},l}^{-1}$. We compute $\boldsymbol{J}_{\mathrm{s},l}^{-1}$ as [16, Lemma 1]

$$\boldsymbol{J}_{\mathrm{s},l}^{-1} = \frac{1}{\left|\boldsymbol{J}_{\mathrm{s},l}\right|}\left[\frac{J'_{\tau'_l}}{c^2}\boldsymbol{\nu}_{l,\perp}\boldsymbol{\nu}_{l,\perp}^{\mathrm{T}} + \frac{J_{\tilde{\theta}_{\mathrm{T},l}}}{d_{\mathrm{T,s},l}^2}\boldsymbol{u}(\theta_{\mathrm{T},l})\boldsymbol{u}^{\mathrm{T}}(\theta_{\mathrm{T},l}) + \frac{J_{\tilde{\theta}_{\mathrm{R},l}}}{d_{\mathrm{R,s},l}^2}\boldsymbol{u}(\theta_{\mathrm{R},l})\boldsymbol{u}^{\mathrm{T}}(\theta_{\mathrm{R},l})\right], \tag{A6.10}$$

with $\boldsymbol{\nu}_{l,\perp} = \boldsymbol{u}_{\perp}(\theta_{\mathrm{T},l}) + \boldsymbol{u}_{\perp}(\theta_{\mathrm{R},l})$ and

$$\left|\boldsymbol{J}_{s,l}\right| = \frac{J'_{\tau'_l}}{c^2}(1+\cos(\Delta\theta_l))^2\left(\frac{J_{\tilde{\theta}_{\mathrm{T},l}}}{d_{\mathrm{T,s},l}^2} + \frac{J_{\tilde{\theta}_{\mathrm{R},l}}}{d_{\mathrm{R,s},l}^2}\right) + \frac{J_{\tilde{\theta}_{\mathrm{T},l}}J_{\tilde{\theta}_{\mathrm{R},l}}}{d_{\mathrm{T,s},l}^2 d_{\mathrm{R,s},l}^2}\sin^2(\Delta\theta_l). \tag{A6.11}$$

Therefore, using (A6.8)-(A6.11), $\boldsymbol{u}^{\mathrm{T}}(\theta_{\mathrm{T},l})\boldsymbol{u}(\theta_{\mathrm{R},l}) = \cos(\Delta\theta_l)$ and $\boldsymbol{u}^{\mathrm{T}}(\theta_{\mathrm{T},l})\boldsymbol{u}_{\perp}(\theta_{\mathrm{R},l} = \sin(\Delta\theta_l)$, after some algebraic manipulations we find that

$$\begin{aligned}
&\boldsymbol{T}_{\mathrm{po}}\boldsymbol{J}_{\tilde{\boldsymbol{\nu}}}\boldsymbol{T}_{\mathrm{np}}^{\mathrm{T}}\left(\boldsymbol{T}_{\mathrm{np}}\boldsymbol{J}_{\tilde{\boldsymbol{\nu}}}\boldsymbol{T}_{\mathrm{np}}^{\mathrm{T}} + \frac{1}{\sigma_{\mathrm{clk}}^2}\boldsymbol{e}_1\boldsymbol{e}_1^{\mathrm{T}}\right)^{-1}\boldsymbol{T}_{\mathrm{np}}\boldsymbol{J}_{\tilde{\boldsymbol{\nu}}}\boldsymbol{T}_{\mathrm{po}}^{\mathrm{T}} \\
&\quad= \sum_{l=1}^{L-1}\left[\frac{(J'_{\tau'_l})^2}{c^4}\frac{(1+\cos(\Delta\theta_l))^2}{\left|\boldsymbol{J}_{s,l}\right|}\left(\frac{J_{\tilde{\theta}_{\mathrm{T},l}}}{d_{\mathrm{T,s},l}^2} + \frac{J_{\tilde{\theta}_{\mathrm{R},l}}}{d_{\mathrm{R,s},l}^2}\right)\boldsymbol{z}_{\tau_l}\boldsymbol{z}_{\tau_l}^{\mathrm{T}}\right. \\
&\quad\quad+\frac{J_{\tilde{\theta}_{\mathrm{R},l}}^2}{d_{\mathrm{R,s},l}^4}\left(\frac{J'_{\tau'_l}\left(1+\cos(\Delta\theta_l)\right)^2}{c^2\left|\boldsymbol{J}_{s,l}\right|} + \frac{J_{\tilde{\theta}_{\mathrm{T},l}}\sin^2(\Delta\theta_l)}{d_{\mathrm{T,s},l}^2\left|\boldsymbol{J}_{s,l}\right|}\right)\boldsymbol{z}_{\theta_{\mathrm{R},l}}\boldsymbol{z}_{\theta_{\mathrm{R},l}}^{\mathrm{T}} \\
&\quad\quad\left.+\frac{J'_{\tau'_l}J_{\tilde{\theta}_{\mathrm{T},l}}J_{\tilde{\theta}_{\mathrm{R},l}}}{c^2 d_{\mathrm{T,s},l}^2 d_{\mathrm{R,s},l}^2}\frac{\left(1+\cos(\Delta\theta_l)\right)\sin(\Delta\theta_l)}{\left|\boldsymbol{J}_{s,l}\right|}\left(\boldsymbol{z}_{\tau_l}\boldsymbol{z}_{\theta_{\mathrm{R},l}}^{\mathrm{T}} + \boldsymbol{z}_{\theta_{\mathrm{R},l}}\boldsymbol{z}_{\tau_l}^{\mathrm{T}}\right)\right] + \frac{1}{\hat{K}_{\epsilon_{\mathrm{clk}}}}\hat{\boldsymbol{z}}_{\epsilon_{\mathrm{clk}}}\hat{\boldsymbol{z}}_{\epsilon_{\mathrm{clk}}}^{\mathrm{T}},
\end{aligned} \tag{A6.12}$$

where

$$\hat{K}_{\epsilon_{\mathrm{clk}}} = \frac{J'_{\tau'_0} + \frac{1}{\sigma_{\mathrm{clk}}^2}}{c^2} + \sum_{l=1}^{L-1}\frac{J'_{\tau'_l}J_{\tilde{\theta}_{\mathrm{T},l}}J_{\tilde{\theta}_{\mathrm{R},l}}}{c^2 d_{\mathrm{T,s},l}^2 d_{\mathrm{R,s},l}^2\left|\boldsymbol{J}_{s,l}\right|}\sin^2(\Delta\theta_l), \tag{A6.13}$$

$$\hat{\boldsymbol{z}}_{\epsilon_{\mathrm{clk}}} = \sum_{l=1}^{L-1}\frac{J'_{\tau'_l}J_{\tilde{\theta}_{\mathrm{T},l}}J_{\tilde{\theta}_{\mathrm{R},l}}}{c^2 d_{\mathrm{T,s},l}^2 d_{\mathrm{R,s},l}^2\left|\boldsymbol{J}_{s,l}\right|}\sin(\Delta\theta_l)[\boldsymbol{\nu}_l^{\mathrm{T}},\ -(1+\cos(\Delta\theta_l))d_{\mathrm{R,s},l}]^{\mathrm{T}}. \tag{A6.14}$$

Combining (A6.7), (A6.11) and (A6.12) and using the trigonometric identities

$$\begin{aligned}
1+\cos(\Delta\theta_l) &= 2\cos^2(\Delta\theta_l/2), \\
\sin(\Delta\theta_l) &= 2\sin(\Delta\theta_l/2)\cos(\Delta\theta_l/2),
\end{aligned}$$

we obtain the desired result.

A7 Entries of $\boldsymbol{M}_l$

The entries of $\boldsymbol{M}_l$, which is involved in the computation of the position and orientation EFIM when prior knowledge of the VAs' locations is available, are given by:

$$M_{l,1,1} = \frac{i_{\tau_l}}{Q_l}\left(Q_l - i_{\tau_l}\left((i_{\theta_{\mathrm{T},l}} + i_{\theta_{\mathrm{R},l}})\left(\frac{d_{\mathrm{R,s},l}}{d_l}\right)^2 + \frac{1}{(1-\rho_l^2)\sigma_{l,\perp}^2}\right)\right), \tag{A7.1}$$

$$M_{l,2,2} = \frac{i_{\theta_{\mathrm{T},l}}}{Q_l}\left(\frac{d_{\mathrm{T,s},l}}{d_l}\right)^2\left(i_{\tau_l}\left(i_{\theta_{\mathrm{R},l}}\left(\frac{d_{\mathrm{R,s},l}}{d_l}\right)^2 + \frac{1}{(1-\rho_l^2)\sigma_{l,\perp}^2}\right) + \frac{1}{(1-\rho_l^2)\sigma_{l,\parallel}^2}\left(i_{\theta_{\mathrm{R},l}}\left(\frac{d_{\mathrm{R,s},l}}{d_l}\right)^2 + \frac{1}{\sigma_{l,\perp}^2}\right)\right), \tag{A7.2}$$

$$M_{l,3,3} = \frac{i_{\theta_{\mathrm{R},l}}}{Q_l}\left(\frac{d_{\mathrm{R,s},l}}{d_l}\right)^2\left(Q_l - i_{\theta_{\mathrm{R},l}}\left(\frac{d_{\mathrm{R,s},l}}{d_l}\right)^2\left(i_{\tau_l} + \frac{1}{(1-\rho_l^2)\sigma_{l,\parallel}^2} + i_{\theta_{\mathrm{T},l}}\tan^2(\Delta\theta_l/2)\right)\right), \tag{A7.3}$$

$$\begin{aligned} M_{l,1,2} = M_{l,2,1} = \frac{i_{\tau_l} i_{\theta_{\mathrm{T},l}}}{Q_l}\frac{d_{\mathrm{T,s},l}}{d_l}\Bigg(&\tan(\Delta\theta_l/2)\left(i_{\theta_{\mathrm{R},l}}\left(\frac{d_{\mathrm{R,s},l}}{d_l}\right)^2 + \frac{1}{(1-\rho_l^2)\sigma_{l,\perp}^2}\right) \\ &- \frac{d_{\mathrm{R,s},l}}{d_l}\frac{\rho_l}{(1-\rho_l^2)\sigma_{l,\parallel}\sigma_{l,\perp}}\Bigg), \end{aligned} \tag{A7.4}$$

$$M_{l,1,3} = M_{l,3,1} = \frac{i_{\tau_l} i_{\theta_{\mathrm{R},l}}}{Q_l}\left(\frac{d_{\mathrm{R,s},l}}{d_l}\right)^2\left(\frac{\rho_l}{(1-\rho_l^2)\sigma_{l,\parallel}\sigma_{l,\perp}} + i_{\theta_{\mathrm{T},l}}\tan(\Delta\theta_l/2)\frac{d_{\mathrm{R,s},l}}{d_l}\right), \tag{A7.5}$$

$$\begin{aligned} M_{l,2,3} = M_{l,3,2} = \frac{i_{\theta_{\mathrm{T},l}} i_{\theta_{\mathrm{R},l}}}{Q_l}\left(\frac{d_{\mathrm{R,s},l}}{d_l}\right)^2\frac{d_{\mathrm{T,s},l}}{d_l}\Bigg(&\frac{d_{\mathrm{R,s},l}}{d_l}\left(i_{\tau_l} + \frac{1}{(1-\rho_l^2)\sigma_{l,\parallel}^2}\right) \\ &- \tan(\Delta\theta_l/2)\frac{\rho_l}{(1-\rho_l^2)\sigma_{l,\parallel}\sigma_{l,\perp}}\Bigg), \end{aligned} \tag{A7.6}$$

where

$$\begin{aligned} Q_l = i_{\tau_l}\Bigg(&(i_{\theta_{\mathrm{T},l}} + i_{\theta_{\mathrm{R},l}})\left(\frac{d_{\mathrm{R,s},l}}{d_l}\right)^2 + \frac{1}{(1-\rho_l^2)\sigma_{l,\perp}^2}\Bigg) + \left((i_{\theta_{\mathrm{T},l}} + i_{\theta_{\mathrm{R},l}})\left(\frac{d_{\mathrm{R,s},l}}{d_l}\right)^2 + \frac{1}{\sigma_{l,\perp}^2}\right)\frac{1}{(1-\rho_l^2)\sigma_{l,\parallel}^2}, \\ &+ i_{\theta_{\mathrm{T},l}}\tan^2(\Delta\theta_l/2)\left(i_{\theta_{\mathrm{R},l}}\left(\frac{d_{\mathrm{R,s},l}}{d_l}\right)^2 + \frac{1}{(1-\rho_l^2)\sigma_{l,\perp}^2}\right) - 2i_{\theta_{\mathrm{T},l}}\frac{d_{\mathrm{R,s},l}}{d_l}\tan(\Delta\theta_l/2)\frac{\rho_l}{(1-\rho_l^2)\sigma_{l,\parallel}\sigma_{l,\perp}}, \end{aligned} \tag{A7.7}$$

$$d_l = d_{\mathrm{T,s},l} + d_{\mathrm{R,s},l}. \tag{A7.8}$$

A8 Detection of New Paths

In this section, we provide the justification for the formulation of the optimization problem (3.17) that is solved to obtain a new potential path in the channel parameter estimation algorithm (Alg. 1). It can also be found in [48], but we also provide it here for the reader's convenience.

We introduce the sparse atomic measure $\mu(\tau', \tilde{\theta}_\mathrm{T}, \tilde{\theta}_\mathrm{R})$ over the space $\Omega = [0, N_\mathrm{CP}T_\mathrm{s}]\times[-\pi, \pi)\times[-\pi, \pi)$, which is supported on a small number of points, i.e.,

$$\mu(\tau', \tilde{\theta}_\mathrm{T}, \tilde{\theta}_\mathrm{R}) = \sum_{l=0}^{L'-1} h_l \delta_{\tau'-\tau'_l, \tilde{\theta}_\mathrm{T}-\tilde{\theta}_{\mathrm{T},l}, \tilde{\theta}_\mathrm{R}-\tilde{\theta}_{\mathrm{R},l}} \tag{A8.1}$$

where $\delta_{\tau', \tilde{\theta}_\mathrm{T}, \tilde{\theta}_\mathrm{R}}$ is the Dirac function. We can write the observation model as

$$\boldsymbol{Y} = C\mu + \boldsymbol{N}, \tag{A8.2}$$

where C is the forward operator, defined as

$$C\mu = \int_{\tau', \tilde{\theta}_\mathrm{T}, \tilde{\theta}_\mathrm{R}\in\Omega} \boldsymbol{C}(\tau', \tilde{\theta}_\mathrm{T}, \tilde{\theta}_\mathrm{R})\mu(\tau', \tilde{\theta}_\mathrm{T}, \tilde{\theta}_\mathrm{R})\,\mathrm{d}\tau'\,\mathrm{d}\tilde{\theta}_\mathrm{T}\,\mathrm{d}\tilde{\theta}_\mathrm{R}. \tag{A8.3}$$

Making use of the above mathematical description and utilizing the knowledge that μ is a sparse measure (otherwise recovery of μ would be impossible), we can now rewrite the original optimization problem (3.11) as

$$\min_{\mu} \Lambda(\boldsymbol{Y} - C\mu) \quad \text{s.t. } |\operatorname{supp}\mu| \leq L_\mathrm{max}, \tag{A8.4}$$

where $\operatorname{supp}\mu$ is the support of μ. The problem is non-convex, due to the non-convex constraint. Finally, we replace the constraint on the cardinality of the support of μ with a (convex) constraint on its total variation norm [85] of μ, which is defined as

$$\|\mu\|_\mathrm{TV} = \sup_{\|f\|_\infty\leq 1} \Re\left\{\int_{\tau', \tilde{\theta}_\mathrm{T}, \tilde{\theta}_\mathrm{R}\in\Omega} f^*(\tau', \tilde{\theta}_\mathrm{T}, \tilde{\theta}_\mathrm{R})\mu(\tau', \tilde{\theta}_\mathrm{T}, \tilde{\theta}_\mathrm{R})\,\mathrm{d}\tau'\,\mathrm{d}\tilde{\theta}_\mathrm{T}\,\mathrm{d}\tilde{\theta}_\mathrm{R}\right\}. \tag{A8.5}$$

For measures of the form of (A8.1), the total variation norm is

$$\|\mu\|_\mathrm{TV} = \sum_{l=0}^{L-1} |h_l| = \|\boldsymbol{h}\|_1, \tag{A8.6}$$

where $\boldsymbol{h} = [h_0, \ldots, h_{L-1}]^\mathrm{T}$. Hence, we can express the problem in a Lagrangian form as

$$\min_{\mu} \Lambda(\boldsymbol{Y} - C\mu) \quad \text{s.t. } \|\mu\|_\mathrm{TV} \leq \xi, \tag{A8.7}$$

where $\xi > 0$ is the regularization parameter. Problem (A8.7) is a convex optimization problem.

Conditional gradient methods are based on successive linear approximations of the convex objective (using the first order derivative) and minimizations of the resulting linear function over the bounded convex feasible set Ω. Let $f(\mu) = \Lambda(\boldsymbol{Y} - C\mu)$ be the objective function, $\mu^{(i)}$ the

recovered sparse measure at the i-th iteration and $\boldsymbol{R}_i = \boldsymbol{Y} - C\mu^{(i)}$ the corresponding residual. The directional derivative of f at $\mu^{(i)}$ in the direction of the measure s is [48]

$$\begin{aligned} f'(s, \mu^{(i)}) &= \lim_{t \to 0} \frac{f(\mu^{(i)} + ts) - f(\mu^{(i)})}{t} \\ &= \lim_{t \to 0} \frac{\Lambda(\boldsymbol{R}_i + tCs) - \Lambda(\boldsymbol{R}_i)}{t} \\ &= \Lambda'(Cs; \boldsymbol{R}_i) = \langle \nabla \Lambda(\boldsymbol{R}_i), Cs \rangle, \end{aligned} \tag{A8.8}$$

where for our problem the inner product $\langle \nabla \Lambda(\boldsymbol{R}_i), Cs \rangle$ is defined as

$$\langle \nabla \Lambda(\boldsymbol{R}_i), Cs \rangle = \operatorname{tr}(\nabla \Lambda(\boldsymbol{R}_i) Cs) = \operatorname{tr}(\boldsymbol{R}_i^{\mathrm{H}} Cs). \tag{A8.9}$$

The linear approximation $\bar{f}$ of f at $x = \mu^{(i)} + s$ is

$$\bar{f}(\mu^{(i)} + s) = f(\mu^{(i)}) + f'(s; \mu^{(i)}). \tag{A8.10}$$

The minimization of $\bar{f}$ is achieved by the minimization of the directional derivative $f'(s; \mu^{(i)})$. Hence, interchanging the integration in C with the inner product, we have to solve

$$\min_{s} \int_{\tau', \tilde{\theta}_{\mathrm{T}}, \tilde{\theta}_{\mathrm{R}}} \operatorname{tr}(\boldsymbol{R}_i^{\mathrm{H}} \boldsymbol{C}(\tau', \tilde{\theta}_{\mathrm{T}}, \tilde{\theta}_{\mathrm{R}})) s(\tau', \tilde{\theta}_{\mathrm{T}}, \tilde{\theta}_{\mathrm{R}}) \, \mathrm{d}\tau' \, \mathrm{d}\tilde{\theta}_{\mathrm{T}} \, \mathrm{d}\tilde{\theta}_{\mathrm{R}} \quad \text{s.t. } \|s\|_{\mathrm{TV}} \leq \xi. \tag{A8.11}$$

Noting that the objective is lower bounded by $-\max_{\tau', \tilde{\theta}_{\mathrm{T}}, \tilde{\theta}_{\mathrm{R}}} |\operatorname{tr}(\boldsymbol{R}_i^{\mathrm{H}} \boldsymbol{C}(\tau', \tilde{\theta}_{\mathrm{T}}, \tilde{\theta}_{\mathrm{R}}))| \|s\|_{\mathrm{TV}}$, an optimal solution is the point mass $-\xi \operatorname{sgn}(\operatorname{tr}(\boldsymbol{R}_i^{\mathrm{H}} \boldsymbol{C}(\tau'^{(i)}, \tilde{\theta}_{\mathrm{T}}^{(i)}, \tilde{\theta}_{\mathrm{R}}^{(i)})))\delta_{\tau' - \tau'^{(i)}, \tilde{\theta}_{\mathrm{T}} - \tilde{\theta}_{\mathrm{T}}^{(i)}, \tilde{\theta}_{\mathrm{R}} - \tilde{\theta}_{\mathrm{R}}^{(i)}}$, where

$$\tau'^{(i)}, \tilde{\theta}_{\mathrm{T}}^{(i)}, \tilde{\theta}_{\mathrm{R}}^{(i)} = \operatorname*{argmax}_{(\tau', \tilde{\theta}_{\mathrm{T}}, \tilde{\theta}_{\mathrm{R}}) \in \Omega} \left| \operatorname{tr}(\boldsymbol{R}_i^{\mathrm{H}} \boldsymbol{C}(\tau', \tilde{\theta}_{\mathrm{T}}, \tilde{\theta}_{\mathrm{R}})) \right|. \tag{A8.12}$$

A9 Proof of Theorem 4.1

Since we consider the LOS-only case, the channel parameter vector is $\tilde{\boldsymbol{\nu}} = [\tau',\ \tilde{\theta}_{\mathrm{T}},\ \tilde{\theta}_{\mathrm{R}},\ |h|,\ \arg(h)]^{\mathrm{T}}$ and the position parameter vector is $\boldsymbol{\nu} = [\boldsymbol{p}_{\mathrm{R}},\ \alpha_{\mathrm{R}},\ |h|,\ \arg(h)]^{\mathrm{T}}$. Here, we do not consider the clock synchronization error ϵ_{clk}. As we have seen in Chapter 2, it cannot be estimated in the LOS-only case and its effect on the SPEB is an additional term equal to $c^2\sigma_{\mathrm{clk}}^2$, which is independent of the reference signal.

With the Tx array's centroid $\bar{\boldsymbol{p}}_{\mathrm{T}} = \sum_{j=1}^{N_T} \boldsymbol{p}_{\mathrm{T},j}$ chosen as its reference point we have $\boldsymbol{a}_{\mathrm{T}}^{\mathrm{H}}(\tilde{\theta}_{\mathrm{T}})\boldsymbol{D}_{\mathrm{T}}(\tilde{\theta}_{\mathrm{T}})\boldsymbol{a}_{\mathrm{T}}(\tilde{\theta}_{\mathrm{T}}) = 0$, that is, $\boldsymbol{f}_{\mathrm{opt},1}(\tilde{\theta}_{\mathrm{T}})$ and $\boldsymbol{f}_{\mathrm{opt},2}(\theta_{\mathrm{T}})$, as defined in (4.7)-(4.8), are orthogonal. Hence, we write

$$\boldsymbol{x}[p,b] = \left[\boldsymbol{f}_{\mathrm{opt},1}(\tilde{\theta}_{\mathrm{T}}),\ \boldsymbol{f}_{\mathrm{opt},2}(\tilde{\theta}_{\mathrm{T}}),\ \boldsymbol{W}(\tilde{\theta}_{\mathrm{T}})\right]\boldsymbol{\zeta}[p,b], \tag{A9.1}$$

where $\boldsymbol{W}(\tilde{\theta}_{\mathrm{T}}) \in \mathbb{C}^{N_{\mathrm{T}}\times N_{\mathrm{T}}-2}$ is a set of vectors which span the subspace of $\mathbb{C}^{N_{\mathrm{T}}}$ that is orthogonal to $\boldsymbol{f}_{\mathrm{opt},1}(\tilde{\theta}_{\mathrm{T}})$ and $\boldsymbol{f}_{\mathrm{opt},2}(\tilde{\theta}_{\mathrm{T}})$. This imposes no restrictions on the reference signal, as we have just expressed it as a linear combination of basis vectors of $\mathbb{C}^{N_{\mathrm{T}}}$. Computing $\boldsymbol{J}_{\tilde{\boldsymbol{\nu}}}$ according to (2.45), we find that transmission on the subspace spanned by $\boldsymbol{W}(\tilde{\theta}_{\mathrm{T}})$ does not contribute to the Fisher information. Therefore, all the energy should be allocated to the subspace spanned by $\boldsymbol{f}_{\mathrm{opt},1}(\tilde{\theta}_{\mathrm{T}})$ and $\boldsymbol{f}_{\mathrm{opt},2}(\tilde{\theta}_{\mathrm{T}})$.

After some computations we get

$$\mathrm{SPEB} = \frac{c^2}{J'_{\tau} - \left(J'_{\tau\theta_{\mathrm{T}}}\right)^2/J'_{\theta_{\mathrm{T}}}} + \frac{d^2}{J'_{\theta_{\mathrm{T}}} - \left(J'_{\tau\theta_{\mathrm{T}}}\right)^2/J'_{\tau}}, \tag{A9.2}$$

where

$$J'_{\tau} = \frac{2N_{\mathrm{R}}N_{\mathrm{T}}|h|^2}{\sigma_{\eta,\mathrm{R}}^2}\left(\sum_{p\in\mathcal{P}}\sum_{b=0}^{N_{\mathrm{B}}-1}\left|\zeta_1[p,b]\right|^2\omega_p^2 - \frac{\left(\sum_{p\in\mathcal{P}}\omega_p\sum_{b=0}^{N_{\mathrm{B}}-1}\left|\zeta_1[p,b]\right|^2\right)^2}{\sum_{p\in\mathcal{P}}\sum_{b=0}^{N_{\mathrm{B}}-1}\left|\zeta_1[p,b]\right|^2}\right), \tag{A9.3}$$

$$J'_{\theta_{\mathrm{T}}} = \frac{2N_{\mathrm{R}}N_{\mathrm{T}}|h|^2}{\sigma_{\eta,\mathrm{R}}^2}\frac{\omega_{\mathrm{c}}^2}{c^2}\Xi_{\mathrm{T}}^2\left(\tilde{\theta}_{\mathrm{T}}\right)\left(\sum_{p\in\mathcal{P}}\sum_{b=0}^{N_{\mathrm{B}}-1}\left|\zeta_2[p,b]\right|^2 - \frac{\left|\sum_{p\in\mathcal{P}}\sum_{b=0}^{N_{\mathrm{B}}-1}\zeta_1[p,b]\zeta_2^*[p,b]\right|^2}{\sum_{p\in\mathcal{P}}\sum_{b=0}^{N_{\mathrm{B}}-1}\left|\zeta_1[p,b]\right|^2}\right), \tag{A9.4}$$

$$J'_{\tau\theta_{\mathrm{T}}} = \frac{2N_{\mathrm{R}}N_{\mathrm{T}}|h|^2}{\sigma_{\eta,\mathrm{R}}^2}\frac{\omega_{\mathrm{c}}}{c}\Xi_{\mathrm{T}}\left(\tilde{\theta}_{\mathrm{T}}\right)\sum\nolimits_{p\in\mathcal{P}}\sum_{b=0}^{N_{\mathrm{B}}}\Im\left\{\zeta_1[p,b]\zeta_2^*[p,b]\right\}\tilde{\omega}_p, \tag{A9.5}$$

with $\Im\{\cdot\}$ denoting the imaginary part, $\zeta_i[p,b]$ being the i-th element of $\boldsymbol{\zeta}[p,b]$ and

$$\tilde{\omega}_p = \frac{\sum_{p'\in\mathcal{P}}\sum_{b=0}^{N_{\mathrm{B}}}\left|\zeta_1[p',b]\right|^2\left(\omega_p - \omega_{p'}\right)}{\sum_{p'\in\mathcal{P}}\sum_{b=0}^{N_{\mathrm{B}}}\left|\zeta_1[p',b]\right|^2}.$$

From (A9.2)-(A9.5) we conclude that in order to minimize the SPEB we have to choose the sequences $\zeta_1[p,b], \zeta_2[p,b]$ such that

$$\sum_{p\in\mathcal{P}}\sum_{b=0}^{N_{\mathrm{B}}}\zeta_1[p,b]\zeta_2^*[p,b] = 0, \tag{A9.6}$$

$$\sum_{p\in\mathcal{P}}\sum_{b=0}^{N_{\mathrm{B}}}\Im\left\{\zeta_1[p,b]\zeta_2^*[p,b]\right\}\tilde{\omega}_p = 0. \tag{A9.7}$$

A straightforward way to achieve that is to choose

$$\zeta_k[p,b] = \begin{cases} \lambda_k[p,b], & (p,b) \in \mathcal{R}_k, \\ 0, & \text{otherwise}, \end{cases} \tag{A9.8}$$

where $\mathcal{R}_k$, $k = 1, 2$, are disjoint subsets of the available resources $\mathcal{R}$ and $\lambda_k[p,b]$ are defined in (2.17), so that $\zeta_1[p,b]\zeta_2[p,b] = 0$, $\forall (p,b) \in \mathcal{R}$. We have, hence, shown that $\boldsymbol{f}_{\text{opt},1}(\tilde{\theta}_\text{T})$ and $\boldsymbol{f}_{\text{opt},2}(\tilde{\theta}_\text{T})$ are an optimal codebook for SPEB minimization. Using (A9.8) and (2.17), we write (A9.2) as

$$\text{SPEB}(\sigma_1^2, d, \tilde{\theta}_\text{T}, |h|) = \frac{c^2}{g q_1 \beta_1^2} + \frac{c^2 d^2}{g q_2 \omega_\text{c}^2 \Xi_\text{T}^2\left(\tilde{\theta}_\text{T}\right)}, \tag{A9.9}$$

where

$$g = \frac{2 N_\text{R} N_\text{T} \Delta f E_\text{tot} |h|^2}{\sigma_{\eta,\text{R}}^2}. \tag{A9.10}$$

Replacing $q_2 = 1 - q_1$ in (A9.9), as dictated by the power constraint, we find that the SPEB is a convex function of q_1. Setting its derivative w.r.t. q_1 to zero gives us (4.9).

A10 Energy Allocation Optimization for the Line-of-Sight (LOS) Path

Here we show how to formulate (4.27) as an SDP using only a 1D quadrature rule for the approximation of the expectation over $\tilde{\theta}_{\mathrm{T},0}$. This is accomplished in two steps:

- In the first step we show that the integration over d_0 and $\tilde{\theta}_{\mathrm{T},0}$ can be carried out separately;
- in the second step, after averaging over d_0, we exploit the form of the resulting function of $\tilde{\theta}_{\mathrm{T},0}$ and formulate the problem as an SDP.

We write $\mathbb{E}_{d_0,\tilde{\theta}_{\mathrm{T},0}}[\cdot]$ instead of $\mathbb{E}_{\boldsymbol{p}_{\mathrm{R}}}[\cdot]$. Also, for notational brevity we write

$$\bar{\boldsymbol{J}} = \mathbb{E}_{\alpha_{\mathrm{R}},\boldsymbol{h}_0|d_0,\tilde{\theta}_{\mathrm{T},0}}[\boldsymbol{J}_{\boldsymbol{\nu}_{\mathrm{LOS}}}(\boldsymbol{q}, d_0, \tilde{\theta}_{\mathrm{T},0}, \alpha_{\mathrm{R}}, \boldsymbol{h}_0)]. \tag{A10.1}$$

We index the elements of $\bar{\boldsymbol{J}}$ with the pair of parameters to which they correspond.

First, after some algebra we find that

$$\mathrm{tr}(\boldsymbol{E}^{\mathrm{T}}\bar{\boldsymbol{J}}^{-1}\boldsymbol{E}) = \frac{c^2}{\bar{J}_{\tau_0,\tau_0} - \frac{\bar{J}^2_{\tau_0,\tilde{\theta}_{\mathrm{T},0}}}{\bar{J}_{\tilde{\theta}_{\mathrm{T},0},\tilde{\theta}_{\mathrm{T},0}}}} + \frac{d_0^2}{\bar{J}_{\tilde{\theta}_{\mathrm{T},0},\tilde{\theta}_{\mathrm{T},0}} - \frac{\bar{J}^2_{\tau_0,\tilde{\theta}_{\mathrm{T},0}}}{\bar{J}_{\tau_0,\tau_0}}} + c^2\sigma^2_{\mathrm{clk}}, \tag{A10.2}$$

where

$$\bar{J}_{\nu_i,\nu_j} = \mathbb{E}_{\alpha_{\mathrm{R}},\boldsymbol{h}_0|d_0,\tilde{\theta}_{\mathrm{T},0}}[J_{\nu_i,\nu_j}], \tag{A10.3}$$

$$J_{\nu_i,\nu_j} = \frac{2}{\sigma^2_\eta}\sum_{b=1}^{N_{\mathrm{B}}}\sum_{p\in\mathcal{P}} \Re\left\{\frac{\partial \boldsymbol{m}^{\mathrm{H}}[p,b]}{\partial \nu_i}\frac{\partial \boldsymbol{m}[p,b]}{\partial \nu_j}\right\}, \tag{A10.4}$$

with $\nu_i, \nu_j \in \{d_0, \tilde{\theta}_{\mathrm{T},0}\}$. We can show that $J_{\nu_i,\nu_j},\ \nu_i, \nu_j \in \{d_0, \tilde{\theta}_{\mathrm{T},0}\}$, are independent of α_{R} and the phase of h_0. Hence, they can be expressed as

$$\begin{aligned}\bar{J}_{\nu_i,\nu_j} &= \mathbb{E}_{\boldsymbol{h}_0|d_0,\tilde{\theta}_{\mathrm{T},0}}[J_{\nu_i,\nu_j}(\boldsymbol{q}, \tilde{\theta}_{\mathrm{T},0}, |h_0(d_0)|^2)] \\ &= \mathbb{E}_{\boldsymbol{h}_0|d_0,\tilde{\theta}_{\mathrm{T},0}}[|h_0(d_0)|^2 j_{\nu_i,\nu_j}(\boldsymbol{q}, \tilde{\theta}_{\mathrm{T},0})] \\ &= g_0(d_0) j_{\nu_i,\nu_j}(\boldsymbol{q}, \tilde{\theta}_{\mathrm{T},0}),\end{aligned} \tag{A10.5}$$

where $g_0(d_0) = \mathbb{E}_{\boldsymbol{h}_0|d_0}[|h_0(d_0)|^2]$ and $j_{\nu_i,\nu_j}(\boldsymbol{q}, \tilde{\theta}_{\mathrm{T},0}) = J_{\nu_i,\nu_j}(\boldsymbol{q}, \tilde{\theta}_{\mathrm{T},0}, |h_0(d_0)|^2)/|h_0(d_0)|^2$ is a function of $\boldsymbol{q}$ and $\tilde{\theta}_{\mathrm{T},0}$. For the second equality in (A10.5), we used the fact that J_{ν_i,ν_j} can be expressed as the product of two terms, one dependent on the gain magnitude and the other on $\boldsymbol{q}$ and $\tilde{\theta}_{\mathrm{T},0}$. We can then rewrite (A10.2) as

$$\mathrm{tr}(\boldsymbol{E}^{\mathrm{T}}\bar{\boldsymbol{J}}^{-1}\boldsymbol{E}) = \frac{1}{g_0(d_0)}\left(\frac{c^2}{I_{\tau_0}(\boldsymbol{q}, \tilde{\theta}_{\mathrm{T},0})} + \frac{d_0^2}{I_{\tilde{\theta}_{\mathrm{T},0}}(\boldsymbol{q}, \tilde{\theta}_{\mathrm{T},0})}\right) + c^2\sigma^2_{\mathrm{clk}}, \tag{A10.6}$$

where

$$I_{\tau_0}(\boldsymbol{q}, \tilde{\theta}_{\mathrm{T},0}) = j_{\tau_0,\tau_0}(\boldsymbol{q}, \tilde{\theta}_{\mathrm{T},0}) - \frac{j^2_{\tau_0,\tilde{\theta}_{\mathrm{T},0}}(\boldsymbol{q}, \tilde{\theta}_{\mathrm{T},0})}{j_{\tilde{\theta}_{\mathrm{T},0},\tilde{\theta}_{\mathrm{T},0}}(\boldsymbol{q}, \tilde{\theta}_{\mathrm{T},0})}, \tag{A10.7}$$

$$I_{\tilde{\theta}_{\mathrm{T},0}}(\boldsymbol{q}, \tilde{\theta}_{\mathrm{T},0}) = j_{\tilde{\theta}_{\mathrm{T},0},\tilde{\theta}_{\mathrm{T},0}}(\boldsymbol{q}, \tilde{\theta}_{\mathrm{T},0}) - \frac{j^2_{\tau_0,\tilde{\theta}_{\mathrm{T},0}}(\boldsymbol{q}, \tilde{\theta}_{\mathrm{T},0})}{j_{\tau_0,\tau_0}(\boldsymbol{q}, \tilde{\theta}_{\mathrm{T},0})}. \tag{A10.8}$$

It is apparent from (A10.6) that integration of the function over d_0 and $\tilde{\theta}_{\mathrm{T},0}$ can be carried out separately.

For the second step, taking the expectation over d_0 and defining

$$\bar{g}_0(\tilde{\theta}_{\mathrm{T},0}) = 1/\mathbb{E}_{d_0|\tilde{\theta}_{\mathrm{T},0}}[1/g_0(d_0)], \tag{A10.9}$$

$$\bar{d}_0(\tilde{\theta}_{\mathrm{T},0}) = \sqrt{\mathbb{E}_{d_0|\tilde{\theta}_{\mathrm{T},0}}\left[\frac{\bar{g}_0(\tilde{\theta}_{\mathrm{T},0})}{g_0(d_0)} d_0^2\right]} \tag{A10.10}$$

we get

$$\mathbb{E}_{d_0|\tilde{\theta}_{\mathrm{T},0}}[\mathrm{tr}(\boldsymbol{E}^{\mathrm{T}}\bar{\boldsymbol{J}}^{-1}\boldsymbol{E})] = \frac{1}{\bar{g}_0(\tilde{\theta}_{\mathrm{T},0})}\left(\frac{c^2}{I_{\tau_0}(\boldsymbol{q},\tilde{\theta}_{\mathrm{T},0})} + \frac{\left(\bar{d}_0(\tilde{\theta}_{\mathrm{T},0})\right)^2}{I_{\tilde{\theta}_{\mathrm{T},0}}(\boldsymbol{q},\tilde{\theta}_{\mathrm{T},0})}\right) + c^2\sigma_{\mathrm{clk}}^2. \tag{A10.11}$$

Comparing (A10.11) to (A10.2), we can conclude that, in order to be able to formulate the problem in a convex form, $\mathbb{E}_{d_0|\tilde{\theta}_{\mathrm{T},0}}[\mathrm{tr}(\boldsymbol{E}^{\mathrm{T}}\bar{\boldsymbol{J}}^{-1}\boldsymbol{E})]$ can be expressed as

$$\begin{aligned}&\mathbb{E}_{d_0|\tilde{\theta}_{\mathrm{T},0}}[\mathrm{tr}(\boldsymbol{E}^{\mathrm{T}}\check{\boldsymbol{J}}^{-1}\boldsymbol{E})]\\ &\quad= \mathrm{tr}(\boldsymbol{E}^{\mathrm{T}}\boldsymbol{J}_{\boldsymbol{\nu}_{\mathrm{LOS}}}^{-1}(\boldsymbol{q}, \bar{d}_0(\tilde{\theta}_{\mathrm{T},0}), \tilde{\theta}_{\mathrm{T},0}, \check{\alpha}_{\mathrm{R}}, \sqrt{\bar{g}_0(\tilde{\theta}_{\mathrm{T},0})}\,\mathrm{e}^{\mathrm{j}\beta_g})\boldsymbol{E}),\end{aligned} \tag{A10.12}$$

where $\check{\alpha}_{\mathrm{R}}$ and β_g can be chosen arbitrarily, since they do not have an impact on the objective. Finally, using (A10.12) and the identity

$$\mathbb{E}_{d_0,\tilde{\theta}_{\mathrm{T},0}}\left[\,\mathrm{tr}(\boldsymbol{E}^{\mathrm{T}}\bar{\boldsymbol{J}}\boldsymbol{E})\right] = \mathbb{E}_{\tilde{\theta}_{\mathrm{T},0}}[\mathbb{E}_{d_0|\tilde{\theta}_{\mathrm{T},0}}[\mathrm{tr}(\boldsymbol{E}^{\mathrm{T}}\bar{\boldsymbol{J}}^{-1}\boldsymbol{E})]], \tag{A10.13}$$

we can employ a 1D quadrature rule to approximate the expectation integral over $\tilde{\theta}_{\mathrm{T},0}$ to get the following SDP

$$\begin{aligned}&\min_{\boldsymbol{q},\boldsymbol{B}_1,\ldots,\boldsymbol{B}_{N_{\tilde{\theta}_{\mathrm{T},0}}}} \sum\nolimits_{j=1}^{N_{\tilde{\theta}_{\mathrm{T},0}}} p_j\,\mathrm{tr}(\boldsymbol{B}_j)\\ &\text{s.t. } \boldsymbol{q} \succcurlyeq \boldsymbol{0},\ \boldsymbol{1}^{\mathrm{T}}\boldsymbol{q} \le 1,\\ &\begin{bmatrix}\boldsymbol{B}_j & \boldsymbol{E}^{\mathrm{T}}\\ \boldsymbol{E} & \boldsymbol{J}_{\boldsymbol{\nu}_{\mathrm{LOS}}}(\boldsymbol{q}, \bar{d}_0(\theta_{\mathrm{T},0,j}), \theta_{\mathrm{T},0,j}, \check{\alpha}_{\mathrm{R}}, \sqrt{\bar{g}_0(\theta_{\mathrm{T},0,j})}\,\mathrm{e}^{\mathrm{j}\beta_g})\end{bmatrix} \succcurlyeq \boldsymbol{0},\\ &j = 1,\ldots,N_{\tilde{\theta}_{\mathrm{T},0}}.\end{aligned} \tag{A10.14}$$

Acronyms and Abbreviations

1D	one-dimensional.
1G	first generation.
2D	two-dimensional.
2G	second generation.
3D	three-dimensional.
3GPP	Third Generation Partnership Project.
5G	fifth generation.
ADC	analog-to-digital conversion.
ADCGM	Alternating Descent Conditional Gradient Method.
AOA	angle of arrival.
AOD	angle of departure.
AWGN	additive white Gaussian noise.
BS	base station.
cdf	cumulative distribution function.
CID	cell identity.
CP	cyclic prefix.
CRLB	Cramér-Rao lower bound.
DAC	digital-to-analog conversion.
DCS-SOMP	distributed compressed sensing-simultaneous orthogonal matching pursuit.
DFT	discrete Fourier transform.
DL	downlink.
EFIM	equivalent FIM.
ESPEB	expected SPEB.
EXIP	extended invariance principle.
FCC	Federal Communications Commission.
FI	Fisher information.
FIM	Fisher information matrix.
FR	frequency range.
GNSS	global navigation satellite system.

GPS Global Positioning System.

LHS left-hand side.
LOS line-of-sight.

MIMO multiple-input multiple-output.
mm-Wave millimeter-wave.

NF noise figure.
NLOS non-LOS.
NR new radio.

OEB orientation error bound.
OFDM orthogonal frequency-division multiplexing.

PA physical anchor.
PAPR peak-to-average power ratio.
pdf probability density function.
PEB position error bound.
POI point of incidence.
PSD positive semidefiniteness.

QPSK quadrature phase shift keying.

RCRLB root CRLB.
RE resource element.
RF radio frequency.
RHS right-hand side.
rms root mean square.
RMSE root mean square error.
Rx receiver.

SAAF squared array aperture function.
SAGE space-alternating generalized expectation maximization.
SDP semidefinite program.
SL sidelink.
SNR signal-to-noise ratio.
SotA state of the art.
SPEB squared position error bound.

TDOA time difference of arrival.
TOA time of arrival.
TOF time of flight.
TOT time of transmisssion.
TR technical report.
TS technical specification.
Tx transmitter.

UCA uniform circular array.

UE user equipment.
UL uplink.
ULA uniform linear array.
US United States.

VA virtual anchor.
VEB velocity error bound.

w.r.t. with respect to.

ZZLB Ziv-Zakai lower bound.

List of Figures

List of Publications

Parts of the thesis have been published in the following papers:

- A. Kakkavas, M. H. Castañeda García, R. A. Stirling-Gallacher, and J. A. Nossek, "Multiarray 5G V2V relative positioning: Performance bounds," in *Proc. IEEE Global Commun. Conf. (GLOBECOM)*, Abu-Dhabi, UAE, Dec. 2018, pp. 206–212., DOI: 10.1109/GLOCOM.2018.8647812.
- A. Kakkavas, M. H. Castañeda García, R. A. Stirling-Gallacher, and J. A. Nossek, "Performance limits of single-anchor millimeter-wave positioning," *IEEE Trans. Wireless Commun.*, vol. 18, no. 11, pp. 5196–5210, Nov. 2019, DOI: 10.1109/TWC.2019.2934460.
- A. Kakkavas, G. Seco-Granados, H. Wymeersch, M. H. Castañeda García, R. A. Stirling- Gallacher, and J. A. Nossek, "5G downlink multi-beam signal design for LOS positioning," in *Proc. IEEE Global Commun. Conf. (GLOBECOM)*, Waikoloa, HI, USA, Dec. 2019, pp. 1– 6, DOI: 10.1109/GLOBECOM38437.2019.9013374.
- A. Kakkavas, H. Wymeersch, G. Seco-Granados, M. H. Castañeda García, R. A. Stirling- Gallacher, and J. A. Nossek, "Power allocation and parameter estimation for multipath-based 5G positioning," *IEEE Trans. Wireless Commun.*, vol. 20, no. 11, pp. 7302–7316, Nov. 2021. DOI: 10.1109/TWC.2021.3082581.
- A. Kakkavas, M. H. Castañeda García, G. Seco-Granados, H. Wymeersch, R. A. Stirling- Gallacher, and J. A. Nossek, "Position information from reflecting surfaces," *IEEE Commun. Lett.*, vol. 10, no. 6, pp. 1300–1304, 2021, DOI: 10.1109/LWC.2021.3064915.

Furthermore, the following papers, which are not closely related to the content of the thesis, have been published during its preparation:

- A. A. Zaidi *et al.*, "Evaluation of Waveforms for Mobile Radio Communications above 6 GHz," in *Proc. IEEE GLOBECOM Workshops (GC Wkshps)*, Washington, DC, USA, 2016, pp. 1-6, DOI: 10.1109/GLOCOMW.2016.7848900.
- A. Kakkavas, M. H. Castañeda García, J. Luo, T. Laas, W. Xu and J. A. Nossek, "FBMC-OQAM with phase noise: Achievable performance and compensation," in *Proc. IEEE 18th Int. Workshop on Signal Process. Advances in Wireless Commun. (SPAWC)*, Sapporo, Japan, Jul. 2017, pp. 1-5, DOI: 10.1109/SPAWC.2017.8227811.
- A. Kakkavas, W. Xu, J. Luo, M. Castañeda and J. A. Nossek, "On PAPR characteristics of DFT-s-OFDM with geometric and probabilistic constellation shaping," in *Proc. IEEE 18th Int. Workshop on Signal Process. Advances in Wireless Commun. (SPAWC)*, Sapporo, Japan, Jul. 2017, pp. 1-5, DOI: 10.1109/SPAWC.2017.8227810.
- N. Ul Hassan, W. Xu and A. Kakkavas, "Applying Coded Modulation with Probabilistic and Geometric Shaping for Wireless Backhaul Channel," in *Proc. IEEE 29th Annual Int. Sympo-*

sium on Personal, Indoor and Mobile Radio Commun. (PIMRC), Bologna, Italy, 2018, pp. 1-5, DOI: 10.1109/PIMRC.2018.8580849.

- Y. Wu *et al.*, "Cooperative Localization with Angular Measurements and Posterior Linearization," in *Proc. IEEE Int. Conf. Commun. Workshops (ICCW)*, Dublin, Ireland, Jun. 2020, pp. 1-6, DOI: 10.1109/ICCWorkshops49005.2020.9145275.
- Q. Wang, A. Kakkavas, X. Gong and R. A. Stirling-Gallacher, "Towards Integrated Sensing and Communications for 6G," in *Proc. 2nd IEEE Int. Symposium Joint Commun. & Sensing (JC&S)*, Seefeld, Austria, 2022, pp. 1-6, DOI: 10.1109/JCS54387.2022.9743516.

Bibliography

[1] H. G. Schantz, "On the origins of RF-based location," in *Proc. IEEE Topical Conf. Wireless Sensors and Sensor Netw. (WiSNet),* Phoenix, AZ, USA, 2011, pp. 21–24. DOI: 10.1109/WISNET.2011.5725029.

[2] K. Krizman, T. Biedka, and T. Rappaport, "Wireless position location: Fundamentals, implementation strategies, and sources of error," in *1997 IEEE 47th Vehicular Technology Conference. Technology in Motion*, vol. 2, 1997, 919–923 vol.2. DOI: 10.1109/VETEC.1997.600463.

[3] J. A. del Peral-Rosado, R. Raulefs, J. A. López-Salcedo, and G. Seco-Granados, "Survey of cellular mobile radio localization methods: From 1G to 5G," *IEEE Commun. Surveys Tuts.*, vol. 20, no. 2, pp. 1124–1148, 2018. DOI: 10.1109/COMST.2017.2785181.

[4] R. S. Campos, "Evolution of positioning techniques in cellular networks, from 2g to 4g," *Wireless Communications and Mobile Computing*, vol. 2017, 2017. DOI: 10.1155/2017/2315036.

[5] 3rd Generation Partnership Project (3GPP), "Technical Specification Group Radio Access Network, NG-RAN; Stage 2 functional specification of User Equipment (UE) positioning in NG-RAN (Release 17)," TS38.305 V17.0.0, Mar. 2022.

[6] A. Dammann, R. Raulefs, and S. Zhang, "On prospects of positioning in 5G," in *IEEE Int. Conf. Commun. Workshop (ICCW),* London, UK, Jun. 2015, pp. 1207–1213. DOI: 10.1109/ICCW.2015.7247342.

[7] K. Witrisal *et al.*, "High-accuracy localization for assisted living: 5G systems will turn multipath channels from foe to friend," *IEEE Signal Process. Mag.*, vol. 33, no. 2, pp. 59–70, Mar. 2016. DOI: 10.1109/MSP.2015.2504328.

[8] K. Witrisal, S. Hinteregger, J. Kulmer, E. Leitinger, and P. Meissner, "High-accuracy positioning for indoor applications: RFID, UWB, 5G, and beyond," in *IEEE 10th Int. Conf. RFID (RFID),* Orlando, FL, USA, May 2016, pp. 1–7. DOI: 10.1109/RFID.2016.7487999.

[9] H. Wymeersch, G. Seco-Granados, G. Destino, D. Dardari, and F. Tufvesson, "5G mmWave positioning for vehicular networks," *IEEE Wireless Commun.*, vol. 24, no. 6, pp. 80–86, Dec. 2017. DOI: 10.1109/MWC.2017.1600374.

[10] A. Hakkarainen, J. Werner, M. Costa, K. Leppanen, and M. Valkama, "High-efficiency device localization in 5G ultra-dense networks: Prospects and enabling technologies," in *IEEE 82th Veh. Technol. Conf. (VTC-Fall),* Boston, MA, USA, Sep. 2015, pp. 1–5. DOI: 10.1109/VTCFall.2015.7390965.

[11] P. Kela *et al.*, "Location based beamforming in 5G ultra-dense networks," in *IEEE 84th Vehicular Technology Conference (VTC-Fall),* Montréal, Canada, Sep. 2016, pp. 1–7. DOI: 10.1109/VTCFall.2016.7881072.

[12] F. Maschietti, D. Gesbert, P. de Kerret, and H. Wymeersch, "Robust location-aided beam alignment in millimeter wave massive MIMO," in *IEEE Global Commun. Conf. (GLOBECOM),* Singapore, Dec. 2017, pp. 1–6. DOI: 10.1109/GLOCOM.2017.8254901.

[13] Y. Shen and M. Z. Win, "Fundamental limits of wideband localization - Part I: A general framework," *IEEE Trans. Inf. Theory*, vol. 56, no. 10, pp. 4956–4980, Oct. 2010, ISSN: 0018-9448. DOI: 10.1109/TIT.2010.2060110.

[14] Y. Shen, H. Wymeersch, and M. Z. Win, "Fundamental limits of wideband localization - part II: Cooperative networks," *IEEE Trans. Inf. Theory*, vol. 56, no. 10, pp. 4981–5000, Oct. 2010, ISSN: 0018-9448. DOI: 10.1109/TIT.2010.2059720.

[15] Y. Shen and M. Z. Win, "Fundamental limits of wideband localization accuracy via Fisher information," in *IEEE Wireless Commun. Netw. Conf. (WCNC),* Kowloon, Hong Kong, Mar. 2007, pp. 3046–3051. DOI: 10.1109/WCNC.2007.564.

[16] Y. Shen and M. Z. Win, "On the use of multipath geometry for wideband cooperative localization," in *IEEE Global Commun. Conf. (GLOBECOM),* Honolulu, HI, USA, Nov. 2009, pp. 1–6. DOI: 10.1109/GLOCOM.2009.5425798.

[17] Y. Han, Y. Shen, X. P. Zhang, M. Z. Win, and H. Meng, "Performance limits and geometric properties of array localization," *IEEE Trans. Inf. Theory*, vol. 62, no. 2, pp. 1054–1075, Feb. 2016. DOI: 10.1109/TIT.2015.2511778.

[18] A. Shahmansoori, G. E. Garcia, G. Destino, G. Seco-Granados, and H. Wymeersch, "5G position and orientation estimation through millimeter wave MIMO," in *Proc. IEEE GLOBECOM Workshops (GC Wkshps),* San Diego, CA, USA, Dec. 2015, pp. 1–6. DOI: 10.1109/GLOCOMW.2015.7413967.

[19] A. Guerra, F. Guidi, and D. Dardari, "Single anchor localization and orientation performance limits using massive arrays: MIMO vs. beamforming," *IEEE Trans. Wireless Commun.*, vol. 17, no. 8, pp. 5241–5255, Aug. 2018. DOI: 10.1109/TWC.2018.2840136.

[20] Z. Abu-Shaban, X. Zhou, T. D. Abhayapala, G. Seco-Granados, and H. Wymeersch, "Error bounds for uplink and downlink 3D localization in 5G mmWave systems," *IEEE Trans. Wireless Commun.*, vol. 17, no. 8, pp. 4939–4954, Aug. 2018. DOI: 10.1109/TWC.2018.2832134.

[21] R. Mendrzik, H. Wymeersch, G. Bauch, and Z. Abu-Shaban, "Harnessing NLOS components for position and orientation estimation in 5G millimeter wave MIMO," *IEEE Trans. Wireless Commun.*, vol. 18, no. 1, pp. 93–107, Jan. 2019. DOI: 10.1109/TWC.2018.2877615.

[22] A. Shahmansoori, G. E. Garcia, G. Destino, G. Seco-Granados, and H. Wymeersch, "Position and orientation estimation through millimeter-wave MIMO in 5G systems," *IEEE Trans. Wireless Commun.*, vol. 17, no. 3, pp. 1822–1835, Mar. 2018. DOI: 10.1109/TWC.2017.2785788.

[23] J. Talvitie, M. Koivisto, T. Levanen, M. Valkama, G. Destino, and H. Wymeersch, "High-accuracy joint position and orientation estimation in sparse 5G mmWave channel," in *Proc. IEEE Int. Conf. Commun. (ICC),* Shanghai, China, May 2019, pp. 1–7. DOI: 10.1109/ICC.2019.8761910.

[24] J. Palacios, G. Bielsa, P. Casari, and J. Widmer, "Single- and multiple-access point indoor localization for millimeter-wave networks," *IEEE Trans. Wireless Commun.*, vol. 18, no. 3, pp. 1927–1942, Mar. 2019. DOI: 10.1109/TWC.2019.2899313.

[25] Y. Liu, Y. Shen, and M. Z. Win, "Single-anchor localization and synchronization of full-duplex agents," *IEEE Trans. Commun.*, vol. 67, no. 3, pp. 2355–2367, Mar. 2019. DOI: 10.1109/TCOMM.2018.2878843.

[26] T. Wang, H. Zhao, and Y. Shen, "An efficient single-anchor localization method using ultra-wide bandwidth systems," *Applied Sciences*, vol. 10, no. 1, Dec. 2019. DOI: 10.3390/app10010057.

[27] M. Rath, J. Kulmer, E. Leitinger, and K. Witrisal, "Single-anchor positioning: Multipath processing with non-coherent directional measurements," *IEEE Access*, vol. 8, pp. 88 115–88 132, May 2020. DOI: 10.1109/ACCESS.2020.2993197.

[28] A. Fascista, A. Coluccia, H. Wymeersch, and G. Seco-Granados, "Millimeter-wave downlink positioning with a single-antenna receiver," *IEEE Trans. Wireless Commun.*, vol. 18, no. 9, pp. 4479–4490, Sep. 2019. DOI: 10.1109/TWC.2019.2925618.

[29] A. Fascista, A. Coluccia, H. Wymeersch, and G. Seco-Granados, "Low-complexity accurate mmWave positioning for single-antenna users based on angle-of-departure and adaptive beamforming," in *Proc. IEEE Int. Conf. Acoustics, Speech and Signal Process. (ICASSP),* Barcelona, Spain, May 2020, pp. 4866–4870. DOI: 10.1109/ICASSP40776.2020.9053493.

[30] C. Gentner, T. Jost, W. Wang, S. Zhang, A. Dammann, and U. Fiebig, "Multipath assisted positioning with simultaneous localization and mapping," *IEEE Trans. Wireless Commun.*, vol. 15, no. 9, pp. 6104–6117, Sep. 2016. DOI: 10.1109/TWC.2016.2578336.

[31] E. Leitinger, F. Meyer, F. Hlawatsch, K. Witrisal, F. Tufvesson, and M. Z. Win, "A belief propagation algorithm for multipath-based SLAM," *IEEE Trans. Wireless Commun.*, vol. 18, no. 12, pp. 5613–5629, Dec. 2019. DOI: 10.1109/TWC.2019.2937781.

[32] H. Wymeersch, N. Garcia, H. Kim, G. Seco-Granados, S. Kim, F. Wen, and M. Fröhle, "5G mmWave downlink vehicular positioning," in *Proc. IEEE Global Commun. Conf. (GLOBECOM),* Abu Dhabi, UAE, Dec. 2018, pp. 206–212. DOI: 10.1109/GLOCOM.2018.8647275.

[33] J. Talvitie, T. Levanen, M. Koivisto, K. Pajukoski, M. Renfors, and M. Valkama, "Positioning of high-speed trains using 5G new radio synchronization signals," in *Proc. IEEE Wireless Commun. and Netw. Conf. (WCNC)*, Apr. 2018, pp. 1–6. DOI: 10.1109/WCNC.2018.8377225.

[34] X. Li, E. Leitinger, M. Oskarsson, K. Åström, and F. Tufvesson, "Massive MIMO-based localization and mapping exploiting phase information of multipath components," *IEEE Trans. Wireless Commun.*, vol. 18, no. 9, pp. 4254–4267, Sep. 2019. DOI: 10.1109/TWC.2019.2922264.

[35] R. Mendrzik, F. Meyer, G. Bauch, and M. Z. Win, "Enabling situational awareness in millimeter wave massive MIMO systems," *IEEE J. Sel. Areas Commun.*, vol. 13, no. 5, pp. 1196–1211, Sep. 2019. DOI: 10.1109/JSTSP.2019.2933142.

[36] H. Kim, K. Granström, S. Kim, and H. Wymeersch, "Low-complexity 5G SLAM with CKF-PHD filter," in *Proc. IEEE Int. Conf. Acoustics, Speech and Signal Process. (ICASSP),* Barcelona, Spain, May 2020, pp. 5220–5224. DOI: 10.1109/ICASSP40776.2020.9053132.

[37] B. Zhou, A. Liu, and V. Lau, "Successive localization and beamforming in 5G mmWave MIMO communication systems," *IEEE Trans. Signal Process.*, vol. 67, no. 6, pp. 1620–1635, Mar. 2019. DOI: 10.1109/TSP.2019.2894789.

[38] N. Garcia, H. Wymeersch, and D. T. M. Slock, "Optimal precoders for tracking the AoD and AoA of a mmWave path," *IEEE Trans. Signal Process.*, vol. 66, no. 21, pp. 5718–5729, Nov. 2018. DOI: 10.1109/TSP.2018.2870368.

[39] R. Koirala, B. Denis, D. Dardari, and B. Uguen, "Localization bound based beamforming optimization for multicarrier mmWave MIMO," in *14th Workshop on Positioning, Navigation and Communications (WPNC),* Bremen, Germany, Oct. 2017, pp. 1–6. DOI: 10.1109/WPNC.2017.8250057.

[40] R. Koirala, B. Denis, B. Uguen, D. Dardari, and H. Wymeersch, "Localization optimal multi-user beamforming with multi-carrier mmwave mimo," in *IEEE 29th Annual Int. Symposium Personal, Indoor and Mobile Radio Commun. (PIMRC),* Bologna, Italy, Sep. 2018, pp. 1–7. DOI: 10.1109/PIMRC.2018.8580712.

[41] H. Zhao, L. Zhang, and Y. Shen, "On the optimal beamspace design for direct localization systems," in *Proc. IEEE Int. Conf. Commun. (ICC),* Kansas City, MO, USA, May 2018, pp. 1–6. DOI: 10.1109/ICC.2018.8422344.

[42] H. Zhao, N. Zhang, and Y. Shen, "Robust beamspace design for direct localization," in *Proc. IEEE Int. Conf. Acoustics, Speech and Signal Process. (ICASSP),* Brighton, UK, May 2019, pp. 4360–4364. DOI: 10.1109/ICASSP.2019.8682597.

[43] W. W. Li, Y. Shen, Y. J. Zhang, and M. Z. Win, "Robust power allocation for energy-efficient location-aware networks," *IEEE/ACM Trans. Netw.*, vol. 21, no. 6, pp. 1918–1930, Dec. 2013. DOI: 10.1109/TNET.2013.2276063.

[44] A. Shahmansoori, G. Seco-Granados, and H. Wymeersch, "Power allocation for OFDM wireless network localization under expectation and robustness constraints," *IEEE Trans. Wireless Commun.*, vol. 16, no. 3, pp. 2027–2038, Mar. 2017. DOI: 10.1109/TWC.2017.2662678.

[45] R. Vaughan and J. Bach-Anderson, *Channels, propagation and antennas for mobile communications* (Electromagnetic Waves). Stevenage: The Institution of Engineering and Technology, 2003. DOI: 10.1049/PBEW050E.

[46] T. S. Rappaport, E. Ben-Dor, J. N. Murdock, and Y. Qiao, "38 Ghz and 60 Ghz angle-dependent propagation for cellular & peer-to-peer wireless communications," in *Proc. IEEE Int. Conf. Commun. (ICC),* Ottawa, Canada, Jun. 2012, pp. 4568–4573. DOI: 10.1109/ICC.2012.6363891.

[47] M. T. Martinez-Ingles, D. P. Gaillot, J. Pascual-Garcia, J. M. Molina-Garcia-Pardo, M. Lienard, and J. V. Rodríguez, "Deterministic and experimental indoor mmW channel modeling," *IEEE Antennas Wireless Propag. Lett.*, vol. 13, pp. 1047–1050, May 2014. DOI: 10.1109/LAWP.2014.2327054.

[48] N. Boyd, G. Schiebinger, and B. Recht, "The alternating descent conditional gradient method for sparse inverse problems," *SIAM Journal on Optimization*, vol. 27, no. 2, pp. 616–639, Apr. 2017. DOI: 10.1137/15M1035793.

[49] T. Rappaport, *Wireless Communications: Principles and Practice*, 2nd. Upper Saddle River, NJ, USA: Prentice Hall PTR, 2001, ISBN: 0130422320.

[50] H. Messer, "The hybrid Cramér-Rao lower bound - from practice to theory," in *Proc. Fourth IEEE Workshop on Sensor Array and Multichannel Process. (SAM),* Waltham, MA, USA, Jul. 2006, pp. 304–307. DOI: 10.1109/SAM.2006.1706142.

[51] Y. Rockah and P. Schultheiss, "Array shape calibration using sources in unknown locations – Part I: Far-field sources," *IEEE Trans. Acoust., Speech, Signal Process.*, vol. 35, no. 3, pp. 286–299, Mar. 1987. DOI: 10.1109/TASSP.1987.1165144.

[52] E. L. Lehmann and G. Casella, *Theory of Point Estimation*, 2nd. Springer New York, Aug. 1998, ISBN: 0387985026.

[53] S. M. Kay, *Fundamentals of Statistical Signal Processing: Estimation Theory*. Upper Saddle River, NJ, USA: Prentice-Hall, Inc., 1993, ISBN: 0-13-345711-7.

[54] T. Laas, "Physically consistent modeling of multi-antenna systems," Ph.D. dissertation, Technical University of Munich, 2022.

[55] J. Chen, "When does asymptotic orthogonality exist for very large arrays?" In *Proc. IEEE Global Commun. Conf. (GLOBECOM),* Atlanta, GA, USA, Dec. 2013, pp. 4146–4150. DOI: 10.1109/GLOCOM.2013.6831723.

[56] H. Q. Ngo, E. G. Larsson, and T. L. Marzetta, "Aspects of favorable propagation in massive MIMO," in *22nd European Signal Processing Conference (EUSIPCO),* Lisbon, Portugal, Sep. 2014, pp. 76–80, ISBN: 978-099286261-9.

[57] C. Masouros and M. Matthaiou, "Space-constrained massive MIMO: Hitting the wall of favorable propagation," *IEEE Commun. Lett.*, vol. 19, no. 5, pp. 771–774, May 2015. DOI: 10.1109/LCOMM.2015.2409832.

[58] P. Meissner, C. Steiner, and K. Witrisal, "UWB positioning with virtual anchors and floor plan information," in *7th Workshop on Positioning, Navigation and Communication,* Dresden, Germany, 2010, pp. 150–156. DOI: 10.1109/WPNC.2010.5650374.

[59] 3rd Generation Partnership Project (3GPP), "Technical Specification Group Radio Access Network; Study on positioning support (Release 16)," TR38.855 V16.0.0, Mar. 2019.

[60] Z. Abu-Shaban, H. Wymeersch, T. Abhayapala, and G. Seco-Granados, "Single-anchor two-way localization bounds for 5G mmWave systems," *IEEE Trans. Veh. Technol.*, vol. 69, no. 6, pp. 6388–6400, 2020. DOI: 10.1109/TVT.2020.2987039.

[61] 3rd Generation Partnership Project (3GPP), "Technical Specification Group Radio Access Network; Study on NR positioning enhancements; (Release 17)," TS38.857 V17.0.0, Mar. 2021.

[62] Q. Denoyelle, V. Duval, G. Peyré, and E. Soubies, "The sliding Frank–Wolfe algorithm and its application to super-resolution microscopy," *Inverse Problems*, vol. 36, no. 1, p. 014 001, Dec. 2019. DOI: 10.1088/1361-6420/ab2a29.

[63] E. J. Candès and C. Fernandez-Granda, "Towards a mathematical theory of super-resolution," *Communications on pure and applied Mathematics*, vol. 67, no. 6, pp. 906–956, 2014. DOI: 10.1002/cpa.21455.

[64] V. Duval and G. Peyré, "Exact support recovery for sparse spikes deconvolution," *Foundations of Computational Mathematics*, vol. 15, no. 5, pp. 1315–1355, 2015. DOI: 10.1007/s10208-014-9228-6.

[65] D. Sage, T.-A. Pham, H. Babcock, T. Lukes, T. Pengo, J. Chao, R. Velmurugan, A. Herbert, A. Agrawal, S. Colabrese, *et al.*, "Super-resolution fight club: Assessment of 2D and 3D single-molecule localization microscopy software," *Nature methods*, vol. 16, no. 5, pp. 387–395, 2019. DOI: 10.1038/s41592-019-0364-4.

[66] N. Decarli, D. Dardari, S. Gezici, and A. A. D'Amico, "Los/nlos detection for uwb signals: A comparative study using experimental data," in *IEEE 5th International Symposium on Wireless Pervasive Computing 2010*, 2010, pp. 169–173. DOI: 10.1109/ISWPC.2010.5483704.

[67] K. Levenberg, "A method for the solution of certain non-linear problems in least squares," *Quarterly of Applied Mathematics*, vol. 2, no. 2, pp. 164–168, Jul. 1944. DOI: 10.1090/qam/10666.

[68] D. W. Marquardt, "An algorithm for least-squares estimation of nonlinear parameters," *Journal of the Society for Industrial and Applied Mathematics*, vol. 11, no. 2, pp. 431–441, Jun. 1963. DOI: 10.1137/0111030.

[69] P. Zhang, L. Gan, S. Sun, and C. Ling, "Atomic norm denoising-based channel estimation for massive multiuser MIMO systems," in *Proc. IEEE Int. Conf. Commun. (ICC),* London, UK, Jun. 2015, pp. 4564–4569. DOI: 10.1109/ICC.2015.7249042.

[70] F. Meyer, T. Kropfreiter, J. L. Williams, R. Lau, F. Hlawatsch, P. Braca, and M. Z. Win, "Message passing algorithms for scalable multitarget tracking," *Proc. IEEE*, vol. 106, no. 2, pp. 221–259, 2018. DOI: 10.1109/JPROC.2018.2789427.

[71] U. R. O. Nickel, "Fundamentals of signal processing for phased array radar," 2006.

[72] A. Dammann, T. Jost, R. Raulefs, M. Walter, and S. Zhang, "Optimizing waveforms for positioning in 5G," in *Proc. IEEE 17th Int. Workshop on Signal Process. Advances in Wireless Commun. (SPAWC),* Edinburgh, UK, Jul. 2016, pp. 1–5. DOI: 10.1109/SPAWC.2016.7536783.

[73] A. Kakkavas, G. Seco-Granados, H. Wymeersch, M. H. Castañeda García, R. A. Stirling-Gallacher, and J. A. Nossek, "5G downlink multi-beam signal design for LOS positioning," in *Proc. IEEE Global Commun. Conf. (GLOBECOM),* Waikoloa, HI, USA, Dec. 2019, pp. 1–6. DOI: 10.1109/GLOBECOM38437.2019.9013374.

[74] M. F. Keskin, F. Jiang, F. Munier, G. Seco-Granados, and H. Wymeersch, "Optimal spatial signal design for mmwave positioning under imperfect synchronization," *IEEE Trans. Veh. Technol.*, vol. 71, no. 5, pp. 5558–5563, 2022. DOI: 10.1109/TVT.2022.3149974.

[75] A. Kakkavas, H. Wymeersch, G. Seco-Granados, M. H. Castañeda García, R. A. Stirling-Gallacher, and J. A. Nossek, "Power allocation and parameter estimation for multipath-based 5G positioning," *IEEE Trans. Wireless Commun.*, vol. 20, no. 11, pp. 7302–7316, Nov. 2021. DOI: 10.1109/TWC.2021.3082581.

[76] R. Cools, "An encyclopaedia of cubature formulas," *Journal of Complexity*, vol. 19, no. 3, pp. 445–453, Jun. 2003, Oberwolfach Special Issue. DOI: 10.1016/S0885-064X(03)00011-6.

[77] D. Crouse, "Basic tracking using nonlinear 3D monostatic and bistatic measurements," *IEEE Aerosp. Electron. Syst. Mag.*, vol. 29, no. 8, pp. 4–53, Aug. 2014.

[78] R. Cools, *Cubature formulae for the n-dimensional space with weight function* $\exp(-r^2)$, https://nines.cs.kuleuven.be/research/ecf/mtables.html, Accessed: 2022-10-20.

[79] A. Kakkavas, M. H. Castañeda García, R. A. Stirling-Gallacher, and J. A. Nossek, "Performance limits of single-anchor millimeter-wave positioning," *IEEE Trans. Wireless Commun.*, vol. 18, no. 11, pp. 5196–5210, Nov. 2019. DOI: 10.1109/TWC.2019.2934460.

[80] J. Ziv and M. Zakai, "Some lower bounds on signal parameter estimation," *IEEE Trans. Inf. Theory*, vol. 15, no. 3, pp. 386–391, 1969. DOI: 10.1109/TIT.1969.1054301.

[81] T. Laas and W. Xu, "On the Ziv-Zakai bound for time difference of arrival estimation in CP-OFDM systems," in *Proc. IEEE Wireless Commun. Netw. Conf. (WCNC),* Nanjing, China, Mar. 2021, pp. 1–5. DOI: 10.1109/WCNC49053.2021.9417566.

[82] S. Gault, W. Hachem, and P. Ciblat, "Joint sampling clock offset and channel estimation for OFDM signals: Crame/spl acute/r-rao bound and algorithms," *IEEE Trans. Signal Process.*, vol. 54, no. 5, pp. 1875–1885, May 2006. DOI: 10.1109/TSP.2006.871975.

[83] W. Tan, S. Jin, J. Wang, and Y. Huang, "Achievable sum-rate analysis for massive MIMO systems with different array configurations," in *IEEE Wireless Commun. Netw. Conf. (WCNC),* Istanbul, Turkey, Mar. 2015, pp. 316–321. DOI: 10.1109/WCNC.2015.7127489.

[84] T. H. Cormen, C. E. Leiserson, R. L. Rivest, and C. Stein, *Introduction to Algorithms, Third Edition*, 3rd. The MIT Press, 2009.

[85] C. Fernandez-Granda, "Super-resolution of point sources via convex programming," in *Proc. IEEE 6th Int. Workshop on Computational Advances in Multi-Sensor Adaptive Process. (CAMSAP)*, Dec. 2015, pp. 41–44. DOI: 10.1109/CAMSAP.2015.7383731.